Dipartimento di Matematica e Fisica
PhD Course in Physics
XXXVII cycle

Title of Thesis

Electromagnetic Characterization of Dirty Ice and NaCl Doped Ice for Radar Investigations of Jupiter Icy Moons

PhD Candidate
Alessandro Brin

Supervisor
Prof. Sebastian Lauro

Coordinator
Prof. Giorgio Matt

Academic Year 2024/2025

Contents

List of Figures

List of Tables

Acknowledgments

Firstly, I would like to thank my supervisor, Prof. Sebastian Lauro, whose guidance has been essential to me. He gave me the space to make mistakes, do my best, and improve every day, and I will be eternally grateful for that. Your dedication has greatly helped me become a better researcher, allowing me to grow in confidence.

I am grateful for the support and patience of Dr. Barbara Cosciotti, who guided me in my first steps in a physics laboratory. I would also like to thank all the members of the Roma Tre Geophysics Laboratory—Elena Pettinelli, Elisabetta Mattei, Francesca Paolucci— and Francesco Basile for helping and supporting me throughout this journey.

I am also grateful for the support of Chloe Martella: we grew up together and have been there for each other in the most difficult times—I will always remember this. I would like to thank Gabriele Turchetti: our trips together to Bormio, Trento, and Florence were special and will always be among my happiest memories. Matteo Dossi was my lunch friend, and I will miss our trivia quizzes together, especially the ones about the US states! Many students and colleagues have been fundamental to me through their support and friendship: Elena, Giorgia, Jamal, Federico, and Emanuele deserve a special mention, thank you.

My family has always been there when I needed them, ever since I left Naples in 2015, and I definitely couldn't have done it without them. Your words and presence have guided me for years, helping me grow and making me the peaceful person I feel I am today: vi voglio bene, mamma, papà e brodino, grazie di tutto.

Trashless boys and girls: you are the friends I always dreamed of having as a child, thank you for always being there.

Dulcis in fundo, Giulia, I cannot fully express how grateful I am for your support. We started living together before I started my PhD, and you have accompanied me with love and tenderness throughout this exhausting journey: you are and will forever be the love of my life.

Introduction

Jupiter's icy satellites, namely Europa, Ganymede and Callisto will be the main target of two space missions in the near future, Juice and Europa Clipper, by the European Space Agency and NASA, respectively. These bodies have several exceptional characteristics for our Solar System: first, they are so-called "ocean worlds," since they harbor oceans of liquid water beneath their icy crusts. Europa, of the three the closest to Jupiter, has a geologically young and active surface that is constantly reshaping itself; while Callisto, the farthest from the planet, has the most cratered surface in the solar system. Ganymede is the largest satellite in our system, and the only one to have its own magnetic field with associated magnetosphere. In addition to these unique features from a scientific point of view, these three satellites are extraordinary objects of study for two main reasons: a) they are very promising in terms of the search for extraterrestrial life; in particular, Europa, whose subsurface ocean interacts directly with the seafloor, would have at its disposal the three ingredients that we believe are essential for life, namely liquid water, a source of energy and access to nutrients and organic compounds; b) studying them will prove essential for understanding the formation patterns of planets and satellites from the protoplanetary disk in this region of the Solar System, moreover the Jovian system being an archetype of gas giant systems.

The two space missions will thus represent the necessary step for the exploration of the outer Solar System, and will have the opportunity for the first time in history to study the internal structure of the first kilometers of these objects. This will be possible through the Radio Echo Sounding technique, which has already been successfully employed on Earth, Mars and Moon, and through the use of radar will be able to detect layers of water and discontinuities within the crust, creating images of the subsurface. In fact, radio waves emitted by radar travel through the sub-surface of the investigated body and attenuate and reflect according to the electromagnetic properties (electrical permittivity and magnetic permeability) of the medium they penetrate. For proper interpretation and understanding of the images produced by this technique, it is necessary to characterize materials and analogs that accurately simulate the surface and subsurface of these bodies. The purpose of this dissertation is to characterize through extensive experimental work the electrical permittivity and magnetic permeability of two types of ice that have been observed on the surface of Jupiter's icy moons: namely, so-called "dirty ice," i.e., ice contaminated with mineral grains mechanically trapped within its matrix, and NaCl doped ice, i.e., ice formed from liquid solutions of sodium chloride.

Electrical permittivity and magnetic permeability are two parameters that depend first on the frequency and temperature at which they are being studied, and then on the physical characteristics of the material under investigation, such as porosity in the case of powders and salinity in the case of doped ices. In the present work, these two physical quantities were characterized at 9 and 60 MHz, the working frequencies of the two planetary radars that will investigate the moons (RIME and REASON, aboard the Juice and Europa Clipper missions, respectively), and at the expected temperatures on the surface of the three satellites. Contextually, indications were given of the performance of the two radars, estimating their attenuation.

The first chapter of this manuscript detailed the main physical and geological features of Europa, Ganymede and Callisto, focusing on the state of the art knowledge of the compounds observed on the surfaces of the three moons. In the second chapter, electromagnetic theory useful in the course of this work was addressed, starting with Maxwell's equations and polarization phenomena within dielectrics, and then describing the electromagnetic properties of several geomaterials used in this thesis. In the third chapter, the mixing formula theory was exposed, presenting a discussion of the main equations used to reproduce the permittivity of multiphase compounds. The two measurement techniques employed in this experimental work are the subject of the fourth and fifth chapters of this thesis: in particular, the experimental setups and instrument calibration procedures were described. The main types of ice found on Earth and observed and speculated to be present in the Solar System together with their electrical properties were reviewed in the sixth chapter, and the theory behind the inversion processes used to fit the experimental data was described in the seventh. In the eighth chapter, granular and iced samples were characterized and the experimental procedure used for their preparation was also described. Finally, the measurements and their analysis were presented in the last two chapters: in chapter nine measurements of “dirty ice” were presented and discussed, modeling its electrical properties as a function of temperature and dust inclusions; measurements and modeling of electrical properties of NaCl doped ice as a function of temperature and sodium chloride concentration were presented in chapter ten.

Chapter 1

Jupiter Icy Moons

The four largest moons of Jupiter, Io, Europa, Ganymede and Callisto are also named *Galilean* moons after Galileo Galilei, who discovered them in 1610. The observation of these satellites took place through a telescope, the invention of which opened an era of discovery in astronomy and provided new evidence to support the Copernican heliocentric theory, which stated that Earth and the other planets orbited around the sun, positioned at center of the universe. Nowadays these moons are once again of great interest to the scientific community, due to their physical-geological characteristics that could make them capable of harboring extraterrestrial life.

Europa, Ganymede and Callisto are perfect case studies of so-called "ocean worlds", i.e. bodies that host oceans of liquid water globally at the surface or at depth (as in this case), and for this reason they are promising candidates for the search for extraterrestrial life. Europa, Ganymede and Callisto are found in a 1:2:4 Laplace resonance, probably because of early formed satellite's interaction within the primordial circumjovian disk [1]. Moreover, they are in 1:1 spin-orbit resonance, such as many satellites in the Solar System.

This chapter will report on the main features of the moons of interest to this work along with the most up-to-date models of the surface and first kilometers of crust, focusing on the physical properties of their ice.

In the end, the two spacecraft missions that will be responsible for in-depth study of Jupiter's icy moons in the future will be detailed: Jupiter Icy Moons Explorer (Juice), launched by the European Space Agency in April 2023, and Europa Clipper, scheduled to launch in October 2024 by NASA.

1.1 Europa

Europa is the smallest of the four Galilean moons and it has the smoothest surface of any satellite in the Solar System in contrast to the heavily cratered terrain of Callisto (see tab. 1.1 for the main physical parameters of the moon). The extreme paucity of impact craters suggest that the moon is geologically young and active. Moreover, beneath the icy crust the moon harbors a water ocean that probably lies directly on the silicate mantle. Due to its chemical and physical features Europa represents one of the most promising target in our Solar System for the search of extraterrestrial life.

R (km)	1560.8 ± 0.5
M (10×10^{22} kg)	1.593
V (10×10^{19} m^3)	5.9
ρ (g/cm^3)	3.013
C/MR^2	0.346 ± 0.005
Albedo (visible)	0.7
Mean surface temperature (K)	90

Table 1.1: Europa's main physical parameters [2],[3],[4].

1.1.1 Surface

Europa's surface characterized by several geological features (see Fig. 1.1): a) *linae*, i.e., long, curvilinear narrow fractures in the ice crust that can span over a hemisphere and might provide a direct or indirect connection with the water ocean below; b) *chaos terrain*, highly disrupted areas with jumbled, broken ice blocks probably formed by the upwelling of warmer material from below the ice crust [5]; c) *lenticulae*, i.e., round, reddish spots that are most often interpreted to be the product of upwelling of hot, less dens material rising to the surface; d) *double ridges*, quasi-symmetric ridge pairs flanking a medial trough which is hypothesized to be formed through a complex process consisting of successive refreezing, pressurization and fracture of the water within the shallow crust [6]; e) *pits*, i.e. depressions in the surface that are often associated with the collapse of the ice crust.

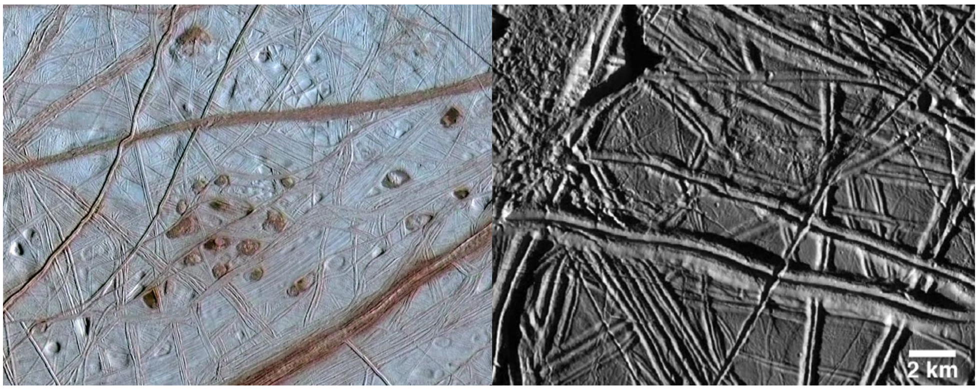

Figure 1.1: Typical lenticulae (left) and double ridges (right) on Europa's surface (NASA/JPL-Caltech).

A combination of endogenic and exogenic processes affects the surface of the moon, influencing the composition and the albedo (see Fig. 1.2). The exogenic processes include the impact cratering and charged particle bombardment from the Jupiter's rotating magnetosphere. The trailing hemisphere is the more affected by the sulfur radiolysis since the sulfur plasma ions from the volcanos of Io corotate with the Jupiter's magnetosphere and then precipitate on Europa's surface [7]. For this reason, the trailing hemisphere appears significantly darker and redder than the leading hemisphere [8]. Furthermore, far-UV oxygen and hydrogen emission have been observed in the tenuous atmosphere of the moon: they were interpreted as dissociation products of water, as a result of plume activity triggered by an active endogenous cryovolcanism, long hypothesized and still a matter of debate [9], [10],[11].

The magnesium sulfate detected on the trailing hemisphere is an example of combination of both endogenic and exogenic processes; in fact it is hypothesized to be formed by the magnesium, endogenous and coming from the underlying ocean, and the sulfur, coming from Io. Several models try to explain the origin and the spatial variability of the compounds detected on the surface: future space missions will be able to shed light on the distinction between endogenous and exogenous compounds.

Table 1.2 reports the result of the main observations of the surface of the moon.

1.1.2 Interior

The measurements of Europa's density, quadrupole gravitational coefficients and shape indicate that the moon is fully differentiated into a metallic core, silicate mantle, a water ocean and an ice shell [12].

The thickness of Europa's ice shell is estimated to vary widely, ranging from a few kilometers [13] to several tens of kilometers [14]. It is not yet clear what the salinity values of the satellite's crust ice are, but recently several models have made comparisons between the Europa's ice and the types of ice on Earth described in 4.4. As a first approximation the ice crust formed and evolved under two different thermal gradients, depending on the depth at which it grew [15]: i) Europa shallow ice shell (<1 km) experiences an high thermal gradient due to the 100 K surface and it has high impurities uptake, even possibly larger than that of terrestrial sea ice; ii) on the contrary, at greater depths Europa's ice shell presumably formed with a lower thermal gradient similar to that of terrestrial marine ice, where salt entrainment has approached its lower limit and where the regions inside the ice begin to be no longer

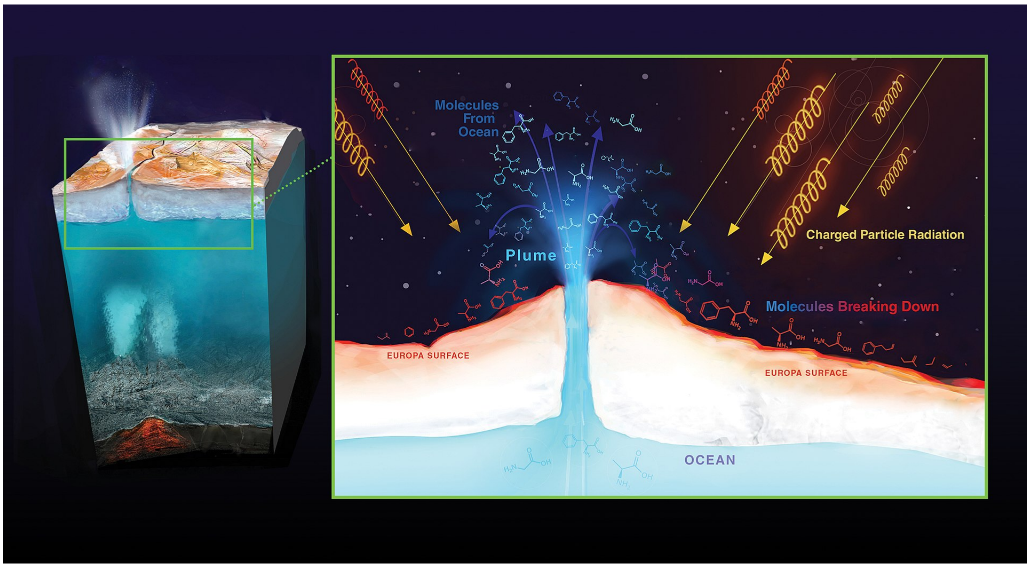

Figure 1.2: Artistic depiction of the combination of exogenic and endogenic processes on Europa's surface (NASA/JPL-Caltech).

hydraulically connected in a pore network due to the lack of salts.

It was found that tidally induced stress field generates surface cracks that are may able to penetrate to the whole brittle layer of Europa's shell [16]. Both sea ice measurements on Earth and radar backscattering data from Europa show that the ice is highly porous and the size of the pores inside of it is on the order of the millimeter, but the porosity-induced scattering should not be significant [16]. Using the methods developed in [17] it was observed that high porosity may exist in the brittle layer's upper half (up to 1500 meters deep) and decreases to zero in the lower half. From reflectance and polarization phase curve measurements of highly reflective planetary regolith analogues it has been noted that a strong resemblance of the polarization phase curves of Europa to those of highly porous samples, suggesting that the surface of both hemispheres may have porosities exceeding 90% [18] and confirming the work done in [19]. Moreover, at least low porosities of the ice on Europa's surface are required to explain the existence of icy plate tectonics [20], hypothesized to be present locally on the moon [21]. The extensional tectonic patterns on Europa's surface imply that the conductive part of its ice shell may have significant porosity.

Ocean

The composition of the subsurface ocean can only be inferred from the study of the surface of the moon. Currently there are several scenarios, depending on which compound is most present on the surface, information still unknown. Nevertheless, there are two endmember compositions for Europa's ocean in current models: Cl-dominated and SO_4-dominated.

One of the main non-ice components on the surface of Europa has likewise been identified as NaCl (see Tab 1.2). It is possible to obtain such a surface composition in two ways, according to [22]: i) if the ocean is mostly composed of sodium and chloride, with a low presence of magnesium sulphate or ii) if the quantities of sodium, magnesium, sulfate, and chloride in the ocean are nearly equivalent, and the freezing rate is fast enough to produce noticeable amounts of NaCl on the surface. Moreover, if epsomite ($MgSO4 \cdot 7H_2O$) is eventually confirmed on Europa's surface, it may indicate that the underlying ocean is relatively sodium-poor or that $MgCl_2$ is being radioactively converted to $MgSO_4$, as proposed in [23]. In this scenario mirabilite and $MgCl_2$ hydrates brines froze at the surface and with the implantation of sulfur ions from Io, $MgCl_2$ become epsomite. To understand the composition of the ocean it is necessary to know which compounds detected on the surface may be of endogenous origin and which are of exogenous origin. So, if the epsomite, of the other hand, is of endogenous origin, this would imply that the underlying ocean is rich in magnesium and sulfate, and relatively poor in sodium [22].

Detected compounds	**Region investigated**	**Methods**	**Reference**
Sulfates (hexahydrite, epsomite), arbonates (natron), mixtures of carbonate and sulfate minerals	Optically dark regions in a near-hemispheric area (leading hemisphere)	Galileo NIMS	[24]
Complex mixtures of sulfate hydrates (e.g. hexahydrite, espomite bloedite, mirabilite, sodium sulfide nonahydrate, magnesium solfate dodecahydrate) and other materials, mirabilite brines, mixtures of carbonate and sulfate minerals	Icy terrain located at approximately (25°N, 205° W) and non-icy terrains located at approximately (8°N, 235° W), midlatitude northern hemisphere on the trailing side, equatorial plains on the leading side	Galileo NIMS	[25], [26]
$MgSO_4$ brine; lack of any clear detection of sulfate salt; predicted $NaCl$ and KCl	Dark low latitude trailing hemisphere; bright low latitude leading hemisphere	Infrared spectrographs coupled with adpative optics system on large ground-based telescopes (W. M. Keck Observatory)	[23]
H_2SO_4; anhydrous salts (e.g. NaCl and KCl)	Trailing hemisphere; leading hemisphere (chaos units)	Infrared spectrographs coupled with adpative optics system on large ground-based telescopes Keck II telescope (Keck/NIRSPEC)	[27]
Mixture of magnesium chloride, magnesium chlorate and magnesium perchlorate; hydrate sulfuric acid	Chaos terrains and darker areas; trailing hemisphere	VT/SINFONI	[28]
Spectra consistent with NaCl	Leading hemisphere equatorial area	Keck II/NIRSPEC	[29]
NaCl	Leading hemisphere chaos terrain and older terrains	HST/STIS	[30]
H_2O_2	Leading hemisphere Low latitude chaos therrains	Keck II/NIRSPEC	[31]
Sulfur allotropes, endogenous material altered by sulfur radiolysis	Trailing hemisphere	HST/STIS	[32]
NaCl	Leading hemisphere chaos terrain	HST/STIS	[33]
Hexahydrite, sulfuric acid, magnesium chloride, sodium solfate decahydrate	Leading hemisphere	Galileo NIMS	[34]
UV-absorbing contaminants mixed within the water ice; sulfur dioxide	Leading hemisphere; trailing hemisphere	HST/STIS	[35]

Table 1.2: Compounds detected on the Europa's surface; the instrument that performed the observation is reported together with the region investigated.

1.2 Ganymede

Ganymede presents a compelling target for Solar System exploration due to its unique characteristics and potential insights into planetary evolution. Having a radius of 2631 km, is the largest moon of the Solar System and the only one with a permanent magnetic field. In fact, its mini-magnetosphere is constantly interacting with the co-rotational plasma flow and electromagnetic fields of the fast-rotating Jovian magnetosphere. Thus a dynamic interaction region, similar to the Earth's magnetosphere, is created.
Its main physical parameters are reported in table 1.3.

R (km)	2634.1 ± 0.3
M (10×10^{23} kg)	1.482
V (10×10^{19} m^3)	7.6
ρ (g/cm^3)	1.942
C/MR^2	0.311 ± 0.003
Albedo (visible)	0.45
*Mean surface temperature (*K*)*	125 ± 25

Table 1.3: Ganymede's main physical parameters [2],[3],[36].

1.2.1 Surface

Ganymede is characterized by a wide range of impact features, much more than most other planetary surfaces: extensive multi-ring structures, ancient impact scars termed *palimpsests* in low relief, craters with central pits and domes, pedestal craters, dark floor craters and craters with dark or bright rays [37]. The surface of the moon undergoes space weathering processes caused by the impact of solar flux (UV), micro-meteoroids and energetic particles. For example, the opening of the satellite's magnetic field's lines shapes and modifies the surface, and for this reason polar caps are brighter than the equatorial region. Moreover, the leading hemisphere is brighter than the trailing hemisphere [38], due to a higher abundance of non-ice materials of the latter. The magnetosphere plays a key role in shielding the regions at latitudes below 40°from electrons with energies up to approximately 40 MeV [39]; moreover, the trailing hemisphere is also shielded from heavy ions up to hundreds of keV [40], while at polar polar latitudes the ion bombardment is much higher [41], [42].
Amorphous ice is present at the polar regions, as revealed by the Near Infrared Mapping Spectrometer (NIMS) on board *Galileo* [43], probably due to more energetic bombardments [44]. In any case, spectral modeling confirms that on Ganymede the H_2O-ice, predominantly crystalline thanks to the intrinsic magnetic field, is the major constituent of the satellite, especially at the equatorial regions. Water ice is ubiquitous on its surface and several papers suggest that it represents 50-60 $wt\%$ up to 90 $wt\%$ of the surface. The size of ice is small ($\leq$50 μm) at the polar regions, while equatorial regions are mostly composed of larger grains ($\geq$200 μm up to 1 mm) [36].
Current knowledge about the composition of the surface is given by different observations performed on board the NASA *Galileo* and Juno spacecrafts, and by ground-based and space-based telescopes. A brief review of the main compounds detected on the moon's surface is shown in Table 1.4. It has been observed that the dark regions are characterized by dirty ice, which it is thought to be composed by an intraparticle mixture (water ice grains containing dust inclusions [45]) of three components [46], [47], [48]:

- water ice;
- hydrated salt minerals;
- non-ice hydrated material (the darkening agent), with a composition compatible with a C-type carbonaceous material, tholins, amorphous carbon, graphite and silicates.

Moreover, internal structure models of the rock/iron constituent of the the three icy satellites point to a chemical composition similar to the material of L/LL ordinary chondrites [49]. From thermal continuum observations of Ganymede at millimeter wavelengths it was speculated that on the moon there is a compaction gradient from a surface porosity of 85% to a deep porosity of 10%, in the scale of tens centimeter range. In any case, porosity should rapidly drop to zero at a depth of few hundred meters because of the expected pressure [50], based on model of Ganymede's interior elaborated in [51].

Detected compounds	**Region investigated**	**Methods**	**Reference**
SO_2 frost	Trailing hemisphere	Observations with the space-based telescope International Ultraviolet Explorer (IUE)	[52]
Darkening agent (hydrated silicates), Mg and Na sulfates, chlorinated brines	Surface fully covered by a mosaic of ten overlapping observations	Near-infrared ground-based integral ield spectrometer SINFONI of the Very Large Telescope (VLT)	[36]
Intraparticle mixtures of ice and darkening agent (silicates, Triton-type tholin, or H_2O_2	Leading and trailing hemispheres	Reflectance spectra obtained with Hubble Space Telescope Cosmic Origins Spectrograph (HST/COS)	[45]
Dense-phase O_2	From low to midlatitudes on the trailing hemisphere and at high latitudes on the leading one	Infrared observations with HST using the Space Telescope Imaging Spectrograph (STIS)	[53]
Darkening agent (Hydrated silicates, carbonaceous compounds or hydrated salts; magnesium chloride and magnesium sulfate salts; hydrated sulfuric acid	Galileo Regio, Osiris Crater, Polar region	High spatial resolution near-infrared observation from the ground-based VLT/SPHERE instrument	[54]
CO_2, H_2O_2, sulfuric acid hydrates	Leading and trailing hemispheres	Near-infrared Spectrograph and Mid-Infrared Instrument of the James Webb Space Telescope (JWST/NIRSpec-MIRI)	[48]
Mixtures of $NaCl \cdot H_2O$, NH_4Cl, $NaHCO_3$ or $\left(NH_4\right)_2CO_3$ and $Na_2Mg\left(SO_4\right)_2 \cdot 4H_2O$	Trailing hemisphere: latitudes 10°N to 30°N longitudes -35°N to +40°E	High spatial resolution infrared spectra observed with the Jovian InfraRed Auroral Mapper (JIRAM) on board Juno spacecraft	[47]

Table 1.4: Compounds detected on the Ganymede's surface; the instrument that performed the observation is reported together with the region investigated.

From the geological point of view, Ganymede is divided in the first instance into dark and bright terrains, two areas with different features.

Dark Terrain

This type of terrain is heavily cratered and estimated to be >4 Gyr old [55]; these areas represent about 1/3 of Ganymede's total surface. The dark material has a higher abundance of impurities and is composed of a dark deposit overlying the icy material; it's been modified over the years by several surface endogenic processes (it is still under debate weather tectonism or icy volcanism) and exogenic processes (sublimation and deposition of volatiles such as H_2O, mass wasting and sputtering by particles coming from Jupiter's magnetosphere [56]). In these regions Galileo's spacecraft images have shown the presence of old multi-ringed structures, named *furrow systems*, which indicate that tectonic activity has been present at some point in the past. These regions are also supposed to have a thicker regolith layer.

Bright Terrain

The bright grooved terrain is tens to hundreds kilometers wide and it crosscuts the dark terrain, creating a peculiar mixture. These closely spaced grooves are termed *sulci.* This type of soil is generally younger, being approximately 2 Gyr old, and less dens (2 to 10 times) than the darker one, extending in long swaths which alternate with ridges and troughs, even for hundred of kilometers.

Furthermore, high resolution Galileo images suggest an extensional tectonic model of grooved terrain formation (see Fig. 1.3): the bright terrain have formed at the expense of dark soil, with the tectonic resurfacing consisting of extensional rifting; in this way dark terrain transforms into bright.

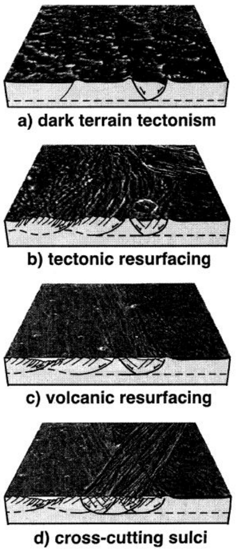

Figure 1.3: Tectonic model for the evolution and formation of grooved terrain [56]: (a) furrows in dark terrain can be explained with the presence of normal faults; (b) tectonic deformation may later create some grooved terrain by the disruption of the old surface and it is believed that icy volcanism does not contribute; (c) the combined action of icy volcanism and tectonism brightens and smooths the surface; (d) eventually bright swaths can overlap one another, originating the peculiar patchwork visible at the surface (taken from [56]).

1.2.2 Interior

Galileo observations show that Ganymede has a core size which ranges between one-quarter and one-third of the surface radius, depending on thickness of the ice shell and its sulfur content; on the other hand the mantle mineralogy is dominated by olivine [57]. The presence of a intrinsic magnetic field indicates that his iron core is currently partially melt and hot . This core is probably relatively small, as shown by the small quadrupole coefficient measured by the Galileo magnetometer, and it has likely a $Fe - FeS$ eutectic composition [51].

Differentiation

Differentiation provides important quantities of energy in planetary bodies and can support a subsurface. C/MR^2 value (see Tab. 1.3) for a perfect spherical body with uniform density is equal to 0.4. Ganymede's value is lower and this implies that it has a concentration of denser material towards its own center. So almost all rocky components has sunk in the mantle or the core during the differentiation process and therefore the satellite can be considered fully differentiated.

Ocean

For a standard icy satellite, an H_2O layer will sit directly on the silicate core, but for Ganymede, larger than the average of the icy satellites, the structure is different. Going deep, because of the high pressure,

ice will transform in an high-pressure phase ice, denser than the ice I. In this case it is realistic to believe that there is a "water sandwich"[58]: the ocean will take place between the ice I shell and the higher pressure phase, ice V and VI. Another model suggests that the moon might harbor ice and oceans stacked up in several layer, such as a "club sandwich".
After differentiation, Ganymede's pressure at the water-rock interfaces would tend to obstruct all the micro-fractures and avoid in this way water-rock interactions.

The presence of the ocean is supported by several observations:

- anomalous transitions in morphology of the multi-ringed structures; this phenomenon can be explained by the effect of a subsurface fluid;
- Galileo magnetometer data suggest an induced magnetic field component, so the existence of electrically conductive and saline oceans is possible [59], causing also the aurorae observed by the Hubble Space Telescope [60];
- the internal dynamo and surface that is geologically younger than other satellites implies that Ganymede is warm enough to support an ocean [51];
- tidal activity by Jupiter and the presence of salts or ammonia can help maintain a subsurface liquid water layer.

Although Ganymede is not experiencing a strong tidal heating at the moment, an ancient orbital resonance (which caused an heat spike), can explain the formation of a subsurface ocean [58]. Heat transfer on the satellite is expected to happen via convection.
Lastly, it's still unclear how much is thick Ganymede's ocean, though some models suggest thickness in the order of 100 km [61], at a nominal depth of about 170 km.

1.3 Callisto

Callisto is the outermost Galilean satellite with the oldest surface, being the most densely cratered body of the Solar System. The lack of any geological activity on the surface such as resurfacing makes the satellite a remnant of the early phases of the Jovian System. For this reason, the study of this moon will offer a great opportunity to deepen the knowledge about the formation of planets and satellites in the outer Solar System.
The main physical parameters of the moon are reported in Table 1.5.

R (km)	2408.4 ± 0.3
M (10×10^{23} kg)	1.076
V (10×10^{19} m^3)	5.9
ρ (g/cm^3)	1.839
C/MR^2	0.359 ± 0.005
Albedo (visible)	0.2
Mean surface temperature (K)	134 ± 11

Table 1.5: Callisto's main physical parameters [2],[3],[62].

1.3.1 Surface

The ancient surface of the moon is highly contaminated with a darkening agent (visually dark non ice-materials), such as the Ganymede's surface. Callisto is dominated by crystalline water ice and, as in the case of Ganymede, the ice grain sizes are larger in the equatorial region, decreasing toward the poles [63]. CO_2 is found everywhere on the surface except at high latitudes, and it is probably formed through trapping mechanisms such as ice clathrates. The abundance of this compound is higher in the trailing hemisphere and in the floor, rim and impact craters [64]. The detected compounds are shown in Table

1.6.
The surface diurnal temperature on Callisto varies between $\approx 80\,K$ and $\approx 165\ K$ [65].

Detected compounds	**Region investigated**	**Methods**	**Reference**
$SO_2 - H_2S$ mixtures, SO_2, CO_2, tholins	Trailing and leading hemisphere	Galileo NIMS	[66], [67]
CO_2, SO_2	Trailing and leading hemisphere	Galileo NIMS	[68]
Weathered organic species (e.g., CN compounds, azoethane $C_2H_5N = NC_2H_5$	South polar regions	Galileo Ultraviolet Spectrometer (UVS)	[69]
S-bearing species: thermally altered sulfur, disulfanide, HS_2	Leading hemisphere	NIR SpeX spectrograph/imager on NASA's Infrared Telescope Facility (IRTF)	[70]

Table 1.6: Compounds detected on the Callisto's surface; the instrument that performed the observation is reported together with the region investigated.

1.3.2 Interior

The Callisto's C/MR^2 value indicates that it is only partially differentiated and therefore the non-water materials are probably more homogeneously distributed in the whole body, that is essentially a mixture of rock and ice. The density and moment inertia values are compatible with the existence of a small silicate core, incapable of generating an intrinsic magnetic field [71] and it is very likely that the region of mixed ice and rock-metal extends to the center of the satellite [72]. The ice-rock differentiation is a slow ongoing process and rock-metal should eventually sink through the ice shell to the center of the moon [72].

Magnetic field perturbations measured during Galileo flybys are consistent with the presence of a salty ocean 150-200 km deep, at least a few kilometers thick [73].

1.4 Spacecraft Missions

The Jupiter system has been investigated by several spacecraft missions, starting from the 1970s. The first ones were Pioneer 10 and 11, that provided the first close-up images of the gas giant and its moons, and then Voyager 1 and 2 offered more detailed views, revealing complex geological features and suggesting subsurface oceans on the moons. Galileo, the first spacecraft to orbit Jupiter, provided compelling evidence for a subsurface ocean on Europa, Ganymede and Callisto. Finally Juno, currently in orbit around Jupiter, is focused on studying the planet's interior, but has also provided valuable data on the surface of the moons.
In the future two spacecraft missions will focus mainly on the moons of Jupiter: Juice and Europa Clipper. The mission will characterize the three moons both as planetary objects, since the systems such as the Jupiter one are less understood than the terrestrial planets [58], and as habitats, since they harbor liquid water which wold make potentially habitable for extraterrestrial life.

1.4.1 Juice

Juice will use a suite of ten scientific instruments, one experiment and one radiation monitor to make detailed observations of Jupiter's and icy moons' environments, focusing on Ganymede.
Juice will conduct flybys of Venus, Earth, and the Earth-Moon system throughout the course of its eight-year journey to Jupiter. Six months before entering the Jupiter's orbit in July 2031, Juice will begin its nominal science phase. The spacecraft will eventually mainly focus on Ganymede, effectively entering the

satellite's orbit. In Table 1.7 the timeline of the mission is detailed. Juice will be the first spacecraft in the history of space exploration to: a) perform a lunar-Earth gravity assist, b) change orbit from another planet to one of its moons (in this case from Jupiter to Ganymede), and c) orbit a satellite other than Earth's Moon.

Date	Phase
14 April 2023	Launch from Kourou with Ariane 5
August 2024	First Earth flyby
August 2025	Venus flyby
September 2026	Second Earth flyby
January 2029	Third Earth flyby
July 2031	Jupiter orbit insertion
July 2031-June 2032	Energy reduction phase
July 2032	2 Europa flybys
August 2032-August 2033	Jupiter inclined phase - Callisto flybys
November 2033-November 2034	Transfer to Ganymede
December 2034	Ganymede orbit insertion
September 2035	End of nominal mission

Table 1.7: Timeline after launch of the Juice mission.

Payload

Juice will carry 10 instruments (see Fig. 1.4): a *remote sensing package* (JANUS, MAJIS, UVS, SWI) that will perform spectral imaging from the ultraviolet to the sub-millimeter wavelengths; a *geophysical package* that comprises a radar sounder (RIME), a laser altimeter (GALA) and a radio science experiment (3GM) to probe the atmospheres and measure the gravity fields; and an *in situ package* with a suite of instruments to study the particle environment (PEP), a radio and plasma wave instrument (RPWI) and a magnetometer (J-MAG).

The science teams and the instruments are provided primarily by ESA member states, with the exception of one instrument (UVS) provided by NASA and hardware for various instruments, developed by NASA, JAXA (Japan Aerospace Exploration Agency) and ISA (Israel Space Agency).

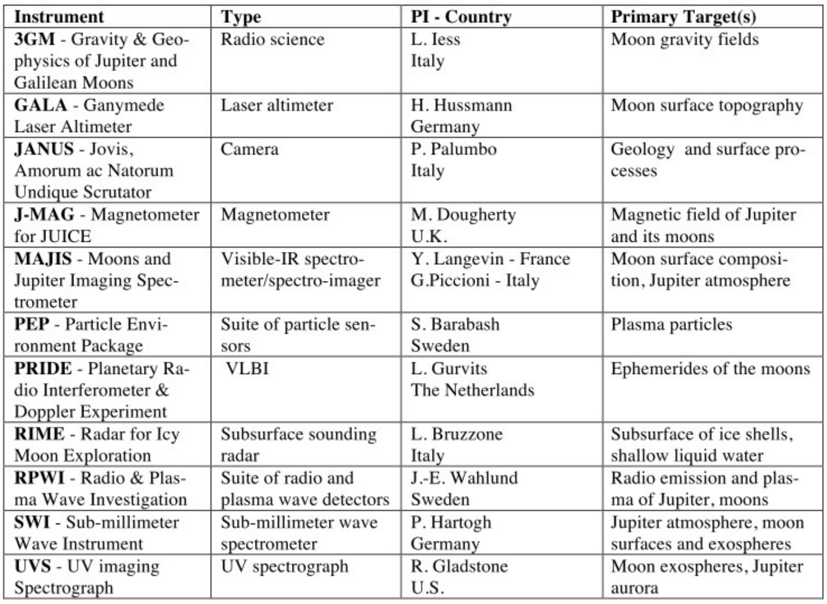

Instrument	Type	PI - Country	Primary Target(s)
3GM - Gravity & Geophysics of Jupiter and Galilean Moons	Radio science	L. Iess Italy	Moon gravity fields
GALA - Ganymede Laser Altimeter	Laser altimeter	H. Hussmann Germany	Moon surface topography
JANUS - Jovis, Amorum ac Natorum Undique Scrutator	Camera	P. Palumbo Italy	Geology and surface processes
J-MAG - Magnetometer for JUICE	Magnetometer	M. Dougherty U.K.	Magnetic field of Jupiter and its moons
MAJIS - Moons and Jupiter Imaging Spectrometer	Visible-IR spectrometer/spectro-imager	Y. Langevin - France G.Piccioni - Italy	Moon surface composition, Jupiter atmosphere
PEP - Particle Environment Package	Suite of particle sensors	S. Barabash Sweden	Plasma particles
PRIDE - Planetary Radio Interferometer & Doppler Experiment	VLBI	L. Gurvits The Netherlands	Ephemerides of the moons
RIME - Radar for Icy Moon Exploration	Subsurface sounding radar	L. Bruzzone Italy	Subsurface of ice shells, shallow liquid water
RPWI - Radio & Plasma Wave Investigation	Suite of radio and plasma wave detectors	J.-E. Wahlund Sweden	Radio emission and plasma of Jupiter, moons
SWI - Sub-millimeter Wave Instrument	Sub-millimeter wave spectrometer	P. Hartogh Germany	Jupiter atmosphere, moon surfaces and exospheres
UVS - UV imaging Spectrograph	UV spectrograph	R. Gladstone U.S.	Moon exospheres, Jupiter aurora

Figure 1.4: List of the Juice experiment, their primary science contribution and key characteristics (taken from [74]).

RIME

The Radar for Icy Moons Exploration (RIME) is a radar sounder optimized for the penetration of Ganymede, Europa and Callisto up to a depth of 9 km [75]. Its primary goal will be to locate the ice-ocean interface and present or past reservoirs of liquid water inside the ice shell of these moons, such as unconnected water pockets. Moreover, the radar will be employed to map the existence of thermal structures in the icy crusts and to identify the brittle-ductile transition of the ice, also measuring its thickness. The data sheet of the radar RIME is shown in table 1.8

Main Instrument parameters	Parameter values
Operating height (km)	<1000
Transmitted central frequency (MHz)	9
Antenna type	Dipole
Optimal antenna length (m)	16
Peak radiated power (W)	10
Chirp length (μs)	50-250 (programmable)
Pulse repetition frequency (Hz)	10-1000 (programmable)
Vertical resolution in ice (m)	50-140
Cross-track resolution (km)	2-10
Along-track resolution (km)	0.3-1.0

Table 1.8: Data sheet of the radar RIME (taken from [76]).

1.4.2 Europa Clipper

Europa Clipper is a spacecraft developed by NASA planned for launch on October 2024. Its main goal is to study the moon Europa with multiple flybys, assessing the composition and geology of the ice crust and the ocean beneath it and evaluating the its habitability. The spacecraft will gather data after the insertion in Jupiter's orbit with 49 close flybys of Europa at distances ranging from 25 to 100 kilometers. In Table 1.9 the timeline of the phases of the mission is detailed.

Date	Phase
10 October 2024	Launch from Cape Canaveral with SpaceX Heavy Falcon
28 February 2025	Mars gravity assist
2 December 2026	Earth gravity assist
11 April 2030	Jupiter orbit insertion
April 2030-Mars 2031	Ganymede gravity assists
Mars 2031	Beginning of Europa flybys

Table 1.9: Timeline after launch of the Europa Clipper mission [77].

Payload

The Europa Clipper mission is equipped with a comprehensive suite of nine scientific instruments, consisting in *remote sensing* and *in situ* instruments. The imagers of the payload are EIS (Europa Imaging System) that will produce high-resolution color and stereoscopic images of the moon and the Europa Thermal Emission Imaging System (E-THEMIS), a thermal imager; the spectrometry will be covered by Europa-UVS, an ultraviolet spectrograph and the Mapping Imaging Spectrometer for Europa (MISE), an infrared spectrometer. The in situ instruments consist of the Europa Clipper Magnetometer (ECM) for measuring magnetic fields, the Plasma Instrument for Magnetic Sounding (PIMS) for analyzing the plasma environment, the Mass Spectrometer for Planetary Exploration/Europa (MASPEX) for studying atmospheric composition, and the SUrface Dust Analyzer (SUDA) for analyzing dust particles.

REASON

The Radar for Europa Assessment and Sounding: Ocean to Near-surface (REASON) is a dual-frequency ice-penetrating radar on board the Europa Clipper mission. This instrument will search for the ice-ocean interface, characterizing the ice shell's global structure and investigating the processes governing the material exchange between the ocean and the surface [78].
The data sheet of REASON is shown in table 1.10

Main Instrument parameters	**Parameter values**
Operating height (km)	<1000
Transmitted central frequency (MHz)	9 (HF) and 60 (VHF)
Antenna type	Dipole
Optimal antenna length (m)	16
Peak radiated power (W)	12 to 30
Chirp length (μs)	30-100 (programmable)
Pulse repetition frequency (Hz)	50-3000 (programmable)
Vertical resolution in ice (m)	<300 (HF), <30 (VHF)
Along-track resolution (km)	<5.5 (HF), <2 (VHF)

Table 1.10: Data sheet of the radar REASON [78].

Chapter 2

Electromagnetic Theory

Electromagnetic (EM) methods play an important role in geophysics, offering useful tools and techniques to investigate the subsurface's EM properties. By inducing EM energy into the subsurface and analyzing the subsequent responses of the materials composing it, these methods can provide critical insights into subsurface structures and compositions. Subsurface EM energy is propagated depending on three physical quantities: electrical conductivity, dielectric permittivity, and magnetic permeability, which, in turn, are a function of different physical quantities, such as the frequency of the external EM field, the temperature, the mineralogy of the materials in the case of rocks and the presence of water.
Starting from Maxwell's equations and focusing on the materials electromagnetic properties, this chapter will outline the fundemental concepts of the electromagnetic wave theory which will be used throughout this dissertation.

2.1 Maxwell's Equations and Constitutive Relations

Electric and magnetic phenomena were firstly unified and summarized by Maxwell in a famous paper [79], which led to the discovery by Hertz and Marconi of EM wave propagation. The electromagnetic theory developed by Maxwell can be condensed and described by a set of partial differential equations which relates the variations of electric and magnetic fields to charges and currents associated to the propagation of the electromagnetic waves. The general form of time-varying Maxwell's equations can be written in differential form as [80]

$$\nabla \times \mathbf{e}(\mathbf{r}, t) = -\frac{\partial \mathbf{b}(\mathbf{r}, t)}{\partial t} \tag{2.1}$$

$$\nabla \times \mathbf{h}(\mathbf{r}, t) = \mathbf{j}_i(\mathbf{r}, t) + \mathbf{j}_c(\mathbf{r}, t) + \frac{\partial \mathbf{d}}{\partial t} = \mathbf{j}_i(\mathbf{r}, t) + \mathbf{j}_c(\mathbf{r}, t) + \mathbf{j}_d(\mathbf{r}, t) \tag{2.2}$$

$$\nabla \cdot \mathbf{d}(\mathbf{r}, t) = \rho_q(\mathbf{r}, t) \tag{2.3}$$

$$\nabla \cdot \mathbf{b}(\mathbf{r}, t) = 0 \tag{2.4}$$

where:

$\mathbf{e}$ is the the electric field intensity in V/m

$\mathbf{b}$ is the magnetic flux density in Wb/m^2

$\mathbf{h}$ is the magnetic field density in A/m

$\mathbf{d}$ is the electric flux density in C/m^2

$\mathbf{j}_i$ is the impressed (source) electric current density in A/m^2

$\mathbf{j}_c$ is the conduction electric current density in A/m^2

$\mathbf{j}_d$ is the displacement electric current density in A/m^2

ρ_q is the electric charge density in C/m^3

$\mathbf{j}_i$ and ρ_q are the sources of the EM field and all the field quantities ($\mathbf{e}$,$\mathbf{b}$,$\mathbf{h}$,$\mathbf{d}$,$\mathbf{j}$) are function of the space coordinate $\mathbf{r}$ and the time coordinate t. Eqs. 2.1 and 2.2 embodie respectively the Faraday's law of induction and the Ampere's law, while eqs. 2.3 and 2.4 are based on the Gauss' laws of electric and magnetic field.
From eqs. 2.1-2.4 it is possible to define the constitutive relations that describe the macroscopic interaction between matter and EM field in the time domain:

$$\mathbf{d}(\mathbf{r},t) = \varepsilon * \mathbf{e}(\mathbf{r},t) \tag{2.5}$$

$$\mathbf{b}(\mathbf{r},t) = \mu * \mathbf{h}(\mathbf{r},t) \tag{2.6}$$

$$\mathbf{j}_c(\mathbf{r},t) = \sigma * \mathbf{e}(\mathbf{r},t) \tag{2.7}$$

where ε is the dielectric permittivity of the medium in F/m, μ is the magnetic permeability of the medium in H/m, σ is the conductivity of the medium in S/m and $*$ indicates a convolution product. In this case these three generally complex quantities are assumed to be *linear*, i.e. they are not functions of the applied field, *homogeneous*, i.e. they are not functions of the position, and *isotropic*, i.e. they do not depend on the direction of the applied field. In the simplest case of free space these three quantities have the following values:

$$\varepsilon = \varepsilon_0 = 8.854 \times 10^{-12} (F/m) \tag{2.8}$$

$$\mu = \mu_0 = 4\pi \times 10^{-7} (H/m) \tag{2.9}$$

$$\sigma = 0 \tag{2.10}$$

In the case of non-linear materials eqs. 2.5-2.7 have the form:

$$\mathbf{d}(\mathbf{r},t) = \varepsilon(\mathbf{e}) * \mathbf{e}(\mathbf{r},t) \tag{2.11}$$

$$\mathbf{b}(\mathbf{r},t) = \mu(\mathbf{h}) * \mathbf{h}(\mathbf{r},t) \tag{2.12}$$

$$\mathbf{j}_c(\mathbf{r},t) = \sigma(\mathbf{e}) * \mathbf{e}(\mathbf{r},t) \tag{2.13}$$

When inhomogeneous materials are treated eqs. 2.5-2.7 show their dependence on the position

$$\mathbf{d}(\mathbf{r},t) = \varepsilon(\mathbf{r}) * \mathbf{e}(\mathbf{r},t) \tag{2.14}$$

$$\mathbf{b}(\mathbf{r},t) = \mu(\mathbf{r}) * \mathbf{h}(\mathbf{r},t) \tag{2.15}$$

$$\mathbf{j}_c(\mathbf{r},t) = \sigma(\mathbf{r}) * \mathbf{e}(\mathbf{r},t) \tag{2.16}$$

and, lastly, with anisotropic materials the most general relation between these quantities takes the form of a tensor of rank two, a dyad, and as example eq. 2.5 can be written as

$$\begin{bmatrix} D_x \\ D_y \\ D_z \end{bmatrix} = \begin{bmatrix} \varepsilon_{xx} & \varepsilon_{xy} & \varepsilon_{xz} \\ \varepsilon_{yx} & \varepsilon_{yy} & \varepsilon_{yz} \\ \varepsilon_{zx} & \varepsilon_{zy} & \varepsilon_{zz} \end{bmatrix} \begin{bmatrix} E_x \\ E_y \\ E_z \end{bmatrix} = \begin{bmatrix} \varepsilon \end{bmatrix} \begin{bmatrix} E_x \\ E_y \\ E_z \end{bmatrix} \tag{2.17}$$

and a similar treatment applies to the other equations.

Dispersive Materials

In the majority of practical applications the materials have a response to an external time-varying EM field which is not instantaneous, but depends on time. Dielectric materials, for example, exhibit a *dispersive* behavior and their permittivity and conductivity are a function of time; on the other hand ferromagnetic materials and ferrites have a dispersive magnetic behavior with magnetic permeability varying with time. With the so-called dispersive materials eqs. 2.5-2.7 have the form:

$$\mathbf{d}(\mathbf{r},t) = \varepsilon(t) * \mathbf{e}(\mathbf{r},t) \tag{2.18}$$

$$\mathbf{b}(\mathbf{r},t) = \mu(t) * \mathbf{h}(\mathbf{r},t) \tag{2.19}$$

$$\mathbf{j}_c(\mathbf{r},t) = \sigma(t) * \mathbf{e}(\mathbf{r},t) \tag{2.20}$$

As example, in integral form eq. 2.18 becomes

$$\mathbf{d}(\mathbf{r},t) = \int_{-\infty}^{t} \varepsilon(t-t')\mathbf{e}(\mathbf{r},t')dt' \tag{2.21}$$

2.1.1 Frequency Domain

It is usually convenient to switch from the time domain to the frequency domain, via Fourier transform pair:

$$\mathbf{F}(\mathbf{r},\omega) = \int_{\infty}^{\infty} \mathbf{f}(\mathbf{r},t)e^{-i\omega t}dt; \qquad \mathbf{f}(\mathbf{r},t) = \frac{1}{2\pi}\int_{\infty}^{\infty} \mathbf{F}(\mathbf{r},\omega)e^{i\omega t}d\omega \tag{2.22}$$

assuming an $e^{i\omega t}$ time dependence and where ω is the angular frequency and i the imaginary unit defined as $i = \sqrt{-1}$. The angular frequency is defined as $\omega = 2\pi\nu$, where ν is the frequency. Furthermore, the convolution theorem states that the Fourier transform of the convolution product is equal to the product of the individual Fourier transforms:

$$F\left\{x(t) * y(t)\right\} = X(\omega)Y(\omega) \tag{2.23}$$

Maxwell's equations in the frequency domain are obtained exploiting the Fourier transform properties by replacing $\partial/\partial t = i\omega$

$$\nabla \times \mathbf{E}(\mathbf{r},\omega) = -i\omega\mathbf{B}(\mathbf{r},\omega) = -i\omega\mu\mathbf{H}(\mathbf{r},\omega) \tag{2.24}$$

$$\nabla \times \mathbf{H}(\mathbf{r},\omega) = \mathbf{J}_i(\mathbf{r},\omega) + \mathbf{J}_c(\mathbf{r},\omega) + i\omega\mathbf{D}(\mathbf{r},\omega) = \mathbf{J}_i(\mathbf{r},\omega) + \sigma\mathbf{E}(\mathbf{r},\omega) + i\omega\varepsilon\mathbf{E}(\mathbf{r},\omega) \tag{2.25}$$

$$\nabla \cdot \mathbf{D}(\mathbf{r},\omega) = \mathrm{P}_q(\mathbf{r},\omega) \tag{2.26}$$

$$\nabla \cdot \mathbf{B}(\mathbf{r},\omega) = 0 \tag{2.27}$$

Moreover, in frequency domain eqs. 2.18-2.20 reduce to a simple product thanks to the Fourier transform property (see eq. 2.23):

$$\mathbf{D}(\mathbf{r},\omega) = \varepsilon(\omega)\mathbf{E}(\mathbf{r},\omega) \tag{2.28}$$

$$\mathbf{B}(\mathbf{r},\omega) = \mu(\omega)\mathbf{H}(\mathbf{r},\omega) \tag{2.29}$$

$$\mathbf{J}_c(\mathbf{r},\omega) = \sigma(\omega)\mathbf{E}(\mathbf{r},\omega) \tag{2.30}$$

Throughout this thesis, linear, homogeneous, isotropic and dispersive materials will be analyzed in the frequency domain.

2.2 Wave equation

Combining the Maxwell's equation in time domain with the constitutive relations, we have

$$\nabla \times \mathbf{e} = -\mu\frac{\partial \mathbf{h}}{\partial t} \tag{2.31}$$

$$\nabla \times \mathbf{h} = \mathbf{j}_i + \sigma\mathbf{e} + \varepsilon\frac{\partial \mathbf{e}}{\partial t} \tag{2.32}$$

$$\nabla \cdot \mathbf{e} = \frac{\rho_q}{\varepsilon} \tag{2.33}$$

$$\nabla \cdot \mathbf{h} = 0 \tag{2.34}$$

considering a region of space with no sources (and therefore $\mathbf{j}_i = 0$, $\rho_q = 0$) and taking the curl of eqs. 2.31 and 2.32 we obtain:

$$\nabla(\nabla \cdot \mathbf{e}) - \nabla^2\mathbf{e} = -\mu\nabla \times \frac{\partial \mathbf{h}}{\partial t} \tag{2.35}$$

$$\nabla(\nabla \cdot \mathbf{h}) - \nabla^2\mathbf{h} = \nabla \times \left(\sigma\mathbf{e} + \varepsilon\frac{\partial \mathbf{e}}{\partial t}\right) \tag{2.36}$$

where the propriety of the curl $\nabla \times \nabla \times \mathbf{X} = \nabla(\nabla \cdot \mathbf{X}) - \nabla^2\mathbf{X}$ was applied. Since in the region of space under consideration no sources are present ($\nabla \cdot \mathbf{e} = 0$ and $\nabla \cdot \mathbf{h} = 0$), the equations of wave propagation through a material are obtained:

$$\nabla^2\mathbf{e} = \mu\varepsilon\frac{\partial^2 \mathbf{e}}{\partial t^2} + \mu\sigma\frac{\partial \mathbf{e}}{\partial t} \tag{2.37}$$

$$\nabla^2\mathbf{h} = \mu\varepsilon\frac{\partial^2 \mathbf{h}}{\partial t^2} + \mu\sigma\frac{\partial \mathbf{h}}{\partial t} \tag{2.38}$$

Moving to the frequency domain the wave equations are

$$\nabla^2\mathbf{E} = (\mu\varepsilon\omega^2 - i\mu\sigma\omega)\mathbf{E} \tag{2.39}$$

$$\nabla^2\mathbf{H} = (\mu\varepsilon\omega^2 - i\mu\sigma\omega)\mathbf{H} \tag{2.40}$$

obtained by replacing $\partial/\partial t = i\omega$ and $\partial^2/\partial^2 t = -\omega^2$ by means of Fourier transform properties. It is useful to define the propagation constant as:

$$k = \sqrt{\mu\varepsilon\omega^2 - i\mu\sigma\omega} \tag{2.41}$$

It is possible to approximate these equations in two different cases:

- if $\mu\varepsilon\omega^2 \ll \mu\sigma\omega$, the displacement currents are much smaller than the conduction currents and wave equation 2.39 and 2.40 are called *diffusion equations*

  $$\nabla^2\mathbf{E} = i\mu\sigma\omega\mathbf{E} \tag{2.42}$$

  $$\nabla^2\mathbf{H} = i\mu\sigma\omega\mathbf{H} \tag{2.43}$$

  and the propagation constant become $k \approx \sqrt{-i\mu\sigma\omega}$.

- if $\mu\varepsilon\omega^2 \gg \mu\sigma\omega$, the displacement currents are much larger than the conduction currents; these generally happens to frequencies $> 10^6\ Hz$ and wave equations are

  $$\nabla^2\mathbf{E} = -\mu\varepsilon\omega^2\mathbf{E} \tag{2.44}$$

  $$\nabla^2\mathbf{H} = -\mu\varepsilon\omega^2\mathbf{H} \tag{2.45}$$

  the propagation constant is then defined as $k \approx \sqrt{\mu\varepsilon\omega^2}$.

2.2.1 Wave attenuation and phase

The propagation constant is a complex quantity and it can be also defined as:

$$k = \beta - i\alpha \tag{2.46}$$

where α is the attenuation constant expressed in Np/m which describes the attenuation of the EM wave during the propagation, and β is the phase constant expressed in rad/m and it defines the phase velocity at which the EM wave propagates. Comparing eqs. 2.41 and 2.46, we obtain

$$\alpha = \frac{\omega}{c}\Im\left\{\sqrt{\varepsilon\mu}\right\} \tag{2.47}$$

$$\beta = \frac{\omega}{c}\Re\left\{\sqrt{\varepsilon\mu}\right\} \tag{2.48}$$

where $c = \frac{1}{\sqrt{\varepsilon_0\mu_0}}$ is the velocity of light in vacuum, $\varepsilon = \varepsilon' - i\varepsilon''$ the dielectric permittivity and $\mu = \mu' - i\mu''$ the magnetic permeability. The attenuation can be also expressed in unit of decibels as:

$$\alpha(dB) = 20\ log_{10}\left(e^{\alpha(Np/m)}\right) = 8.686\,\alpha\,(Np/m) \tag{2.49}$$

Finally the attenuation and the phase propagation constants can be enunciated also as a function of the material parameters as:

$$\alpha = \frac{\omega}{\sqrt{2}}\left[\sqrt{\mu'^2 + \mu''^2}\sqrt{\varepsilon'^2 + \varepsilon''^2} - \varepsilon'\mu' + \varepsilon''\mu''\right]^{1/2} \tag{2.50}$$

$$\beta = \frac{\omega}{\sqrt{2}}\left[\sqrt{\mu'^2 + \mu''^2}\sqrt{\varepsilon'^2 + \varepsilon''^2} + \varepsilon'\mu' - \varepsilon''\mu''\right]^{1/2} \tag{2.51}$$

2.3 Dielectrics and Polarization Mechanisms

An ideal dielectric (also called insulator) is a material composed by atoms and molecules where dominant charges are bound and held in place by atomic and molecular forces, and thus they are not free to travel, such as in conductor materials. In fact, these materials exhibit a very different behavior from the conductors where the electric field is shielded due to the displacement of charges inside it. This feature gives the dielectrics the property of being electrically neutral at a macroscopic level; but, although neutral, if they are exposed to an external EM field their charges can slightly shift in relative positions, creating electric dipoles and leading to a separation of positive and negative charge centers at the microscopic level (see fig 2.1).

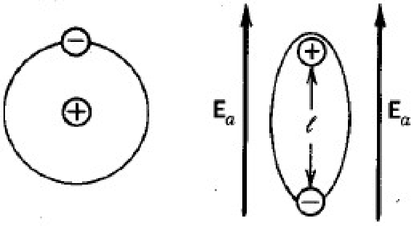

Figure 2.1: Atom without external EM field (left) and under the influence of the EM field (right), (taken from [80]).

The interaction with the EM field provides to the dielectrics the property of store energy (similarly to what happens with springs when they are stretched accumulating potential energy). This behavior can be described using a macroscopic model and the *electrical polarization vector* **P**:

$$\mathbf{P} = \lim_{\Delta V \to 0} \frac{1}{\Delta V} \sum_{i=1}^{N_e \Delta V} d\mathbf{p}_i \qquad \left(C/m^2\right) \tag{2.52}$$

where ΔV is the unit volume under consideration, N_e the number of dipoles per unit volume and $d\mathbf{p}_i$ are the induced moment .
Applying the EM field to a generic dielectric the molecules acquire a non zero mean electric dipole $<\mathbf{p}>$ and orient themselves along the field

$$\mathbf{P} = N_e < \mathbf{p} > \tag{2.53}$$

During the application of an alternating electric field to a dielectric material there is a delay in reaching the state of equilibrium, the so-called *relaxation*; the polarization process, in fact, takes place in two moments: the first one is instantaneous at radar frequencies, given by the distortion of the molecules or atoms, and during the other one the system reaches the equilibrium configuration asymptotically with time. The time needed to reach the state of equilibrium is called *relaxation time*, τ_{rel}. The relaxation frequency is defined as $\nu_{rel} = (2\pi\tau_{rel})^{-1}$. A parameter that describes the dielectrics is the *dielectric permittivity*, indicated with ε, that describes their behavior when subjected to an external EM field.

Applying an alternating electric field **E** to a capacitor in vacuum, the following relationship is obtained

$$\mathbf{D} = \varepsilon_0 \mathbf{E} \tag{2.54}$$

where **D** is the electric displacement vector, defined in eq. 2.28.
Once filled the capacitor with an homogeneous dielectric material (see Fig. 2.2) the electric displacement vector becomes

$$\mathbf{D} = \varepsilon_0 \mathbf{E} + \mathbf{P} \tag{2.55}$$

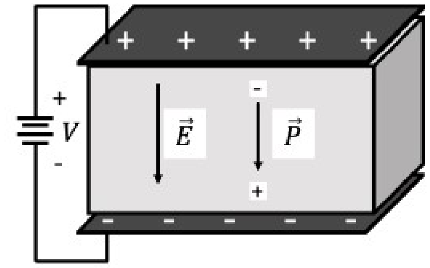

Figure 2.2: Flat capacitor filled by an homogeneous dielectric material. The polarization **P** inside the material is directly proportional to the EM field.

The polarization vector **P** is related to the field by the equation

$$\mathbf{P} = \varepsilon_0 \chi_e \mathbf{E} \tag{2.56}$$

where χ_e is the *electrical susceptibility*, a generally dimensionless-complex quantity that characterizes the dielectric and can be a function of the time, position, temperature, etc. Combining eqs. 2.55 and 2.56 it yields to:

$$\mathbf{D} = \varepsilon_0 \mathbf{E} + \varepsilon_0 \chi_e \mathbf{E} = \varepsilon_0 (1 + \chi_e) \mathbf{E} = \varepsilon \mathbf{E} \tag{2.57}$$

$$\varepsilon = \varepsilon_0 \left(1 + \chi_e\right) \tag{2.58}$$

The relative permittivity of a dielectric material is defined by the ratio of its permittivity and the free space permittivity

$$\varepsilon_r = \frac{\varepsilon}{\varepsilon_0} = (1 + \chi_e) \tag{2.59}$$

The relative permittivity of a dielectric material is a complex quantity where its real part describes the accumulation of energy when exposed to an external EM field, and its imaginary part takes into account the dissipation processes, relaxation losses and static conductivity of the material. The relative permittivity depends in the first place on frequency and then on the physical-chemical properties of the material investigated: temperature, bulk density, mineralogical composition, salinity etc. Evaluating the permittivity represents a key piece for estimating the attenuation and speed of the EM wave propagating in a medium.

2.3.1 Types of Polarization

On the basis of the order of magnitude of the relaxation time it is possible to characterize the material and its relative polarization. Five different types of polarization are described below, providing their relaxation frequencies at room temperature (see Fig. 2.3):

- *Electronic polarization*; it happens when the electric field delocalizes the center of gravity of the electron cloud with respect to the nucleus of the atom and it is evident in many materials (it is more frequent in solids but is also present in liquids). With a polarization time of about 10^{-15} s (period of visible/ultraviolet light) it is the fastest polarization. Electronic polarization establishes a clear relationship between the density of the material and the real part of the relative permittivity. The greater the density of the material, the greater the number of dipoles induced per unit volume, thus increasing the macroscopic response of the material to the electric field.;

- *Ionic or molecular polarization*; the electrical field produces a slight separation of positive and negative charges that generate dipoles, resulting in a distortion of molecules. Materials with positive and negative ions that repel each other when an external

  field is applied are significantly more likely to exhibit this process. It is characterized by a relaxation time of $10^{-13} - 10^{-12}$ s, in far-infrared spectrum; at radar frequencies it is more important than the electronic polarization;

- *Orientational polarization* or *Dipolar polarization*; it is proper to substances (such as water) that have a permanent dipole moment with a random orientation, which makes them macroscopically neutral. Applying the EM field, they tend to line up parallel to the field itself. They have a strong temperature dependence since thermal agitation opposes the polarization given by the field. Due to the frictional force that is generated, this process has a τ of $10^{-11} - 10^{-10}$ s (microwave spectrum, up to a few GHz) for low viscous liquids with small molecules, and $\tau = 10^{-6}$ s for viscous liquids. In the case of pure water at room temperature we find the relaxation frequency at ~ 18.7 GHz;

- *Hopping polarization*; it is the result of localized charges (either electrons and holes or ions and vacancies) moving from one site to the next. In fact, these charges have the ability to move freely between sites for brief periods of time before becoming stuck in certain states and spending the most of their time there, but occasionally they can make a "jump" over the potential barrier to the other sites giving rise to this type of polarization. This is what happens for example with the movement of electrons and holes in glasses and amorphous semiconductors;

- *Space charge polarization* or *Maxwell-Wagner polarization*; it is typical of heterogeneous materials (such as rocks saturated with water), it is due to local displacements of charges towards the interface of the two materials of which the medium is composed of, and it is therefore dependent on its structure and mineralogy. It happens at frequencies lower than 1 MHz, with times ranging from seconds to minutes and it returns a high value of the dielectric constant. A noteworthy case of charges migration polarization is the *polarization of the electrodes* which occurs in capacitors with flat and parallel faces.

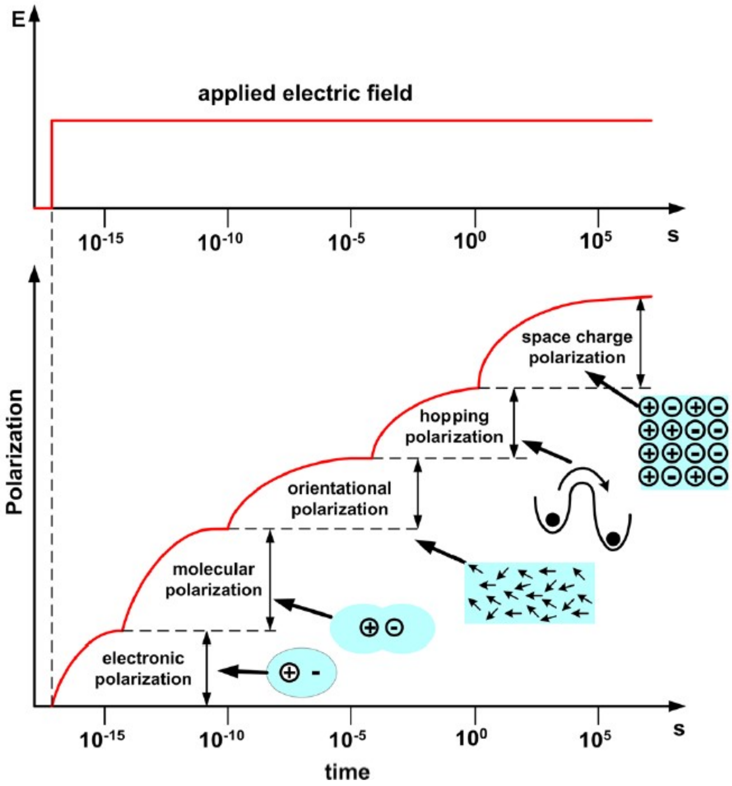

Figure 2.3: Diagram of the most relevant polarization mechanisms in dielectrics (modified after [81]).

2.3.2 Complex Dielectric Permittivity - Circuital Approach

The complex dielectric permittivity can be defined also by means of a different procedure, the circuital approach [82].

Considering a parallel-plate condenser connected to a circuit supplied by a voltage generator $V = V_0 e^{i\omega t}$, the amount of charge stored inside the capacitor will be

$$Q = C_0 V \tag{2.60}$$

where C_0 is the no-load capacitance of the capacitor (the geometric capacitance).
The charging current flowing through the circuit is out of phase by 90° with respect to the voltage and it is equal to the time derivative of the charge Q

$$I_c = \frac{dQ}{dt} = i\omega C_0 V \tag{2.61}$$

In the case where a dielectric is inserted between the plates of the capacitor, its capacitance becomes

$$C = C_0 \frac{\varepsilon'}{\varepsilon_0} = C_0 \varepsilon_r \tag{2.62}$$

In addition to the charging current I_c, a loss current I_l will appear

$$I_l = GV \tag{2.63}$$

in phase with the voltage V and where $G = \frac{1}{R}$ represents the conductance of the dielectric material.
The total current flowing through the capacitor is therefore

$$I = I_c + I_l = (i\omega C + G)\, V \tag{2.64}$$

This current is inclined by a *power factor angle* $\theta < 90°$ with respect to the voltage. Hence, it is possible to define the *loss angle* δ, complementary to θ, which is the angle between I and the component of the current in quadrature with the voltage (see Fig. 2.4). There is a similarity between the behavior of a dielectric and a RC circuit, as the equation points out

$$tg\delta = \frac{I_l}{I_c} = \frac{1}{\omega RC} \tag{2.65}$$

It is more practical to introduce the complex dielectric permittivity to outline the capacitance and conductance because the dissipation process can be caused by a variety of factors, including the dielectric properties of the material inserted into the capacitor:

$$I = (i\omega\varepsilon' + \omega\varepsilon'') \frac{C_0}{\varepsilon_0} V = i\omega C_0 \varepsilon_r V \tag{2.66}$$

where the conductance is defined as $G = \omega\varepsilon'' \frac{C_0}{\varepsilon_0}$.
The loss tangent then becomes the ratio between the imaginary and real part of permittivity

$$tg\delta = \frac{I_l}{I_c} = \frac{\varepsilon''}{\varepsilon'} \tag{2.67}$$

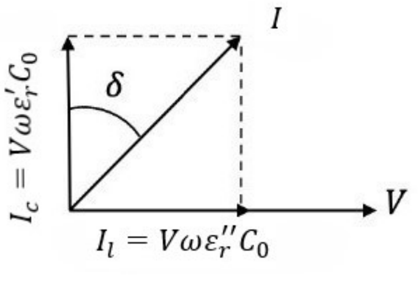

Figure 2.4: Vectorial currents diagram in the capacitor filled with a dielectric material. The total current I is given by the charge current I_c and the loss current I_l; δ is the loss angle. (modified after [83]).

2.3.3 Complex Effective Permittivity and Conductivity

Taking the Maxwell equation in frequency domain 2.25 and considering the complex permittivity $\varepsilon = \varepsilon' - i\varepsilon''$:

$$\begin{aligned}\nabla \times \mathbf{H} = \mathbf{J}_i + \mathbf{J}_c + \mathbf{J}_d &= \mathbf{J}_i + \sigma_s \mathbf{E} + i\omega\varepsilon\mathbf{E} \\ &= \mathbf{J}_i + \sigma_s \mathbf{E} + i\omega(\varepsilon' - i\varepsilon'')\mathbf{E} \\ = \mathbf{J}_i + i\omega\left(\varepsilon' - i\varepsilon'' - i\frac{\sigma_s}{\omega}\right)\mathbf{E} &= \mathbf{J}_i + i\omega\varepsilon_e\mathbf{E}\end{aligned} \tag{2.68}$$

where σ_s is the static conductivity and the complex effective permittivity ε_e was defined as

$$\varepsilon_e = \varepsilon' - i\left(\varepsilon'' + \frac{\sigma_s}{\omega}\right) = \varepsilon'_e - i\varepsilon''_e \tag{2.69}$$

and the complex relative permittivity is then expressed as

$$\varepsilon_{er} = \frac{\varepsilon_e}{\varepsilon_0} = \frac{\varepsilon'}{\varepsilon_0} - i\left(\frac{\varepsilon''}{\varepsilon_0} + \frac{\sigma_s}{\omega\varepsilon_0}\right) = \varepsilon'_{er} - i\varepsilon''_{er} \tag{2.70}$$

where the effective conductivity is defined as

$$\sigma_e = \sigma_s + \omega\varepsilon_i\varepsilon'' \tag{2.71}$$

The first term in eq. 2.71 describes the inelastic scattering of free charge carriers during their migration in the dielectric and is present at all frequencies (also at ω=0). On the other hand, the second term is generated by the friction during the polarization process and it increases linearly with the angular frequency ω [84]. The effective conductivity can be expressed as function of ε_s, ε_∞:

$$\sigma = \sigma_s + (\sigma_\infty - \sigma_s)\frac{\omega^2}{\omega^2 + \omega_{rel}^2} \tag{2.72}$$

where $\sigma_\infty = \sigma_s + \varepsilon_0(\varepsilon_s - \varepsilon_\infty)\omega_{rel}$ is the high-frequency conductivity and σ_s is the static conductivity, i.e. the limit at lower frequencies. For brevity of notation, in the following we refer to the relative complex permittivity ε_{er} as ε and to the effective conductivity σ_e as σ, unless otherwise stated.

2.4 Magnetic properties

When an external EM field is applied, materials that display magnetic polarization are said to be magnetic. The magnetic polarization $\mathbf{M}$ consists of the alignment of the magnetic dipoles in the material when the external magnetic field is applied, in a similar way to what happens with electric dipoles and the electric polarization vector:

$$\mathbf{M} = \lim_{\Delta V \to 0} \frac{1}{\Delta V} \sum_{i=1}^{N_m \Delta V} d\mathbf{m}_i \qquad (A/m) \tag{2.73}$$

where N_m is the number of magnetic dipoles per unit volume, $d\mathbf{m}_i$ are the induced magnetic moment. The induce magnetization vector is proportional to the field $\mathbf{H}$:

$$\mathbf{M} = \chi_m \mathbf{H} \tag{2.74}$$

where χ_m is a dimensionless quantity called the magnetic susceptibility.
The magnetization flux density can be defined starting from the magnetization vector and the magnetic field vector:

$$\mathbf{B} = \mu_0\left(\mathbf{M} + \mathbf{H}\right) = \mu_0\left(1 + \chi_m\right)\mathbf{H} = \mu\mathbf{H} \tag{2.75}$$

where the complex magnetic permeability is then

$$\mu = \mu_0\left(1 + \chi_m\right) \tag{2.76}$$

$$\mu_r = \frac{\mu}{\mu_0} = \left(1 + \chi_m\right) \tag{2.77}$$

Similarly to the case of complex permittivity, μ_r is the complex relative magnetic permeability that describes the magnetization of the material exposed to the external EM field.

2.5 Frequency Dependence of the Permittivity

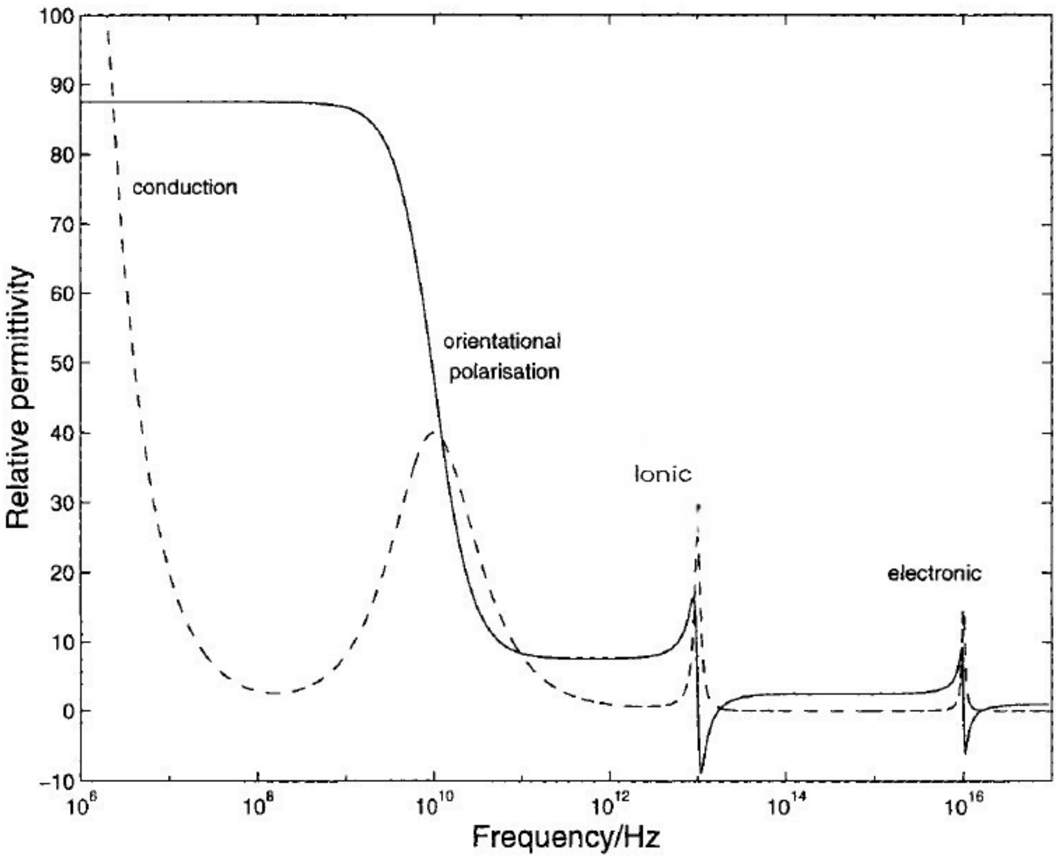

Figure 2.5: Frequency dependence of the real part of relative permittivity $\varepsilon'_r(\omega)$ (solid line) and the the imaginary part of relative permittivity $\varepsilon''_r(\omega)$ (dashed line). Some of the main polarization mechanisms have been reported. The relation between real and imaginary part of relative permittivity is well described by the Kramers-Kronig equations. (taken from [85]).

As already discussed in section 2.3.1, the polarization processes are strongly related to the oscillation of the EM field: in fact, each type of polarization mechanism has a peculiar relaxation time (or relaxation frequency, in the frequency domain). The complex permittivity is dependent on the frequency in the first place; approaching the relaxation frequency the real part generally decrease presenting an inflection point, while the imaginary part increases, having a maximum point (see Fig. 2.5).
The coupling of real and imaginary part is described by the Kramers-Kronig relations [86]:

$$\varepsilon'(\omega) = 1 + \frac{2}{\pi} PV \int_0^{\infty} \frac{x\varepsilon''(x)}{x^2 - \omega^2} dx \tag{2.78}$$

$$\varepsilon''(\omega) = \frac{2\omega}{\pi} PV \int_0^{\infty} \frac{1 - \varepsilon'(x)}{x^2 - \omega^2} dx \tag{2.79}$$

where PV stands for the principal value part (i.e., the singular point $x = \omega$ is simmetrically excluded).

2.5.1 Debye Model

A well-known model that describes the dependence of complex permittivity of a broad range of geomaterials on frequency is the *Debye model*. The model describes a single relaxation process and it is valid up to the GHz frequencies [87]:

$$\varepsilon(\omega) = \varepsilon_\infty + \frac{\varepsilon_s - \varepsilon_\infty}{1 + i\omega\tau} - i\frac{\sigma_s}{\omega\varepsilon_0} \tag{2.80}$$

Separating the real and the imaginary part

$$\begin{aligned} \varepsilon'(\omega) &= \varepsilon_\infty + \frac{\varepsilon_s - \varepsilon_\infty}{1 + (\omega/\omega_{rel})^2} \\ \varepsilon''(\omega) &= \frac{(\varepsilon_s - \varepsilon_\infty)\omega}{\omega_{rel}\,(1 + (\omega/\omega_{rel})^2)} + \frac{\sigma_s}{\omega \varepsilon_0} \end{aligned} \tag{2.81}$$

where the quantity $\omega_{rel} = 1/\tau$ is the relaxation angular frequency, ε_s is the static permittity (i.e. the low-frequency limit of permittivity) and ε_∞ is the high frequency limit permittivity.
The effective conductivity can be expressed in terms of the relaxation angular frequency:

$$\sigma = \sigma_\infty - \sigma_s \frac{\omega^2}{\omega^2 + \omega_{rel}^2} \tag{2.82}$$

where the high frequency conductivity σ_∞ can be also defined in terms of the static conductivity σ_s and the relaxation angular frequency:

$$\sigma_\infty = \sigma_s + \varepsilon_0(\varepsilon_s - \varepsilon_\infty)\omega_{rel} \tag{2.83}$$

When the static conductivity is negligible, the relaxation frequency is found at the imaginary part's maximum, while the real part of permittivity exhibits the inflection point (see Fig. 2.5):

$$\frac{d\varepsilon''(\omega)}{d\omega} = 0 \rightarrow \omega/\omega_{rel} = 1 \tag{2.84}$$

$$\varepsilon''_{max} = \frac{\varepsilon_s - \varepsilon_\infty}{2} \tag{2.85}$$

$$\varepsilon' = \frac{\varepsilon_s + \varepsilon_\infty}{2} \tag{2.86}$$

These equations are generally visualized in the so-called *Cole-Cole diagram*, where ε'' is plotted against ε', generating a circle where only the positive region has actually a physical meaning (see Fig. 2.6).

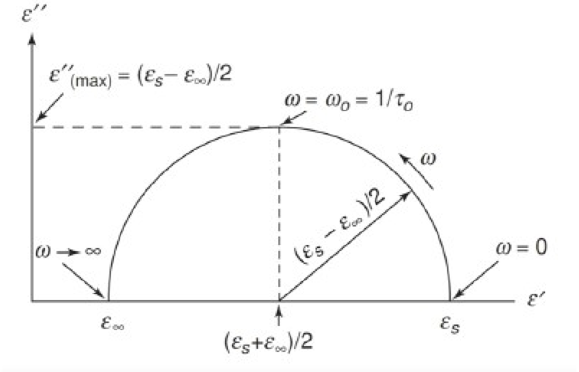

Figure 2.6: The Cole-Cole diagram in the case of a single-relaxation Debye model with the static conductivity negligible.

2.5.2 Cole-Cole and Havriliak–Negami Models

Debye's model has limitations and to describe a broader spectrum of materials another model consisting in a distribution of relaxation time is needed. Cole and Cole proposed an empirical equation where the complex permittivity is defined as [88]:

$$\varepsilon(\omega) = \varepsilon_\infty + \frac{\varepsilon_s - \varepsilon_\infty}{(1 + (i\omega/\omega_{rel})^\alpha} \tag{2.87}$$

where α is a factor that lies in the range $0 < \alpha < 1$. When $\alpha = 1$, the model coincides with that of Debye.

The Havriliak–Negami is a more general model that explains the dielectric dispersion curve's asymmetry and broadness of a wider range of materials (e.g., polymers), in contrast to the Debye model, adding two exponential to the model [89]:

$$\varepsilon(\omega) = \varepsilon_\infty + \frac{\varepsilon_s - \varepsilon_\infty}{((1 + (i\omega/\omega_{rel})^\alpha)^\beta} \tag{2.88}$$

for $\beta = 1$ the model reduces to the Cole-Cole model.

2.6 Temperature Dependence of the Permittivity

The dielectric parameters ε and σ are also temperature dependent [82] (see Fig. 2.7); in particular the relaxation angular frequency follows the Arrhenius equation:

$$\omega_{rel} = \omega_0 e^{-\frac{E_a}{k_B T}} \tag{2.89}$$

where ω_0 is a proportional constant, E_a is the activation energy, k_B is the Boltzmann constant and T is the temperature expressed in kelvin. Also the difference between the static permittivity and the high-frequency permittivity has a dependence on temperature:

$$\varepsilon_s - \varepsilon_\infty = \frac{a}{T} \tag{2.90}$$

where a is a constant.

Inserting the two relations 2.90 and 2.90 into the Debye model (eq. 2.81), it is possible to express the permittivity as a function of the temperature:

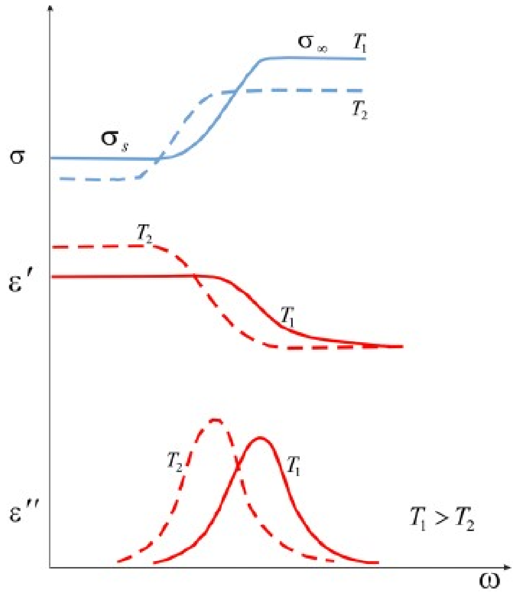

Figure 2.7: Effect of the temperature on the dielectric permittivity and conductivity (taken from [84]).

$$\begin{aligned} \varepsilon'(\omega) &= \varepsilon_\infty + \frac{a/T}{1 + (\omega/\omega_0)^2 e^{2E_a/k_B T}} \\ \varepsilon''(\omega) &= \frac{a/T\, e^{2E_a/k_B T}}{\omega_0 \left[1 + (\omega/\omega_0)^2 e^{2E_a/k_B T}\right]} \end{aligned} \tag{2.91}$$

For decreasing temperatures the real part of permittivity increases and the peak of the imaginary part of permittivity shifts to lower frequencies. The static conductivity has a temperature dependence as well:

$$\sigma_s = \sigma_{s0} e^{-E_a/k_B T} + \frac{a}{T} \omega_0 e^{-E_a/k_B T} \frac{\omega^2\, e^{2E_a/k_B T}}{\omega_0^2 + \omega^2\, e^{2E_a/k_B T}} \tag{2.92}$$

where σ_{s0} is a proportional constant.

2.7 Moisture Dependence of Permittivity

The low frequency behavior of complex permittivity and conductivity is strongly related to the presence of residual amount of water [90] and many experiments observed the influence of moisture on the electrical properties of materials, since it brings an additional space charge polarization [91]. It is well known that the presence of a ionic conductive path inside a material generally can yield to an additional polarization and electrode effects [92]. Furthermore, it was observed that the complex bulk permittivity of the material under investigation is not altered when a single layer of water is adsorbed onto its dry surface; only with multiple adsorbed layers there's an increase of both the real and imaginary part of permittivity at low frequencies (this effect is particularly evident below 1 MHz). Above about seven layers, the electrical properties of water dominate over the overall behavior of the material [90]. In Figure 2.8 it is shown the effect of a small amount of moisture (0.1 % weight percent of water): the main outcome is to increase the overall real part of permittivity and loss tangent, especially below 10 kHz; this effect progressively disappears lowering the temperature and eliminating the residual water.

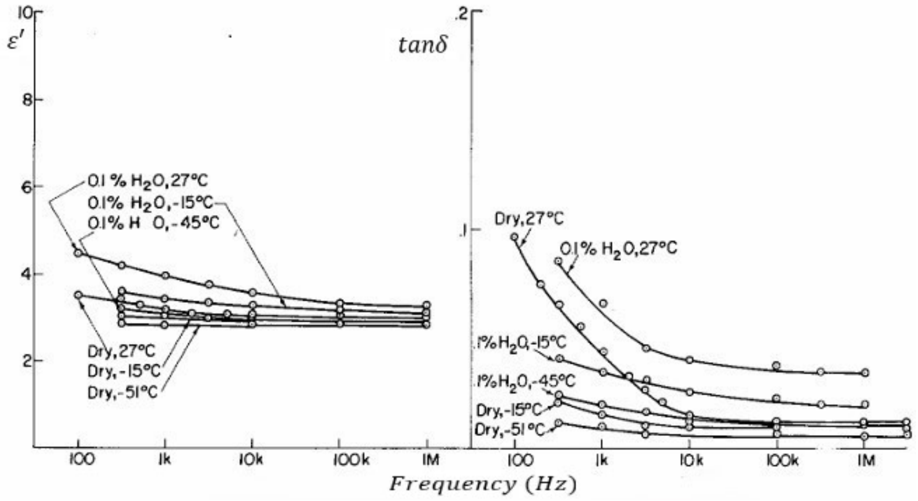

Figure 2.8: Real part of permittivity and loss tangent of a basalt at different temperatures (27°C, -15°C, -45°C, -51°C) in a dry form and with 0.1 weight percent water in the frequency range 100 Hz-1 MHz (modified after [91]).

2.8 Dielectric Properties of Geomaterials

The goal of this section is to detail the dielectric properties and behavior of geomaterials of interest for the space exploration, such as water, rocks and soils; the electrical properties of water ice will instead be discussed separately in chapter 4.

2.8.1 Pure Water Dielectric Properties

For pure water, i.e. distilled water with no dissolved salts, the dielectric properties below 50 GHz are described by a simple single-relaxation Debye model [93]:

$$\begin{aligned} \varepsilon'_w(\omega) &= \varepsilon_{w,\infty} + \frac{\varepsilon_{w,s} - \varepsilon_{w,\infty}}{1 + (\omega/\omega_{w,rel})^2} \\ \varepsilon''_w(\omega) &= \frac{(\varepsilon_{w,s} - \varepsilon_{w,\infty})\omega}{\omega_{w,rel}\,(1 + (\omega/\omega_{w,rel})^2)} \end{aligned} \tag{2.93}$$

where $\varepsilon_{w,\infty}$ is the water high frequency complex permittivity, $\varepsilon_{s,\infty}$ is the water static permittivity and $\omega_{w,rel}$ is the water relaxation frequency. $\varepsilon_{w,\infty}$ is weakly dependent on the temperature and can be considered constant and equal to 4.9 [94]. The pure water relaxation time $\tau_{w,rel}$, on the other hand, has a temperature dependence that can be expressed by the empirical law:

$$2\pi\tau_{w,rel}(T) = 1.1109 \times 10^{-10} - 3.824 \times 10^{-12}T + 6.938 \times 10^{-14}T^2 - 5.096 \times 10^{-16}T^3 \tag{2.94}$$

where the temperature T is expressed in celsius degrees. The relative relaxation frequency $\nu_{w,rel}$ lies in the microwave region:

$$\begin{aligned} \nu_{w,rel}(0°C) &\approx 8.9\ GHz \\ \nu_{w,rel}(20°C) &\approx 16.7\ GHz \end{aligned} \tag{2.95}$$

The pure water static permittivity also has a temperature dependence and it is expressed by the following relationship [95]

$$\varepsilon_{s,w} = 88.045 - 0.4147T + 6.925 \times 10^{-4}T^2 + 1.075 \times 10^{-5}T^3 \tag{2.96}$$

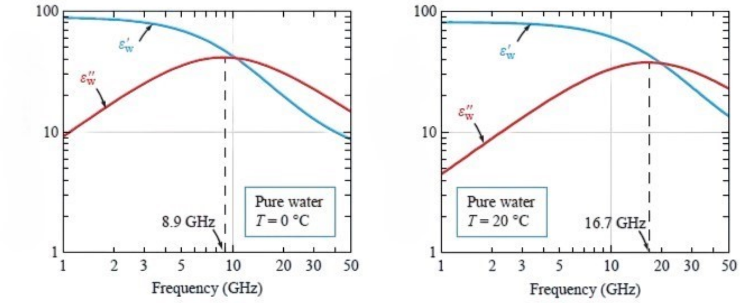

(a) $T = 0$ °C (b) $T = 20$ °C

Figure 2.9: Microwave spectra of the complex permittivity of pure water at two different temperatures (modified after [96]).

2.8.2 Saline Water Dielectric Properties

A different model was developed to describe the complex permittivity of saline water. It is based on a double-relaxation Debye dielectric model and it reduces to a model for pure water when the salinity is equal to zero [97]:

$$\begin{aligned} \varepsilon'_w(\omega) &= \varepsilon_{w,\infty} + \frac{\varepsilon_{w,s} - \varepsilon_{w,1}}{1 + (\omega/\omega_{rel,1})^2} + \frac{\varepsilon_{w,s} - \varepsilon_{w,\infty}}{1 + (\omega/\omega_{rel,2})^2} \\ \varepsilon''_w(\omega) &= \frac{(\varepsilon_{w,s} - \varepsilon_{w,1})\omega}{\omega_{rel,1}\left(1 + (\omega/\omega_{rel,1})^2\right)} + \frac{(\varepsilon_{w,s} - \varepsilon_{w,\infty})\omega}{\omega_{rel,2}\left(1 + (\omega/\omega_{rel,2})^2\right)} + \frac{\sigma}{\omega\varepsilon_0} \end{aligned} \tag{2.97}$$

where there are two angular relaxation frequency terms ($\nu_{rel,1} = \frac{\omega_{rel,1}}{2\pi} = 8.9\ GHz$ and $\nu_{rel,2} = \frac{\omega_{rel,2}}{2\pi} = 201.8\ GHz$) and σ is the ionic conductivity of the saline water (for pure water $\sigma = 0$).

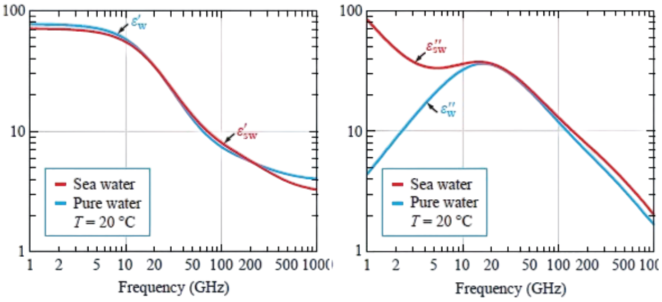

Figure 2.10: Comparison between the microwave spectra of the complex permittivity of pure water and sea water at $T = 20°C$ (modified after [96]).

2.8.3 Rocks

Rocks, in geology, are naturally occurring and coherent aggregate of one or more minerals. Their electrical properties are not the simple sum of the electrical properties of the minerals that constitute them: in fact, they show wide variations in permittivity. A pattern of permittivity as their chemical and mineralogical characteristics varies has not yet been clearly identified, although a trend has been recognized as a function of the silica content. Within the same mineral class or group, variations in electrical properties can be attributed to impurities and distinct crystalline structures, which can play a role in electrical anisotropy. However, the real part of permittivity of the most abundant rock-forming minerals generally lies in the range 4-10, with some minerals that exhibits larger values. A comprehensive investigation of dielectric properties of solid rocks was carried out in the literature [98]. In Figure 2.11 the real part of permittivity of 36 solid rocks is shown at 450 MHz and 35 GHz. There is no significant variation in the values at these two frequencies, pointing out a very slight frequency dependent behavior for most common rocks. Moreover, a small dependence on temperature variation was also observed, particularly at high temperatures (see [99] and references therein).

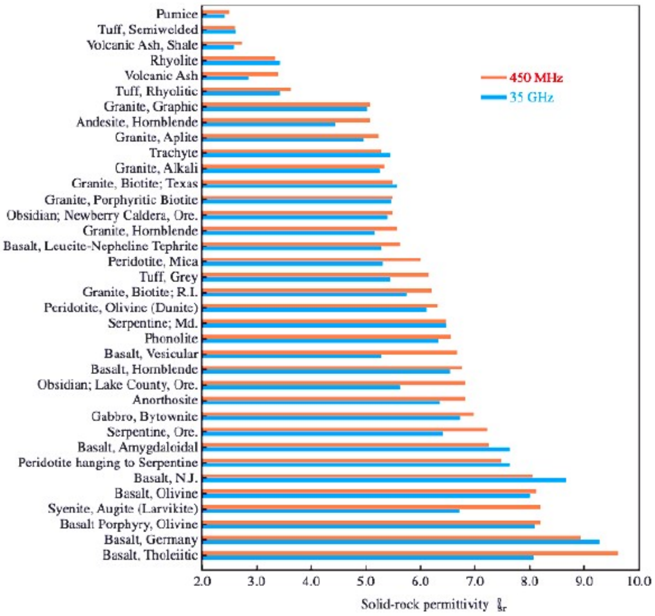

Figure 2.11: Comparison of the real part of permittivity of solid rocks at two different frequencies, 450 MHz and 35 GHz (modified after [96]).

2.8.4 Soils

Soil, or dry powder, is a porous media composed of grains derived from rocks or minerals and voids of air. It is an heterogeneous material, whose permittivity depends mainly on the bulk density of the powder ρ_b. This quantity varies between 1 g/cm^3 for very porous powder to about 3.4 g/cm^3 for powders formed from high density rocks like peridotites. The electrical properties of soils can be described be means of the EM mixing models in a quite predictable way as a function of their porosity (detailed in chapter 3). For example, a simple empirical formula was retrieved to describe the real part of permittivity of soils a as a function of their bulk density [100]:

$$\varepsilon'_{soil} = (1.01 + 0.44\rho_b)^2 - 0.062 \tag{2.98}$$

In any case, in the absence of residual moisture it has been indicated in the literature that for most soils the real part of permittivity ranges from 2 to 4 and the imaginary part is lower than 0.05.

2.8.5 Meteorites

Meteorites are solid bodies coming from space and found on a planet's surface. They are different from meteoroids, which are small rocky or metallic bodies in outer space: in fact meteorites are the result of the ablation process experienced by the meteoroids entering the atmosphere.

The meteorites dielectric properties are directly correlated to their metal content, which could locally vary inside them, explaining the strong fluctuations observed in many samples [101]. The imaginary part of permittivity increases in a significant way with metal proportion in the sample, as expected. In Table 2.1 the dielectric properties of different types of meteorites, both granular and solid, are shown as example.

Classification	Name	Real part of permittivity	Imaginary part of permittivity	Porosity	Metal (vol. %)	Frequency (MHz)	Reference
CR2	NWA 801	2.6	-	0.3	5-8	20-1000	[102]
CM	NWA 5797	2.9	-	0.3	0.1	20-1000	[102]
LL5	MAC 88122	4.7	0.019	0.3	2.0	20-1000	[103]
L5	NWA 12857	4.7	0.057	0.3	4.1	10-100	[104]
L6	Holbrook	7.8	0.12	Solid	4.1	450	[98]
H5	LEW 85320	5.7	0.29	0.3	8.4	20-1000	[103]
H5	Plainview (sample 1)	25.4-30.4	2.5-6.1	Solid	8.4	420-1800	[105]
EH4	Indarch	130-150	8.5-18.0	Solid	10	450	[98]

Table 2.1: Examples of dielectric properties of various meteorites samples. CR2 and CM are two types of carbonaceous chondrites; LL5, L5, L6 are ordinary chondrites with low metal content, and H5 and EH5 are chondrites with high iron content. (modified after [106]). Metal content is

2.9 Radar Sounder

The radar sounder technique is a non-invasive high-resolution geophysical technique that uses radio waves to probe the subsurface. Since it allows the identification of deep buried targets, it has numerous fields of application: geology, glaciology, archaeology, engineering, ground water, among the others.
A typical radar sounder configuration consists of a transmitter and receiver antennas arranged in a fixed geometric pattern; this method is based on the transmission of EM energy pulses that propagate through the medium, and then are reflected at EM interfaces, finally going back at the receiver.

Reflected signals obtained from radar sounders can be represented in a two-dimensional diagram known as radargram. In this representation, the vertical axis displays the two-way travel time of the electromagnetic pulses, whereas the horizontal axis indicates the position of the radar system (see Fig. 2.12).

A radar sounder is characterized by a bandwidth B, which give the EM pulse width at half amplitude generated by the instrument:

$$W = \frac{1}{B} \tag{2.99}$$

Scattering of the radar signal occurs due to the variations in material properties at the boundary between two different media on the spatial scale of the wavelength of the emitted EM wave. It can consist of reflection, refraction and diffraction. The reflection is defined as the the abrupt change in the direction of portion of the EM wave when it encounters the boundary between adjacent media with different EM properties (i.e. dielectric permittivity and magnetic permeability). The greater the EM contrast, the greater the amount of energy reflected. This phenomenon is described by the Fresnel coefficient:

$$R = \left(\frac{\sqrt{\varepsilon_1/\mu_1} - \sqrt{\varepsilon_2/\mu_2}}{\sqrt{\varepsilon_1/\mu_1} + \sqrt{\varepsilon_2/\mu_2}} \right)^2 \tag{2.100}$$

where ε_1,μ_1 are the EM properties of the first medium and ε_2,μ_2 are those of the second medium. This coefficient is not effective in describing transitional boundaries and thin layers [108].

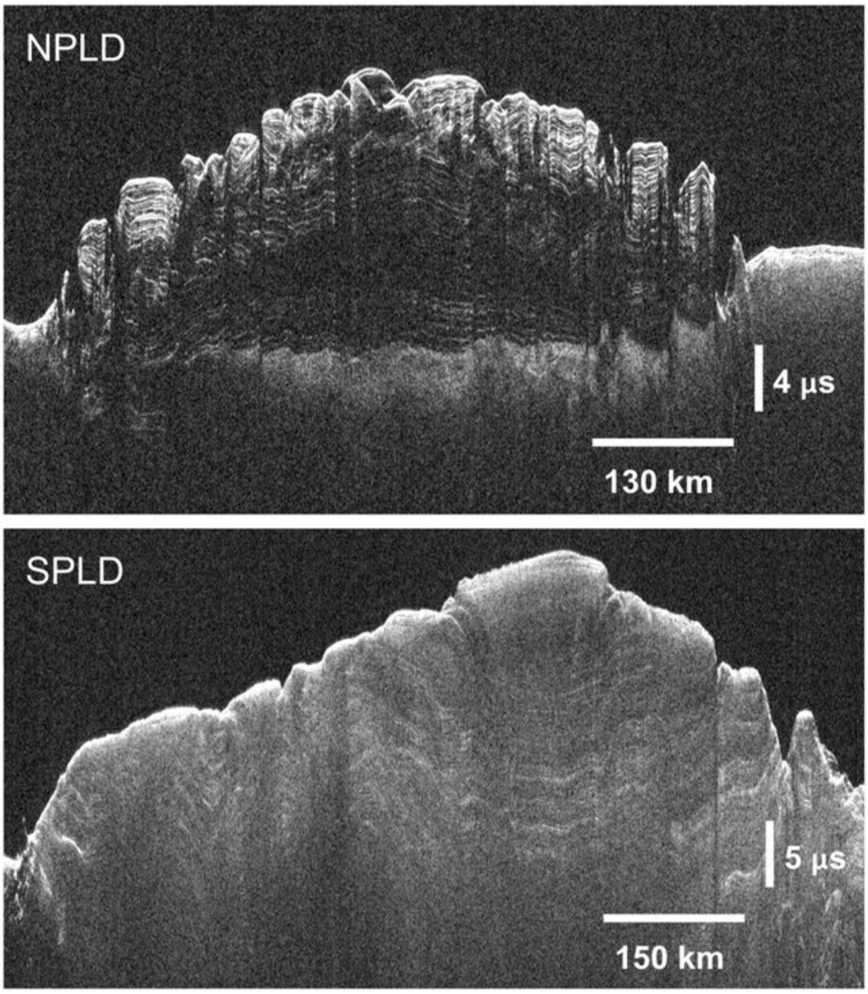

Figure 2.12: Example of radargram: cross section of the north polar layered deposits (NPLD, top) and south polar layered deposits (SPLD, bottom) on Mars (taken from [107]).

2.9.1 Radar Range Equation

The radar range equation (RRE) is a simple model that has been in use within the context of radar sounding applications for a significant time. The main goal of employing the radar range equation is to evaluate how effectively radar can penetrate materials and detect objects embedded within them. By utilizing simplified parameterization, the RRE condenses the three-dimensional response into a more manageable form. The principal conclusion drawn from the RRE analysis is the identification of the considerable role that attenuation plays in affecting the radar performance [109]. Such equation related the received-signal power P_r to the transmitted signal power P_t

$$P_r = \xi_t \xi_r G_t G_r g C_s \frac{V^2}{4\pi\nu^2} \frac{e^{-4\alpha L}}{16\pi^2 L^4} P_s \tag{2.101}$$

where:

ξ_t: Transmitter antenna efficiency

ξ_r: Receiver antenna efficiency

G_t: Transmitter antenna gain

G_r: Receiver antenna gain

g: Back-scatter gain of target

C_s: Target scattering cross section area

α: Attenuation coefficient

V: Propagation velocity in the medium

L: Target distance

The equation takes different forms or is simplified according to the characteristics of the target and source geometry; for example, in the case of a smooth and plane reflector, eq. 2.101 becomes:

$$P_r = \xi_t \xi_r G_t G_r \Gamma \frac{V^2}{64\pi^2 \nu^2} \frac{e^{-4\alpha L}}{16\pi^2 L^4} P_s \tag{2.102}$$

where Γ is the power reflection coefficient of the interface radiating upwards and it is related to the product of the back-scatter gain and scattering cross-section:

$$gC_s = \pi L^2 \Gamma \tag{2.103}$$

Chapter 3

Electromagnetic Mixing Formulas

The powdered and regolith samples studied in this thesis can be treated as heterogeneous mixtures, since they are composed by multiple phases. In this work two-phases mixtures were studied: dry powdered samples made up of solid mineral grains and voids of air, and samples made up of solid grains and water pure ice. The bulk (or effective) permittivity ε_b is defined as the permittivity of the whole mixture, with the contributions from the single phases, and it is the quantity effectively measured in laboratory by the experiments. The two phases of the mixture are labeled as guest or inclusion phase with permittivity ε_i and as background or environment, with permittivity ε_e. Following the nomenclature of [85], the volume fraction of the inclusion will be labeled as f_v and the volume fraction of the environment as $1-f_v$; if f_v is the air volume fraction for mixtures containing a phase made of air voids, then it is equal to the porosity ϕ.

The mixing formulas (MF) are theoretical equations that describe the behavior of ε_b of the heterogeneous material [85]. Through these equations it is possible to extract the value of the solid sample permittivity:

$$\varepsilon_b = MF(\varepsilon_e, \varepsilon_i, f_v) \tag{3.1}$$

The mixing formulas are strongly dependent on the micro-structure of the mixture, the shape of the inclusions and the contrast between constituent permittivities [110]. At the frequencies used in this work, the mixtures can be assumed as quasi-static because the wavelength of the incoming electric field is significantly larger than the size of the inclusions within the mixture (as determined by the average grain size of the measured granular samples).

This chapter provides a review of the main mixing formulas employed in the literature.

3.1 Non Symmetric Mixing Formulas

In this section the non-symmetric mixing formulas will be outlined: with this type of equations the result given by the model depends on the the choice on the phase treated as inclusion and on the phase treated as environment.

3.1.1 Maxwell Garnett Formula

The Maxwell Garnett formula was derived in 1904 by James Clerk Maxwell Garnett to describe the electrical properties of metal spheres embedded in a liquid [111]; it assumes the presence of spherical inclusions randomly incorporated in an environment material (see Fig. 3.1).

$$\varepsilon_b = \varepsilon_e + 3 f_v \varepsilon_e \frac{\varepsilon_i - \varepsilon_e}{\varepsilon_i + 2\varepsilon_e - f_v(\varepsilon_i - \varepsilon_e)} \tag{3.2}$$

This equation has two limits, the first one when the inclusion phase disappears

$$f_v \longrightarrow 0 \quad \Longrightarrow \quad \varepsilon_b \longrightarrow \varepsilon_e$$

and the other one if host medium vanishes

$$f_v \longrightarrow 1 \quad \Longrightarrow \quad \varepsilon_b \longrightarrow \varepsilon_i$$

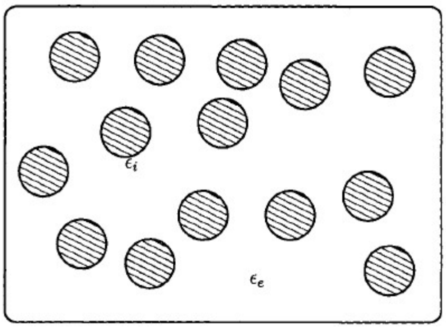

Figure 3.1: Dielectric spheres with dielectric permittivity ε_i with random positions in the environment material with dielectric permittivity ε_e (taken from [85]).

A perturbation expansion for the Maxwell Garnett rule gives an expression valid for dilute mixtures when $f_v \ll 1$

$$\varepsilon_b \approx \varepsilon_e + 3f_v\varepsilon_e\frac{\varepsilon_i - \varepsilon_e}{\varepsilon_i + 2\varepsilon_e} \tag{3.3}$$

Maxwell Garnett: Particle Shape

The inclusion for the classical Maxwell Garnett formula are assumed to be spherical but the expression can be generalized to ellipsoids by using the depolarization factors N_x, N_y and N_z of an ellipsoid in a 3D Cartesian space (see Fig. 3.2). The depolarization factor N_x in the $\hat{x}$ direction for an ellipse with semi-axes a_x, a_y and a_z is given by [85]

$$N_x = \frac{a_x a_y a_z}{2}\int_0^\infty \frac{ds}{(s+a_x^2)\sqrt{(s+a_x^2)(s+a_y^2)(s+a_z^2)}} \tag{3.4}$$

For the other depolarization factor N_y and N_z the a_x is replaced by a_y and a_z. The three depolarization factors satisfy the equality

$$N_x + N_y + N_z = 1 \tag{3.5}$$

A sphere inclusion has a depolarization factor $(1/3, 1/3, 1/3)$, whereas discs and needles respectively $(1, 0, 0)$ and $(0, 1/2, 1/2)$.
The polarizability component of the ellipsoid in the $\hat{x}$ direction is defined as

$$a_x = \frac{4\pi a_x a_y a_z}{3}(\varepsilon_i - \varepsilon_e)\frac{\varepsilon_e}{\varepsilon_e + N_x(\varepsilon_i - \varepsilon_e)} \tag{3.6}$$

In the case of ellipsoidal inclusions, the polarizability is anisotropic and is represented by a 3 × 3 sensor; the bulk permittivity is also anisotropic, except for the case of randomly oriented ellipsoidal inclusions. The Maxwell Garnett equation for randomly oriented ellipsoids inclusion, when there is no external force orienting the inclusions is given by

$$\varepsilon_b = \varepsilon_e + \varepsilon_e\frac{\frac{f}{3}\sum_{j=x,y,z}\frac{\varepsilon_i-\varepsilon_e}{\varepsilon_e+N_j(\varepsilon_i-\varepsilon_e)}}{1-\frac{f}{3}\sum_{j=x,y,z}\frac{\varepsilon_i-\varepsilon_e}{\varepsilon_e+N_j(\varepsilon_i-\varepsilon_e)}} \tag{3.7}$$

And for example, the case of randomly oriented discs gives

$$\varepsilon_b = \varepsilon_e + f_v(\varepsilon_i - \varepsilon_e)\frac{2\varepsilon_i + \varepsilon_e}{(3-f_v)\varepsilon_i + f_v\varepsilon_e} \tag{3.8}$$

and for randomly oriented discs

$$\varepsilon_b = \varepsilon_e + f_v(\varepsilon_i - \varepsilon_e)\frac{\varepsilon_i + 5\varepsilon_e}{(3-2f_v)\varepsilon_i + (3+2f_v)\varepsilon_e} \tag{3.9}$$

The Maxwell Garnett equations are widely employed in the literature [98] due to its legacy, but generally the accuracy of the this theory is lower than other mixing models because of its dilute mixture limit.

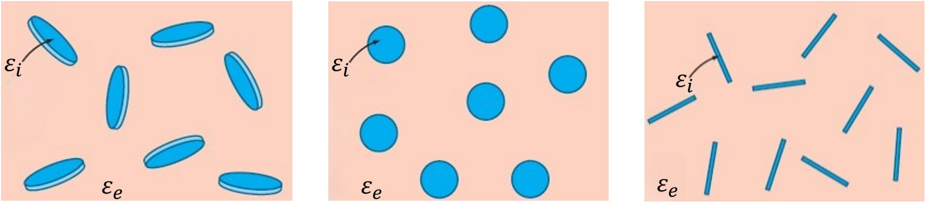

Figure 3.2: Examples of randomly distributed ellipsoidal configurations (modified after [96]).

3.2 Symmetric Mixing Formulas

Unlike the non-symmetric case, this type of mixing formulas are defined by the symmetry with respect to the mixture phases [110]. The combination of topology and micro-geometry of the mixture is taken into account as statistical averages and generally the mixture can be approximated as homogeneous. These equations generally are independent of particle shapes of the inclusions.

3.2.1 Bruggeman Formula

Bruggeman formula was derived in 1935 [112] and it had an extensive use in the field of mixing theories since it does not have the limits of the Maxwell Garnett equations due to dilute mixtures.

$$(1-f)\frac{\varepsilon_e-\varepsilon_b}{\varepsilon_e+2\varepsilon_b}+f_v\frac{\varepsilon_i-\varepsilon_b}{\varepsilon_i+2\varepsilon_b}=0 \tag{3.10}$$

In [113] permittivity measurements of several powders samples were performed at 20 MHz and at 9.375 GHz finding out that the Bruggeman mixing formula returned solid permittivity values in agreement with the literature. Nevertheless they noticed that the equation was less accurate for powders with particle sizes less than $30\,\mu m$ and for predicting the imaginary part.
In [114] the bulk permittivity of powder mixtures of the polar compound 1-cyanoadamantane was measured in the frequency range 1 kHz - 1 GHz and pointed out that the Bruggeman model fits the experimental data more accurately for volume fractions of the inclusion $f_v < 0.25$.
In another paper [115] the Bruggeman equation was found out to predict well the permittivity of a powdered granite and two basalt samples in the frequency range 4-19 GHz.
It was also observed that Bruggeman and LLL equations return values that are very similar to each other, and exactly equal for a volume fraction of the inclusion $f_v = 0.57$.
Finally, it was observed that the Bruggeman equation is more accurate in describing the bulk permittivity of low dielectric contrast mixtures with volumetric fractions of the phases as similar as possible [110].

3.2.2 Looyenga-Landau-Lifshitz Formula

The Looyenga-Landau-Lifschitz (LLL) equation was independently derived in [116] and [117], assuming a small dielectric contrast between the phases of the mixture. It was considered a system composed of two materials with $\varepsilon_b+\delta\varepsilon_b$ and $\varepsilon_b-\delta\varepsilon_b$; the bulk permittivity is then the volume average of the electrical properties of these two components. LLL equation is independent of the particle shape and structure.

$$\varepsilon_b^{1/3}=f_v\varepsilon_i^{1/3}+(1-f_v)\varepsilon_e^{1/3} \tag{3.11}$$

In [116] the LLL equation was found out to fit experimental data more accurately for powders with high volume fractions of the inclusions, especially for mineral with real part of permittivity values of 9 and above. Also in [114] the authors pointed out that the LLL formula worked better for $f_v > 0.65$. Moreover in [118] it was noted that the LLL formula is valid only for mixtures with low permittivity contrast between the phases.
In summary, it has been shown that the formula fits well the data coming from mixture with low dielectric contrast and high volume fractions of inclusions, returning in each case values very similar to the Bruggeman equation.

3.2.3 Complex Refractive Index Model CRIM

The complex refractive index model (CRIM) equation was developed to describe the refractive index of nonmagnetic mixtures, considering a simple volume average of mixture's components refractive indices [85]

$$\sqrt{\varepsilon_b} = f_v\sqrt{\varepsilon_i} + (1 - f_v)\sqrt{\varepsilon_e} \tag{3.12}$$

This equation is successful in describing the dielectric behavior of liquid mixtures: in particular for bentonite clays mixed with water at 4 GHz [119], soils with increasing water content [120], saturated sedimentary rocks starting from 800 MHz [121] and dry sand/clay mixtures as well [122].
For water with high salinity values the CRIM model does not return accurate values, probably due to chemical interactions between the phases of the mixture.

3.2.4 Lichtenecker Formula

The Lichtenecker formula was originally derived as semi-empirical [123], without a strong theoretical framework. Only later in [124] an analysis of the equation was carried out, showing that the Lichtenecker equation describes a specific topology, i.e. a randomly oriented spheroids with uniform shape distribution. Moreover, [125] proved that the equation is physically founded and that it is a reasonable mixing formula for soils and rocks since they have oblate spheroidal grains.

$$\varepsilon_b = \varepsilon_i^{f_v}\varepsilon_e^{1-f_v} \tag{3.13}$$

In [126] it was showed that the Lichtenecker equation predicted the measured permittivities for a wide range of basalt samples better than the other equations.
92 measurements of the complex permittivity of lunar regolith samples retrieved during the NASA's Apollo missions were reviewed in [127] and it was discovered that the real part pf permittivity was well fitted by the function

$$\varepsilon_b = a^{\rho_b} \tag{3.14}$$

with $a = 1.93 \pm 0.17$ and where ρ_b is the bulk density of the samples.
It was shown that eq. 3.14 is equivalent to the Lichtenecker formula assuming a real part of the solid permittivity $\varepsilon' = 7.7$ and a grain density of lunar regolith of 3.1 g/cm^3. The imaginary part of the bulk permittivity on the other hand did not follow a trend as a function of the density, but it depends on the TiO_2 and FeO weight percent oxide; the loss tangent in fact was modeled by the equation [128]

$$tan\delta = 10^{[0.038(\%TiO_2 + \%FeO) + 0.312\rho_b - 3.260]} \tag{3.15}$$

The a value in eq. 3.14 is found empirically and it varies from paper to paper (see Tab. 3.1).

Reference	a
[127]	1.93
[129]	2.10
[130]	1.87
[131]	1.92
[132]	1.96
[133]	2.15
[96]	1.96

Table 3.1: Values of a found in the literature (adapted from [134]).

3.3 Mixing Bounds

For a two-phase mixtures it is possible to express the bulk permittivity with two bounds that cannot be exceeded under any circumstances, i.e. the bulk permittivity falls between two values:

$$min\{\varepsilon_e, \varepsilon_i\} \leq \varepsilon_b \leq max\{\varepsilon_e, \varepsilon_i\} \tag{3.16}$$

The mixing bound are used in the literature for constraining the possible bulk permittivity with a conservative approach, useful when only little information is known about the dielectric properties of the mixture.
In the literature there are two sets of bounds, the Wiener bounds and Hashin-Shtrickman bounds.
The Wiener bounds represent the maximum and minimum values for an anisotropic mixture, corresponding to a capacitor that are connected in parallel or series in a circuit [85]

$$\begin{aligned} \varepsilon_{b,min} &= \frac{\varepsilon_i \varepsilon_e}{f_v \varepsilon_e + (1-f_v)\varepsilon_i} \\ \varepsilon_{b,max} &= f_v \varepsilon_i + (1-f_v)\varepsilon_e \end{aligned} \tag{3.17}$$

The Hashin-Shtrickman bounds [135], on the other hand, were developed for isotropic mixtures and coincide to the Maxwell Garnett equation swapping the role of the inclusions and environment. In figure 3.3 an example of these two types of mixing bounds is reported.

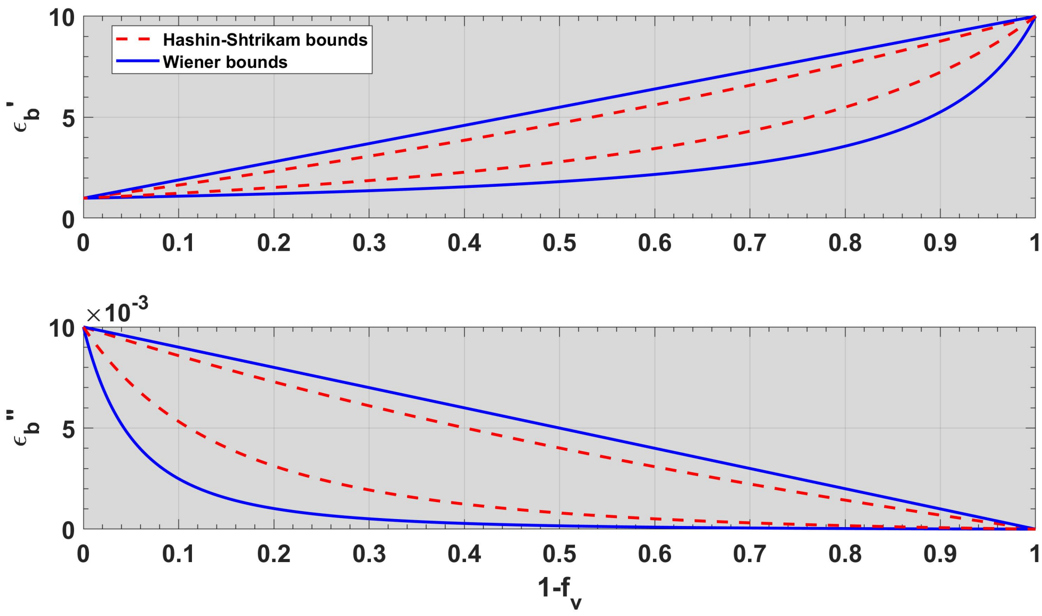

Figure 3.3: Example of Hashin-Shtrickman and Wiener bounds for a material composed of two phases: one phase is the air and the other one, treated as the environment, has permittivity $\varepsilon = 10 - i0.01$. The complex permittivity is reported as a function of the environment volume fraction.

3.4 Archie Law

The Archie law [136] is an empirical formula that relates the conductivity of a granular medium saturated with a conducting fluid by means of the equation

$$\sigma = \sigma_w \phi^m \tag{3.18}$$

where σ is the conductivity of the porous media, σ_w is the conductivity of the fluid, ϕ is the porosity of granular medium and m is the so-called cementation exponent, playing the role of a curve-fitting parameter. It is an empirical factor with value determined experimentally, generally lying between 1.3 and 2; it is dependent on the consolidation of the material. Archie's law implicitly assumes that all electrical conductivity in water-saturated soils or rocks is due to the migration of ions in solutions through the entire porous matrix. It was originally derived as a trend analysis on bilogarithmic graph paper and, although it works well in many real cases, it has never been fully understood. Also Archie himself warned the readers in his original paper:
“ It should be remembered that the equations given are not precise and represent only approximate

relationships. It is believed, however, that under favorable conditions, their application falls within useful limits of accuracy.”

Nevertheless recent discussions [137] and a brilliant paper [138] have returned a more solid theoretical framework to the theory of Archie. In [138] it was concluded that given also the irreducible scatter in brine volume-conductivity data, Archie law predicts water saturation accurately enough. Moreover, since σ_w and ϕ do not contain information about the geometry of the brine, m must contain some information about it, although not in an interpretable form.

Other papers have tried to give an interpretation to the geometric factor m : in particular, [139] showed that for $m = 1.5$ inclusions were spherical, for $m > 1.5$ inclusions were plate-like or cylinders whose major axis was perpendicular to the external electric field, and that for values of $m < 1.5$ plate-like inclusions had their major axis parallel to the electric field.

Chapter 4

Physics of Ice

Measurements of the electrical properties of ice represent the core of this thesis, and for this reason this chapter reviews some useful physical characteristics and electrical properties of the main types of ice found on earth and observed and speculated to be present in the Solar System.

4.1 Ice in the Solar System

The cryosphere, i.e. the portions of the Earth's surface where water is in solid form (such as glaciers, snow deposits, sea ice, etc.), is an exceptional investigative tool for geophysics, capable of reconstructing the climate of our planet over hundreds of thousands of years, acting as a true paleoclimatic thermometer. Approximately 10% of the surface of the land mass is covered in ice to a depth of a few kilometers, and, depending on the time of year, there can be around 5% ice coverage of the surface of the oceans in polar areas. The presence of ice on Earth is a crucial element in the global climate system, significantly influencing the planet's energy balance and hydrological cycles. In fact, since ice is very reflective, it reflects more Sun radiation than the land mass, and a change in the area of ice caps, glaciers and sea ice would impact remarkably in the global climate change, regulating global temperatures. Moreover, the glacial deposits serve as rich source of freshwater reserves for numerous ecosystem: environment on Earth is thus critically dependent on the physical properties of ice [140].

Water ice is present throughout the entire Solar System, both in terrestrial planet regions and in outer regions beyond the *snow line*, which mark the distance from the sun where the temperature allows icy masses to originate and persist [141]. On Mercury and the moon, water ice has been identified in permanently shadowed craters in polar regions where it may have remained in a stable form for billions of years [142],[143]; furthermore on Mars the water ice is present at the polar caps and in craters [144], [145]. Although its abundance is still not fully known, water both in liquid and solid form has been observed in the lower cloud layers on Saturn and Jupiter and in the rings of the giant planets, at various fractions [146],[147],[148]. Ice is ubiquitous also in small Solar System Bodies: solid ice features have been detected on comets via ground-based telescopes [149] and in situ measurements [150]; dwarf planet Ceres, the largest object in the main asteroid belt, has substantial subsurface ice [151], and Kuiper Belt objects (KBOs), objects that populate the region of the solar system beyond the planets, are largely composed of frozen volatiles such as water [152],[153].

4.2 Structure and Properties of ice

Water is the most common chemical compound on Earth but also one of the most peculiar, with the largest number of anomalies in its properties. The thee nuclei of this molecule form an isosceles triangle with the oxygen at the apex and the two hydrogens at the base line (see Fig. 4.1); the protons are attached to the oxygen atom at an angle of 104.45°.

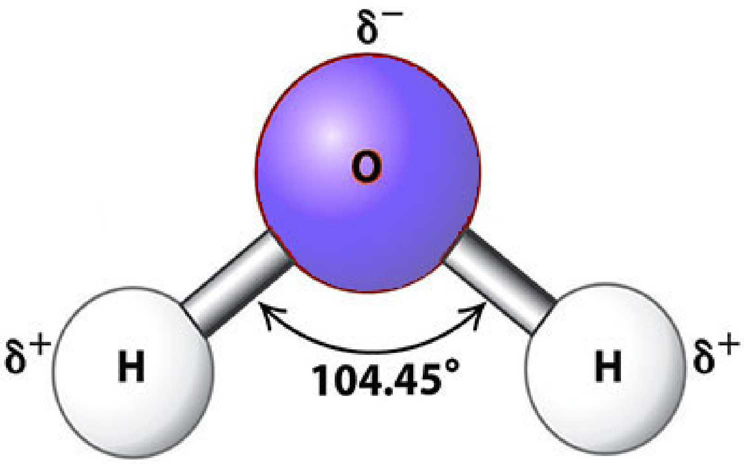

Figure 4.1: Electromagnetic model of the H_2O molecule.

4.2.1 Ice Crystal Structure

Ice possesses twelve crystal structures and two amorphous forms. Under low-pressure conditions, the stable phase is known as ice I. This type of ice has two different variants: ice *Ih*, also termed *ordinary ice*, which is hexagonal and results from water freezing at standard pressure, and ice *Ic*, which is cubic and develops via vapor deposition at low temperatures ($\approx -130°C$) [154].
In the Ih ice crystal structure the oxygen atoms lie in hexagonal layers, raised and lowered alternatively [155] (see Fig. 4.2). Each H_2O molecule is surrounded by four closest neighbors located near the vertices of a regular tetrahedron centered on the molecule at a distance of 2.76 Å. The oxygen atom in each molecule forms strong covalent bonds with two hydrogen atoms, and the molecules are weakly linked to each other by hydrogen bonds [156].

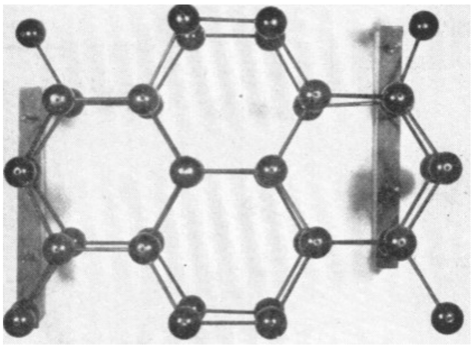

Figure 4.2: Model of an Ih pure water ice crystal (taken from [155]).

Ice rules or *Bernal-Fowler* rules, are a set of rules that describes the arrangement of hydrogen atoms in an ice crystal considered "ideal" [157]:

1. Each water molecule is surrounded by other four molecules such that his two hydrogen atoms are approximately directed toward two of the four surrounding oxygen atoms;
2. In every O-O linkage only one hydrogen atom is involved;
3. Each oxygen atom has two nearest neighboring hydrogen atoms so that the structure of the water molecule is preserved.

Local violations of these three rules produce structural defects in ice and control the behavior of the electrical conductivity and the relaxation time.

4.3 Water Ice Dielectric Properties

In this section the basic principles and the most important result of the theories for water pure ice Ih are outlined.
It is important to point out that the water ice does not posses magnetic properties.

4.3.1 Jaccard Theory

Although Debye model (detailed in the previous chapter) is able to describe the behavior of dielectric permittivity of pure water ice up to hundreds of MHz [158], it was observed that the Cole Cole model is more effective up to 250 K. The Jaccard Theory, on the other hand, is a widely accepted model for the polarization mechanisms of ice [159], [160]; it is based on the presence of protonic point defects (also called *intrinsic defects*), that are places in the ice lattice where the Bernal-Fowler rules are locally violated, and on their motion (*protonic motion path*) in the crystalline lattice of the ice which has the effect of reorienting the molecules encountered along its path. In Jaccard work two types of protonic defects are addressed and described:

- the first one is linked to the rotation of the H_2O molecules inside the lattice that generate the so-called L and D Bjerrum defect pair. The L Bjerrum defect is a proton-deficient site (of the type $O \cdots O$), while the D Bjerrum defect is a site where two adjacent protons face each others (of the type $O - H \cdots H - O$).
- the second one is due to proton motion along the bond of two molecules. This phenomenon transfers the ionization state generating a pair of ionic defects H_3O^+ and OH^-.

Unlike other geomaterials, the polarization and conduction phenomena are strongly interconnected in the ice [140], due to the protonic hopping.
For each type of defect the conductivity is defined as:

$$\sigma_i = n_i \mu_i |e_i| \tag{4.1}$$

where the subscript i indicates the type of defect, n_i is the defect volume concentration, μ_i the mobility and e_i the effective charge. These values were tabulated in [140] and are shown in table 4.1. The volumetric concentration of the intrinsic defects is given by

$$n_i = N_i e^{-\frac{E_i^F}{2k_B T}} \tag{4.2}$$

where E_i^F are the energies of formation of defect pairs and $N_i = \frac{2}{3}N$ for ionic defects and $N_i = N$ for Bjerrum defects, with N the number of molecules per unit volume [84]. The mobility is defined by an Arrhenius-like equation

$$\mu_i = M_i \frac{1}{T} e^{-\frac{E_i^M}{k_B T}} \tag{4.3}$$

where M_i is a normalization coefficient and E_i^M is the motion activation energy.
It is possible to define the ionic conductivity and the Bjerrum conductivity, given respectively by:

$$\begin{aligned} \sigma_\pm &= \sigma_{H_3O^+} + \sigma_{OH^-} \\ \sigma_{DL} &= \sigma_L + \sigma_D \end{aligned} \tag{4.4}$$

Defect Type	e_i /$1.61 \times 10^{-19} C$	Intrinsic concentration n_i/N	μ_i $(10^{-8} m^2 V^{-1} s^{-1})$	Activation energy for formation and motion $\frac{1}{2}E_i^F + \frac{1}{2}E_i^M$ (eV)
H_3O^+	0.62	$\leq 10^{-13}$	10	> 0.7
OH^-	-0.62	$\leq 10^{-13}$	3	?
L	0.38	10^{-7}	2	0.58

Table 4.1: Parameters for water ice protonic point defects at 253 K. It is important to note that these values are affected by larger uncertainties and should be taken cautiously (taken from [140])

For pure water ice, at frequencies much higher than relaxation frequencies, $\nu \gg \nu_{rel}$ each type of defect activates and moves independently of the others, and the high-frequency conductivity is given by

$$\sigma_\infty = \sigma_\pm + \sigma_{DL} \tag{4.5}$$

The low-frequency or static conductivity σ_s, on the other hand, can be evaluated from the equation

$$\frac{e^2}{\sigma_s} = \frac{e_\pm^2}{\sigma_\pm} + \frac{e_{DL}^2}{\sigma_{DL}} \tag{4.6}$$

where the static conductivity is different from zero only if both types of defects are present in the ice lattice.

In general the high-frequency conductivity is controlled by the majority carriers, that are the defects with a higher product $n_i \times \mu_i$; the static conductivity, conversely, is mainly controlled by the minority carriers [140].

Above 230 K, as example, the majority carriers in pure ice are the Bjerrum defects and the minority carries the ionic defects, $\sigma_{DL} \gg \sigma_\pm$; for this reason $\sigma_\infty \simeq \sigma_{DL}$ and $\sigma_s \simeq \sigma_\pm \left(e^2/e_\pm^2\right)$.

Eventually it is possible to express the relaxation angular frequency and static permittivity as a function of the parameters defined by Jaccard's theory

$$\omega_{rel} = \Phi \left(\frac{\sigma_{DL}}{e_{DL}^2} + \frac{\sigma_\pm}{e_\pm^2} \right) \tag{4.7}$$

$$\varepsilon_s = \varepsilon_\infty + \frac{\left(\sigma_\pm/e_\pm - \sigma_{DL}/e_{DL}\right)^2}{\varepsilon_0 \Phi \left(\sigma_\pm/e_\pm^2 + \sigma_{DL}/e_{DL}^2\right)^2} \tag{4.8}$$

where Φ is the polarizability constant that depend on temperature and the distance between the two oxygen atoms.

The trend of relaxation frequency of pure ice versus temperature has been studied for decades by various research groups: in every set of data there's a change in slope at about 230 K except for [161], probably due to differences in the formation of the ice sample (see Fig. 4.3).

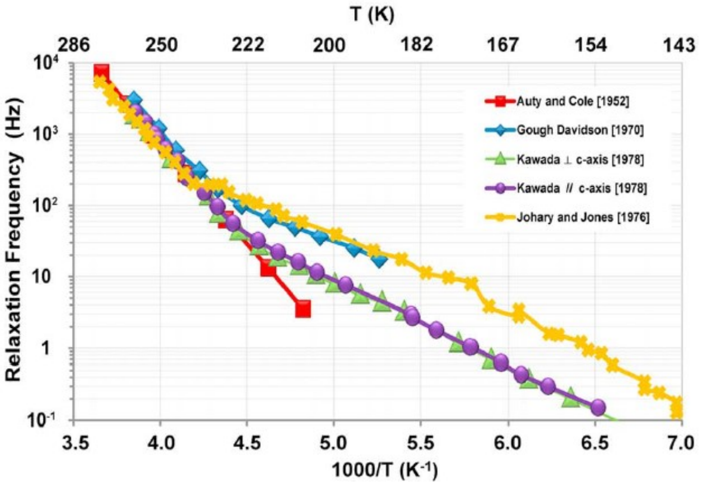

Figure 4.3: Trend of relaxation frequency of pure ice versus temperature according to literature [162], [161], [163], [164] (taken from [84]).

The static permittivity can also be expressed as [165]

$$\varepsilon_s = \frac{A}{T} exp\left[\frac{E_a}{k_B(T - T_0)} \right] \tag{4.9}$$

where $A = \sigma_s/(\varepsilon_0 \omega_0)$, E_a is the difference between the activation energy from relaxation time and the activation energy from the high frequency conductivity $E_a = E_a^\tau - E_a^\sigma$. Eq. 4.9 is a single relation both

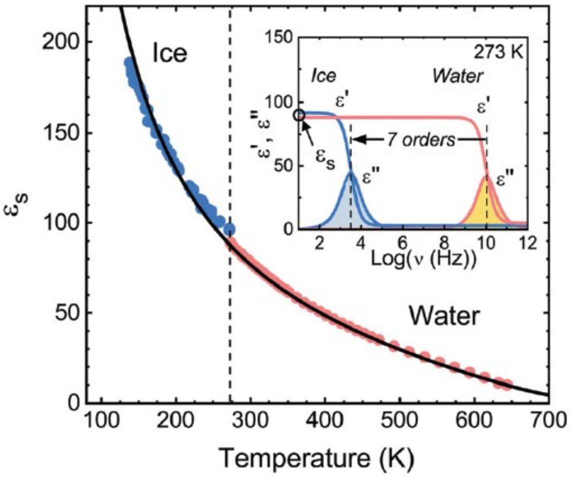

Figure 4.4: Temperature dependence of the static dielectric permittivity of ice and water. The black solid line is the fit of experimental data according to eq. 4.9. The box inside the figure shows the real and imaginary part of permittivity of ice and water at 273 K (taken from [165]).

for ice and water and it fits accurately the experimental static permittivity of both ice and water (see Fig. 4.4).

The high-frequency permittivity for pure ice slightly depends on temperature (see Fig. 4.5) and it was evaluated in [166] with the equation:

$$\varepsilon_\infty = 3.093 \pm 0.003 + (0.72 \pm 0.60)10^{-4}T + (0.11 \pm 0.02)10^{-5}T^2 \tag{4.10}$$

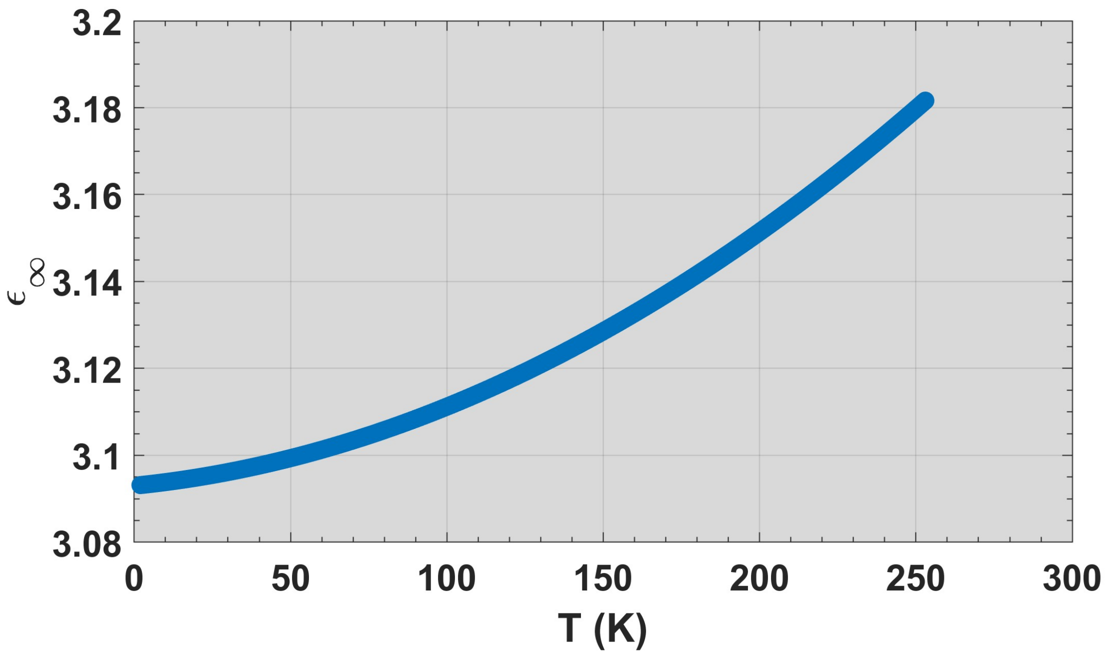

Figure 4.5: Pure ice high-frequency permittivity in the the temperature interval 2 K-253 K [166].

High frequency conductivity and static conductivity can also be expressed as a function of the parameters of Jaccard theory; for example, above 230 K with only one dominant defect type (L defects), the conductivity is given by

$$\sigma_\infty - \sigma_s \propto \frac{1}{T} e^{-\frac{E_{\sigma_\infty}}{k_B T}} \tag{4.11}$$

4.3.2 Wait-and-Switch Model

The other model employed to describe the dielectric behavior of pure water ice in addition to the phenomenological Jaccard theory is the *wait-and-switch* model [140], [167]. According to this commonly accepted model, the water dipoles switch between different dipole directions following the Bernal-Fowler rules. The water molecule only experiences these reorientations when it encounters an ice lattice defect (both L-D Bjerrum defects and H_3O^+- OH^- ionic defects); otherwise, it stays in a waiting mode. The activation energy of the Bjerrum defects diffusion E_{LD} is higher than the one associated to the migration of the ionic defects: despite this, in the pure ice at high temperatures (above $235\,K$) the overall polarization is more likely to be influenced by Bjerrum defects than by ionic ones, given the larger quantity of the former. At low temperatures, however, it becomes more and more difficult to overcome the potential barrier linked to Bjerrum defects and therefore the overall polarization is more likely to be affected by ionic defects, which have an activation energy that is about one third of that of the L-D defects. In this case, it is crucial to note that the two types of migration are closely related: in fact, the orientation left by the migration of L-D defects could prevent the diffusion of the ionic ones and, in general, the hopping proton can be released only by a rotation by the whole water molecule [168], [169]. At higher temperatures the diffusion is fast and the defects are stuck in these lattice "traps" for a relatively short time: the two kind of migrations ca be considered uncorrelated and the system is schematized by an equivalent circuit with two resistances R_{LD} and $R_{\pm}$in parallel. Thus, the ice complex permittivity can be expressed as:

$$\varepsilon(\omega) = \varepsilon_\infty + \frac{\varepsilon_s - \varepsilon_\infty}{1 + \left[(i\omega\tau_{LD})^{-1} + (i\omega\tau_{\pm})^{-\alpha_\pm}\right]^{-1}} \tag{4.12}$$

where τ_{LD} and $\tau_{\pm}^{\alpha_\pm}$ are respectively the relaxation times of orientation defects L-D and ion defects. At high temperatures (above 240 K), the relaxation time τ_{LD} is much smaller than the ionic one $\tau_\pm$ due to a large difference in their activation energy ($E_{LD} > E_\pm$) and thus the overall relaxation time is controlled manly by L-D defects, $\tau \approx \tau_{LD}$.

Below 240 K, the transition from the dominating motion of orientation defects at high temperatures to the dominant motion of ionic defects at low temperatures causes an adjustment in the activation energy, and the ion defects play the dominant role, thus $\tau \approx \tau_\pm$.

Dropping further in temperature, below 170 K, the motion of orientation defects appreciably slows down creating traps for ionic defects. Consequently, the protons diffusion motion is correlated with the movements of the L-D defects and the complex permittivity can be determined as:

$$\varepsilon(\omega) = \varepsilon_\infty + \frac{\varepsilon_s - \varepsilon_\infty}{1 + \left[(i\omega\tau_{LD})^{-1} + ((i\omega\tau_{\pm})^{\alpha_\pm} + (i\omega\tau_t)^{\alpha_t})^{-1}\right]^{-1}} \tag{4.13}$$

where the relaxation time $\tau_t^{\alpha_t}$ is related to the newly created traps for ionic defects. In case $\alpha_\pm$ and α_t are close to one, eq. 4.13 reduces to the Cole-Cole model.

4.3.3 Influence of Dopants

Impurities are able to introduce protonic *extrinsic* defects in the ice lattice; for examples the acids HF and HCl are sources of H_3O^+, with the halides that generate numerous Bjerrum defects. Such phenomenon changes drastically the electrical properties, that turn out to be different from the case of pure ice. In fact, saline ice exhibits a different behavior compared to that of pure ice and, in particular:

- below the eutectic concentration of the salt, ice is formed first and the excluded salts are concentrated in the brines, that subsequently freeze at the eutectic temperature;
- above the eutectic concentration of the salt, hydrates freeze first and then, at the eutectic temperature, the ice-hydrate mixture forms.

As soon as the concentration of impurities is increased to a few μM and decreasing the temperature, the ionic defects become the majority charge carrier (the Bjerrum ones on the other hand become the minority) [170]. Only certain chemical compounds at low concentrations in the mother solution (in the range $10^{-3} - 10^{-2}\ M$) can be incorporated in the ice lattice, forming a solid solution. At higher concentrations, on the other hand, impurities can induce imperfections in the ice structure such as air bubbles:

the impurities are located in these sites as inclusions in the grains or at the grain boundaries. Some salt are more effective in changing the dielectric properties of ice, for example this is the case of HCl and HF; other species as H_2SO_4 are less efficient in creating protonic defects.

The high-frequency conductivity for ices doped with low salt concentrations and at high temperatures is controlled by the L-D defects that are the majority carriers; since these defects have high activation energy ($E_a = 0.6\ eV$), σ_∞ rapidly decreases as a function of temperature. Moreover, such parameter is weakly dependent on the impurity concentration: the dopants, in fact, introduce a small number of extrinsic L-D defects. The static conductivity instead is strongly dependent on the ionic defects H_3O^+ and it increases with the impurity concentration, being practically independent of temperature. Above the so called *crossover temperature* T_c the H_3O^+ are the minority carriers and control σ_s, whereas the L defects are the majority carriers and influence σ_∞. For temperatures below T_c, the opposite occurs: the L defects become the minority carriers and control σ_s, while H_3O^+, now the majority carriers, dominate σ_∞. As a result, the slope of the two conductivities interchange. Finally increasing the impurities concentration the magnitude of σ_∞ and σ_s become comparable. Figure 4.6 summarizes the behavior of the conductivity as a function of the impurities concentrations and temperature.

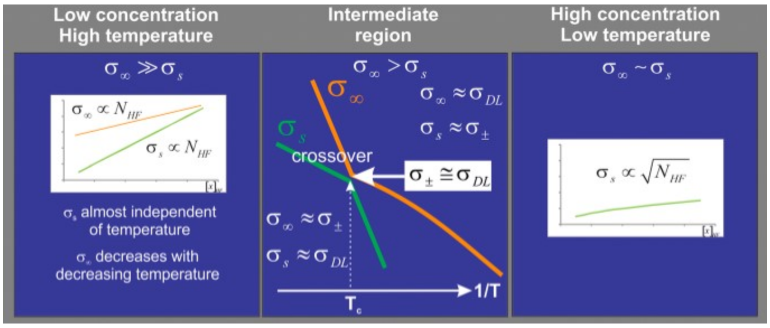

Figure 4.6: Summary of the behavior of the high-frequency and low-frequency conductivity as a function of the impurity concentration and temperature. From left to right, as the concentration increases and the temperature decreases, the trends of these two parameters are described (taken from [84]).

4.3.4 Influence of Anisotropy and Density

In this case the term "anisotropy" refers to the variation in permittivity that results from an ice crystal's orientation with regard to the wave propagation path. The ice Ih crystal has the optical axis that coincides with crystallographic c axis and then the complex permittivity is described by a tensor

$$\varepsilon = \begin{bmatrix} \varepsilon_{\perp c} & 0 & 0 \\ 0 & \varepsilon_{\perp c} & 0 \\ 0 & 0 & \varepsilon_{\parallel c} \end{bmatrix} \tag{4.14}$$

where $\varepsilon_{\perp c}$ and $\varepsilon_{\parallel c}$ are respectively the components when the electrical field is perpendicular and parallel to the c axis [171], [162]. The effect of anisotropy on the dielectric permittivity is higher at low frequencies, where there is a variation of about 15% between $\varepsilon_{\perp c}$ and $\varepsilon_{\parallel c}$; above 1 MHz the variation reduces to 1%. An example of the effect of anisotropy on the static permittivity of pure ice is shown in Fig. 4.7.

For the isotropic polycristalline ice, the complex permittivity is given by a combination of parallel and perpendicular permittivities

$$\varepsilon = (2\varepsilon_{\perp c} + \varepsilon_{\parallel c})/3 \tag{4.15}$$

Density has a non-negligible influence on both the real and the imaginary part of permittivity. This is mainly due to the air content (or bubbles) inside the ice structure and it is indipendent of the presence of chemical impurities.

4.3.5 Preparation of Ice Sample

The way ice forms and grows strongly influences its electrical properties [172]. Due to the lack of a reproducible standard procedure it is very difficult to compare the complex permittivities obtained from

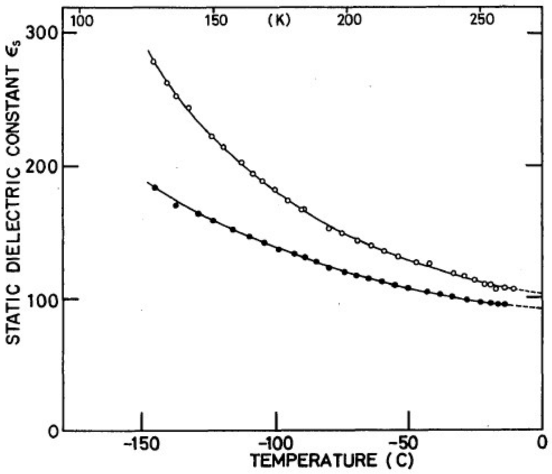

Figure 4.7: Effect of anistropy on the static permittivity of pure ice. Open and closed circles represent $\varepsilon_s^{\parallel}$ and $\varepsilon_s^{\perp}$ respectively (taken from [162]).

different experiments, since microscopic and macroscopic differences can appear in the ice sample such as: 1) cracks and fractures, 2) air bubbles, 3) chemical impurities and 5) lattice imperfections.
In [172] it was shown that the relaxation time of pure ice samples formed with a rapid crystallization are the same to those obtained in [173], while pure ice samples obtained with a slow crystallization process exhibit a relaxation time different, equal to that retrieved in [161]. Finally the study concludes that the growth rate of the ice crystal can affect the relaxation time (and thus the whole behavior of the complex permittivity) since a slow growth speed of ice crystal generates a smaller impurity content of ice.

4.4 Terrestrial Water Ice

As far as is currently known, all terrestrial ices are formed by polycristalline hexagonal ice, and, in general, it is possible to divide terrestrial ice into three different typologies, based on its formation: meteoric ice, sea ice and marine ice.

4.4.1 Meteoric Ice

The meteoric ice is formed by the transformation of snow into solid ice by densification, and it is found on the ice caps. The snow, after becoming firn, further compacts to a density (around 830 $kg\,m^{-3}$), at which polycrystalline ice contains only individual air bubbles, and not the paths between air or water and the ice grains, which have been closed. In the ice sheets these bubbles are usually present up to 500-1000 m depth. Beyond this point high pressure forces the bubbles to disappear, and the gas to diffuse into the ice lattice, forming the clathrate hydrates.
Snow can be thought of as a porous element consisting of air, ice crystals, and small amounts of chemical impurities. These, after traveling through the atmosphere, are deposited in the ice attached to the snowflakes, or as independent aerosols. They fluctuate over time, being the product of different chemical and climatic conditions at a certain time in the Earth's atmosphere. Either way, aerosols are mainly continental dust (such as silicates, $CaCO_3$, $CaSO_4$) or marine sprays (e.g. Na^+, K^+, Cl^-, SO_4^{2-}), or (see the H_2SO_4) are formed directly from gases in the atmosphere.

Electrical Properties

The ion concentration in meteoric ice tends to be low, by $1-10\,\mu M$, with exceptions in some basal layers of glaciers. Dielectric profiling (DEP) measurements showed that at high frequencies the conductivity is linearly dependent on the ionic impurity concentrations in the de-icing water, according to the relationship

$$\sigma_\infty = \sigma_{\infty_{pure}} + \sum_i \hat{\sigma_i}[x_i] \tag{4.16}$$

where $\sigma_{\infty_{pure}}$ is the high-frequency conductivity of pure ice, $[x_i]$ are the concentrations of specific ions, and $\hat{\sigma_i}$ are the molar conductivities.
Another widely used relationship for meteoric ice is the following, where σ_∞ is expressed in $\mu S/m$ and ion concentrations in μM

$$\sigma_\infty = 9 + 4[H^+] + 1[NH_4^+] + 0.55[Cl^-] \tag{4.17}$$

(conductivity is normalized to the temperature of -15°C).
Lattice impurities and sea salt contribute to reducing the relaxation time τ_{rel}; when impurities begin to become very present in the ice, then Maxwell-Wagner polarization can occur, which, due to the high conductivity of the grains, tends to increase polarization at the interface.

4.4.2 Sea Ice

Sea ice is formed by freezing ocean water: it starts by forming *frazil ice* characterized by a multi phase structure, which in addition to the classical hexagonal structure, includes gas, salt water, solid salt and other impurities. It is a type of ice with high salinity, due to the contribution of saltwater inclusions. The high salinity values of sea ices are due to the presence of brine inclusion with mirabilite ($Na_2SO_4 \cdot 10H_2O$) and hydrohalite ($NaCl \cdot 2H_2O$), the most common solid salts present in sea ice. Even at -40°C a non negligible fraction of brines persist in this type of ice.
Sea ice is commonly classified into three distinct categories based on its age: (a) *young ice*, which generally has a thickness of less than 30 centimeters, (b) *first-year ice*, characterized by a thickness ranging from 30 centimeters to 2 meters, and (c) *multiyear ice*, which typically exceeds a thickness of 2 meters [174]. The initial two categories of ice exhibit structural similarities and are often regarded as a unified category. A significant distinction between multiyear ice and the other categories lies in their respective brine concentrations.

Brine Volume Fraction

The volume fraction of brine inside sea ice is defined as

$$f_b = \frac{S_i}{S_b}\frac{\rho_i}{\rho_b} \tag{4.18}$$

where S_i is the salinity of the ice, S_b is the salinity of the brines, ρ_i is the density of pure ice and ρ_b is the density of the brine [96]. S_b and ρ_b are two quantities temperature-dependent. Furthermore, based on experimental data reported in [175], the sea ice brine volume fraction can also be expressed as a function of temperature T [176]

$$f_b^{sea\,ice} = 10^{-3} S_i \left(-\frac{49.185}{T} + 0.532\right) \tag{4.19}$$

where the equation is valid in the temperature range $-0.5°C \geq T \geq -22.9°C$.

Electrical Properties

Given the multiphase composition of sea ice and the presence of brine pockets, it is very difficult to assign fixed complex permittivity values to this type of ice, which is very site-dependent. In general, the complex dielectric permittivity of sea ice depends on several parameters, such as: the complex permittivity of pure ice, the complex permittivity of brine pockets, the shape and orientation of these latter and the brine volume fraction $f_b^{sea\,ice}$.
In the literature, there are in the first instance two types of experiments conducted on sea ice: the first is a granular ice grown in the laboratory and obtained by pouring synthetic brines into a sample of porous snow, the second, the so-called natural mosaic sea ice, by taking samples in situ [177], [178],[179]. Both samples have similar dielectric behavior with two abrupt changes in permittivity and conductivity at the NaCl eutectic temperature of 251 K, when the salt begins to precipitate into brines and produce a mixture of ice and brine, and the second below 218 K, when the brines freeze completely. Three relaxation phenomena are present in these sea ice samples (see Fig. 4.8):

- at low frequencies the migrations of ions within the brine channels produce an additional static permittivity and a ion-space charge polarization;

- at higher frequencies a Debye-like relaxation of protons in the ice was observed;
- in the MHz region a Maxwell-Wagner relaxation occurs between the ice matrix and the brine channels.

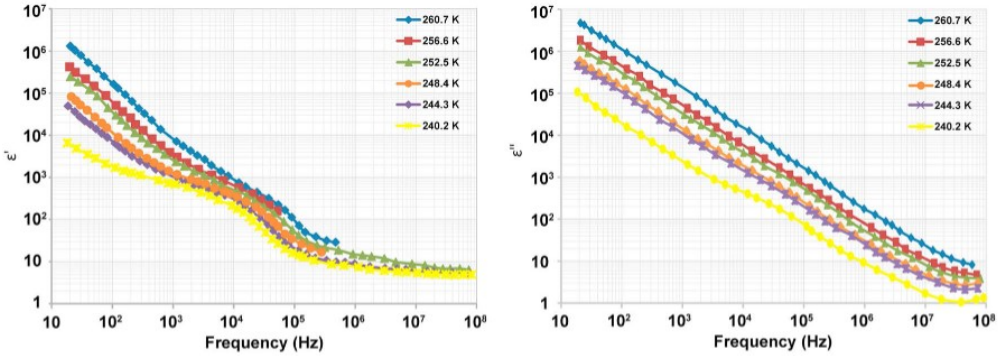

Figure 4.8: Real and imaginary part of dielectric permittivity of artificial sea ice as a function of frequency from 260 K to 240 K [84]. (modified after [178]).

Other papers studied the behavior of in situ complex permittivity of sea ice, pointing out that [180], [181]: 1) the brine conductivity increases as the temperature decreases down to -8°C, then it starts to decrease, 2) the real part of permittivity is highly dependent on the brine volume fraction but less dependent on the orientation of their orientations, and on the contrary 3) the imaginary part of permittivity is strongly dependent on the brine inclusion orientation and less dependent on the brine volume fraction.
In [181] the complex permittivity of natural sea ice as a function of the depth were modeled (see Fig. 4.9).

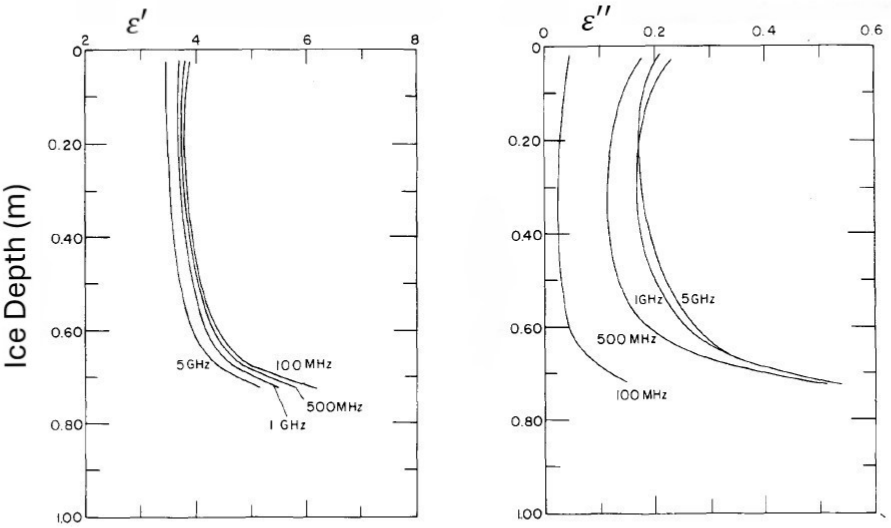

Figure 4.9: Real and imaginary part of dielectric permittivity of model sea ice as a function of depth (modified after [181]).

The temperature dependence of the three types of sea ice is shown in Fig. 4.10.

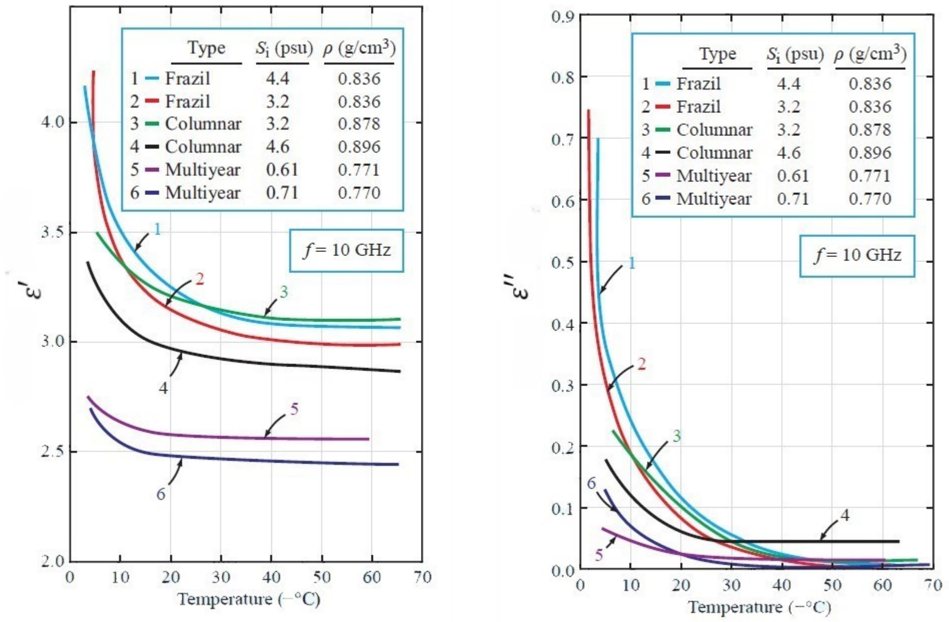

Figure 4.10: Real and imaginary part of dielectric permittivity versus temperature of three types of sea ice at 10 GHz (modified after [96]).

4.4.3 Marine Ice

Marine ice originates from thermohaline circulation that fills the cavities below an ice shelf with water. Melting ice near the base contributes to lowering the salinity and density of seawater, which subsequently flows outward along the bottom of the shelf. Thus the water re-gels, first forming frazil ice, and later compacts generating marine ice. Because of its composition, it is opaque to radio waves, unlike meteoric ice. The upper part of the marine ice layer is characterized by an air bubble free structure with brine pockets, while the lower part is hydraulically connected with the ocean water through a system of brine drainage channels [182], [183].

Electrical Properties

The electrical properties of marine ice are poorly studied and there's only one paper that effectively analyzed the conductivity of marine ice samples at different depths [184]. It was highlighted that only the conductivities of few samples follow the linear trend of the low-salinity data of meteoric ice, wheres others significantly differ from such trend (see Fig. 4.11). It was explained that the lower-salinity samples are well described by the Jaccard theory, with L defects created in proportion to the salinity. Higher salinity samples have the Cl^- concentration above the solubility limit of about 300 μM, causing the ions to concentrate at the grain boundaries. Finally, the liquid brines are present at temperatures between -10°C and -30 °C.

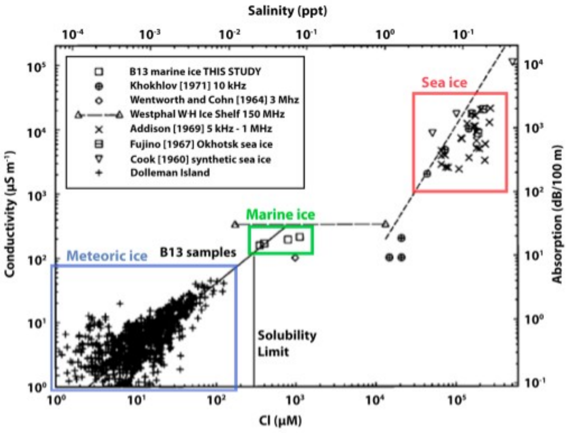

Figure 4.11: Conductivity versus Cl concentration for marine ice samples. The meteoric ice samples and sea ice samples belong to two distinct populations with different electrical behaviors; the marine ice samples have conductivities that lie in an intermediate region between these two populations. (modified after [184]).

4.5 NaCl Doped Ice

NaCl solutions take into the ice lattice H_3O^+ and Cl^-, with the chloride substitution that depends on the pH of the sample. The impurity saturation (for both H_3O^+ and Cl^-) of the ice lattice lies in the range $0.1 - 0.3\ mM$; so the above this limit the impurites that cannot be incorporated in the lattice are precipitated as hydrates [185]. Moreover, in literature it has been calculated that the relaxation time of ice saturates for initial NaCl concentration of $\sim 0.3\ M$ [185].

Below eutectic composition (i.e., 23.3 wt %) ice is the initial phase to form; the salt that is not incorporated into the ice becomes concentrated in the brines, which then freeze into a mixture of ice and hydrate at the eutectic temperature (i.e., $\approx 252\ K$, see Fig. 4.12). On the other hand, above the eutectic composition, hydrates are formed first, with the ice-hydrate mixture freezing subsequently, again at the eutectic temperature [185]. The Cl^- partition coefficient, i.e. the ratio of the concentration of a substance in one medium to the concentration in a second phase when the two concentrations are at equilibrium, is approximately equal to $k \approx 4 \times 10^{-4}$ for NaCl solutions [185].

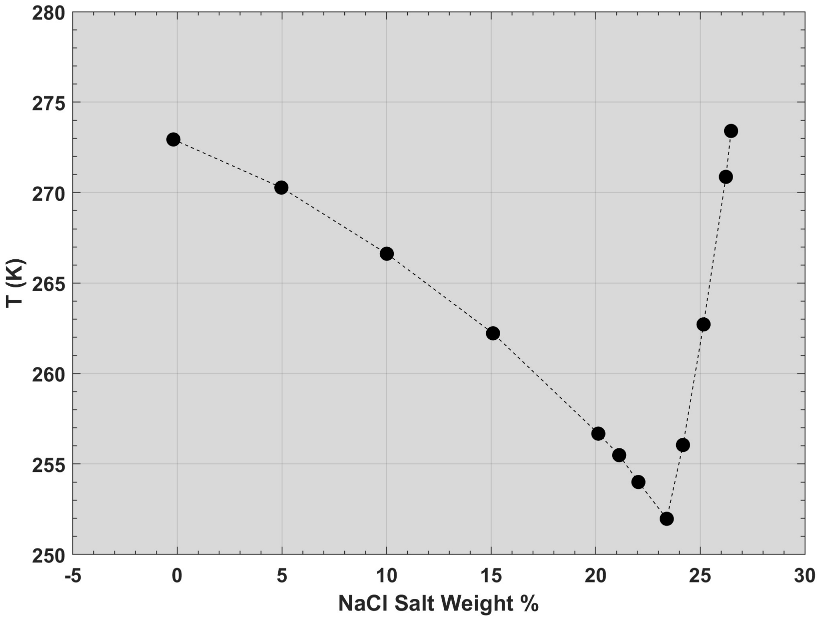

Figure 4.12: Phase diagram of NaCl solutions.

The static conductivity versus temperature of NaCl doped ice was studied at different salt concentrations [185]. In Figure 4.13 it can be noticed that the static conductivity is dependent on the NaCl concentration and the temperature and that it shows an abrupt increase at the eutectic temperature (i.e., $\approx 252\ K$) regardless of the concentration, due to the appearance of the brines in the ice.

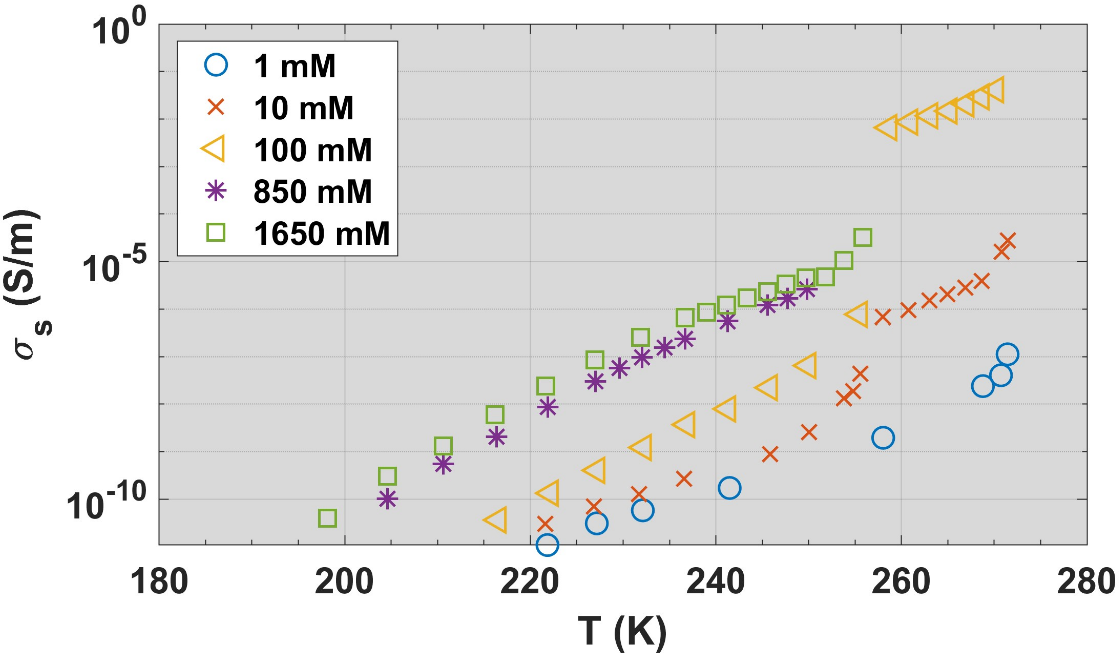

Figure 4.13: Conductivity versus temperature of NaCl doped ice at different concentrations (data taken from [185]).

4.5.1 Dielectric Permittivity of NaCl Brine

The complex permittivity of brines composed by mainly NaCl solutions is given by [186]

$$\varepsilon'_{brine} = \varepsilon_{w\infty} + \frac{\varepsilon_{0,brine} - \varepsilon_{w\infty}}{1 + (2\pi\nu\tau_{brine})^2} \tag{4.20}$$

$$\varepsilon''_{brine} = (2\pi\nu\tau_{brine})\frac{\varepsilon_{0,brine} - \varepsilon_{w\infty}}{1 + (2\pi\nu\tau_{brine})^2} + \frac{\sigma_{brine}}{2\pi\nu\varepsilon_0} \tag{4.21}$$

where $\varepsilon_{w,\infty} = 4.9$ and τ_{brine}, $\varepsilon_{0,brine}$ are tabulated in the literature [96].

4.6 Dirty Ice

The dirty ice is the type of ice where mineral grains are mechanically trapped in the polycristalline structure of the ice. It is quite uncommon on Earth; the meteoric ice, as example, has a negligible amount of grain inclusions (less than 1 %). Nevertheless, in the Solar System dirty ice is found quite often. For example, it has been observed on the surface of three of the Jovian icy moons, Callisto, Ganymede and Europa [56] and on the Martian polar caps [187].

Despite this, only few measurements of the electrical properties of dirty ice have been carried out in the literature. In [188] the low-frequency electrical properties of ice-silicate mixtures were measured, finding out that the ice relaxation frequencies are higher than those measured in defect-saturated saline ice: this has been interpreted as indicating the formation of additional defects near the silicate surfaces. Moreover from the complex spectra five different relaxations related to H_2O were identified.

The electrical properties of ice/chondrites mixtures were studied in [103] as a function of the inclusion volume fraction and temperature (113-298 K) in the frequency range 1 MHz -1 GHz. It was found out that the real part of permittivity increases as the temperature rises (see Fig. 4.14); nevertheless it was not possible to measure the imaginary part of permittivity since it was too low and below the instrumental limit. In the framework of the Rosetta mission, the dielectric properties of analog materials for the refractory component of comets mixed with ice were studied at low frequencies (kHz range) as a function of temperature (see Fig. 4.15). The authors of the paper concluded that the complex permittivity of dirty ice is characterized by two components: the first one acts as "background" permittivity with little dispersion and it depends firstly on the density of the granular material and its chemical composition; the second one that has a strongly dispersive permittivity which depends on the properties of water ice. It was pointed out that the background-mineral permittivity dominates at low temperatures, whereas the ice permittivity has more influence at higher temperature, around 200 K. In the Mars framework [189] studied the influence of basalt dust in ice, measuring the complex permittivity for temperatures ranging from 150 K up to 250 K in the frequency range 20 Hz -1 MHz. In this case a particular behavior was observed: the imaginary part of permittivity is approximately a linear combination between the electrical properties of ice and those of basalt grains, whereas the real part at high frequencies is very similar to the one of pure ice.

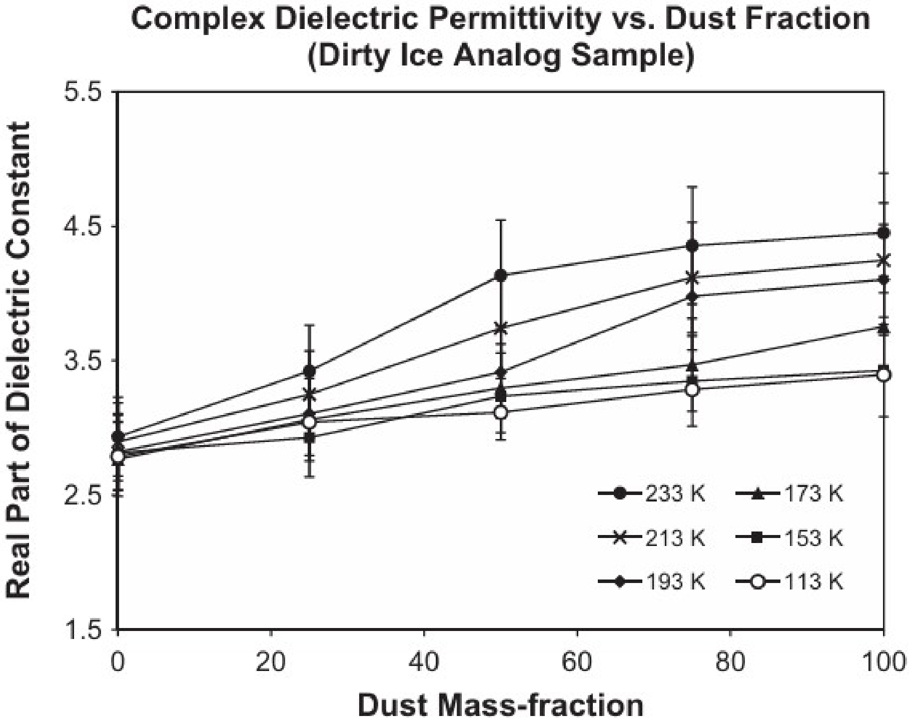

Figure 4.14: Real part of permittivity versus dust mass-fraction of a LL5 chondrite/ice mixture at different temperatures (taken from [103]).

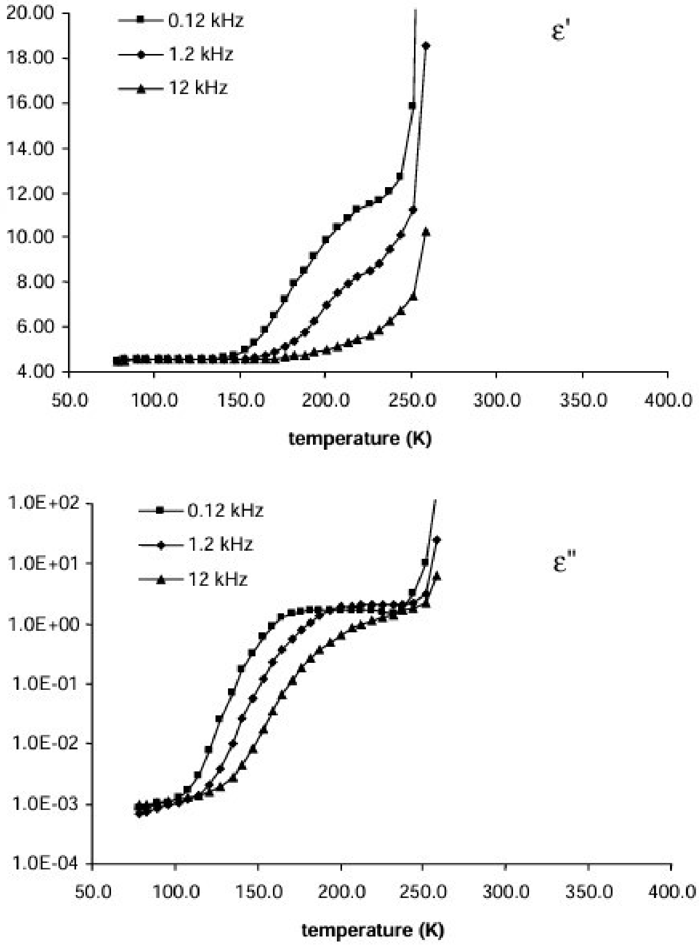

Figure 4.15: Complex permittivity versus temperature of dunite/ice mixtures at different frequencies in the kHz range (taken from [190]).

Chapter 5

Transmission Line Theory and Vector Network Analyzer Setup

A transmission line is a physical structure designed to guide an electromagnetic wave from point to point in a confined manner. A transmission line have conductors long enough to take wave propagation into account. Generally, transmission lines are made from metallic materials (generally filled with low-loss dielectrics) used to transmit high-frequency signals over both short and long distances with minimal energy loss. In this work a coaxial transmission line has been used in order to estimate the EM parameters of several materials in the frequency range 1 MHz-1 GHz.
The theory behind the wave propagation in a transmission line can be approached with two different viewpoints: starting from the classical Maxwell's equations or from an extension of circuit theory. In the following, both approcheas will be described and compared.

5.1 From Maxwell Equations: EM Approach

Maxwell's equations in the frequency domain are

$$\begin{aligned} \nabla \times \mathbf{E}(\mathbf{r},\omega) &= -i\omega\mu(\omega)\mathbf{H}(\mathbf{r},\omega) \\ \nabla \times \mathbf{H}(\mathbf{r},\omega) &= -i\omega\varepsilon(\omega)\mathbf{E}(\mathbf{r},\omega) \end{aligned} \tag{5.1}$$

The simplest scenario is the one where the electric and magnetic polarization lie in the plane $\{x, y\}$ and the wave propagates along the z axis, with E_z and H_z related by (*TEM wave propagation*)

$$\begin{aligned} \partial_z E_y = i\omega\mu H_x \qquad & \partial_z H_y = -i\omega\varepsilon E_x \\ \partial_z E_x = -i\omega\mu H_y \qquad & \partial_z H_y = i\omega\varepsilon E_y \\ \partial_x E_y - \partial_y E_x = 0 \qquad & \partial_x H_y - \partial_y H_x = 0 \end{aligned} \tag{5.2}$$

Using equations (5.2) and factorizing both fields with vector and scalar functions (respectively $\mathbf{f}(x, y)$, $\mathbf{g}(x, y)$, $v(z, \omega)$) and $i(z, \omega)$), the dependence in the $\{x, y\}$ plane can be expressed as the gradient of a scalar function, which is the solution of the Laplace's equation

$$\nabla^2\phi(x, y) = 0 \tag{5.3}$$

So electric and magnetic field can be written as

$$\begin{aligned} \mathbf{E}(\mathbf{r},\omega) &= -\nabla_{x,y}\phi(x, y)v(z, \omega) \\ \mathbf{H}(\mathbf{r},\omega) &= \nabla_{x,y}\phi(x, y)i(z, \omega) \end{aligned} \tag{5.4}$$

Replacing (5.4) in (5.2) and deriving with respect to z, two one-dimensional wave equations are obtained

$$\begin{aligned}\frac{\partial^2 i(z,\omega)}{\partial z^2}+k^2 i(z,\omega)=0\\ \frac{\partial^2 v(z,\omega)}{\partial z^2}+k^2 v(z,\omega)=0\end{aligned}\tag{5.5}$$

where $k=\frac{2\pi}{\lambda}=\frac{\omega}{c}\sqrt{\varepsilon(\omega)\mu(\omega)}$ is the magnitude of the wave vector, with λ the wavelenght of the EM wave.
These equations have as their solution the sum of two plane waves, a progressive one and a regressive one

$$\begin{aligned}v(z)=v^+e^{-ikz}+v^-e^{ikz}\\ i(z)=[v^+e^{-ikz}-v^-e^{ikz}]/\eta\end{aligned}\tag{5.6}$$

where $\eta=\eta_0\sqrt{\mu(\omega)/\varepsilon(\omega)}$ is the wave impedance.
By imposing initial, boundary and on section conditions the final solution for $\mathbf{E}(\mathbf{r},\omega)$ and $\mathbf{H}(\mathbf{r},\omega)$ is obtained.

5.1.1 Coaxial Transmission Line and Characteristic Impedance

Taking as example the case of a coaxial transmission line, the characteristic impedance Z_0, a fundamental parameter of these structurescan be defined [191]. The geometry of a coaxial line is cylindrical and it is defined by two conductors (an inner one and an outer one) that delimit the space of propagation of the wave $r\in[a,b]$. It is possible to determine the scalar potential $\phi(x,y)$ with the Laplace equation in polar coordinates $\{r,\theta\}$:

$$\frac{1}{r}\frac{\partial}{\partial r}\left(r\frac{\partial\phi}{\partial r}\right)+\frac{1}{r^2}\frac{\partial^2\phi}{\partial\theta^2}=0$$

Considering the boundary conditions, i.e. $\phi(a,\theta)=V_a$ and $\phi(b,\theta)=V_b$ (ϕ has to be constant on the conductors), the potential is defined as:

$$\phi(r)=V_b+\frac{V_a-V_b}{ln(a/b)}ln(r/b)=\frac{V_0}{ln(a/b)}ln(r/b)\tag{5.7}$$

assuming for the sake of simplicity $V_b=0$ and $V_0=V_a-V_b$.

It follows that the electric field is directed in the radial direction $\hat{\mathbf{r}}$, and the magnetic field in the azimuthal one $\hat{\theta}$:

$$\begin{aligned}\mathbf{E}(\mathbf{r},\omega)=\hat{\mathbf{r}}\tfrac{V_0}{ln(b/a)}\tfrac{1}{r}\left[v^+e^{-ikz}+v^-e^{ikz}\right]\\ \mathbf{H}(\mathbf{r},\omega)=\hat{\theta}\tfrac{V_0}{\eta ln(b/a)}\tfrac{1}{r}\left[v^+e^{-ikz}-v^-e^{ikz}\right]\end{aligned}\tag{5.8}$$

For the coaxial lines it is convenient to use a circuital approach (detailed in the next section), because these structure are powered by a voltage generator $v_g(t)$. For this reason the voltage $V(z,\omega)$ and the current $I(z,\omega)$ can be defined: the first one can be calculated with a line integer (as the potential difference between the two conductors) and the second one with the Ampère theorem (as the circulation around one conductor):

$$\begin{aligned}V(z,\omega)=\textstyle\int_a^b \mathbf{E}(\mathbf{r},\omega)\cdot\hat{\mathbf{r}}dr\\ I(z,\omega)=\textstyle\int_0^{2\pi}\mathbf{H}(\mathbf{r},\omega)_{r=c\in(a,b)}\cdot\hat{\theta}cd\theta\end{aligned}\tag{5.9}$$

From these equations a relation valid also for other transmission lines is obtained

$$\begin{aligned}V(z,\omega)=V_0\left[v^+(z)+v^-(z)\right]\\ I(z,\omega)=\tfrac{V_0}{Z_0}\left[v^+(z)-v^-(z)\right]\end{aligned}\tag{5.10}$$

where Z_0 is the characteristic impedance and it is defined as the product between a geometrical factor f_g (determined by the transverse dimension of the line) and the wave impedance η:

$$Z_0 = f_g\eta = f_g\eta_0\sqrt{\frac{\mu}{\varepsilon}} \tag{5.11}$$

where, in the case of a coaxial transmission line, $f_g = ln(a/b)/2\pi$.

5.2 Circuital Approach

A transmission line is considered a *distributed-parameter* network, because its physical dimensions are not much smaller than the electrical wavelength, unlike the case of ordinary circuits (that have *lumped elements* and it is assumed $\Delta z \ll \lambda$). In fact, the voltages and currents of a transmission line network can vary in magnitude and phase over its length, and only a piece of line of infinitesimal length Δz can be modeled as a lumped-element circuit (see Fig. 5.1). The transmission line is generally schematized as a two-wire line since it has always at least two conductors in order to permit transverse electromagnetic wave propagation, connecting a voltage generator to a load. It is then possible to define the following quantities [191]:

$R = series\,resistance\,per\,unit\,length \qquad \Omega/m$

$L = series\,inductance\,per\,unit\,length \qquad H/m$

$G = shunt\,capacitance\,per\,unit\,length \qquad S/m$

$C = shunt\,conductance\,per\,unit\,length \qquad F/m$

where R represents the resistance caused by the finite conductivity of the single conductor, L describes the total self-inductance of the two conductors, C is the capacitance caused by the proximity of the two conductors and G is due to the dielectric loss between the two conductors.
These parameters are distributed continuously throughout the circuit material and each infinitesimal length dz is a circuit element.

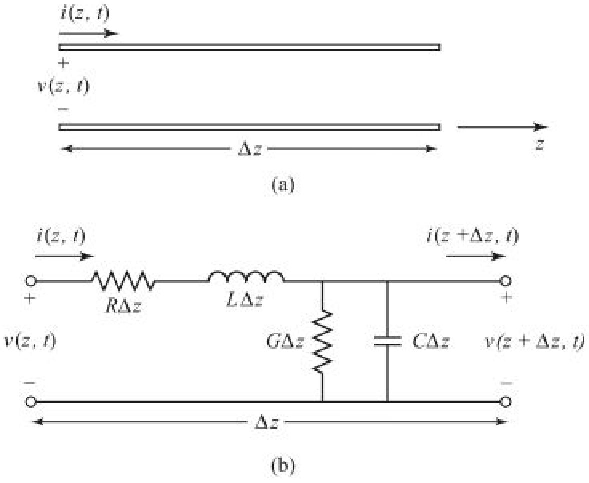

Figure 5.1: (a) voltage and currents of the tranmission line; (b) lumped-element equivalent circuit [191]

Applying the Kirchhoff's voltage and current laws to the circuit 5.1.b and manipulating the equations, the time domain form of the transmission line equations, also known as the *telegrapher equations*, are obtained

$$\begin{aligned}\frac{\partial V(z,\omega)}{\partial z} &= -(R+i\omega L)I(z,\omega)\\ \frac{\partial I(z,\omega)}{\partial z} &= -(G+i\omega C)V(z,\omega)\end{aligned} \tag{5.12}$$

These two equations can be solved, giving wave equations for $I(z)$ and $V(z)$:

$$\frac{d^2V(z)}{dz^2} - k^2V(z) = 0 \tag{5.13}$$

$$\frac{d^2I(z)}{dz^2} - k^2I(z) = 0 \tag{5.14}$$

where $k = \beta - i\alpha = \sqrt{(R+i\omega L)(G+i\omega C)}$ is the complex propagation constant. Travelling wave solutions are then:

$$V(z) = V_0^+e^{-kz} + V_0^-e^{kz} \tag{5.15}$$

$$I(z) = I_0^+e^{-kz} + I_0^-e^{kz} = \frac{V_0^+e^{-kz} + V_0^-e^{kz}}{\eta} \tag{5.16}$$

where the e^{kz} term describes the wave propagation in $-z$ direction, e^{-kz}describes the wave propagation in the $+z$ direction, and $\eta = \eta_0\sqrt{\mu(\omega)/\varepsilon(\omega)}$ is the wave impedance. The current on the line is obtained applying 5.13 to the voltage in 5.15:

$$I(z) = \frac{k}{R+i\omega L}(V_0^+e^{-kz} - V_0^-e^{kz}) \tag{5.17}$$

Then the *characteristic impedance* Z_0 can be found as

$$Z_0 = \frac{R+i\omega L}{k} = \sqrt{\frac{R+i\omega L}{G+i\omega C}} \tag{5.18}$$

These results shown in eq. (5.2) can be compared to those obtained from Maxwell's equations (5.5), highlighting the similarities between circuit parameters and electrical properties

$$\begin{aligned}k = \frac{\omega}{c}\sqrt{\varepsilon\mu} \qquad & k = -i\sqrt{(R+i\omega L)(G+i\omega C)}\\ Z_0 = f_g\eta_0\sqrt{\frac{\mu}{\varepsilon}} \qquad & Z_0 = \sqrt{\frac{R+i\omega L}{G+i\omega C}}\end{aligned} \tag{5.19}$$

with f_g geometric factor that depends on the geometric characteristic of the line.
Eventually the characteristic impedance and the wave vector can be derived

$$\begin{aligned}C = C_0\varepsilon' &= 1/f_g\varepsilon_0\varepsilon'\\ L = L_0\mu' &= f_g\mu_0\mu'\\ G = \omega C_0\varepsilon'' &= 1/fg\varepsilon_0\varepsilon''\\ R = \omega C_0\mu'' &= f_g\mu_0\mu''\end{aligned} \tag{5.20}$$

5.2.1 Input impedance and Scattering function

It is possible to estimate the input impedance $Z_{in}(\omega)$ of the equivalent circuit of the transmission line and the scattering function $S(\omega)$, that describes waves reflections in the line, through two different approaches, a circuital one and another one based on a multi-layer wave propagation analogy [192]. In this section the problem will be analyzed with the first approach, i.e. the circuital one.

It is assumed that the line has length L and it is homogeneous in the electromagnetic parameters, and that at $z = 0$ the line is powered by a voltage generator $v_g(t)$ and at $z = L$ it is connected to a load of impedance Z_L.
It is then possible to define the reflection coefficient $\Gamma(z)$ as the ratio between the reflection wave and the transmitted one:

$$\Gamma(z) = \frac{v^-(z)}{v^+(z)} = \frac{v^-}{v^+}e^{ik2z} = \Gamma(0)e^{ik2z} \tag{5.21}$$

For a coaxial line it stands

$$\begin{aligned} V(z,\omega) &= V_0 v^+(z)[1+\Gamma(z)] \\ I(z,\omega) &= \frac{V_0 v^+(z)}{Z_c}[1-\Gamma(z)] \end{aligned} \tag{5.22}$$

then, reversing and imposing the boundary condition

$$\Gamma_L = \frac{Z_L - Z_c}{Z_L + Z_c} \tag{5.23}$$

The input impedance is obtained for $z = 0$

$$Z_{in} = Z_c \frac{1+\Gamma(0)}{1-\Gamma(0)} = Z_c \frac{Z_L + iZ_c tan(kL)}{Z_c + iZ_L tan(kL)} \tag{5.24}$$

The scattering function $S(\omega)$ is useful to understand the multiple reflection phenomena in the transmission line: these happen because of two impedance mismatches, at $z = 0$ and $z = L$ respectively. Then $S(\omega)$ represents the energy that flows back to the generator

$$S(\omega) = \frac{Z_{in} - Z_g}{Z_{in} + Z_g} = \frac{\Gamma_g + \Gamma_L e^{-ik2L}}{1 + \Gamma_g \Gamma_L e^{-ik2L}} \tag{5.25}$$

where $\Gamma_g = \frac{Z_c - Z_g}{Z_c + Z_g}$ is the mismatch at the beginning of the line.

There are three notable cases: short load, open load and adapted load.

Short load

In this case $Z_L = 0$ and there is total reflection and no transmission ($\Gamma_L = \frac{Z_L - Z_g}{Z_L + Z_g} = 1$). Then, the parameters are

$$\begin{aligned} Z_{in} &= iZ_c tan(kL) \\ S(\omega) &= \frac{\Gamma_g + e^{-i2kL}}{1 + \Gamma_g e^{-i2kL}} \end{aligned} \tag{5.26}$$

Open load

In this case $Z_L = \infty$ and there is once again total reflection at the end of the line (but with $\Gamma_L = -1$). The parameters become

$$\begin{aligned} Z_{in} &= -i\frac{Z_c}{tan(kL)} \\ S(\omega) &= \frac{\Gamma_g - e^{-i2kL}}{1 - \Gamma_g e^{-i2kL}} \end{aligned} \tag{5.27}$$

Adapted load

In this case the load has the same impedance as the characteristic impedance, $Z_L = Z_c$, and there is no reflection ($\Gamma_L = 0$), so the scattering function is

$$S(\omega) = \Gamma_g \tag{5.28}$$

5.3 Impedance and Admittance Matrices

The impedance and admittance matrices are employed in circuit theory to relate the different port of a microwave network, leading to an overall description of the network in terms of equivalent circuits. Considering an arbitrary N-port microwave network (see Fig. 5.2), each nth port at its t_n terminal plane is characterized by equivalent voltages and currents for the incident (V_n^+, I_n^+) and reflected (V_n^-,I_n^-) waves. At the nth terminal plane the total voltage and current is given by

$$V_n = V_n^+ + V_n^- \tag{5.29}$$

$$I_n = I_n^+ + I_n^- \tag{5.30}$$

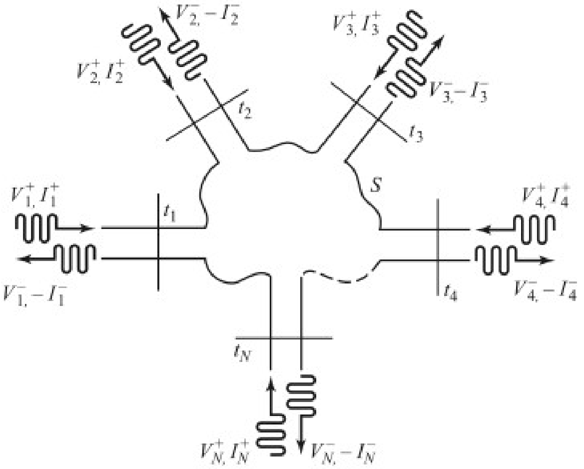

Figure 5.2: N-port microwave network [191].

The total impedance matrix connect the total port currents with total port voltages of the microwave network and can be expressed as

$$\begin{bmatrix} V_1 \\ V_2 \\ \vdots \\ V_N \end{bmatrix} = \begin{bmatrix} Z_{11} & Z_{12} & \cdots & Z_{1N} \\ Z_{21} & \ddots & & \vdots \\ \vdots & & \ddots & \vdots \\ Z_{N1} & \cdots & \cdots & Z_{NN} \end{bmatrix} \begin{bmatrix} I_1 \\ I_2 \\ \vdots \\ I_N \end{bmatrix} \tag{5.31}$$

or, in matrix form, as:

$$\left[V\right] = \left[Z\right]\left[I\right] \tag{5.32}$$

Similarly, the admittance matrix is defined in compact form as

$$\left[I\right] = \left[Y\right]\left[V\right] \tag{5.33}$$

of course, the impedance matrix is the inverse of the admittance matrix:

$$\left[Y\right] = \left[Z\right]^{-1} \tag{5.34}$$

The Z_{ij} element of the matrix can be found in the following way:

$$Z_{ij} = \left.\frac{V_i}{I_j}\right|_{I_k=0,\, k\neq j} \tag{5.35}$$

where $I_k = 0,\ k \neq j$ means that all the ports except the jth have been open-circuited.

In general, Z_{ij} and Y_{ij} may be complex values. If the N-port network is reciprocal (i.e. not containing any nonreciprocal media or active devices), the impedance and admittance matrices are symmetric ($Z_{ij} = Z_{ji}$, $Y_{ij} = Y_{ji}$). Moreover, in case the network is lossless, Z_{ij} and Y_{ij} are solely imaginary (this property can be demonstrated considering that the net real power delivered to a lossless network must be zero, $Re\{P_{av}\} = 0$).

5.4 Scattering Matrix

For high-frequency networks, however, a mathematical discussion that includes the concepts of incident, reflected and transmitted waves is simpler than the previous case with equivalent voltages, currents and the impedance matrix. This representation is well described by the scattering matrix and it is more in agreement with the direct measurements such as those that can be performed by means of a Vector Network Analyzer (VNA) (see Fig. 5.3 for a simplified block diagram of a two-port VNA).

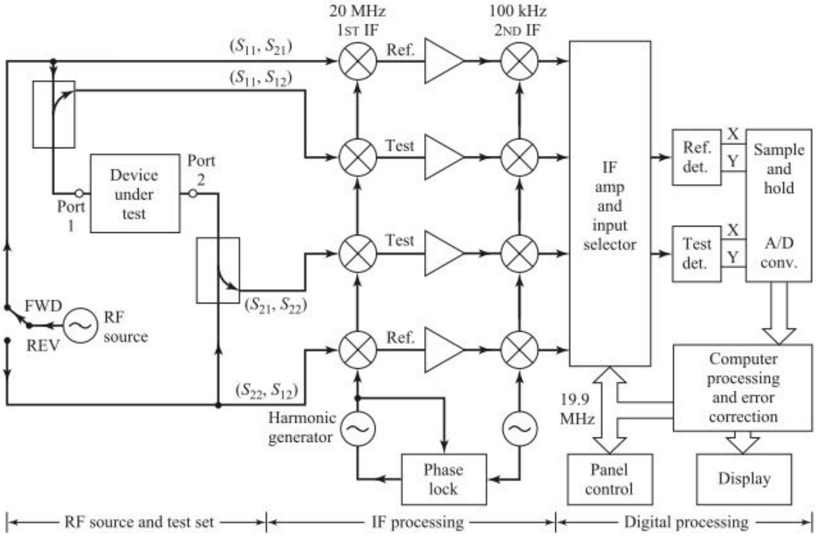

Figure 5.3: Simplified block diagram of a two-port Vector Network Analyzer

The scattering matrix relates the voltage waves incident on the port to those reflected from the ports. Considering the N-port network in figure 5.2, where V_n^+ and V_n^- are respectively the amplitude of the incident or reflected voltage wave, the scattering matrix is defined as

$$\begin{bmatrix} V_1^- \\ V_2^- \\ \vdots \\ V_N^- \end{bmatrix} = \begin{bmatrix} S_{11} & S_{12} & \cdots & S_{1N} \\ S_{21} & \ddots & & \vdots \\ \vdots & & \ddots & \vdots \\ S_{N1} & \cdots & \cdots & S_{NN} \end{bmatrix} \begin{bmatrix} V_1^+ \\ V_2^+ \\ \vdots \\ V_N^+ \end{bmatrix} \tag{5.36}$$

or, in matrix form, as:

$$\left[V^-\right] = \left[S\right] \left[V^+\right] \tag{5.37}$$

The element S_{ij} of the matrix can be found as

$$S_{ij} = \left.\frac{V_i^-}{V_j^+}\right|_{V_k^+=0,\ k\neq j} \tag{5.38}$$

where $V_{k+} = 0,\ k \neq j$ means that all ports should be terminated in matched loads except the jth one. So S_{ii} elements are the reflection coefficients, and S_{ij} are the transmission ones. $\left[S\right]$ matrix is symmetric

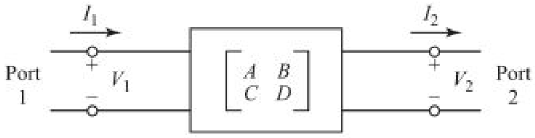

Figure 5.4: Two-port network in terms of the transmission matrix.

for reciprocal networks and unitary for lossless networks.

In a two-port Vector Network Analyzer as the one employed or this work, by measuring the reflection parameters S_{11}, S_{22} and the transmission parameters S_{12}, S_{21} it is possible to estimate the complex permittivity and permeability.

5.5 The Transmission Matrix

It is often more convenient to use a 2×2 *transmission* (or *ABCD*) matrix to describe a two-port network (see Fig. 5.4), instead to use *Z, Y* and *S* matrices.

The *ABCD* matrix is defined in terms of the total voltages and currents of the two-port network:

$$V_1 = AV_2 + BI_2 \qquad I_1 = CV_2 + DI_2 \tag{5.39}$$

or, in matrix form, as

$$\begin{bmatrix} V_1 \\ I_1 \end{bmatrix} = \begin{bmatrix} A & B \\ C & D \end{bmatrix} \begin{bmatrix} V_2 \\ I_2 \end{bmatrix} \tag{5.40}$$

The parameters of both S and Z matrices can be converted in *ABCD* matrix, and vice versa, by employing the formulas tabulated in literature [191].

5.6 Coaxial Tranmission Line Method

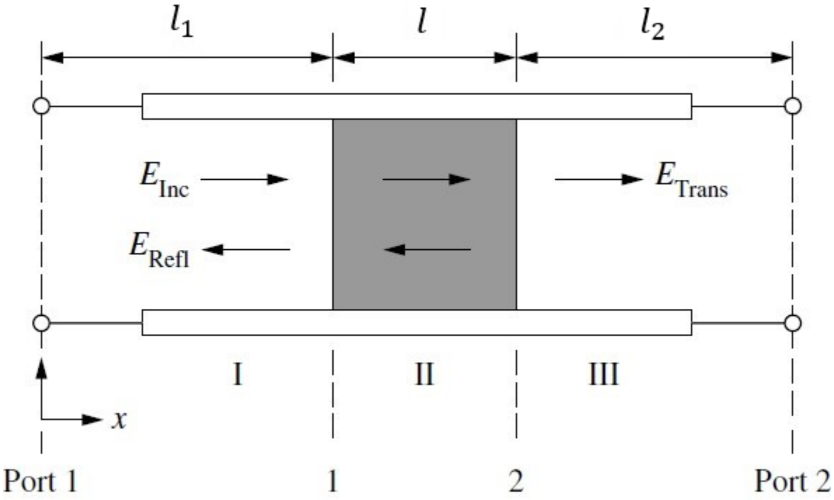

Figure 5.5: Electromagnetic waves reflected from and transmitted through the DUT (modified after [193]).

The measurement configuration looks like the one illustrated in Figure 5.5: a TEM transmission line (region II) filled with the material under-test is connected to a two-port vector network analyzer through two connecting lines (region I and III). The electric fields at the three sections of the setup E_I, E_{II} and E_{III}, in the case of a normalized incident wave will be [194]:

$$E_I = e^{-k_0 x} + C_1 e^{k_0 x} \tag{5.41}$$

$$E_{II} = C_2 e^{-kx} + C_3 e^{kx} \tag{5.42}$$

$$E_{III} = C_4 e^{-k_0 x} \tag{5.43}$$

where k and k_0 are the propagation constants with the sample and in free space respectively.
The constants C_1, C_2, C_3 and C_4 can be determined from imposing boundary conditions on the electric and magnetic field.
The scattering parameters measured by the two-port network can be retrieved solving eqs. 5.41-5.43, considering that the scattering matrix is symmetric (i.e., $S_{12} = S_{21}$):

$$S_{11} = R_1^2 \cdot \frac{\Gamma(1-T^2)}{1-\Gamma^2 T^2} \tag{5.44}$$

$$S_{22} = R_2^2 \cdot \frac{\Gamma(1-T^2)}{1-\Gamma^2 T^2} \tag{5.45}$$

$$S_{12} = R_1 R_2 \cdot \frac{\Gamma(1-T^2)}{1-\Gamma^2 T^2} \tag{5.46}$$

with R_1 and R_2 the reference plane transformations at the two ports given by

$$R_i = e^{-k_0 l_i} \qquad i = 1, 2 \tag{5.47}$$

the transmission coefficient T is defined as

$$T = e^{-kl} \tag{5.48}$$

and the reflection coefficient Γ as

$$\Gamma = \frac{\sqrt{\mu/\varepsilon} - 1}{\sqrt{\mu/\varepsilon} + 1} \tag{5.49}$$

As a result, the system of equations is overdetermined and it can be solved in a variety of ways.

5.6.1 Nicholson-Ross-Weir and Boughriet Algorithms

The electromagnetic properties can be estimated by using the Nicholson-Ross-Weir (NRW) algorithm [195], [196] and, for non-magnetic materials, by employing the Boughriet equation [197]. For this work the algorithm was slightly modified as the transmission line has a larger cross-section than that of the lines connecting the probe to the VNA, causing a mismatch at the probe/connecting line interface (see Fig. 5.6)[198].

In the NRW algorithm, the reflection coefficient Γ and the transmission coefficient T are expressed in terms of the scattering parameters:

$$\Gamma = K \pm \sqrt{K^2 - 1} \tag{5.50}$$

with

$$K = \frac{S_{11}^2 - S_{21}^2 + 1}{2S_{11}} \tag{5.51}$$

$$T = \frac{S_{11} + S_{21} - \Gamma}{1 - (S_{11} + S_{21})\Gamma} \tag{5.52}$$

$$\sqrt{\frac{\varepsilon}{\mu}} F_g = \frac{1-\Gamma}{1+\Gamma} \tag{5.53}$$

$$\sqrt{\varepsilon\mu} l = ic(2\pi\nu)^{-1} ln(T) \tag{5.54}$$

with the probe geometrical factor $F_g = Z_c/Z_p$, where Z_c and Z_p are the impedances of the connecting lines and the probe in air respectively. When $F_g = 1$ the equations coincide to the original NRW

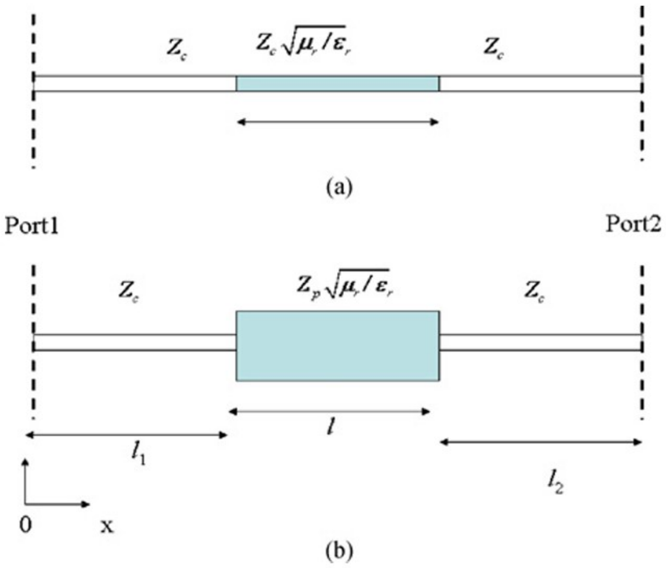

Figure 5.6: Depiction of the transmission line (light blue) connected to the 2-port VNA by means of two connecting lines (white). (a) Classic uniform-air transmission line with no mismatch. (b) Probe used in this work with a different impedance from the connecting lines. (taken from [198]).

algorithm. The choice of positive or negative sign in eq. 5.50 is due to the condition $|\Gamma| \leq 1$. The complex permittivity and complex permeability can be then evaluated combining eqs. 5.53 and 5.54:

$$\varepsilon = ic\frac{ln(T)}{2\pi\nu\, l\, F_g}\frac{1-\Gamma}{1+\Gamma} \tag{5.55}$$

$$\mu = ic\frac{F_g ln(T)}{2\pi\nu\, l}\frac{1+\Gamma}{1-\Gamma} \tag{5.56}$$

The main issue and limit of the such algorithm is that, for low-loss materials, the solutions tend to diverge when $S_{11} = 0$ and $S_{21} = 1$ (eq. 5.51 $\rightarrow 0/0$). It happens at $\nu = 0$ and at frequencies ν_m multiples of the probe line half wavelength [199]:

$$\nu_m \simeq \frac{mc}{2l\, Re\{\sqrt{\varepsilon\mu}\}} \qquad m = 1, 2, 3... \tag{5.57}$$

This problem can be avoided in the simpler cases of non magnetic materials ($\mu = 1$), applying the Boughriet method to estimate the complex permittivity [197]:

$$\varepsilon = \left[\frac{ic\, ln(T)}{(2\pi\nu\, l)}\right]^2 \tag{5.58}$$

5.7 Experimental Setup

5.7.1 Vector Network Analyzer

A 2-port Keysight (formerly known as Agilent) E5071C ENA Vector Network Analyzer (VNA) was used (see Fig. 5.7) for measurements in the frequency range 1 MHz-100 MHz. The VNA is connected to the measuring probe through two 50 Ω coaxial cables terminated with N-type connectors. Through measurements of material with well-known electrical properties, the instrumental limit of VNA for conductivity and imaginary permittivity measurements was identified. The instrumental limit is equal to

$$\sigma_{limit}^{VNA} = 1.3 \times 10^{-5}\ S/m \tag{5.59}$$

which, in terms of permittivity can be expressed as

$$\varepsilon''_{limit} = \frac{\sigma_{limit}^{VNA}}{2\pi\varepsilon_0\nu} \tag{5.60}$$

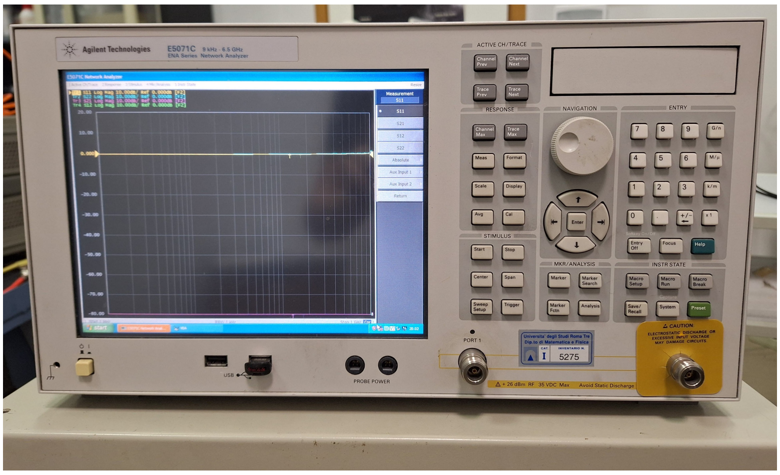

Figure 5.7: Vector Network Analyzer used in this research (Keysight E5071C ENA).

5.7.2 Coaxial Probe Lines

Three coaxial probe lines were employed in this work; they have a multiwire cage shield (see Fig. 5.8): the coaxial-cage transmission line is composed by a cylindrical structure made of eight constantly spaced rods and a central rod all with diameter $d = (3.00 \pm 0.03)\ mm$. All these conductors are made of stainless steel, in order to avoid chemical contamination with water samples. The conductors are surrounded by a Teflon cage, open at the top. This opening has different dimensions based on the probe used (see tab. 5.1).

	Height (mm)	*Width (mm)*	*Length (mm)*
1st probe	60	50	50
2nd probe	60	50	100
3th probe	60	50	150

Table 5.1: Dimensions of the three coaxial probe lines. They substantially differ in length, ranging from 50 mm to 150 mm.

The structure just described easily allows a complete filling of the cell with both granular samples, ensuring an uniform compactness of them, and salty solutions [198]. Figure 5.9 is a photo of the VNA experimental setup at room temperature, with the 10 cm coaxial probe connected to the instrument through two coaxial cables.

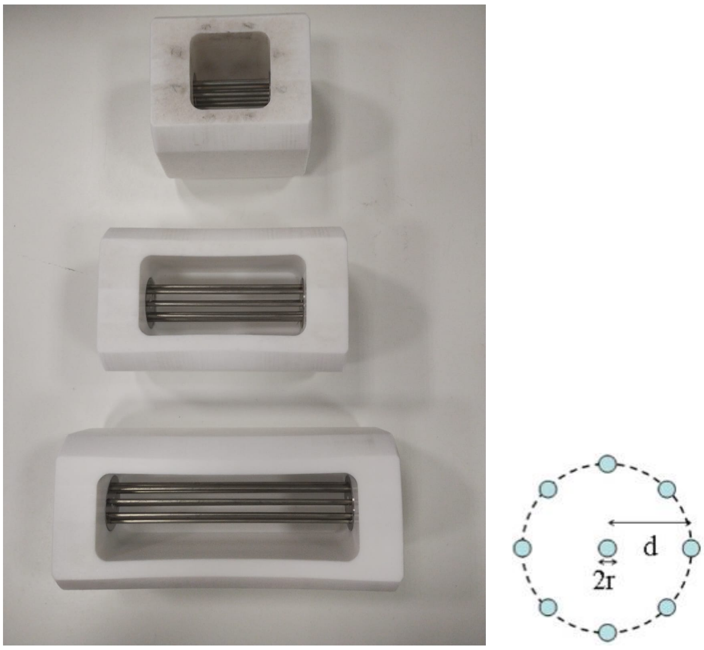

(a) *The three coaxial probe lines with different length employed in this work.* (b) *Depiction of the cage-coaxial line cross-section [198].*

Figure 5.8: Photo and depiction of the cage conductors of the probes used throughout this work.

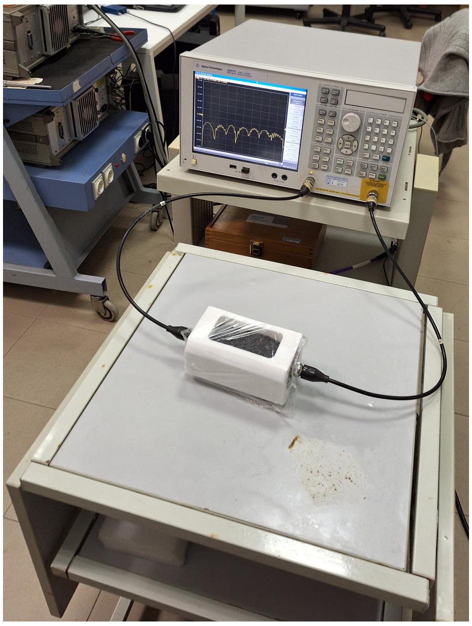

Figure 5.9: VNA experimental setup at room temperature.

5.7.3 Instrumental Limit

From measurements of the proble lines empty (see Fig. 5.10) and of materials of well-known dielectric properties (e.g. low losses materials such as glass beads) it was possible to identify the VNA instrumental limit at two different frequencies, 9 and 60 MHz. The two limits are expressed in terms of minimum conductivity measurable at that fixed frequency:

$$\sigma_{9\,MHz}^{VNA} = 1.3 \times 10^{-5} \quad (S/m) \tag{5.61}$$

$$\sigma_{60\,MHz}^{VNA} = 4.2 \times 10^{-5} \quad (S/m) \tag{5.62}$$

Above these values the measurements at 9 and 60 MHz are considered accurate.

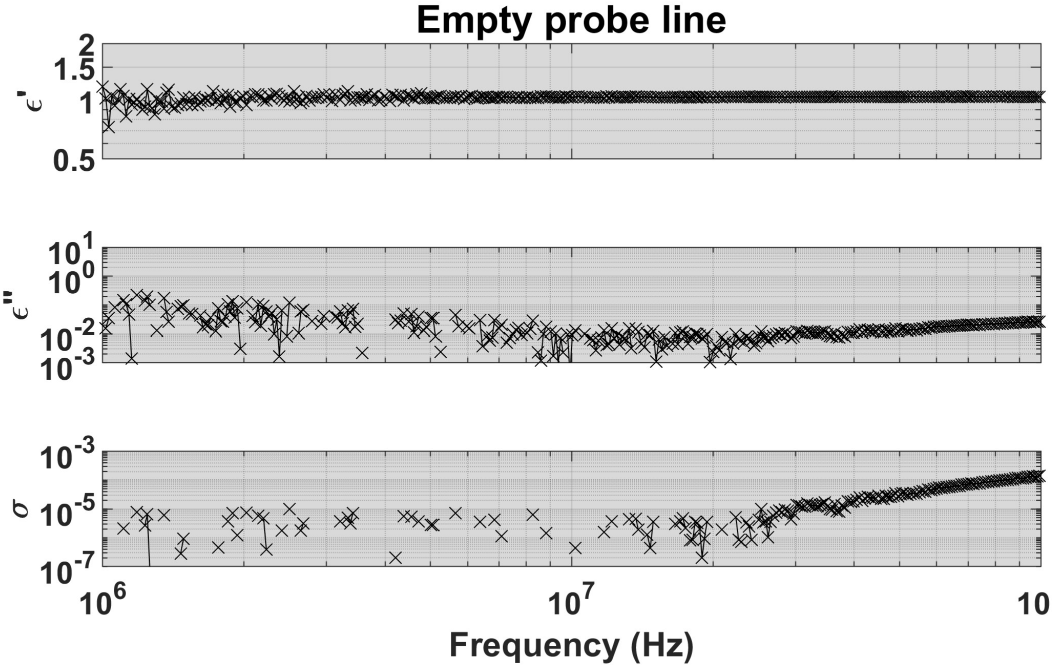

Figure 5.10: Measurement of the dielectric properties of the empty probe line used for the study of the VNA instrumental limit.

5.8 Calibration

VNA Calibration

The VNA can be the source of two types of measurement errors: systematic error and random error. The random error, also called instrumental noise of the VNA, cannot be removed from the measurement and represents the limit below which it is no longer possible to provide an accurate measurement with this type of instrument. Systematic error on the other hand can be corrected via a two-port full calibration using the same coaxial cables employed for the set of measurements. It is very important to note that this type of calibration must take place at the same temperature at which the measurement will then take place: even a small temperature difference between the calibration and the actual measurement can be a source of further errors. A SOLT calibration (or Short, Open, Through and Load method) has been performed prior every set of measurements. It consists of different corrections:

- a measurement of a Short and an Open standard for each port, representing the ideal total reflection of the generated signal;
- a measurement of a Load standard (50 Ω, matching the coaxial cables' impedance), representing the ideal absence of reflection of the generated signal;
- finally a measurement of the Through standard, which connects the port 1 with port 2, representing the ideal transmission.

These measurements are saved by the instrument that automatically corrects every measurement after this calibration.

In addition to the instrument calibration detailed, it was necessary to carry out a calibration that removed the influence of the probes' connectors from the measurements and another calibration that estimated the electrical parameters of the probes (electrical length l and characteristic impedance Z_c) as a function of the frequency and temperature.

5.8.1 Connectors Calibration

Once the effects of coaxial cables have been removed with the SOLT calibration, the probe can be schematized considering that real structure measured by the VNA is composed by three transmission lines: first connector, probe and second connector. In this scenario, it is useful to exploit the transmission matrix approach described in 5.5. In fact, using this approach, the transmission matrix T_{meas} estimated by the VNA of the whole probe is given by:

$$T_{meas} = T_{con} T_{DUT} T_{con} \tag{5.63}$$

where T_{con} is the transmission matrix associated with the two connectors and T_{DUT} is the transmission matrix related to the material under-test inside the probe.

In this case a connector calibrator identical to that present on coaxial cells was employed to simulate the action of the two connectors on the probe (see Fig. 5.11) and therefore to quantify T_{con}.

Figure 5.11: Example of the connector calibrator employed to simulate and subtract the effect of the N-type connectors from the measured values T_{meas}

T_{DUT} is then extracted in the following way:

$$T_{DUT} = T_{con}^{-1} T_{meas} T_{con}^{-1} \tag{5.64}$$

By converting T_{DUT} in the scattering matrix S, then it is possible to estimate the complex permittivity and permeability of the material investigated.

5.8.2 Electrical Length and Characteristic Impedance Calibration

Calibration of the electrical parameters of the probe (electrical length l_e and characteristic impedance Z_c) is crucial to the success of the measurement: for this reason, a preliminary study was conducted for calibration of these parameters. A test was thus carried out: two estimates of electrical parameters were performed, one with the probe line empty and another one with the probe line filled with glass beads, a soil simulant with real part of permittivity $\varepsilon' = 3.2$ and no electrical losses (see Fig. 5.12). In the case of the empty cell (called here "air calibration"), at low frequencies, i.e. those of interest to planetary radar, the parameters tend to be more scattered than in the case of the probe filled with the glass beads. This occurs because in the presence of glass beads the field is well confined, while on the contrary in air the electromagnetic field is not well confined and it tends to open up to the environment.

For this reason, the calibration of glass beads was chosen and a set of measurements as a function of temperature (200-290 K) of the electrical parameters of the probe line was performed. Both the electrical length and the characteristic impedance have a slight dependence on temperature, as can be seen in Fig. 5.13 .

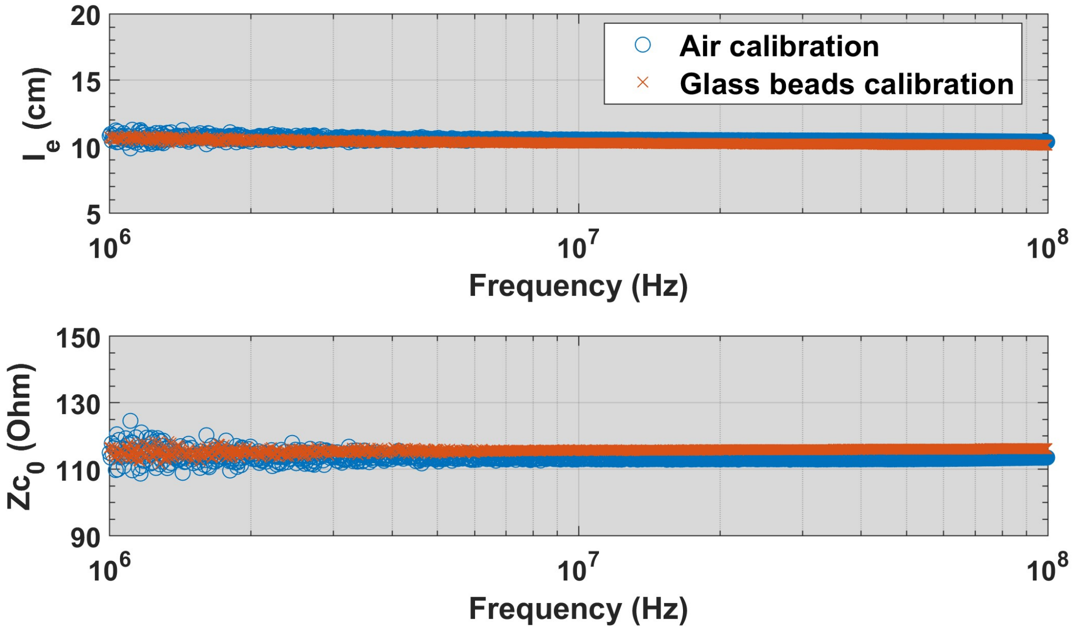

Figure 5.12: Comparison between air and glass beads calibration of the 10 cm probe line, at room temperature, for the estimation of the electrical parameters of the probe line (electrical length l_e and characteristic impedance Z_c).

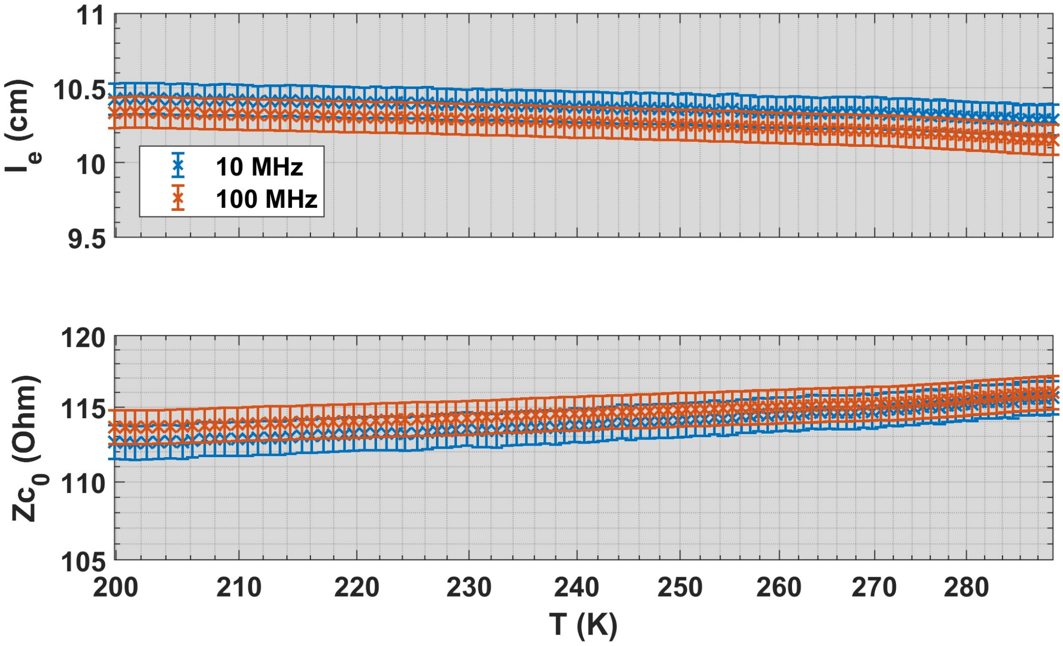

Figure 5.13: Electrical parameters of the 10 cm probe line as a function of temperature at 10 and 100 MHz, obtained with a glass beads calibration.

5.8.3 Validation of the Calibration Procedure

In order to test the experimental setup measurements on well-known dielectric properties material were carried out as a function of temperature. Therefore, the electrical properties of pure ethanol and 96% pure ethanol were measured in the temperature range 200 K - 290 K; thus the relaxation frequencies ν_{rel} observed in the frequency spectra and extracted by means of a fit with a Metropolis algorithm (see section 7.4) were compared with the relaxation frequencies of two ethanol measurements present in the literature, one ranging from 283 K to 323 K [200] and the other one at low temperatures, from 110 K to 159 K [201]. The results are in good agreement with both, as can be seen in Figure 5.14, confirming the goodness of the calibration procedure.

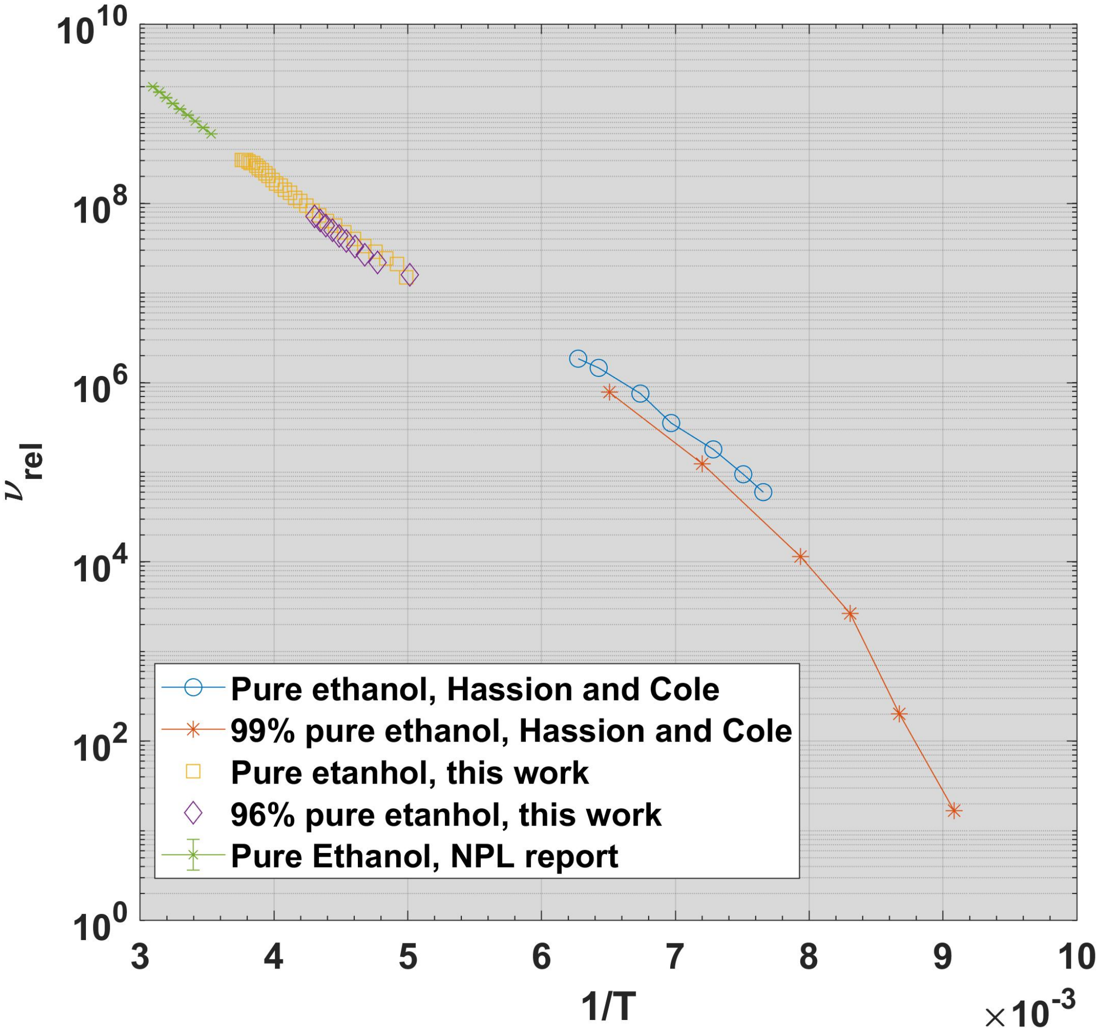

Figure 5.14: Comparison between relaxation frequencies obtained from measurements of various ethanol samples. The results of this work are in good agreement with those found in literature, both at room temperature and lower temperatures.

5.9 Uncertainty Estimation

The uncertainties on the scattering parameters (S-parameters) and, consequently, on the complex dielectric permittivity and magnetic permeability were computed in agreement with ISO Guide to the Expression of Uncertainty in Measurement [202].
The type-A uncertainty was estimated using 500 measurements of the S-parameters of different reference materials (probe line empty, glass beads, double distilled water and 99% ethanol) at a fixed temperature and applying the statistical propagation formula [203]

$$u_{type-A} = \sqrt{\sum_i \left(\frac{\partial y}{\partial x_i} u_{x_i} \right)^2} \tag{5.65}$$

under the assumption that the uncertainties are independent and uncorrelated and where u_{x_i} are the uncertainties on the S-parameters computed from the standard deviation of all reference materials.
The type-B uncertainty in this case was generated by the presence of an asymmetry in the S-parameters [204] due to: a) a not perfect calibration of the cables; b) the intrinsic asymmetry of the experimental setup. Due to this asymmetry, the estimation of ε and μ differs when S_{11} and S_{12} or S_{22} and S_{21} scattering parameters are used [205]. The type-B uncertainty is therefore computed as the standard deviation of the uniform probability distribution of ε (and μ) values whose boundaries are the ε (and μ) values estimated with S_{11}, S_{12} and S_{22}, S_{21} parameters [104]. For the permittivity, for example, it stands

$$u_{type-B} = \frac{\varepsilon_{S_{11},S_{12}} - \varepsilon_{S_{22},S_{21}}}{\sqrt{12}} \tag{5.66}$$

The overall uncertainty u_y on electromagnetic parameters is then

$$u_y = \sqrt{u_{type-A}^2 + u_{type-B}^2} \tag{5.67}$$

Chapter 6

Capacitor Theory and LCR Meter Setup

A parallel plate capacitor is often employed to estimate the dielectric permittivity of materials at low frequencies. A typical measurement using a parallel plate capacitor consists of a LCR meter connected to the measuring cell filled with the material investigated. In this chapter the aforementioned methodology and the experimental setup will be detailed.

6.1 LCR Meter

The LCR meter is able to measure the inductance, capacitance and resistance of the device under test. The instrument works best for accurate measurements in the low frequency range 10 Hz - 10 MHz.
The LCR meter can be schematized into an equivalent circuit with an operational amplifier set on the inverted configuration (see Fig. 6.1). An oscillator (see Fig. 6.1) sends sinusoidal voltage inputs; changing the measurement range of the current flowing through the DUT is made possible by the feedback resistor $R_{feedback}$.

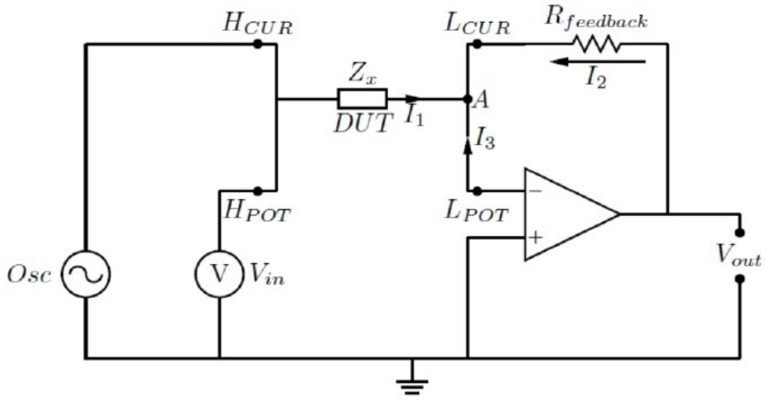

Figure 6.1: The LCR meter equivalent circuit can be summarized in an operational amplifier in inverted configuration.

The instrument measures the output voltage V_{out} in both amplitude and phase, while the voltmeter accurately measures the amplitude and phase of the selected input voltage V_{in} generated by the oscillator. The material is inserted inside a capacitive cell which is connected to the circuit and to the four instrument's BNC by four coaxial cables: H_{cur}, H_{pot}, L_{cur} and L_{pot}, that are respectively the high/low current and the high/low potential.
The DUT has an unknown impedance Z_x that can be estimated by applying the Kirchhoff's junction rule

over the A node [206]:

$$I_1 + I_2 + I_3 = 0 \tag{6.1}$$

The current I_1 that flow through the DUT is given by the ratio between the input voltage and the DUT impedance, as a function of the frequency ν

$$I_1 = \frac{V_{in}(\nu)}{Z_x(\nu)} \tag{6.2}$$

The current I_2 is given by the ratio between the output voltage and the feedback resistance

$$I_2 = \frac{V_{out}}{R_{feedback}} \tag{6.3}$$

On the other hand, the current I_3 is equal to zero, assuming infinite input impedance of the operational amplifier

$$I_3 = 0 \tag{6.4}$$

Substituting the three currents values in 6.1 it is possible to retrieve the impedance of the DUT

$$Z_x = -\frac{V_{in}(\nu)}{V_{out}} R_{feedback} \tag{6.5}$$

6.2 Capacitor Theory

The material under investigation is inserted insider a flat parallel plate capacitor and its complex dielectric permittivity is estimated by studying the equivalent circuit of the system in a parallel configuration, as described in subsection 2.3.2.

The total current that flows through the equivalent circuit is the sum of the charge and loss current, I_c and I_l

$$I = I_c + I_l = V(i\omega C + G) = V\left(i\omega C_0\varepsilon' + \omega C_0\varepsilon'' + \frac{\sigma}{\varepsilon_0}\right) \tag{6.6}$$

where ε is the relative permittivity. Considering that $\varepsilon_e = \varepsilon'' + \sigma/\omega\varepsilon_0$, it is possible to simplify the equation

$$I = V(i\omega C_0\varepsilon' + \omega C_0\varepsilon''_e) \tag{6.7}$$

The LCR meter performs measurements of the capacitance $C_p(\nu)$ and the loss tangent $tan\delta(\nu)$, that allow estimating the electrical permittivity as a function of frequency

$$\varepsilon'(\nu) = \frac{C_p(\nu)}{C_0} \tag{6.8}$$

where C_0 is the air capacitance which can be estimated also from the geometric parameters of the capacitive cell

$$C_0 = \varepsilon\varepsilon_0\frac{\pi r^2}{d} \tag{6.9}$$

where r and d are the radius of the plates of the cell and the distance between the plates respectively. The uncertainty of the air capacitance is computed from the error propagation law

$$u_{C_0} = \pm\sqrt{\left(\frac{\partial C_0}{\partial r}\right)^2 u_r^2 + \left(\frac{\partial C_0}{\partial d}\right)^2 u_d^2} \tag{6.10}$$

As regards the imaginary part of permittivity, it can be obtained from the loss tangent measurement

$$tan\delta(\nu) = \frac{1}{\omega C_p(\nu)R_p(\nu)} \tag{6.11}$$

that can be expressed as the ratio between the loss current and the charge current

$$tan\delta(\nu) = \frac{I_l}{I_c} = \frac{\omega C_0\varepsilon''_e}{\omega C_0\varepsilon'} \tag{6.12}$$

The effective imaginary part of permittivity is then given by

$$\varepsilon''(\nu) = tan\delta(\nu)\varepsilon' \tag{6.13}$$

The related type B uncertainties are computed using the error propagation law, assuming a uniform distribution for these quantities

$$\begin{aligned} u_{\varepsilon'} &= \pm\frac{1}{\sqrt{3}}\sqrt{\left(\frac{\partial\varepsilon'}{\partial C_p}\right)^2 u_{C_p}^2 + \left(\frac{\partial\varepsilon'}{\partial C_0}\right)^2 u_{C_0}^2} = \\ &= \pm\frac{1}{\sqrt{3}}\left(\frac{u_{C_p}}{C_0} + \frac{C_p u_{C_0}}{C_0^2}\right) \end{aligned} \tag{6.14}$$

$$\begin{aligned} u_{\varepsilon_e''} &= \pm\frac{1}{\sqrt{3}}\sqrt{\left(\frac{\partial\varepsilon_e''}{\partial D}\right)^2 u_D^2 + \left(\frac{\partial\varepsilon_e''}{\partial\varepsilon'}\right)^2 u_{\varepsilon'}^2} = \\ &= \pm\frac{1}{\sqrt{3}}\left(\varepsilon' u_D + D u_{\varepsilon'}\right) \end{aligned} \tag{6.15}$$

6.3 Experimental Setup

In this experimental work measurements were carried out by means of an *Agilent HP4284A* in the frequency range 20 Hz - 1 MHz. The capacitive cell (DUT, see 6.2) is connected to the instrument through four RG213 coaxial transmission lines (Teflon dielectric) equipped with four coaxial feedthroughs at the vacuum/air flange transition (see Fig.8.10). These cables maintain their properties at low temperatures, down to 100 K.

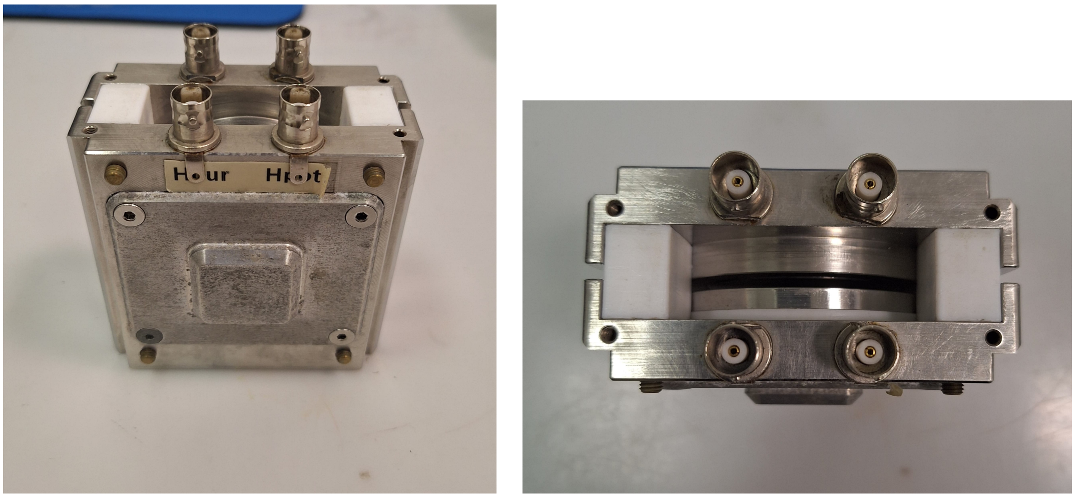

(a) (b)

Figure 6.2: Capacitive cell used in this work in the LCR meter setup.

(a) (b)

Figure 6.3: LCR meter experimental setup used in this research. On the left, the Agilent HP4284A LCR meter; on the right the LCR meter experimental setup at room temperature, with the capacitive cell connected to the instrument.

6.4 Calibration

A zeroing calibration consisting in an open and short circuit correction is performed before each set of measurements. The purpose of this calibration is to correct the data, measuring stray parameters; the open circuit calibration determines the stray admittance $Y_{open} = 1/Z_{open}$ which compensates high impedance measurements; the short calibration measures the residual impedance Z_{short} and it is employed during the estimation of low impedance measurements. The impedance Z_{meas} measured by the instrument is then corrected via means of the equation

$$Z_x = \frac{Z_{meas} - Z_{short}}{1 - (Y_{open}\, Z_{meas})} \tag{6.16}$$

The calibration is stored into the LCR internal memory.

6.5 Pure Ice Measurements

The dielectric properties of pure ice have been studied extensively in the literature [164], [162], [161]. In this work, pure ice measurements were carried out by means of the LCR meter, forming the pure ice by fast temperature cycles (one with a gradient of 2 K/min and the other abruptly using liquid nitrogen). The conductivities at 200 kHz obtained in these two experiments were compared with those present in literature in Figure 6.4. The results of this work are in agreement with those obtained in [164]; this is probably due to the rapid growth of the ice samples in this work, compatible with the experimental procedure carried out in [164], as also pointed out in [172] in the description of the influence of ice sample preparation on their electrical properties.

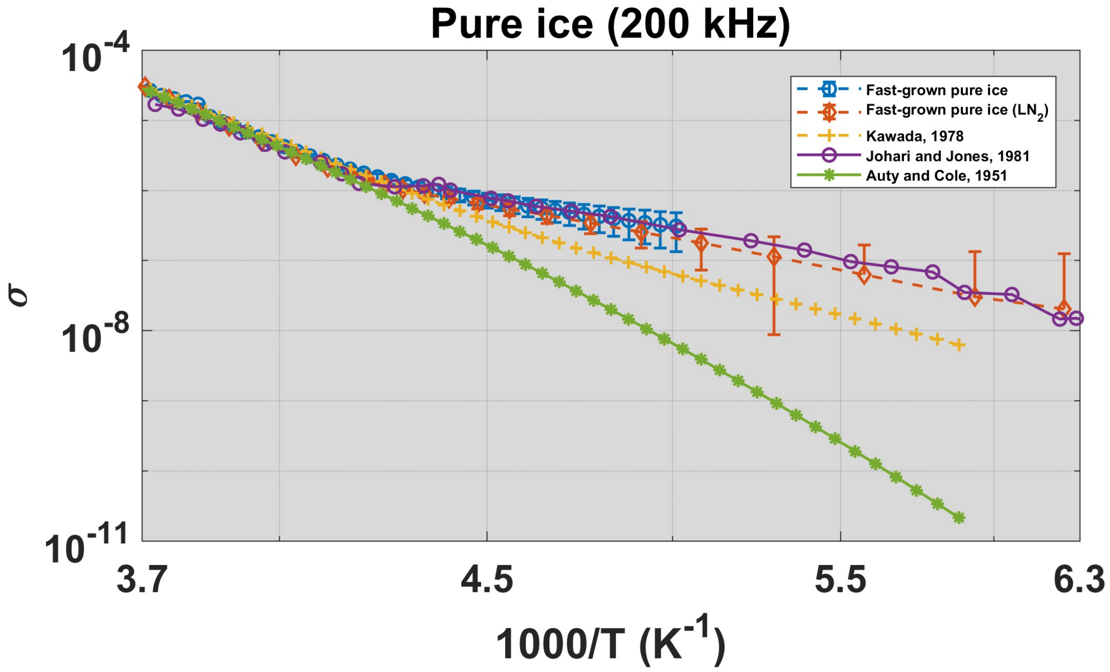

Figure 6.4: Conductivity of pure ice obtained in this work at 200 kHz compared with those found in the literature [164], [162], [161].

Chapter 7

Probabilistic Approach to Discrete Inverse Problems

In geophysics the so-called inverse problems are very frequent: it is often necessary to extract an unknown number of parameters of the physical system from a set of indirect measurements. Unlike so-called *forward* problems, where the results of an experiment are predicted from a physical theory and they are unique, inverse problems are often undetermined. Despite this, starting from the uncertainty on the data, a priori information on the physical system and on the parameter model, it is possible to obtain analytical solutions of this type of problem ([207], [208]).
In this chapter some useful elements of probability are initially defined and then the framework applied to the inversion of the data from the measurements of this thesis is outlined, following the approach delineated in [208].

7.1 Probability

Considering an abstract space S where a point $\mathbf{x}$ is individuated by a set of coordinates $\{x^1, x^2, ...\}$ and A is a subspace of S, the volume $V(A)$ to any region of A will be defined as

$$V(A) = \int_A d\mathbf{x} v(\mathbf{x}) \tag{7.1}$$

where $v(\mathbf{x})$ is the function volume density. The volume element is thus

$$dV(\mathbf{x}) = v(\mathbf{x})d\mathbf{x} \tag{7.2}$$

and it stands $V(A) = \int_A dV(\mathbf{x})$. The probability of the subset is defined in such a way as to satisfy the Kolmogorov axioms [209]

$$P(A) = \int_A d\mathbf{x} f(\mathbf{x}) \tag{7.3}$$

where $f(\mathbf{x})$ is the probability density.
It is also useful to define the concept of *homogeneous probability distribution*, i.e. the probability distribution that assigns to each region of the space a probability proportional to the volume of the region. Setting an arbitrary system of coordinates $\{m, n, s\}$ where the volume element of the space is $dV(m, n, s) = v(m, n, s)dm\ dn\ ds$ then the homogeneous probability density is equal to $h(m, n, s) = k\ v(m, n, s)$, with k a constant that may have a physical dimension.

7.1.1 Conjunction of Probabilities

Given two probabilities distribution P and Q represented respectively by two probability densities $p(\mathbf{x}$ and $q(\mathbf{x})$; let $\mu(\mathbf{x})$ the homogeneous probability density, then $R = (P \wedge Q)$, which is the product of the two initial probabilities, is represented by a probability density, also called *joint probability density*, expressed as

$$(p \wedge q)(\mathbf{x}) = k\frac{p(\mathbf{x})q(\mathbf{x})}{\mu(\mathbf{x})} \tag{7.4}$$

where k is a normalization constant.

7.1.2 Marginal Probability Density

In the special circumstance of a Cartesian product of two spaces, $X = U \times V$ with a joint probability density $f(u, v)$, it is possible to define the marginal probability densities as follows

$$f_u(\mathbf{u}) = \int_V d\mathbf{v} f(\mathbf{uv}) \qquad f_v(\mathbf{v}) = \int_U d\mathbf{u} f(\mathbf{uv}) \tag{7.5}$$

that are the projection of the joint probability density over U and V, respectively.
The variables $\mathbf{u}$ and $\mathbf{v}$ are independent if the joint probability density is equal to the product of the two marginal probability densities

$$f(\mathbf{u}, \mathbf{v}) = f_u(\mathbf{u}) f_v(\mathbf{v}) \tag{7.6}$$

7.1.3 Conditional Probability Density and Bayes Theorem

In the conditions defined above, the conditional probability density function of u given the occurrence of the value $\mathbf{v} = \mathbf{v}_0$ of v is given as follows

$$f_{u|v}(\mathbf{u}|\mathbf{v} = \mathbf{v}_0) = \frac{f(\mathbf{u}, \mathbf{v}_0)}{\int_U d\mathbf{u} f(\mathbf{u}, \mathbf{v}_0)} \tag{7.7}$$

Using this last concept together with the marginal probability density definition it is possible to obtain the *Bayes theorem*, that is the often very useful to solve inverse problems

$$f_{u|v}(\mathbf{u}|\mathbf{v}) = \frac{f_{v|u}(\mathbf{v}|\mathbf{u}) f_u(\mathbf{u})}{f_v(\mathbf{v})} \tag{7.8}$$

7.2 Probabilistic Formulation of Inverse Problem

Inverse modeling consists of using the results of complex measurements to infer the parameters of the physical theory that best describes the observed physical phenomenon. In this widely used approach, the a priori information on model parameters (represented by a probability distribution) is transformed into the *a posteriori* probability distribution, embodying the physical theory and the results of measurements together with their uncertainties.
In the general case of a space not necessarily cartesian and given a set of N parameters $m = \{m^1, m^2, ..., m^N\}$, the *forward problem* that allows to make prediction about the w *observable parameters* $\mathbf{d} = \{d^1, d^2, ..., d^W\}$ is defined as

$$d^i = f^i(m^1, m^2, ..., m^N) \qquad i = 1, 2, ..., W \tag{7.9}$$

or shortly

$$\mathbf{d} = f(\mathbf{m}) \tag{7.10}$$

Since actual theories have uncertainties the relation between the model parameters $\mathbf{m}$ and the data $\mathbf{d}$ are better represented by a probability density

$$\theta(\mathbf{d}, \mathbf{m}) \tag{7.11}$$

describing the *theoretical information.* Moreover, the data associated with the uncertainties are described by a probability distribution over the data space D

$$\rho_D(\mathbf{d}) \tag{7.12}$$

and similarly the a priori information about the model parameters, not given by the measurements data, is represented over the space of the parameters M by the probability distribution

$$\rho_M(\mathbf{m}) \tag{7.13}$$

Combining the information about the model parameters and data, it is possible to obtain the *experimental information*, defined as the joint probability density function over the space $D \times M$:

$$\rho(\mathbf{d},\mathbf{m}) = \rho_D(\mathbf{d})\rho_M(\mathbf{m}) \tag{7.14}$$

The a posteriori state of information is constructed by the combination of the experimental information 7.14 and the theoretical information 7.11 and it gives information about the data-model space:

$$\sigma(\mathbf{d},\mathbf{m}) = k\frac{\rho(\mathbf{d},\mathbf{m})\theta(\mathbf{d},\mathbf{m})}{\mu(\mathbf{m},\mathbf{d})} \tag{7.15}$$

where k is a normalization constant and $\mu(\mathbf{m},\mathbf{d})$ is the homogeneous probability distribution, assuming that the corresponding probability density is proportional to the volume element of the space.
The a posteriori information in the model space and data space are determined applying the marginal probability density equation 7.5:

$$\sigma_m(\mathbf{m}) = \int_D \sigma(\mathbf{d},\mathbf{m})d\mathbf{d} \qquad \sigma_d(\mathbf{d}) = \int_M \sigma(\mathbf{d},\mathbf{m})d\mathbf{m} \tag{7.16}$$

Assuming that the physical correlation between $\mathbf{m}$ and $\mathbf{d}$ is of the form

$$\theta(\mathbf{m},\mathbf{d}) = \theta_{D|M}(\mathbf{d}|\mathbf{m})\theta_M(\mathbf{m}) \tag{7.17}$$

and if the partition 7.14 holds, then typically

$$\mu(\mathbf{m},\mathbf{d}) = \mu_m(\mathbf{m})\mu_d(\mathbf{d}) \tag{7.18}$$

then equations 7.15 and 7.16 give

$$\sigma_m(\mathbf{m}) = k\rho_m(\mathbf{m})\frac{\theta_m(\mathbf{m})}{\mu_m(\mathbf{m})}\int_D d\mathbf{d}\frac{\rho_d(\mathbf{d})\theta(\mathbf{m},\mathbf{d})}{\mu_d(\mathbf{d})} \tag{7.19}$$

Finally, with the simplification $\theta_M(\mathbf{m}) = \mu_m(\mathbf{m})$, that holds in the presence of weak non-linearities

$$\sigma_m(\mathbf{m}) = k\rho_m(\mathbf{m})\int_D d\mathbf{d}\frac{\rho_d(\mathbf{d})\theta(\mathbf{m},\mathbf{d})}{\mu_d(\mathbf{d})} \tag{7.20}$$

Assuming that the uncertainties on the data and model parameters are Gaussian, the probability densities take the form:

$$\rho_d(\mathbf{d}) = \frac{1}{\sqrt{(2\pi)^W det\,(C_D)}}\; exp\left(-\frac{1}{2}(\mathbf{d}-\mathbf{d}_{obs})^t C_D^{-1}(\mathbf{d}-\mathbf{d}_{obs})\right) \tag{7.21}$$

and

$$\rho_m(\mathbf{m}) = \frac{1}{\sqrt{(2\pi)^W det\,(C_M)}}\; exp\left(-\frac{1}{2}(\mathbf{m}-\mathbf{m}_{prior})^t C_M^{-1}(\mathbf{m}-\mathbf{m}_{prior})\right) \tag{7.22}$$

where C_D and C_M are respectively the data covariance matrix and the model covariance matrix, $\mathbf{d}_{obs}$ are the observed data, and $\mathbf{m}_{prior}$ are the a priori model parameters.
It is also interesting to deal with the case in which physical theory is treated as "exact", for example in the case of a linear data space. In this case

$$\theta(\mathbf{d}|\mathbf{m}) = \delta\left(\mathbf{d} - f(\mathbf{m})\right) \tag{7.23}$$

and subsequently, as a result of a change of variables in a nonlinear space, the marginal probability in the parameters space becomes

$$\sigma_m(\mathbf{m}) = \frac{\sqrt{det\,(g_m + F^t g_d F)}}{\sqrt{det\,(g_m)}}\rho_m(\mathbf{m})\rho_d(\mathbf{d})\;|_{\mathbf{d}=f(\mathbf{m})} \tag{7.24}$$

where $\mathbf{F} = \mathbf{F}(\mathbf{m})$ is the matrix of partial derivatives with components $F_{i\alpha} = \frac{\partial f_i}{\partial m_\alpha}$, g_m and g_d are respectively the metrics of the model parameters space M and the data space D.
Now, in the simplest case where Gaussian data and model parameters are treated together with an "exact" physical theory, the a posteriori probability density is

$$\sigma_m(\mathbf{m}) = \sqrt{det\left(C_M^{-1} + F^t C_D^{-1} F\right)} e^{-\frac{1}{2}(\mathbf{d}-f(\mathbf{m}))^t C_D^{-1}(\mathbf{d}-f(\mathbf{m}))} e^{-\frac{1}{2}(\mathbf{m}-f(\mathbf{m}_{prior}))^t C_M^{-1}(\mathbf{m}-f(\mathbf{m}_{prior}))} \tag{7.25}$$

where, since often the covariance operators C_M and C_D are used to define the metrics over the spaces M and D, then it was assumed that $g_d = C_D^{-1}$ and $g_m = C_M^{-1}$.
The marginal probability on the single parameters $\sigma_m(m_1), ..., \sigma_m(m_N)$ is computed by using eq. 7.5 adapted for a N-dimensional case.
The procedure followed to obtain the marginal probability density in the parameters space is summarized graphically in the figure 7.1.

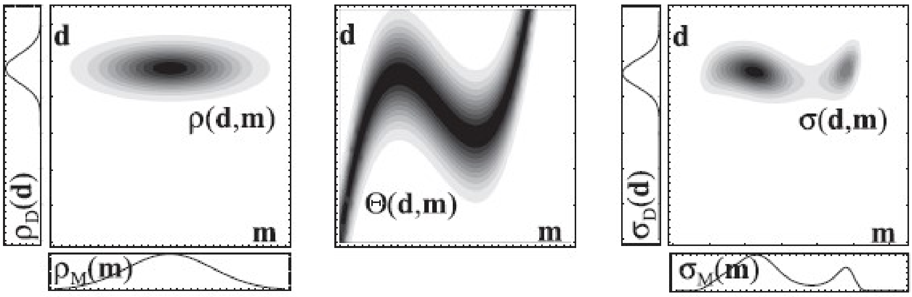

Figure 7.1: (left) the model and data probability densities ρ_M and ρ_D represent the information known *a priori* on the model and data space. The joint probability density $\rho(\mathbf{d}, \mathbf{m})$ gives the *experimental information* in the space $D \times M$. (middle) The *theoretical information* described by the probability density $\Theta(\mathbf{d}, \mathbf{m})$ that takes into account the uncertainties on the physical theory. (right) The combination of the various information that yield to the *a posteriori* probability density, with the two related marginal probability densities (taken from [208]).

7.3 Grid Mode

Throughout this thesis, for the estimation of the marginal probability density $\sigma_m(\mathbf{m})$ in the case of physical theories with few parameters (e.g., for parameters spaces with a maximum of three dimensions), a random uniform sampling strategy was employed. This essentially consisted of creating an N-dimensional grid in the N-parameter space, going to sample uniformly the probability density (or, in other words, applying a rectangular probability distribution to the space M); the sampling is generally linear.
In figure 7.2 is shown an example of the results in terms of the $\sigma_{\mathbf{m}}$ as function of two parameters m_1 and m_2 retrieved by means of this Grid Mode procedure.

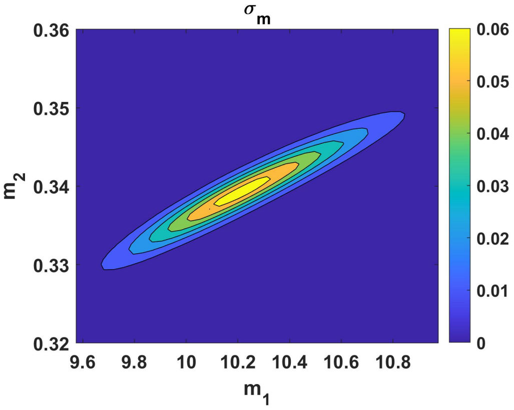

Figure 7.2: Example of contour plot of $\sigma_{\mathbf{m}}$ as a function of two parameters m_1 and m_2 of the model parameter space M.

7.4 Monte Carlo Method

In the case of physical theories that contain many parameters (e.g., for parameters space with more than three dimensions) a Monte Carlo algorithm has been used in order to effectively explore the parameters space M, In this case, a certain class of Monte Carlo algorithms, the *importance sampling algorithms*, permits to sample the space with a sampling density proportional to the given probability density, avoiding the sampling of low-probability areas. These methods are based on *random walk*, i.e. the condition for which in the generation of consecutive points, the point $\mathbf{x}_{i+1}$ sampled in the iteration $i+1$ is close to the point $\mathbf{x}_i$ sampled in iteration i. In the so-called Markov Chain Monte Carlo (MCMC) methods, the $\mathbf{x}_{i+1}$ point depend only on the previous point x_i and not on other points.

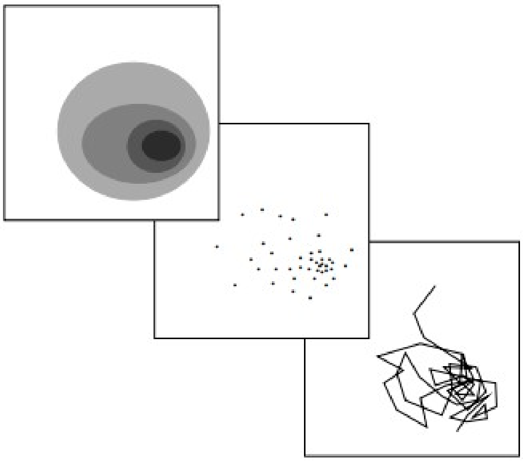

Figure 7.3: A graphical representation of the sampling of the probability distribution that occurs with Monte Carlo-like methods: at the top left a 2D probability distribution is shown and in the middle and the bottom panel is illustrated the generation of arbitrary points where the new point is created in proximity of the previous point (taken from [207]).

7.4.1 Metropolis Algorithm

In this dissertation a particular type of Markov Chain Monte Carlo method was applied: the Metropolis sampler, based on the original Metropolis algorithm [210]. In the employed algorithm a rule define the random walk that samples the probability density as follows:

- Starting from a point m_k in the space of the parameters M established by the values given in input initially, the algorithm makes a jump to a point m_{k+1} such that $m_{k+1} = m_k + z_k$, where z_k is a random variable with a standard normal distribution (having a mean value μ equal to zero and a variance σ^2 equal to one)
- Given the variable $\gamma(\mathbf{m}) = \frac{\sigma_m(\mathbf{m})}{\mu_m(\mathbf{m})}$, if the condition $\gamma(m_{k+1}) \geq \gamma(m_k)$ is met, then the algorithm makes a transition to the point m_{k+1} in the parameter space, $m_k \longrightarrow m_{k+1}$.
- If $\gamma(m_{k+1}) < \gamma(m_k)$ and $\frac{\gamma(m_{k+1})}{\gamma(m_k)} > rand(1)$, where *rand* is a random number with a uniform distribution in the interval $(0, 1)$ then the algorithm makes the transition $m_k \longrightarrow m_{k+1}$
- In all other cases the algorithm does not make the transition in the parameters space.

The fit parameters are finally estimated as the median of the distribution of the parameters explored by the algorithm, as the distribution of the parameters may not be necessarily a Gaussian (it is however possible to display it by graphing$m_k \, vs \, \sigma(m)$).

Chapter 8

Sample Characterization and Preparation

In this work several powdered materials were used in the creation of the dirty ice samples and NaCl doped ice samples were created in order to reproduce the characteristics of the icy crusts of the Jovian moons.
In this chapter all the useful physical properties of these materials are gathered, by also giving information on the procedures carried out for the preparation of both dry powdered and ice samples.

8.1 Characterization

This section will present some physical characteristics of the granular and ice samples of interest for this work, going on to detail for each material the chemical-mineralogical composition.

8.1.1 Powdered Samples

The following granular materials were used for the creation of dirty ice samples: glass beads, Etna basalt, L5 ordinary chondrite and a CI carbonaceous chondrite simulant. Their grain density and grain size are reported in Table 8.1. The grain densities were measured by means of an helium gas pycnometer (Micromeritics Accupyc 1349) since the helium easily diffuses into the pore spaces of the sample material, without contaminating it.
The grain size was retrieved when possible from material datasheets; in other cases, sieves with different mesh sizes were used to estimate an interval of grain-sizes.

Granular material	**Grain density** (g/cm^3)	**Grain size**
Glass beads	2.50 ± 0.01	$400\ \mu m - 800\ \mu m$
Etna basalt	2.961 ± 0.001	$300\ \mu m - 2\ mm$
L5 ordinary chondrite	3.331 ± 0.001	$> 125\ \mu m$
CI simulant	2.905 ± 0.001	$\approx 10\ \mu m$

Table 8.1: Grain density and grain size of the four powdered materials employed in the creation of the dirty ice samples.

Etna Basalt

This sample (see Fig. 8.1) comes from Piana del Trifoglietto lava field at SE of Etna summit craters, generated by an eruption started on December 4, 1991 and stopped on March 31, 1993 [211]. The sample has been classified as a trachybasalt and it is characterized by a potassic geochemical signature (see tab. 8.2).

SiO_2	TiO_2	Al_2O_3	FeO	Fe_2O_3	MnO	MgO	CaO	Na_2O	K_2O	P_2O_5	TOT
48.2	1.7	17.1	2.5	8.6	0.2	5.4	10.4	3.7	1.9	0.4	100.0

Table 8.2: Whole-rock composition of the Etna basalt sample [212].

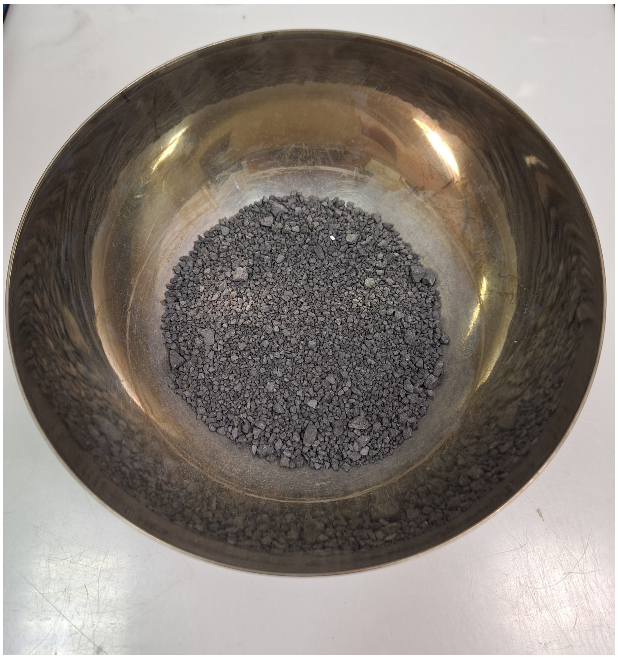

Figure 8.1: Etna basalt sample used in this work.

L5 Ordinary Chondrite

The NWA 12857 chondrite used in this work was collected in Nort West Africa and it belongs to the class of L5 ordinary chondrite, with a shock grade S2 and weathering W2. The ordinary chondrites are mainly composed of silicate minerals [213], and W2 indicates a moderate oxidation of the metal inside the sample, whereas S2 implies that the meteorite was slightly shocked with an undulatory extinction of olivine [101]. Optical analyses on the solid meteorite sample were conducted at the Museum of Planetary Science in Prato (Italy) using a Zeiss Axioplan II optical microscope equipped with a Zeiss Axiocam camera. Additionally, Energy Dispersive X-ray Spectrometry (EDS) microanalysis and elemental mapping were performed at the MEMA laboratories of the University of Florence, utilizing a Zeiss EVO MA15 microscope fitted with a 10 mm^2 Silicon Drift Detector (SDD) and OXFORD INCA 250 microanalysis software. These analyses employed accelerating voltages of 15 keV and beam currents of 5–10 nA to acquire back-scattered electron (BSE) images, energy-dispersive spectroscopy (EDS) maps, and point analyses. Quantitative mineral analyses of primary phases, specifically olivine and pyroxene, were carried out at the IGG-CNR microanalysis laboratory using a JEOL JXA-8600 Electron Microprobe equipped with four wavelength-dispersive spectrometers (WDS). The analyses were performed under operating conditions of 15 keV accelerating voltage, 20 nA beam current, a beam diameter of 1 μm, and data acquisition in wavelength-dispersive spectrometry mode.

These analysis pointed out that the most abundant silicate phase in the sample is the olivine, followed by low-Ca pyroxene, plagioclase and high-Ca pyroxen; Fe-Ni metal, apatite, chromite and troilite are then present with lower abundances. The chemical composition of olivine (Fa 25.1) and low-Ca pyroxene (Fs 21.1) aligns entirely with the characteristics of the L chondrite group as established in prior classification frameworks.

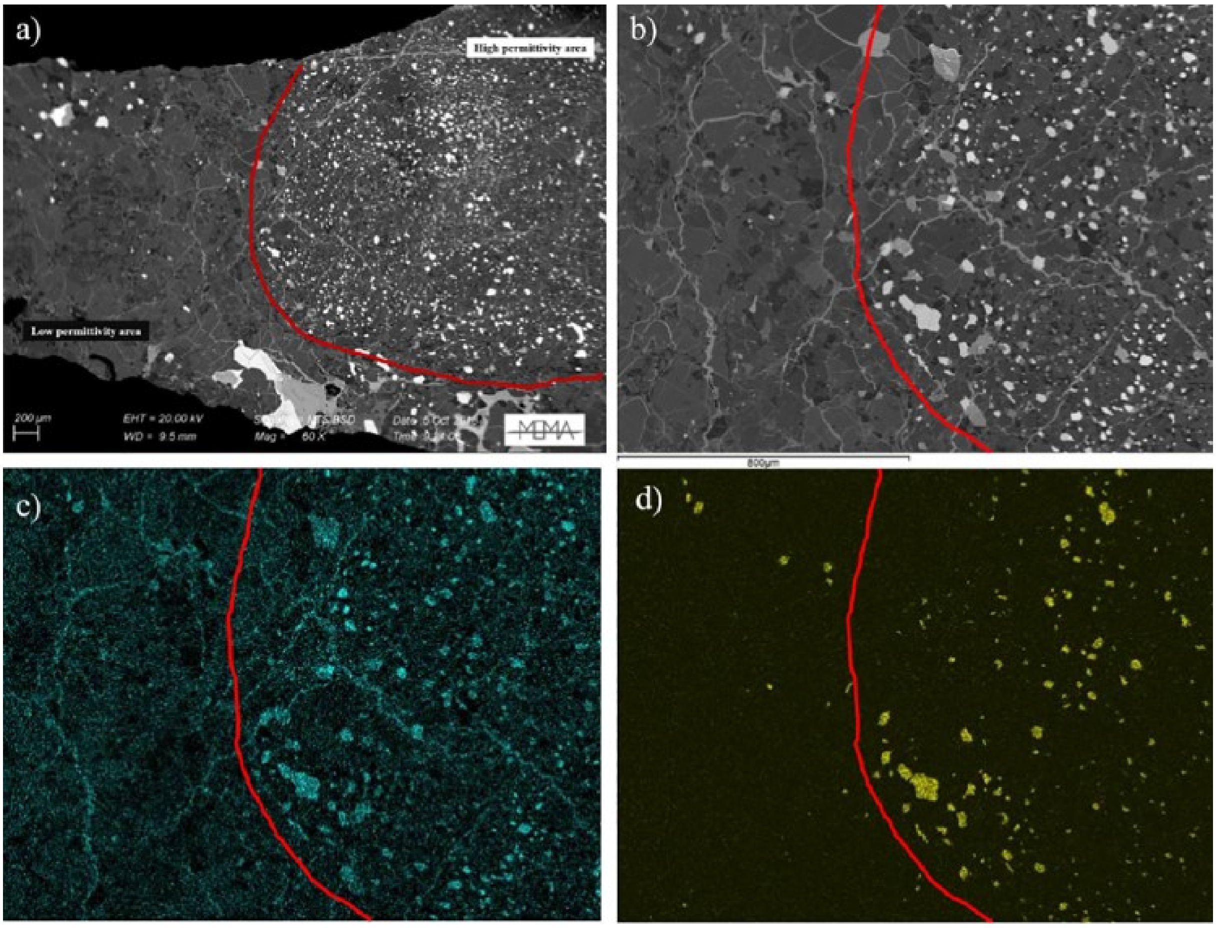

Figure 8.2: Scanning electron microscope image of a slice of the solid L5 ordinary chondrite. In the upper panels it is possible to note the border between the low permittivity areas and high permittivity areas. The lower panels show the x-ray map of sulfur (c) and iron (d): the HP area is characterized by a higher abundance of troilite and iron (taken from [101]).

The solid sample of the L5 ordinary chondrite exhibits two areas with different dielectric characteristics (see Fig. 8.3: one with low dielectric losses (Low-permittivity area, LP) and one characterized by higher values of complex permittivity (high permittivity area, HP). The HP area is characterized by the presence of metallic phases, such as troilite, kamacite and chromite, widely distributed and the grain sizes of these minerals are $< 10\mu m$ up to submicrometric sizes; the LP area, on the other hand, although it has the texture of the silicate phases similar to the HP area, it exhibits the metallic phases more sparsely distributed (see Fig. 8.2 [101]). The variations in complex permittivity are therefore related to the spatial variability of petrographic and mineralogical phases inside the sample. In general, the solid sample exhibits a dispersive behavior, very different from the one that the terrestrial rocks have.

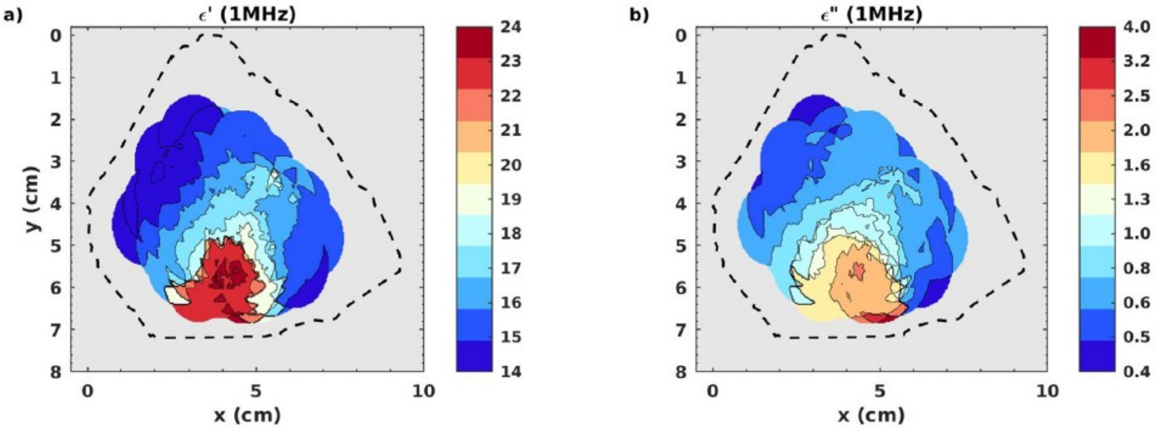

Figure 8.3: Complex permittivity map of a slice of the L5 ordinary chondrite solid sample: a) real and b) imaginary parts. Black dash line indicates the slice outline (taken from [101]).

The granular sample was obtained from the aforementioned solid meteorite by a crushing process. The whole sample has fractions of materials with different grain sizes; the mass percentage of each fraction is: 33 % ($< 125\ \mu m$), 15 % ($250 - 125\ \mu m$), 25 % ($500 - 250\ \mu m$), 21 % ($800 - 500\ \mu m$) and 6 % ($> 800\ \mu m$) [104]. The sample shows irregular grains, the shape of which varies from flat discs to spheroidal (see Fig. 8.4). It is important to note that after crushing the solid sample, the coupling between the polar and non-polar mineralogic phases inside the sample has been destroyed together with the conducting paths in the metallic grain, leading to a decrease of the imaginary part of permittivity (for more details see [104])

Figure 8.4: Closeup of the powdered L5 ordinary chondrite sample (taken from [104]).

A dielectric study was conducted on the granular sample showing that [104]: a) the real part of the permittivity exhibits a variation of approximately 6% across the entire frequency range, with a similar trend observed also for the imaginary part of the permittivity, whose values, considering the associated uncertainties, are reliably determined only within the frequency range of 10–400 MHz; b) the sample has not negligible magnetic properties with a real part of the magnetic permeability larger than one in the entire frequency range and the imaginary part not negligible ($> 10^2$, [104]); and c) the main parameter controlling the electromagnetic properties is the bulk density. Moreover, due to the scarcity of material, the influence of powder size distribution on the choice of mixing formulas was not investigated in this work.

CI Carbonaceous Chondrite Simulant

The CI carbonaceous chondrite simulant studied in this thesis was produced by the Class Exolith Lab, based on the CI Orgueil mineralogy outlined in [214] (see Fig. 8.5). In terms of quantitative metrics in [215], a NASA-developed figure-of-merit (FoM) evaluation system was employed to assess the fidelity of the simulant. In this system, numerical scores are assigned from 0 (low simulant fidelity) to 1 (high simulant fidelity) based on comparisons with the reference material (in this case the Orgueil CI sample and asteroid models). It can be seen from table 8.3 that the CI simulant received high scores, even better than several widely used lunar simulants that have scores ranging from 0.25 to 0.35.

Properties	**FoM Scores**
Magnetic susceptibility	0.96
Elemental chemistry	0.94
Mineralogy	0.83
Mineral grain density	0.75
Cobble bulk density	0.72
Particle sizing	0.55-0.89

Table 8.3: Main properties of the Exolith CI simulant with relative scores according to the NASA-developed rating system.

Figure 8.5: CI carbonaceous chondrite sample used in this work.

It is important to note that this kind of simulant has a remarkable amount of smectite in the sample [216].

Although minor errors were made during the preparation of this class of Exolith simulants (for details see [216]), the simulant is an accurate reproduction of a carbonaceous CI chondrite, and it has already been used in other broadband measurements of the electromagnetic properties [205]. In this study measurements on analog regolith materials representative of asteroid (101955) Bennu, the target of NASA's OSIRIS-REx mission, were performed. These measurements included both individual and mixed components of the CI simulant. The effect of carbonaceous material on the complex relative permittivity of asteroid regolith analogs was assessed by measuring the powdered serpentine component of the simulant mixed with varying concentrations of carbonaceous material under vacuum conditions at 25řC and 40řC. Such paper indicate that, at a bulk density of $1.60 g/cm^3$ and a wavelength of 12.6 cm, serpentine containing 5 $wt\%$ carbonaceous material exhibits a real permittivity of 3.30 ± 0.01 and a loss tangent of 0.016 ± 0.003. It was noted that the presence of carbonaceous material increases the attenuation of electromagnetic energy within the samples. Finally, it is interesting to note that this simulant has high values of complex magnetic permeability: for a a sample with porosity $\phi = 0.51$ the real and imaginary part of magnetic permeability are respectively $\mu' = 1.1$ and $\mu'' = 0.01$ [205].

8.1.2 Ice samples

The ice samples analyzed in this work are sodium chloride doped ices. Samples were created in the laboratory at different initial concentrations of NaCl: Table 8.4 shows all the concentrations studied in this work, along with the weight percentage of the salt inserted in the solution and the conductivity of the initial liquid NaCl solution.

NaCl concentration (mM)	Number of measurements	NaCl wt %	Conductivity of the liquid solution (mS/cm)
10	2	0.06	1.06 ± 0.01, 0.97 ± 0.01
20	4	0.12	1.79 ± 0.01, 1.81 ± 0.01, 1.91 ± 0.01, 1.98 ± 0.01
30	1	0.17	3.01 ± 0.02
40	1	0.23	3.07 ± 0.02
50	1	0.29	5.14 ± 0.02
70	1	0.41	6.79 ± 0.02
80	2	0.47	8.95 ± 0.05
100	1	0.59	9.81 ± 0.05
171	2	1	16.37 ± 0.05, 21.44 ± 0.05
200	2	1.17	18.05 ± 0.05, 18.91 ± 0.05
300	1	1.8	27.30 ± 0.06
500	1	2.9	43.9 ± 0.1
700	1	4.1	64.1 ± 0.1
1000	2	5.8	83.7 ± 0.1, 82.1 ± 0.1
4000	1	23.3	216.9 ± 0.5

Table 8.4: List of NaCl concentrations used in this work to create the doped ice samples together with the number of measurements performed. The salt weight percent and the conductivity of the initial liquid salty solution are reported. The conductivity was measured by a Conductivity meter GLP-31.

8.2 Preparation

8.2.1 Oven Drying Samples

As already discussed in section 2.7, the residual water inside a powdered sample strongly affect its dielectric properties, and in particular it increases the imaginary part of the permittivity considerably. For this reason, the powdered samples were heated at 105°C for at least 12 hours at about 40 mbar in a vacuum oven (SalvisLab Vacucenter VC20, see Fig. 8.6) prior to the the measurements, following the indications given by previous tests with the same materials. This procedure was chosen so as not to alter the samples with, for example, heat-induced oxidation. In fact, in [110] it was observed that heating the samples at 250 degrees for 24 hours altered the granular material, observing a change in the degree of crystallinity and bulk density.

After the heating procedure, the samples were kept in sealed containers before being placed in the measuring cells, in order to keep moisture levels low.

Figure 8.6: Vacuum oven used to heat samples before measurements.

8.2.2 NaCl Solution

The NaCl solutions were prepared employing bidistilled water obtained with a water purification system (Simplicity UV) and the sodium chloride provided by the SIGMA-ALDRICH (see Fig. 8.7).

Figure 8.7: Water purification system and sodium chloride (white box on the left) used in this work.

The sodium chloride was firstly weighed on semi-micro scale (Gibertini E 50 S/3) and then inserted into the bidistilled water. The mixing was fulfilled by means of an hotplate stirrer (Bibby B212, see Fig. 8.8); once the dissolution process was finished, the salt solution was placed inside the measuring cell.

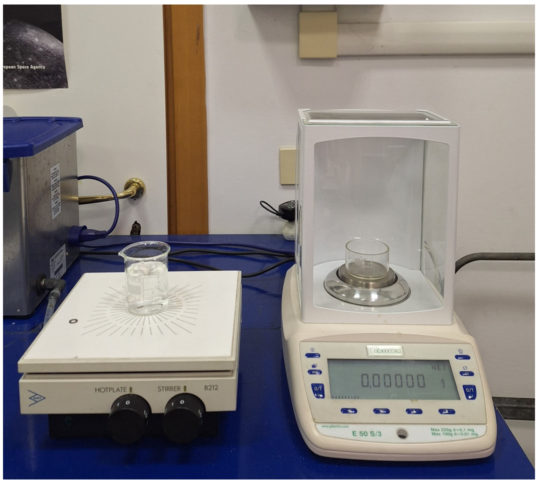

Figure 8.8: Semi-micro scale (right) and hotplate stirrer (left) used in this work for the preparation of the NaCl solutions.

8.2.3 Freezing Procedure

The ice samples were formed directly inside the measuring cell (the capacitive cell for measurements in the range 20 Hz-1 MHz and the coaxial transmission line for measurements in the range 1 MHz-100 MHz). In this work two different instruments were used to create the frozen sample from the saline solutions: a climatic chamber (ACS Angelantoni) capable of control the temperature, setting custom cooling and heating cycles, and an ultra freezer with a working temperature of -80°C (NEXUS H Angelatoni Life Science, see Fig. 8.9). In both cases a pt100 sensor inserted inside the solution constantly monitored the effective temperature of the sample.

Figure 8.9: Ultrafreezer used in this work.

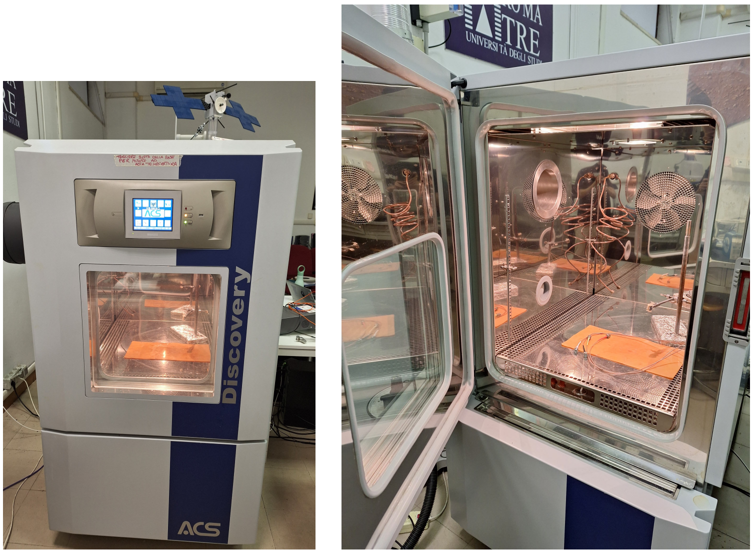

(a) (b)

Figure 8.10: Climatic chamber used in this work.

8.2.4 Annealing Effect

As widely demonstrated and described in the literature [168],[172], the formation of a sample of ice, both pure and doped, is extremely delicate and strongly linked to the way in which it is frozen. Therefore, much attention has to be paid to the temperature protocols used to freeze the sample. For this reason, the electrical properties of the same 10 mM NaCl doped ice were measured by means of the LCR meter, using three different temperature protocols (a,b and c), as can be seen in Fig. 8.11.

The protocols differ in the following way:

- **a**. A a fast annealing was set at 243 K and then the sample was frozen with liquid nitrogen, reaching 90 K.
- **b**. A slower annealing was set, in order to verify the differences in the dielectric behavior compared to the previous case.
- **c**. This cycle is characterized by tho different phases: in the first one the solution was "quenched" from room temperature to 197 K at a rate of 2 K/min; then, a slow annealing cycle was set, trying to establish if the ice structure would adjust, modifying the permittivity trend.

Fig. 8.12 shows the influence of the temperatures cycles on dielectric properties. The annealing protocol helps to rearrange the structure of the crystal, eliminating the spurious relaxation at lower frequencies probably due to the presence of cracks in the sample and approaching the form expressed by the Debye model: it is particularly evident in the phase spectrum defined as $phase = arctan\left(\frac{\varepsilon''}{\varepsilon'}\right)$, with the low-frequency maximum flattening out. The annealing process is particularly useful for ices doped with low concentrations of sodium chloride; in fact, it has been found that for higher concentrations of sodium chloride annealing does not induce evident changes in the spectra at lower frequencies. From Fig. 8.12 it can be seen that at 1 MHz the permittivity and conductivity of the various temperature cycles have fairly the same values; therefore the annealing procedure does not play a significant role on the dielectric properties of NaCl doped ices at the frequencies of interest for planetary radars.

In any case, all ice samples measured in this work were formed through fast temperature cycles, avoiding the annealing effect.

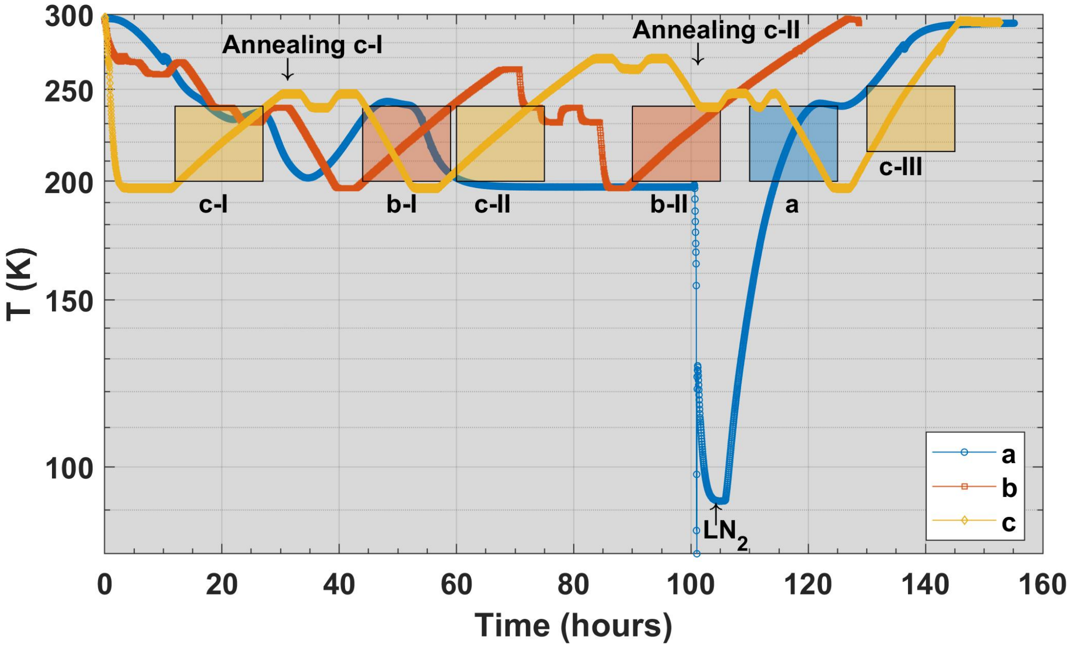

Figure 8.11: Comparison of different temperature protocols for the formation of the 10 mM NaCl doped ice sample. The colored boxes indicate the measurements shown below, i.e. the measurements performed during the warming cycles.

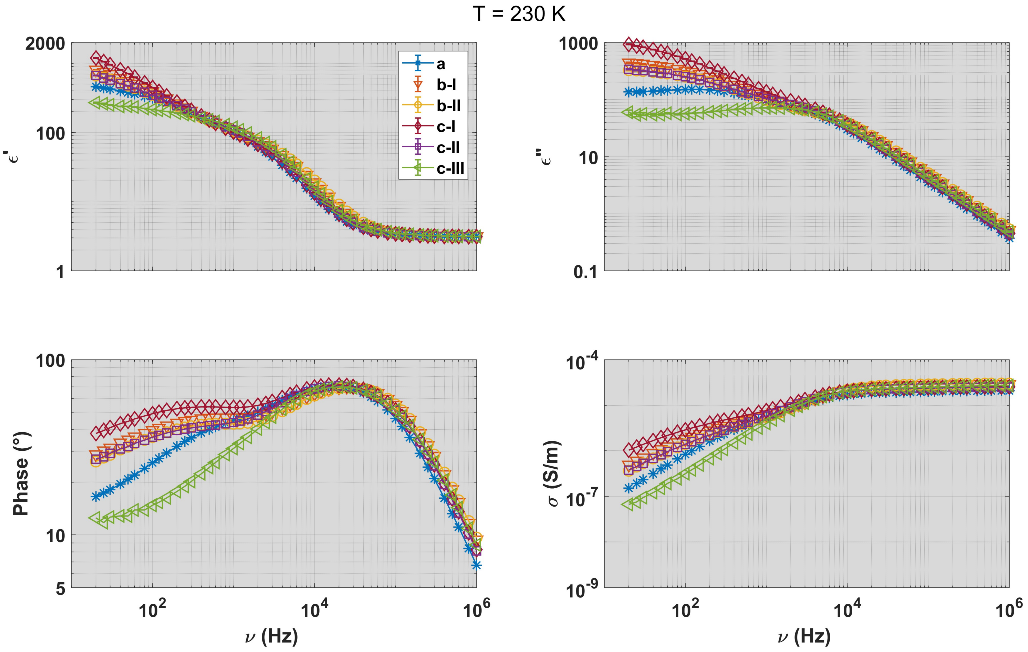

Figure 8.12: Influence of annealing temperature cycles on the dielectric properties of the ice sample. The real and imaginary part of permittivity, the phase and the conductivity are reported for the temperature of 230 K. The cycles are the ones shown in figure 8.11.

Chapter 9

Electromagnetic Characterization of Dirty Ice for the Icy Crust of The Jovian Moons

The radar sounding technique has been widely employed in space missions investigating several Solar System objects, such as Earth [217], planets [218], satellites [219] and comets [102]. The propagation and interaction of the radar signal through the subsurface of these bodies return information on their geophysical properties, on the condition that the electromagnetic properties of the materials encountered are known. Dielectric permittivity and magnetic permeability are primarily functions of frequency, but they are also influenced by several physical properties of the medium under investigation, including temperature, bulk density, salinity, and other factors. For this reason, a deep knowledge of the electromagnetic properties of the planetary materials being investigated is necessary for the interpretation of the radar sounder data. Nevertheless, the EM characterization of dirty ice for Jovian moons and asteroids in the planetary radar frequency range is poorly discussed in the literature: measurements of the dielectric permittivity of dirty ice were performed at lower (from Hz to tens of kHz) [190] [188] or at higher (from hundreds of MHz to GHz) [205] frequencies than those of planetary radars, and they are often at fixed temperatures [103].

In this chapter the EM characterization of dirty pure ice for the Jovian icy moons is reported. The measurements of both dry and frozen saturated samples were performed via mean of a a Vector Network Analyzer (see chapter 5 for more details) in the frequency range 1 MHz - 100 MHz and as a function of temperature. Moreover, in a second phase a study on the main mixing laws was conducted in order to model the EM properties of dry asteroid analogs and pure water ice/rock mixtures as a function of a wide range of dust inclusions in the temperature range 120-270 K.

9.1 Experimental Setup and Procedure

The samples and the freezing procedure used for these measurements are the ones described in subsections 8.1.1 and 8.2.3. The EM properties were studied for both dry and ice saturated samples. To create the latter, granular samples were placed inside the coaxial probe (the 5 and 10 cm ones, depending on the abundance of material) already filled with the right amount of bidistilled water, in such a way as to create a complete saturation. For both dry and ice saturated samples, after about 24 hours in the ultra-freezer, the coaxial probe was taken out, put inside a thermally insulated box and eventually connected to the VNA. For each sample (dry or ice saturated), data were collected every 30 seconds during samples warming, from 200 K to 270 K, and temperature was continuously monitored inside the sample using a pt100 sensor.

9.1.1 Inclusions Volume Fraction Estimation

Inclusions volume fraction and bulk densities of the granular samples were estimated by measuring their mass m and volume V. The mass was measured by means of a scale (Gibertini Europe 4000AR). Since the samples do not completely fill the Teflon box of the coaxial probe (see fig. 9.1a), the volume is calculated through the following equation:

$$V = V_{cell} \frac{(h_{cell} - dh - h_{lid})}{h_{cell}} \tag{9.1}$$

where V_{cell} is the coaxial probe volume, h_{cell} is the height of the coaxial probe, $h_{lid} = 0.20 \pm 0.01$ is the thickness of the metal lid used as the reference plane of the surface of the sample and dh is the height from the metal lid to the top of the Teflon box (see fig. 9.1b). In particular, dh is the average of the heights measured at eight different points by a digital caliper (the height points in figure 9.1a).

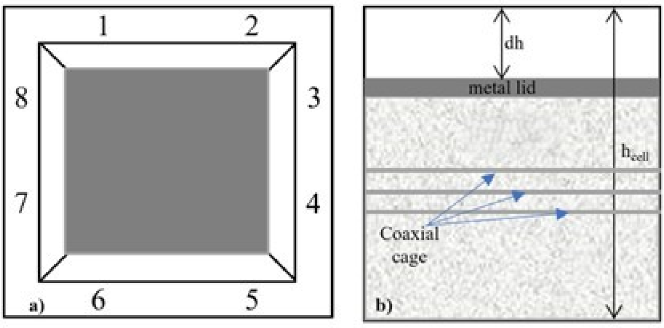

Figure 9.1: Coaxial probe sketch: a) top view; b) section view (taken from [104]).

The bulk density ρ_b and the inclusions volume fraction f_v of the samples were then computed

$$\rho_b = \frac{m}{V} \tag{9.2}$$

$$f_v = 1 - \frac{\rho_b}{\rho_g} \tag{9.3}$$

where ρ_g is the grain density. The uncertainties on inclusions volume fraction and bulk density were calculated propagating the uncertainties on the volume and the grain density, using the error propagation formula. If f_v is the air volume fraction, then it is equal to the porosity ϕ.

For measurement of the EM properties of dry granular samples as a function of the porosity, the sample bulk density was changed before each set of measurements using a vibrating plate (SADEL Medica Mod Duster, see Fig. 9.2). The coaxial probe filled with the granular sample was placed directly on the plate, and then the instrument was set to a different intensity of vibration before each measurement to progressively compact the material, varying its volume. After compaction and volume estimation (by means of eq. 9.1), the coaxial cage was directly connected to the VNA and the measurement performed. Bulk density was then eventually converted into sample porosity using eq. 9.3.

Figure 9.2: Vibrating plate used in this work for the compaction of the powdered samples.

9.1.2 Jupiter Icy Moons' Analogs

Knowledge of Ganymede's surface composition is based on infrared spectroscopy observations of a very thin superficial layer (few μm) ([48], [46], [47]). These measurements suggest that such surface is essentially made by a three-components dirty ice mixture: water ice, hydrated salts and non-ice hydrated material compatible with the composition of carbonaceous chondrites ([46], [54]). Moreover, internal structure models of the rock/iron constituent of the three Jovian satellites suggest a chemical composition similar to the material of L/LL ordinary chondrites ([49], [**?**]). Asteroids, on the other hand, are generally composed of rubble pile/monolithic blocks and at their surface they exhibit layers of regolith, even tens of meters thick ([220], [221]), whose composition is compatible with chondritic materials. Therefore, as a first approximation, the rocky component of both surfaces will be simulated using the same material.

9.1.3 Fitting Procedure

The mixing formulas, as detailed in chapter 3, depend on the geometry of the inclusions inside the mixture, the permittivity contrast between mixture's phases and mixture's porosity. For this reason, a strategy was developed to identify the right mixing formula, able to describe the EM properties for each sample.

In this work, in the case of dry sample measurements, the bulk permittivity and bulk permeability can be defined by a mixing formula MF as follows

$$\varepsilon_b^{dry} = MF(\varepsilon_{air}, \varepsilon_g, f_v) \tag{9.4}$$

$$\mu_b^{dry} = MF(\mu_{air}, \mu_g, f_v) \tag{9.5}$$

where $\varepsilon_{air} = 1$, $\mu_{air} = 1$ are the permittivity and permeability of air, ε_g, μ_g are the permittivity and permeability of the rocky material composing the sample and f_v is the inclusions volume fraction. For saturated measurements similar equations stand

$$\varepsilon_b^{sat} = MF(\varepsilon_{pure\,ice}, \varepsilon_g, f_v) \tag{9.6}$$

$$\mu_b^{sat} = MF(\mu_{pure\,ice}, \mu_g, f_v) \tag{9.7}$$

where $\varepsilon_{pure\,ice}$ is the permittivity of pure ice and $\mu_{pure\,ice} = 1$ is the magnetic permeability of pure ice. Four different mixing formulas were employed, choosing from those most commonly used in the literature: Maxwell Garnett - Random Discs (i.e., inclusions modeled as randomly oriented discs), Maxwell Garnett - Random Needles (i.e., inclusions modeled as randomly oriented needles), Bruggeman and Lichtenecker. Considering the low value of the measured magnetic permeability and the scarce presence of metallic grains in the granular samples, in this work no magnetic interaction was assumed between particles and the same formulas already described for the dielectric permittivity were used [222].

Firstly, the EM properties of each dry sample were measured, obtaining the complex bulk quantities

ε_b^{dry} and μ_b^{dry} as a function of the frequency and temperature. These data were fitted with the four different mixing formulas applying a probabilistic inversion approach with a grid mode, as described in chapter 7, considering also that the inclusions volume fraction has a priori gaussian probability distribution with mean and standard deviation equal to the value measured during the experiment and the related uncertainty, respectively. A grid mode procedure was employed, as it was successful to explore the parameters space. Therefore, four different complex dielectric permittivity and magnetic permeability of the solid grains, ε_g^{dry} and μ_g^{dry} were retrieved as a function of the experimental temperature and at three different frequencies of interest for planetary radar sounders (9, 20, 60 MHz). The grain permittivity and permeability values obtained with this procedure were compared, whenever possible, with the permittivity of the related solid sample found in the literature (this was the case for the Etna basalt and the L5 ordinary chondrite sample [99], [101]; the CI carbonaceous chondrite simulant evidently does not have reference values for the solid part).

Then the same fitting procedure was applied to the ice saturated sample measurements ε_b^{sat} and μ_b^{sat} in the same way as the dry case, with the only difference that in this case the EM properties of the inclusions were equal to the pure ice EM properties: $\varepsilon_{pure\ ice}$ and $\mu_{pure\ ice} = 1$. The pure ice complex permittivity values tabulated in [166] and [162] were used throughout the fitting procedure. Therefore also in this case, four different complex dielectric permittivity and magnetic permeability of the solid grains, ε_g^{sat} and μ_g^{sat} were retrieved as a function of the experimental temperature and at the three different frequencies (9, 20, 60 MHz).

Finally, the permittivity and permeability of the grain in dry condition (ε_g^{dry} and μ_g^{dry}) were compared to those evaluated in saturated condition ε_g^{sat} and μ_g^{sat} as a function of temperature, looking for the mixing formula for which the pairs of values were as similar as possible in the entire temperature range. We assume that the mixing law for which $\varepsilon_g^{dry} \simeq \varepsilon_g^{sat}$ and $\mu_g^{dry} \simeq \mu_g^{sat}$ is the correct one that describes the actual geometry of the inclusions inside the sample.

9.2 Measurements of Powdered Dry Samples

The electromagnetic properties of granular materials used to create dirty ice samples (i.e., etna basalt, L5 ordinary chondrite and CI simulant, see details in subsection 8.1.1) were firstly studied as a function of the volume fraction of air voids within them (i.e., their porosity) at room temperature. Then, the aforementioned experimental procedure was performed to obtain the EM properties versus temperature in subsection 9.2.3.

9.2.1 ε, μ vs ν at Room Temperature

The frequency spectra of the complex permittivity and permeability of the three dry granular materials are shown in Figs. 9.3-9.4 in the frequency range 1 MHz-100 MHz and at two fixed air volume fraction. The Etna basalt is not a magnetic material and for this reason its magnetic permeability is not reported. The imaginary part of both dielectric permittivity and magnetic permeability of all three materials are scattered below 6 MHz: in fact, shadow areas in the plots indicate unreliable values because of the VNA instrumental limit in measuring low-losses materials.
The EM properties of the three dry samples exhibit a dependence on the air volume fraction in the whole frequency spectrum, except the magnetic permeability of the L5 ordinary chondrite, which is quite independent of the air volume fraction (see Fig. 9.4).

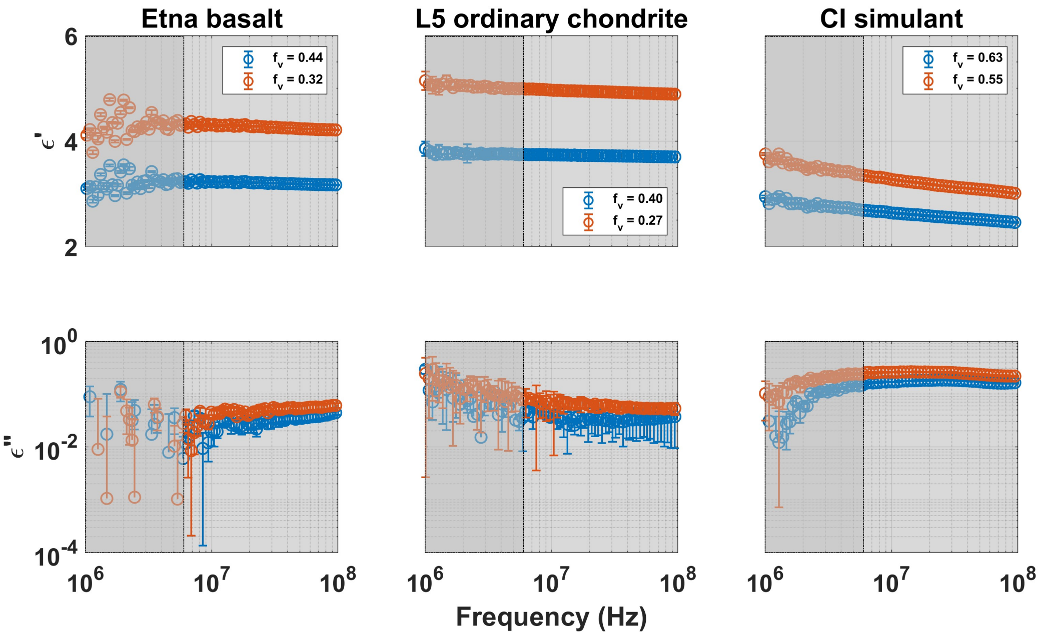

Figure 9.3: Frequency spectra of the complex dielectric permittivity of the three dry granular materials at room temperature, reported at two different inclusions volume fraction.

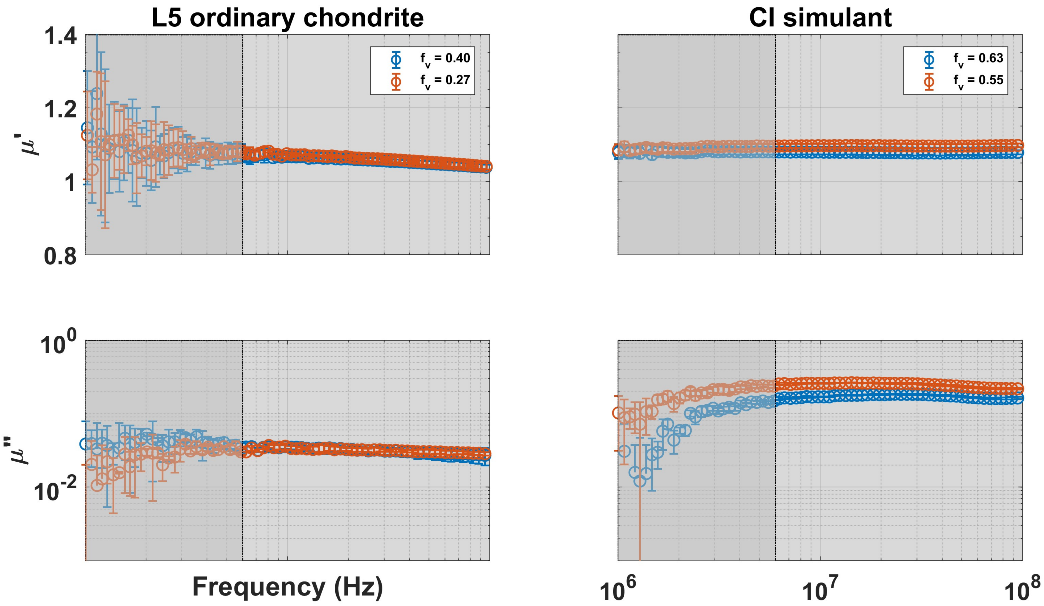

Figure 9.4: Frequency spectra of the complex magnetic permeability of the three dry granular materials at room temperature, reported at two different inclusions volume fraction. The Etna basalt is not a magnetic material and for this reason it ha a magnetic permeability constant at $\mu' = 1$.

9.2.2 ε, μ vs f_v at Room Temperature

The data of the dry samples at room temperature extracted at three frequencies of interest for planetary radar (9, 20 and 60 MHz) were then fitted with the four mixing laws mentioned in 9.1.3 and the results are shown in Figs. 9.5-9.10, where the Hashin-Shtrikman bounds for the three materials are presented too. Such bounds were estimated considering the air as the inclusion phase. It is interesting to note that room temperature ε_g values obtained from the fit with the various mixing formula have great variability, both in the real and imaginary parts. Nevertheless, in the range of experimentally obtained porosities, the mixing laws have very similar values, and differ only at lower porosities. With the experimental set up employed in this work, it is not possible to have more compacted, lower porosity granular samples, and for this reason further measurements at lower porosities will be required in the future.

9 MHz

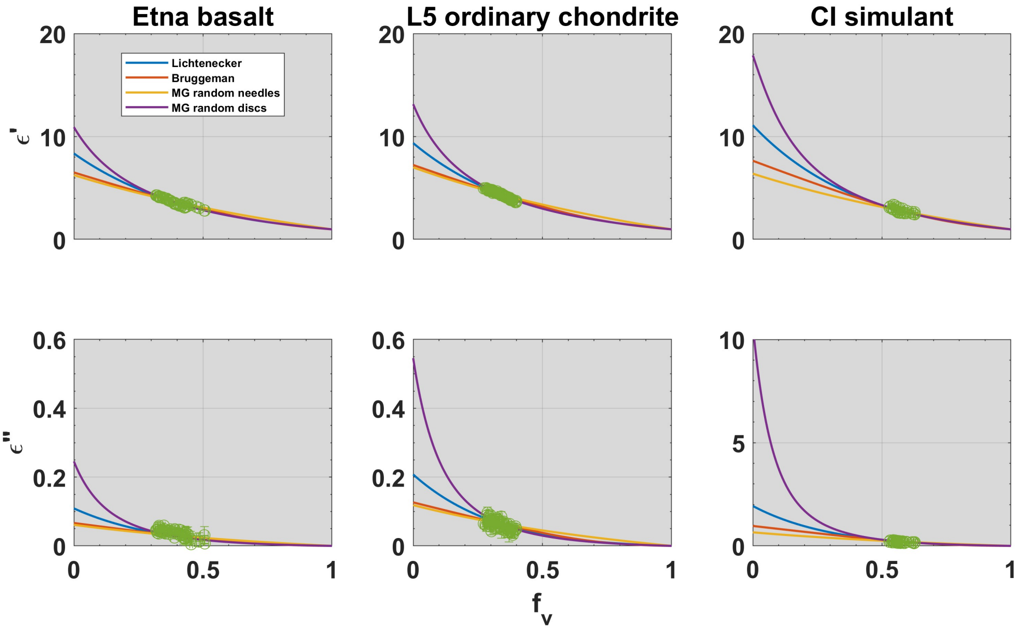

Figure 9.5: Complex permittivity fit as a function of the porosity, at room temperature and 9 MHz.

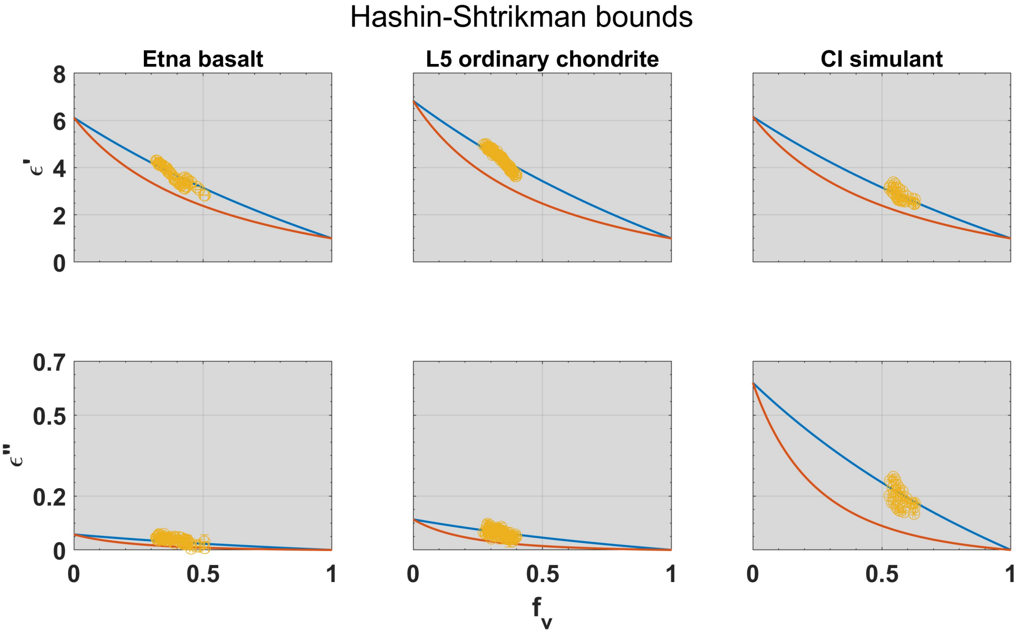

Figure 9.6: Hashin-Shtrikman bounds at 9 MHz and room temperature of the three granular samples.

20 MHz

The magnetic permeability at 20 and 60 MHz is not reported for the sake of brevity, since it is fairly constant in the entire frequency range 1 MHz-100 MHz.

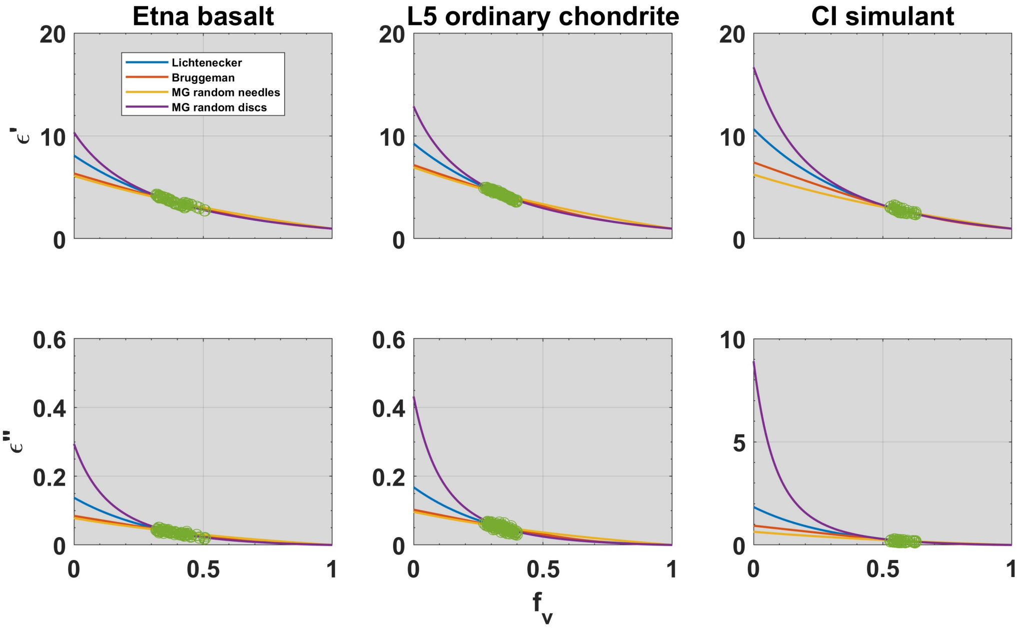

Figure 9.7: Complex permittivity fit as a function of the porosity, at room temperature and 20 MHz.

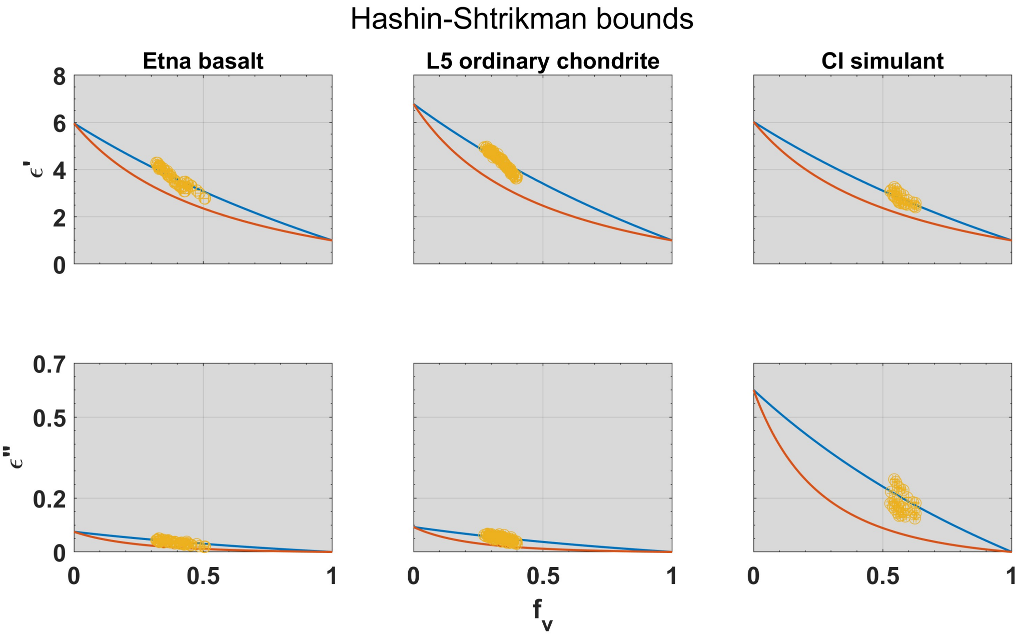

Figure 9.8: Hashin-Shtrikman bounds at 20 MHz and room temperature of the three granular samples.

60 MHz

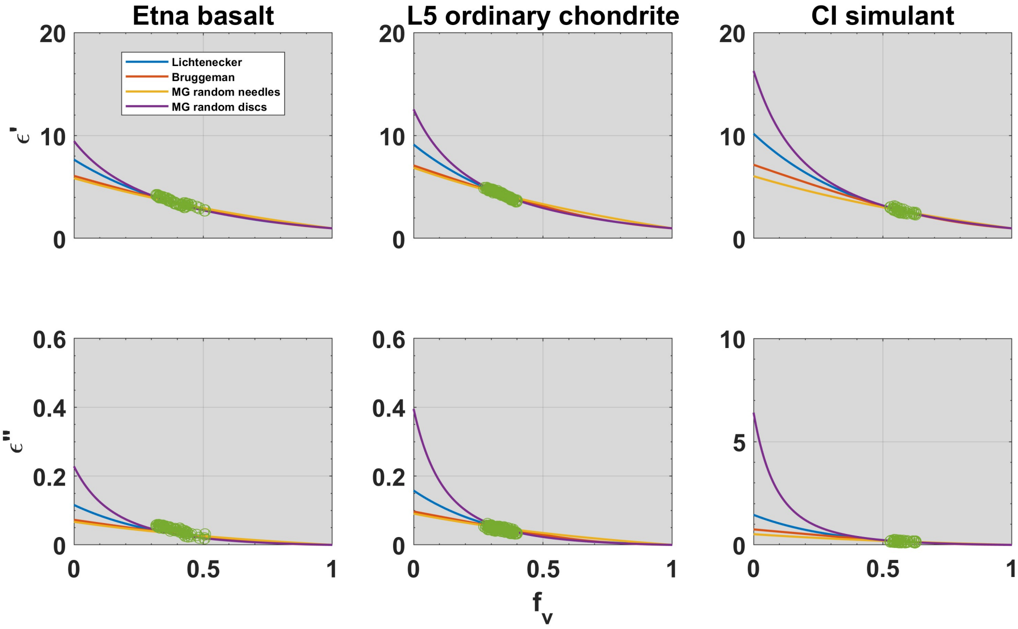

Figure 9.9: Complex permittivity fit as a function of the porosity, at room temperature and 60 MHz.

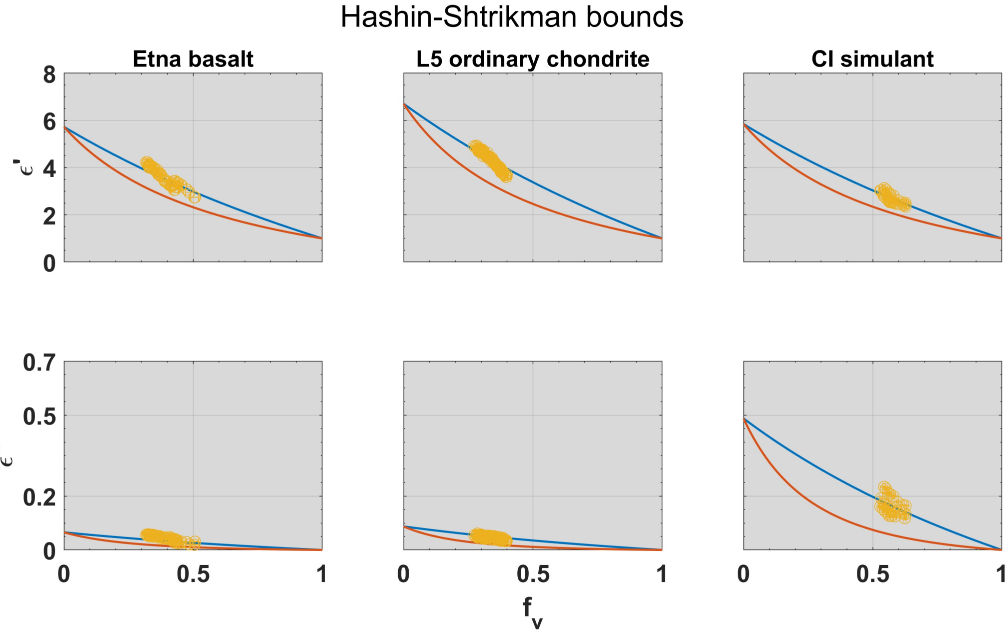

Figure 9.10: Hashin-Shtrikman bounds at 60 MHz and room temperature of the three granular samples.

9.2.3 ε, μ vs T

The EM properties of the samples were measured as a function of temperature at a fixed air volume fraction using an ultrafreezer and the freezing procedure described earlier.
In Figs. 9.11-9.12 the dielectric permittivity and magnetic permeability of the three dry granular materials are reported in the frequency range 1 MHz-100 MHz, for three different temperatures (210 K, 240 K, 270 K). The plots also show the data acquired with the probe line empty which, for the imaginary part, represents the minimum losses measurable in the entire frequency range with this experimental setup. Figures 9.11-9.12 also indicate that measurements below 6 MHz are scattered (gray box), especially in the imaginary part, due to the inability of the instrument to accurately measure low-loss materials in the low frequency range.

Above 6 MHz, the real part of permittivity of the three samples is fairly constant in the entire frequency range, and it has a small variability with temperature. Note that, the L5 sample shows the highest value of the real part of permittivity ($\simeq 4$), the Etna basalt is intermediate ($\simeq 3$) and the CI is the lowest ($\simeq 2.8$). This difference, as expected, reflects the different mineral composition of the samples and their grain density (see subsection 8.1.1). Conversely, the imaginary part of the three samples exhibits a relative constant behavior only up to 60 MHz; beyond such frequency value, this quantity tends to increase.

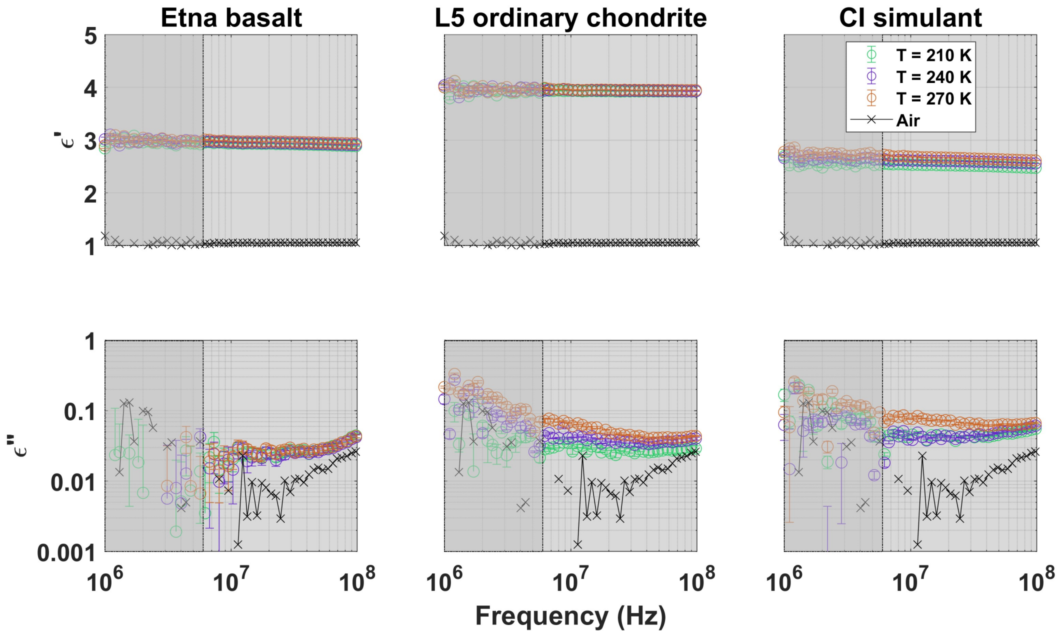

Figure 9.11: Dielectric permittivity of the dry samples at three different temperatures (210, 240, 270 K) in the frequency range 1 MHz-100 MHz. The shadow box indicates values that are not reliable because of the VNA instrumental limits. The air volume fractions of the Etna basalt, L5 ordinary chondrite and CI simulant are $f_v^{Etna} = 0.49\pm0.01$, $f_v^{L5} = 0.37\pm0.01$, and $f_v^{CI} = 0.60\pm0.01$ respectively.

The behavior already described on the dielectric permittivity below 6 MHz, is also recognizable on the magnetic data (see Fig. 9.12). The real part of magnetic permeability of L5 ordinary chondrite sample decreases with frequency, and the imaginary part is always above the line of the data collected with the probe empty. This trend, which is independent of temperature, highlights the magnetic characteristics of the sample. The CI simulant exhibits a constant real part of magnetic permeability of $\simeq 1.1$, which is unaffected by temperature and frequency. Moreover, at lower frequencies its imaginary part is quite overlapped to the air measurements up to 60 MHz; beyond such value, this quantity tends to increase as the measure is approaching the resonance frequency of the probe line. For this reason, these values below 60 MHz are not considered reliable.

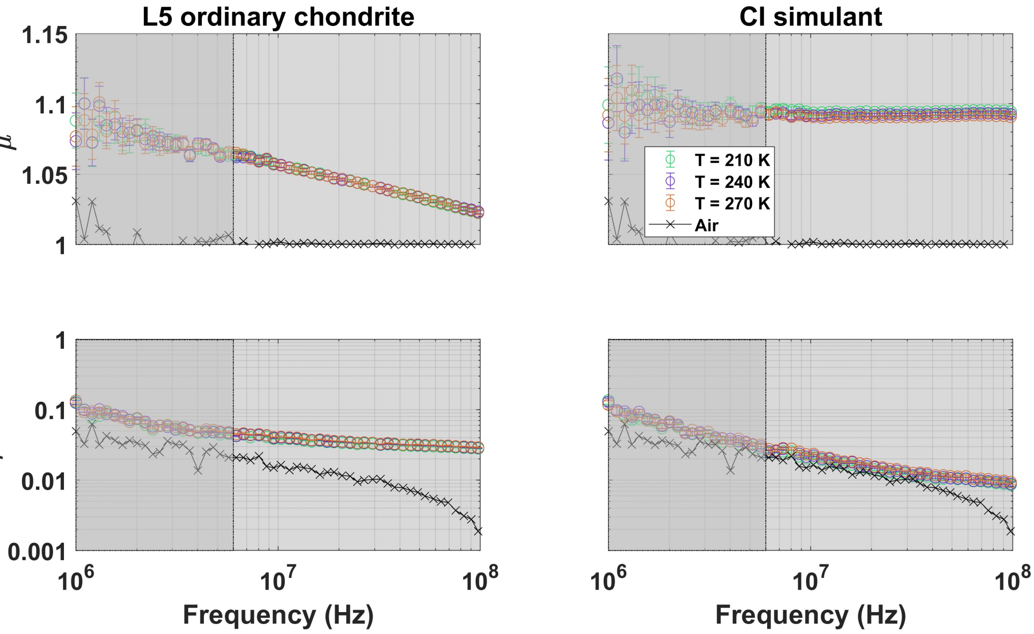

Figure 9.12: Magnetic permeability of the dry samples at three different temperatures (210, 240, 270 K) in the frequency range 1 MHz-100 MHz. Etna magnetic permeability is not shown since the powder does not have magnetic properties. The shadow box indicates values that are not reliable because of the VNA instrumental limits. The air volume fractions of the Etna basalt, L5 ordinary chondrite and CI simulant are $f_v^{Etna} = 0.49 \pm 0.01$, $f_v^{L5} = 0.37 \pm 0.01$, and $f_v^{CI} = 0.60 \pm 0.01$ respectively.

The dielectric permittivity temperature dependence in the range ≈200 K - 270 K, at three fixed frequencies (9, 20 and 60 MHz) is shown in Fig. 9.13; the magnetic permeability is not shown, since it does not exhibit a strong trend in temperature. While the real part of permittivity of Etna basalt is constant in this temperature range, both the L5 ordinary chondrite and CI simulant exhibit a linear trend, although not very pronounced. Furthermore, the imaginary part of the basalt is rather flat whereas the values of the L5 and CI show a trend with temperature, with a slight change in slope above 240K, more pronounced in the CI sample.

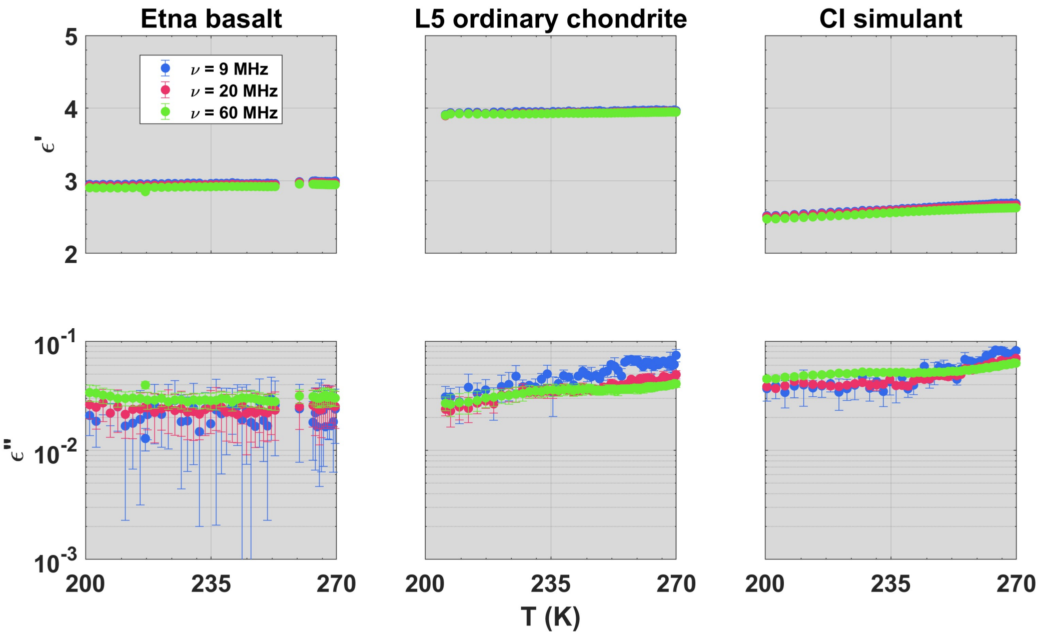

Figure 9.13: Dielectric permittivity of the dry samples as a function of temperature at three fixed frequencies (9, 20 and 60 MHz). The air volume fractions of the Etna basalt, L5 ordinary chondrite and CI simulant are $f_v^{Etna} = 0.49 \pm 0.01$, $f_v^{L5} = 0.37 \pm 0.01$, and $f_v^{CI} = 0.60 \pm 0.01$ respectively.

9.3 Measurements of Powdered Ice Saturated Samples

The EM properties of ice saturated samples were measured at temperatures ranging from 200 to 270 K.

9.3.1 ε, μ vs T

The frequency spectra of dielectric permittivity exhibit a very different behavior compared to the dry measurements (see Fig. 9.14). For comparison, the Figure 9.14 also shows the complex permittivity of the related dry samples at 210 K (black line); in this case the gray box are not reported in the plots since the ice saturated samples have dielectric losses higher than the instrumental limit in the entire frequency range. The real part of the permittivity is fairly flat at 210 K for all samples; at 240 K the dispersive-frequency dependent behavior starts to become appreciable only in the L5 ordinary chondrite and the CI simulant; finally at 270 K the dispersive behavior becomes predominant in all materials, probably due to the presence of pockets of liquid water inside the samples. The imaginary part, on the other hand, has the typical behavior of rocky grains/water ice mixtures [189] with the predominance of a pronounced conductive trend at low frequency and high temperature.

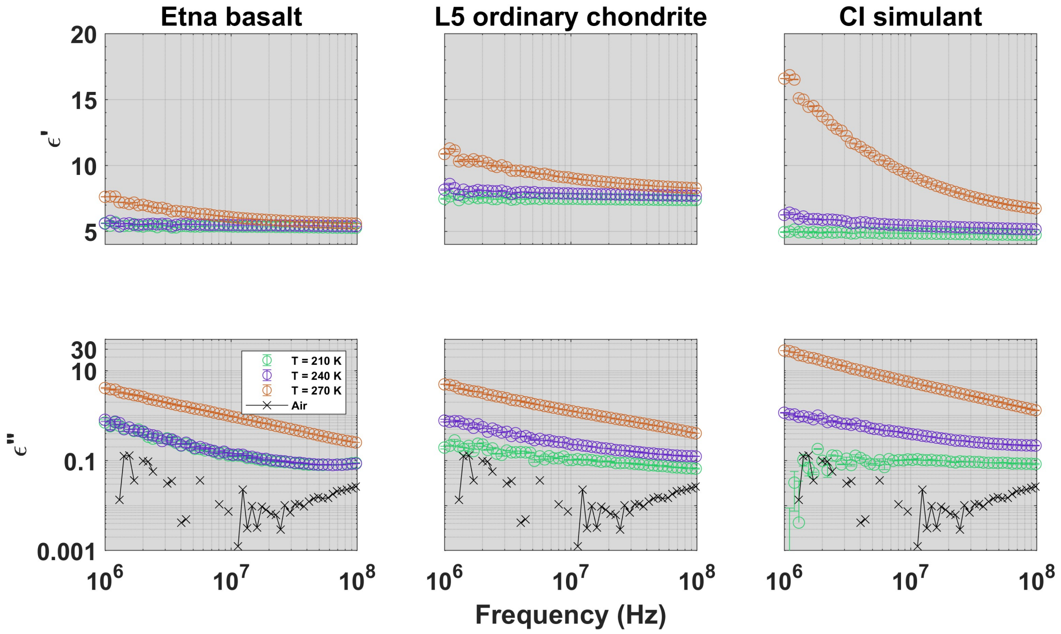

Figure 9.14: Dielectric permittivity of the frozen saturated samples at three different temperatures (210, 240, 270 K) in the frequency range 1 MHz-100 MHz. The ice volume fractions of the Etna basalt, L5 ordinary chondrite and CI simulant are $f_v^{Etna} = 0.46 \pm 0.01$, $f_v^{L5} = 0.33 \pm 0.01$, and $f_v^{CI} = 0.60 \pm 0.01$ respectively.

It is interesting to note that the values of magnetic permeability of the ice saturated samples in Fig. 9.15 are very similar to those observed in the dry measurements (see Fig. 9.12), as the magnetic behavior is independent of the material filling the pores if this is non-magnetic, but only depends on the amount of magnetic materials.

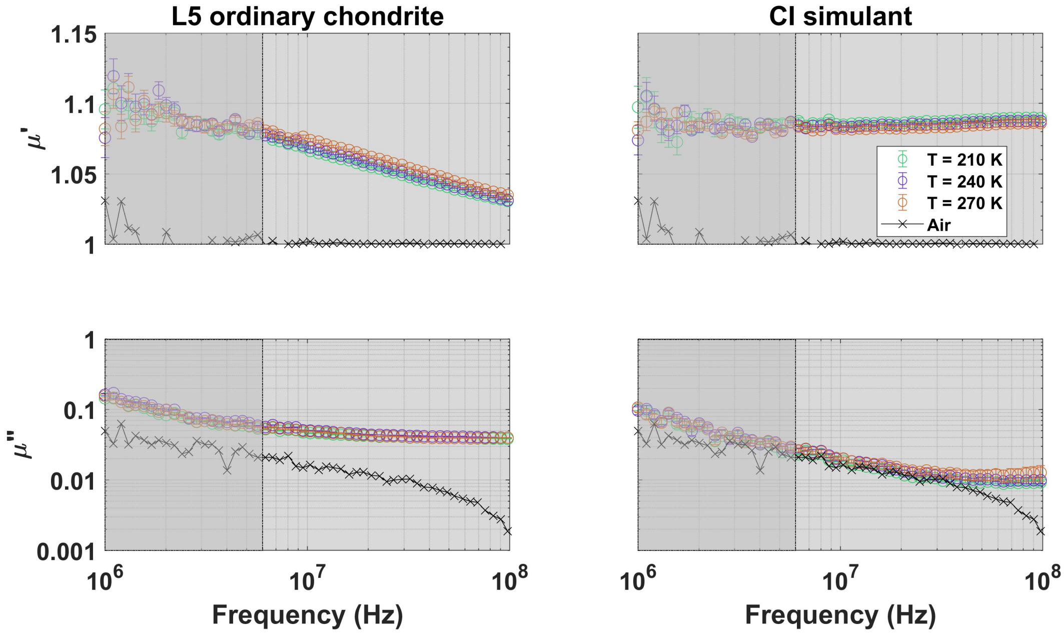

Figure 9.15: Magnetic permeability of the frozen saturated samples at three different temperatures (210, 240, 270 K) in the frequency range 1 MHz-100 MHz. The ice volume fractions of the Etna basalt, L5 ordinary chondrite and CI simulant are $f_v^{Etna} = 0.46 \pm 0.01$, $f_v^{L5} = 0.33 \pm 0.01$, and $f_v^{CI} = 0.60 \pm 0.01$ respectively.

The complex permittivity values obtained from ice saturated measurements exhibit a more significant temperature dependence compared to those measured in dry conditions (see Fig. 9.16), which can be attributed to the presence of ice within the pores. The basalt from Etna exhibits minimal dependence on temperature variations, as evidenced by the nearly constant values of both the real and imaginary components, which only begin to rise beyond 250 K. Two fundamental properties should be considered to explain the differences between the electromagnetic properties of the three materials: a) the amount of ice in the pores, and b) the mineralogical properties exhibited by the grains. The ice volume fraction is controlled by the porosity of the samples, therefore the amount of ice is the largest in CI (60%) and the lowest in L5 (33%), being the Etna basalt intermediate (46%). The mineralogical composition of the samples contributes to a partial counteraction of the ice's effects, as can be seen in the L5 sample, which has the lowest ice content but the highest metallic phase concentration among the three samples. Conversely, the CI simulant exhibits the lowest real part of permittivity at 200 K, alongside the highest ice content. Nevertheless, the complex permittivity of this sample demonstrates significant temperature variability especially at higher temperatures, a characteristic commonly associated with clay materials, likely attributable to the substantial presence of smectite within the sample ($\simeq$ 50%) [216]. The orientational polarization is the mechanism that causes the enhancement of the complex permittivity.

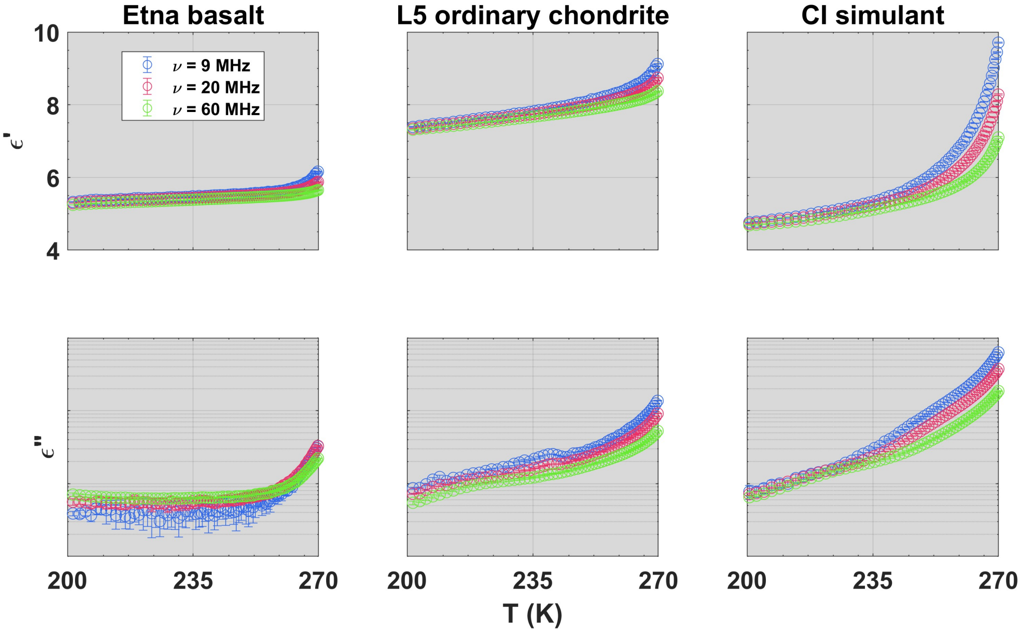

Figure 9.16: Dielectric permittivity of the frozen saturated samples as a function of temperature at three fixed frequencies (9, 20 and 60 MHz). The ice volume fractions of the Etna basalt, L5 ordinary chondrite and CI simulant are $f_v^{Etna} = 0.46 \pm 0.01$, $f_v^{L5} = 0.33 \pm 0.01$, and $f_v^{CI} = 0.60 \pm 0.01$ respectively.

9.4 Extrapolation of Permittivity of Dry Samples to Lower Temperatures

The surface temperatures estimated on the icy moons are lower than the ones measured via this experimental setup that allow to measure down to 200 K [28], [223], [224]. On one hand, the magnetic permeability of dry samples exhibits minimal dependence on temperature, which facilitates the extrapolation of this parameter to lower temperatures without significant complications or the need for additional measurements. Nevertheless, their dielectric permittivity has a more complex behavior in temperature, similar for the three samples: in particular, the real part exhibits a linear dependence on temperature, while the imaginary part remains constant until a certain temperature threshold is attained, beyond which it follows an exponential trend at higher temperatures. As a result, further measurements were carried out to determine if the trend of the the electrical properties remained unchanged at lower temperatures for all three dry samples.

The additional dielectric permittivity measurement at temperatures lower than 200 K were performed in the frequency range 20 Hz-1 MHz by means of the LCR meter setup (see chapter 6 for more details), which is compatible with use of liquid nitrogen. Therefore, by combining the measurements performed with the LCR meter at the frequency of 1 MHz with those performed with the VNA at 9 MHz at the same fixed air volume fraction, it was possible the electrical properties down to 120 K, a temperature compatible to those measured on the surface of the satellites. The comparison between measurements extracted at different frequencies is possible since the EM properties in the range 1 MHz-10 MHz are fairly constant. As example, the result for the CI simulant are shown in Fig. 9.17.
These extrapolations are critical for modeling the EM properties of dirty ice at low temperatures, as will be emphasized in the next section.

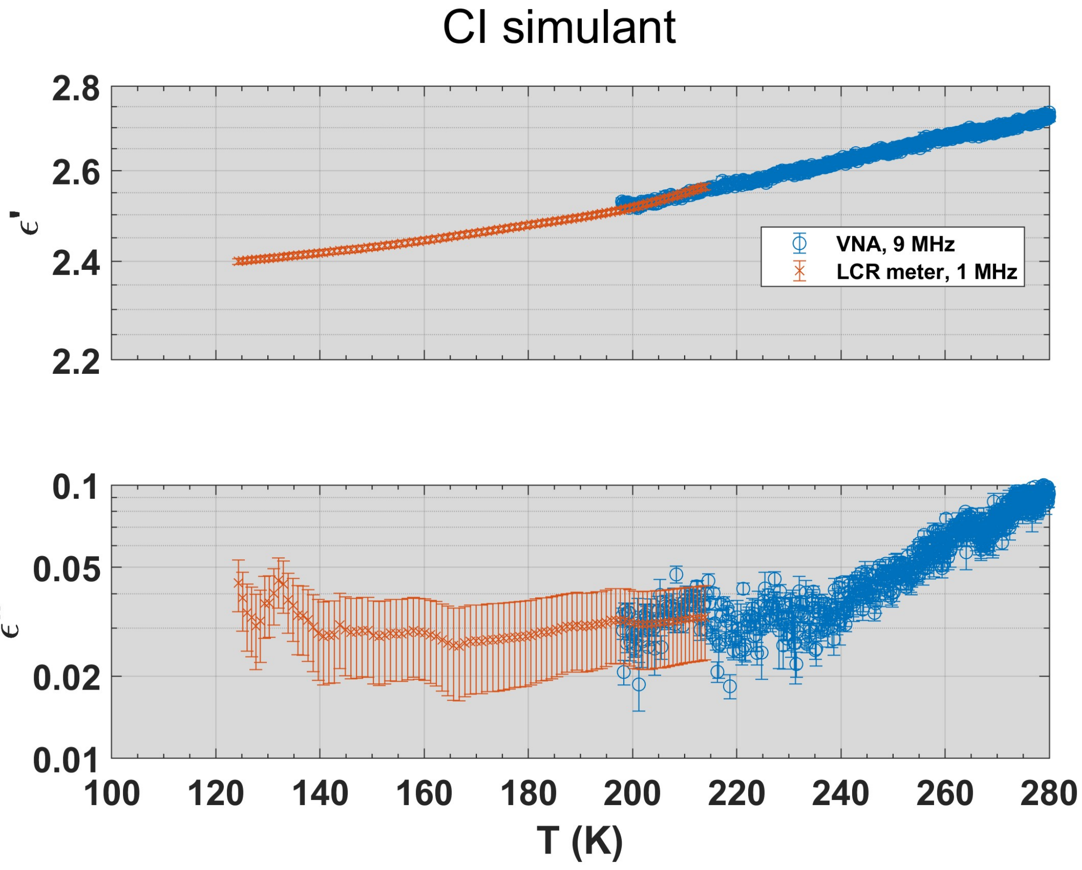

Figure 9.17: Complex permittivity of the CI simulant as a function of temperature estimated by the LCR meter (orange dots) at 1 MHz and the VNA at 9 MHz (blue dots).

9.5 Estimation of ε_g and μ_g

The fitting procedure detailed in subsection 9.1.3 was applied to dry and ice saturated measurements, obtaining the complex values ε_g^{dry},ε_g^{sat} and μ_g^{dry},μ_g^{sat} versus temperature. Figure 9.18, Figure 9.19 and Figure 9.20 report the grain permittivity of Etna basalt, L5 ordinary chondrite and CI simulant, respectively estimated from dry (yellow dots) and ice saturated (blue dots) samples as a function of temperature and at 9 MHz. For comparison, in all plots the pink dot represents the permittivity of the grain retrieved applying the same fitting procedure to data acquired at room temperature and at the same frequency as shown in subsection 9.2.2. For Etna basalt and L5 ordinary chondrite, Figure 9.19 and Figure 9.20 report also a green dot (and also a light blue dot in the case of the meteorite) that indicates the value of the permittivity measured on the related solid samples in the frequency range 1 MHz - 100 MHz [99], [101]. In case of Etna basalt the Lichtenecker equation seems to be the one that correctly describes the mixture and therefore the geometry of the inclusions (spheroidal), as both the fits on the dry (ε_g^{dry}) and ice saturated measurements (ε_g^{sat}) return values in agreement with each other and with the data obtained at room temperature in subsection 9.2.2 and in [99].

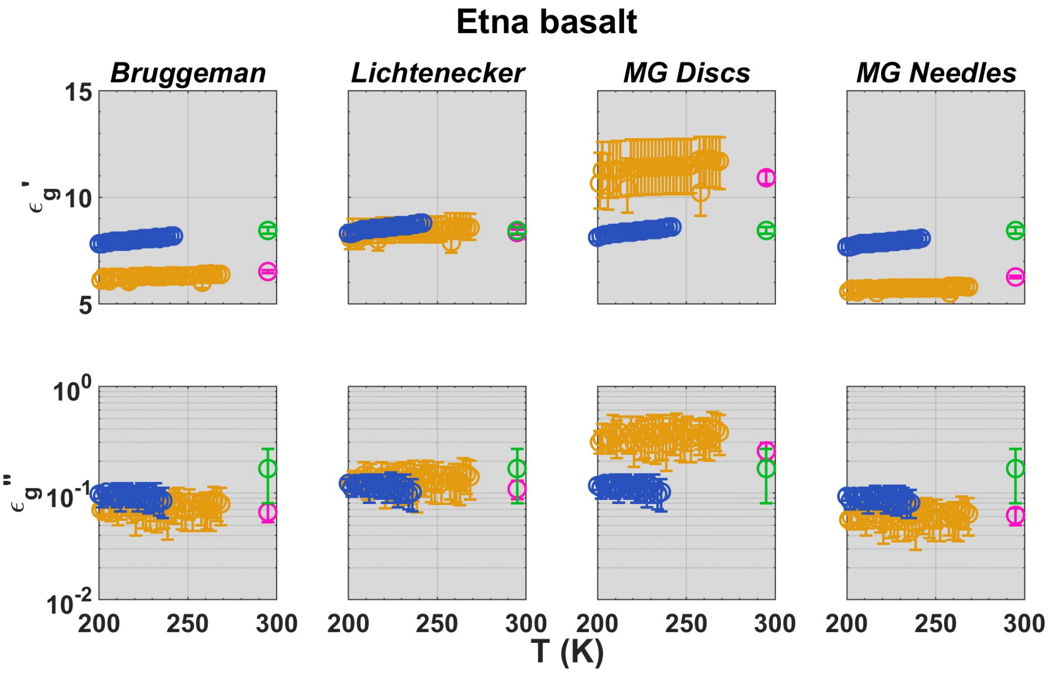

Figure 9.18: The real and imaginary part of ε_g of Etna basalt retrieved from dry and saturated measurements (yellow and blue dots, respectively) by measn of four different mixing formulas; fit result obtained at 9 MHz varying the inclusions volume fraction of the granular sample, at room temperature (pink dot); measurement performed on the solid sample (green dot, [99]).

Figures 9.19 and 9.20 show that L5 ordinary chondrite and CI simulant seem better described by Maxwell Garnett Random Discs equation and Lichtenecker equation respectively. ε_g^{sat} values of the CI simulant are reported below 210 K, since above this value the dispersive behavior becomes predominant, due to the presence of smectite as discussed in section 9.3 (the blue dashed line in the plots represents the results above this temperature).

Moreover, L5 ordinary chondrite fit values were compared with the ones obtained on previous measurements of a solid sample of the same meteorite reported in [101] (light blue and green dots in Fig. 9.19): Lichtenecker fit results are more in agreement with the results obtained on the low permittivity areas of the meteorite solid sample, characterized by a lower iron content; this is probably due to the destruction of the conductive paths in metallic grains inside the solid sample during the solid sample pulverization process [98], [104].

It is interesting to note that both L5 ordinary chondrite and CI simulant display ε_g^{sat} values that deviate from those expected above a certain temperature (at approximately 240 K and 210 K, respectively): this anomalous behavior may be due to the reasons addressed in subsection 9.3.1 and to the partial melting of the ice doped by the granular material, below the freezing temperature.

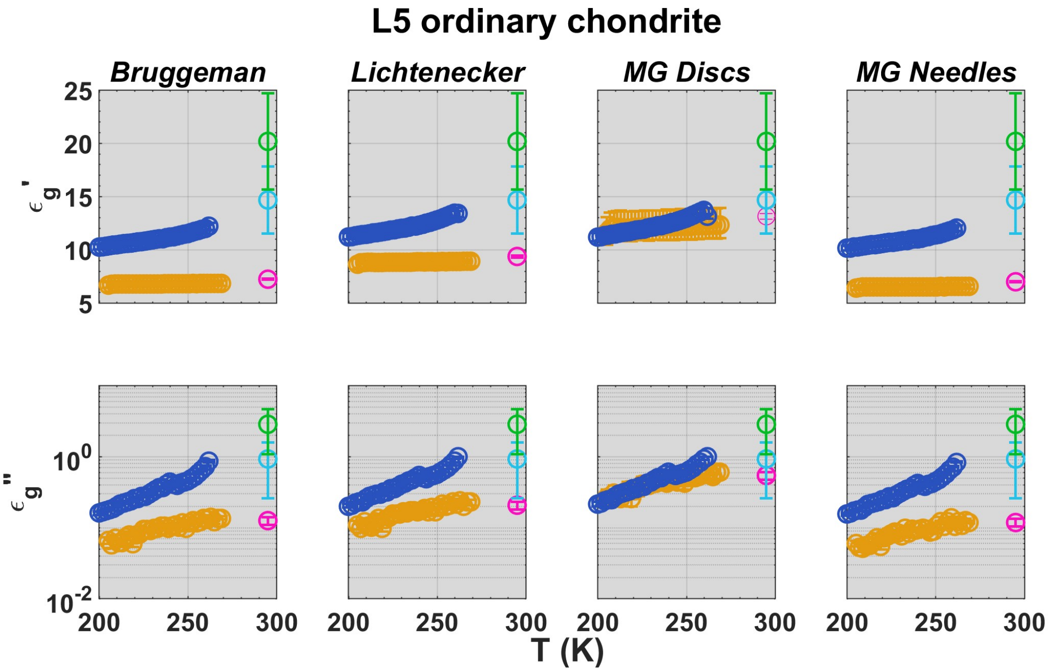

Figure 9.19: The real and imaginary part of ε_g of L5 ordinary chondrite retrieved from dry and saturated measurements (yellow and blue dots, respectively); fit result obtained at 9 MHz varying the air volume fraction of the granular sample, at room temperature (pink dot, [104]); measurements performed on the solid sample low permittivity and high permittivity areas (light blue and green dots respectively, [101]).

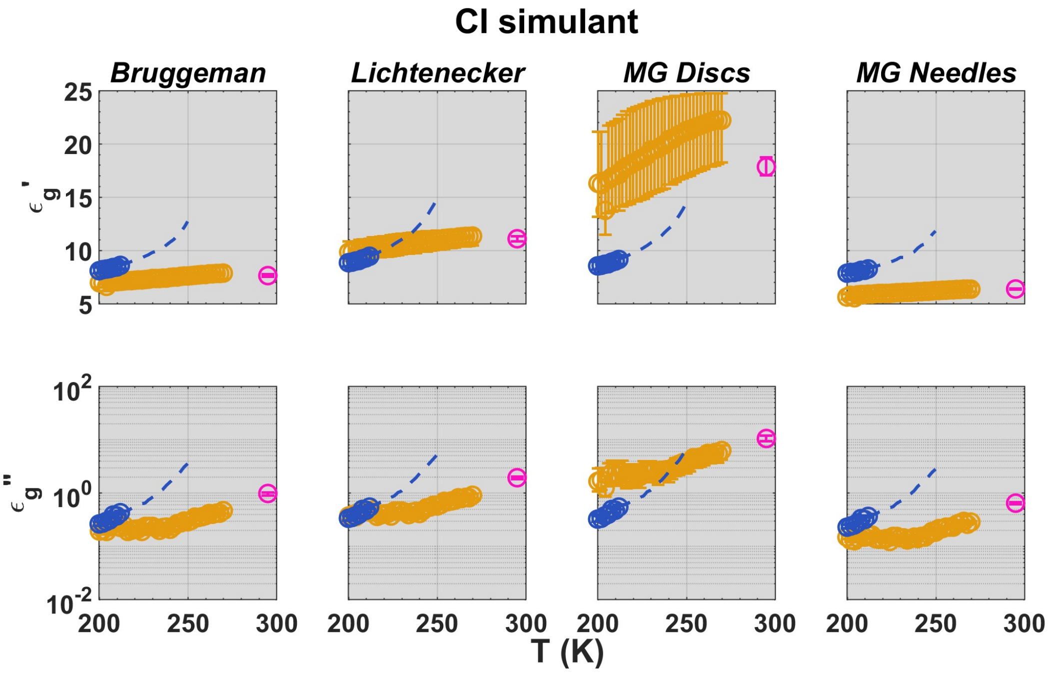

Figure 9.20: The real and imaginary part of ε_g of CI simulant retrieved from dry and saturated measurements (yellow and blue dots, respectively); fit result obtained at 9 MHz varying the air volume fraction of the granular sample, at room temperature (pink dot). The blue dashed line are the fit values from the frozen saturated measurement at the temperatures at which the sample has very dispersive behavior due to its composing clay material.

The grain magnetic permeability has a regular behavior as a function of temperature: in fact its real part is constant in the entire temperature range for both materials (in Fig. 9.21 the grain magnetic permeability of the L5 ordinary chondrite is shown as example). The fitting procedure performed on all measurements indicated that the grain magnetic permeability μ_g values obtained with the four different mixing formulas are the same, due to the very small contrast in magnetic properties between air/ice and the granular materials (see Fig. 9.21).

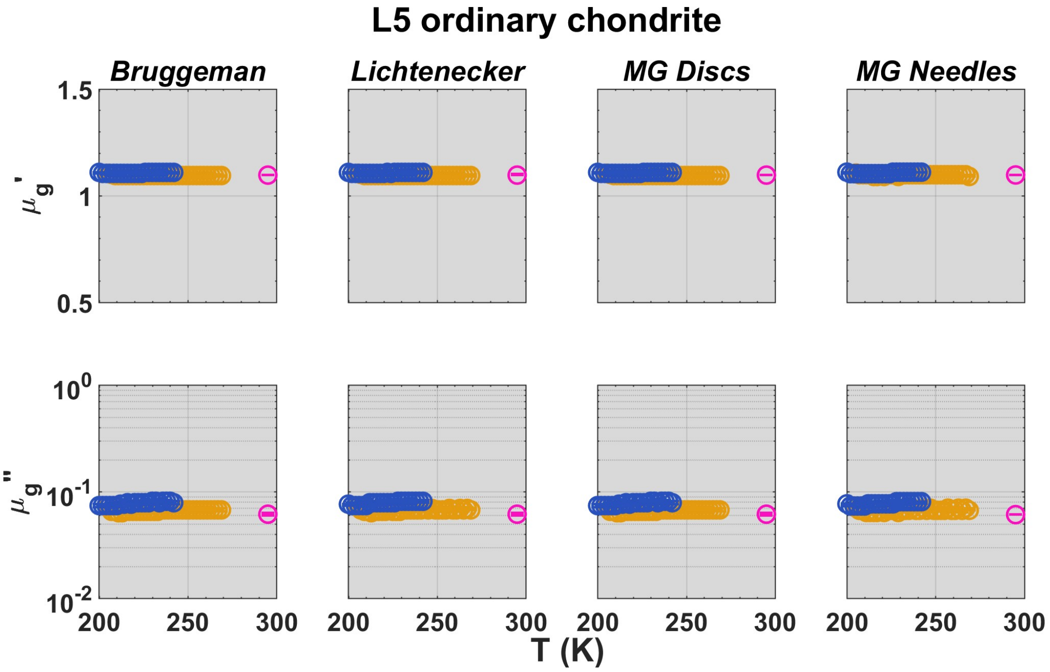

Figure 9.21: The real and imaginary part of μ_g of L5 ordinary chondrite retrieved from dry and saturated measurements (yellow and blue dots, respectively); fit result obtained at 9 MHz varying the inclusions volume fraction of the granular sample, at room temperature (pink dot, [104]).

The theoretical values of the bulk permittivity of the ice saturated samples obtained using eq. 9.6 and the ε_g^{dry} values retrieved by the fit were compared with the experimental values of the bulk permittivity of the ice saturated samples, in order to test the goodness of the fit procedure. As can be noticed, the theoretical values for the L5 ordinary chondrite are compatible with the experimental values considering the uncertainties, while the bulk permittivity theoretical values of the CI simulant are compatible with the measurements up to 210 K; from this temperature the measurement is dominated by a dispersive behavior and for this reason the fit for the CI simulant is considered reliable up to 210 K. Such behavior is probably due to the appearance of unfrozen water inside the sample.

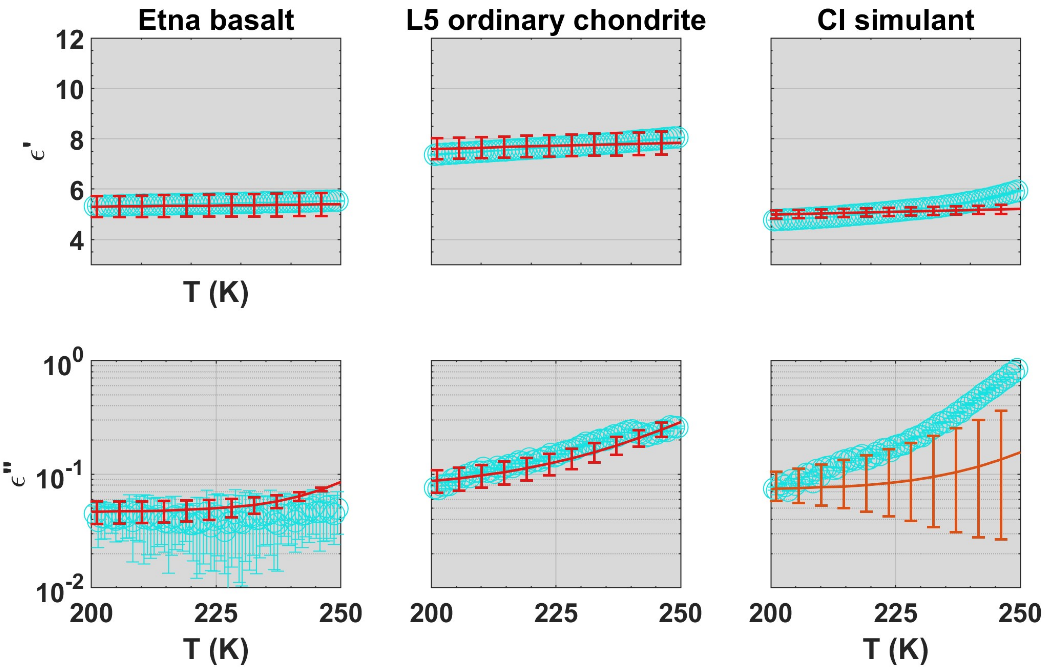

Figure 9.22: Comparison between theoretical values (red line) and experimental values (cyan dots) of complex bulk permittivity at 9 MHz of the fully saturated L5 ordinary chondrite and CI simulant.

The LCR meter measurements at temperatures lower than 200 K were then fitted with the mixing laws using the same procedure implemented for the VNA ones, obtaining a comprehensive trend in temperature for the complex quantity ε_g^{dry} (see Figs. 9.23 and 9.24). In this way it was possible to obtain the grain permittivities of the three samples at 9, 20 and 60 MHz down to temperatures expected on the surface of the moons. In Table 9.1 the result of this fit extrapolation in temperature are summarized, also reporting the mixing law that best describes the experimental data according to the fitting procedure proposed in this work. When it was not possible to accurately estimate the imaginary part of permittivity and permeability due to the constraints imposed by the instruments, only the estimated upper limit of these values are reported.

Sample	**9 MHz**	**20 MHz**	**60 MHz**	**Mixing formula**
Etna basalt	$\varepsilon'_g(T) = 7.4 + 0.004T$ $\varepsilon''_g = 0.14$	$\varepsilon'_g(T) = 7.4 + 0.004T$ $\varepsilon''_g = 0.14$	$\varepsilon'_g(T) = 7.3 + 0.004T$ $\varepsilon''_g = 0.17$	Lichtenecker
L5 Chondrite	$\varepsilon'_g(T) = 9.5 + 0.01T$ $\varepsilon''_g(T) = 0.01 + 0.02e^{0.01T}$ $\mu'_g = 1.1$ $\mu''_g(T) = 0.05 + 0.0001T$	$\varepsilon'_g(T) = 9.6 + 0.01T$ $\varepsilon''_g(T) = 0.002 + 0.04e^{0.01T}$ $\mu'_g = 1.1$ $\mu''_g(T) = 0.05 + 4 \times 10^{-5}T$	$\varepsilon'_g(T) = 11.2 + 0.004T$ $\varepsilon''_g(T) = 0.0003 + 0.08e^{0.01T}$ $\mu'_g = 1.1$ $\mu''_g(T) = 0.04 + 4 \times 10^{-5}T$	Maxwell Garnett Random Discs
CI carbonaceous chondrite simulant	$\varepsilon'_g(T) = 5.9 + 0.02T$ $\varepsilon''_g(T) = 0.3 + 4 \times 10^{-6}e^{0.04T}$ $\mu'_g = 1.3$ $\mu''_g(T) < 0.07$	$\varepsilon'_g(T) = 6.2 + 0.02T$ $\varepsilon''_g(T) = 0.4 + 4 \times 10^{-6}e^{0.04T}$ $\mu'_g = 1.3$ $\mu''_g(T) < 0.05$	$\varepsilon'_g(T) = 4.4 + 0.03T$ $\varepsilon''_g(T) = 0.5 + 1 \times 10^{-5}e^{0.05T}$ $\mu'_g = 1.3$ $\mu''_g(T) = 0.02 + 5 \times 10^{-5}T$	Lichtenecker

Table 9.1: Temperature fitting function and mixing formula chosen for each material studied in this work at three different frequencies (9 MHz, 20 MHz, 60 MHz). The imaginary part of the magnetic permeability of the CI simulant was not measurable below 30 MHz due to instrumental limits: for this reason, only the possible upper limit of these values are reported. For the CI simulant the temperature fitting function is valid only up to 210 K.

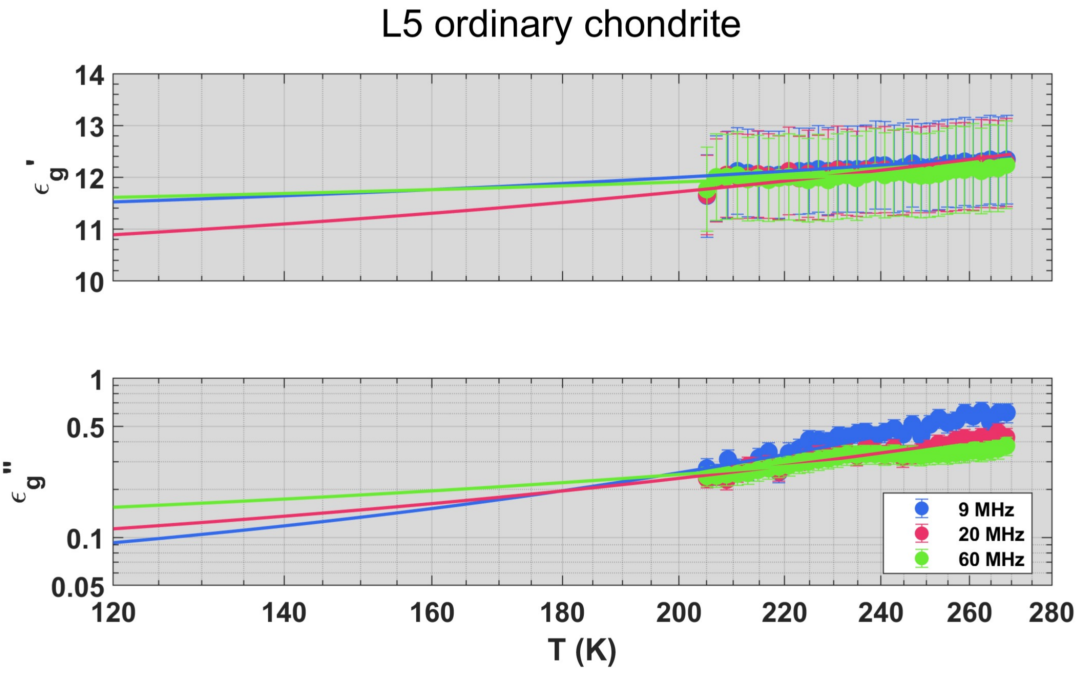

Figure 9.23: Solid grain complex permittivity ε_g of L5 ordinary chondrite (dots) and its extrapolation at lower temperatures (solid line). The extrapolation has been performed at three frequencies: 9, 20 and 60 MHz.

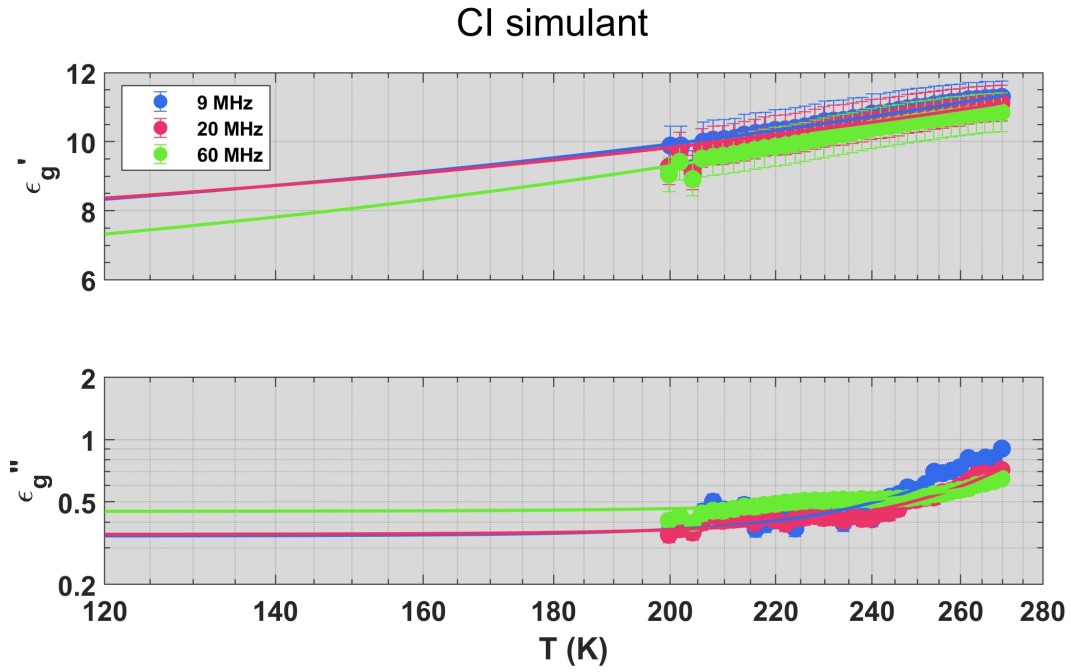

Figure 9.24: Solid grain complex permittivity ε_g of CI simulant (dots) and its extrapolation at lower temperatures (solid line). The extrapolation has been performed at three frequencies: 9, 20 and 60 MHz.

9.6 Discussion and Conclusions

The results obtained from determining the appropriate mixing formula are in agreement with previous measurements of the solid samples: the grain complex permittivity retrieved at 9 MHz for the L5 ordinary chondrite, $\varepsilon_g = 13 - i0.6$ is compatible with the values estimated in [101], where three slices of the chondrite were analyzed. In particular, the low permittivity area of the slices shows permittivities compatible with those obtained through the fitting procedure in this work at room temperature. The Etna basalt study confirms the results obtained with different experimental setups [99]. On the other hand, the comparison of the solid grain permittivity and permeability of the CI carbonaceous chondrite simulant was not possible because there were no measurements available from the actual solid meteorite. Starting from the values retrieved with the fitting procedure and shown in Table 9.1, it is possible to construct a parametric electromagnetic model for these two materials of interest for future spacecraft missions: in fact, by varying the ice volume fraction and the temperature it is possible to create specific models of dirty ice for the icy moons in a wide range of temperatures, from 120 K to 210 K for the CI simulant and from 120 K to 240 K for the L5 ordinary chondrite. Figs. 9.25 and 9.26 show the filled contour plot of the EM properties of mixtures with pure ice as a function of the ice volume fraction and temperature.

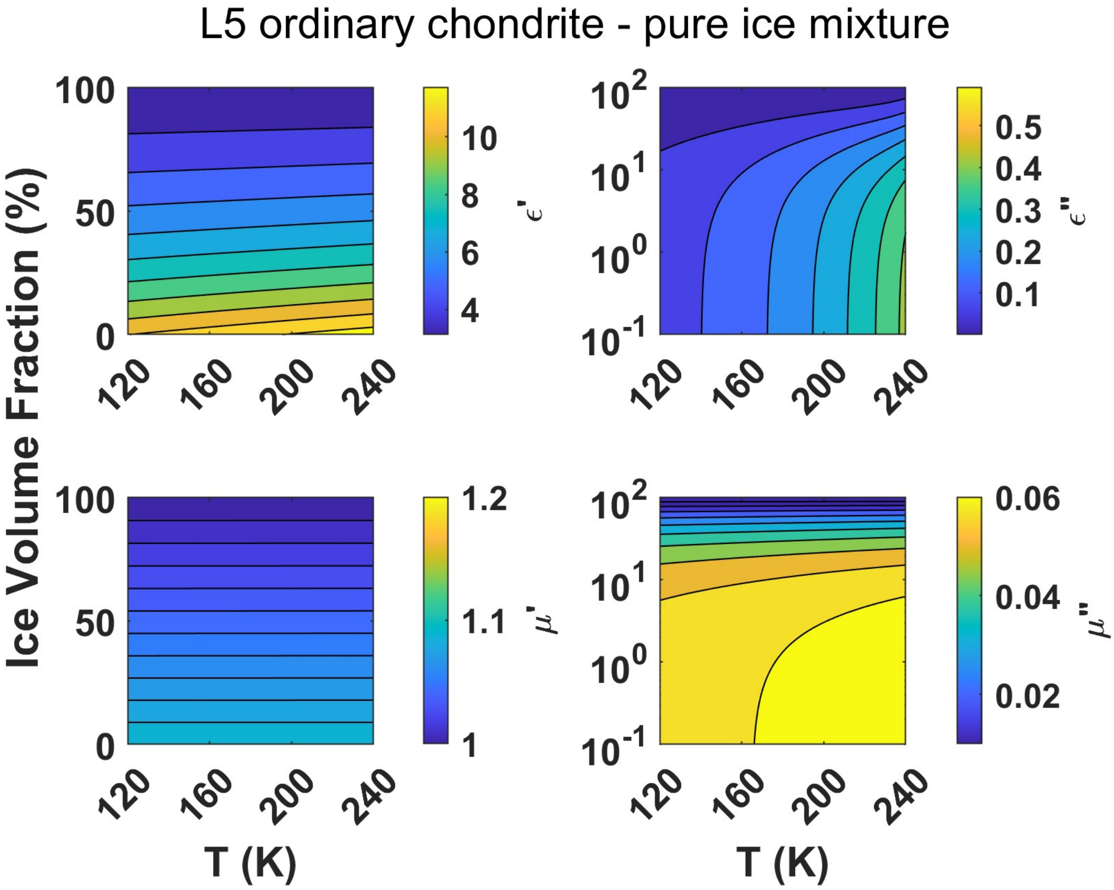

Figure 9.25: Filled contour plot of the EM properties of the mixture of L5 ordinary chondrite and pure ice at 9 MHz, in the temperature range 120-240 K and as a function of ice volume fraction.

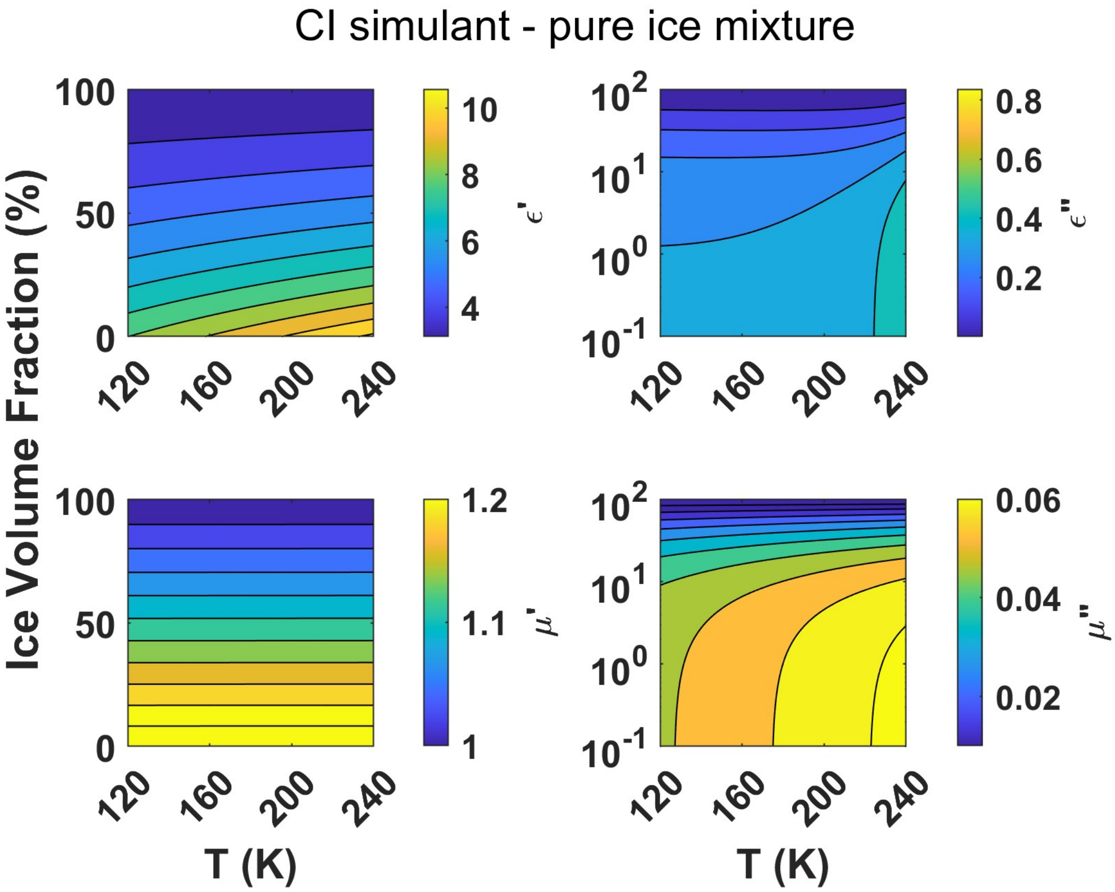

Figure 9.26: Filled contour plot of the EM properties of the mixture of CI simulant and pure ice at 60 MHz, in the temperature range 120-210 K and as a function of ice volume fraction.

One of the goal of this work is to evaluate the performance of the planetary radar sounder that in the future will investigate the Jovian icy moons, i.e. RIME and REASON, and the asteroids, i.e. JuRa on board the HERA mission. The two-way radar signal attenuation can be expressed as:

$$A = e^{\frac{2\pi\nu}{c}\Im\{\sqrt{\varepsilon\mu}\}2z} \tag{9.8}$$

where z is the penetration depth. The velocity of the radar signal can be stated as:

$$v = \frac{c}{\Re\{\sqrt{\varepsilon\mu}\}} \tag{9.9}$$

where c is the speed of light in the vacuum.

Given that the magnetic permeability of the meteoritic samples is significant, it is essential to consider magnetic permeability when evaluating the performance of the radar signal [104].

The velocity of radar signal v for L5 chondrite and CI simulant mixtures are shown in Figs. 9.27 and 9.28.

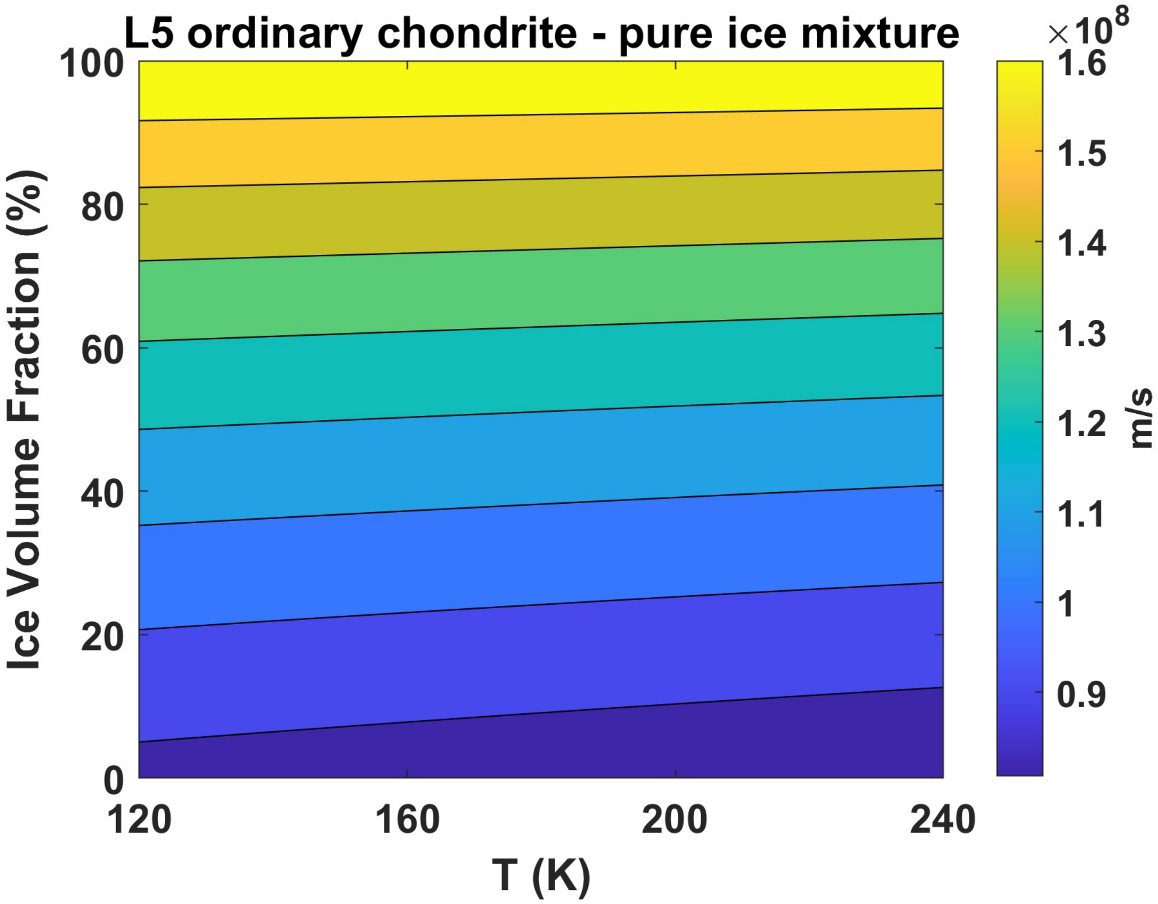

Figure 9.27: Radar signal velocity for mixtures of L5 ordinary chondrite and pure ice as a function of temperature and ice volume fraction and at 60 MHz.

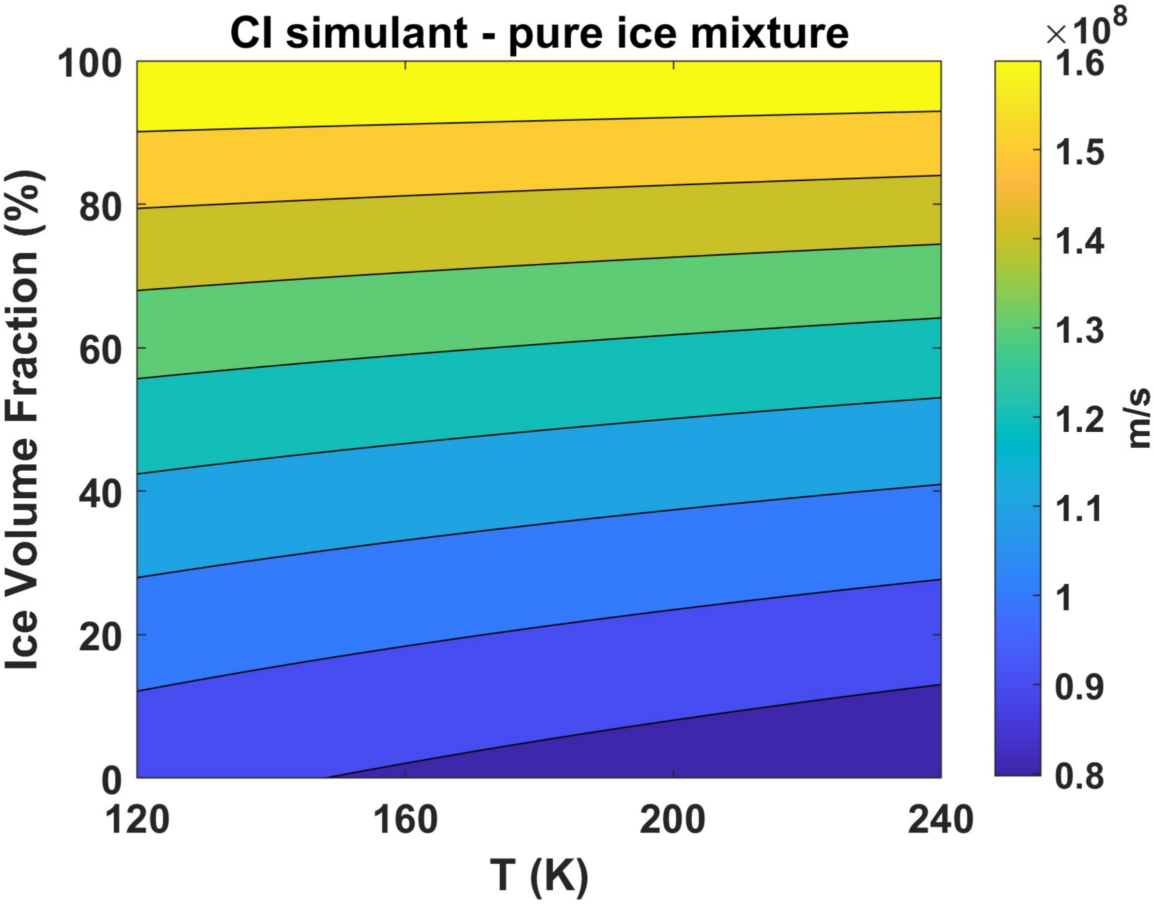

Figure 9.28: Radar signal velocity for mixtures of CI simulant and pure ice as a function of temperature and ice volume fraction and at 60 MHz.

Finally, the attenuations were computed for the meteorite-pure ice mixtures at 9 MHz (see Fig. 9.29) and for meteorite-air mixtures at 60 MHz (see Fig. 9.30) as a function of the dust volume fraction inside the pure dirty ice. It is important to note that it has not been possible to measure the imaginary part of permability of the CI simulant below 60 MHz, and for this reason the relative attenuation below this frequency threshold was not computed taking into account the magnetic permeability. However, as expected, the higher the temperature and the larger the dust inclusions inside the rock-ice and rock-air mixtures, the higher the attenuation. These maps could give useful indications for the performance of the radar sounders that will work in the framework of the oncoming space missions for the study of asteroids and icy moons.

Additionally, a dispersive and attenuating behavior very different from ice dielectric features was noted for the ice saturated CI sample at temperatures exceeding 210 K due to presence of smectite in large quantities inside the sample; therefore, it is not possible to accurately model the CI dielectric permittivity as a function of the ice volume fraction above 210 K, since the common mixing laws used in this work do not work accurately with clay materials [85].

In conclusion, while laboratory data remain essential for understanding the electromagnetic behavior of planetary materials, mixing formulas play a significant role in predicting the behavior of composite materials. Although these equations are widely applied in Earth sciences, a systematic validation of their applicability to planetary materials is still lacking. In this study, the results obtained from dielectric and magnetic measurements performed on planetary simulants at low temperatures were compared with those derived from commonly used mixing formulas. It was found out that only specific models—varying for each simulant—accurately reproduce the electromagnetic behavior of dry granular materials and grain-ice mixtures. Caution is warranted when applying these models to planetary materials with high clay content, as the results of this work demonstrate that their low-temperature electromagnetic behavior, within the frequency range of radar sounders onboard space missions, may significantly deviate from model predictions.

Future work will implement new measurements and parametric EM models for dirty-saline ice doped with different chemical species in order to reproduce the complex behavior observed with near-infrared observation of the surface of the icy moons.

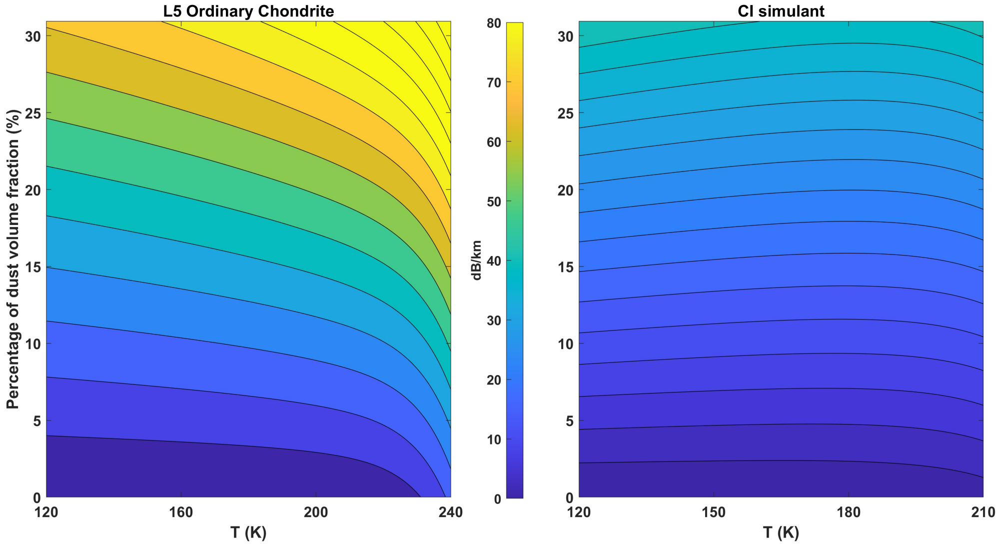

Figure 9.29: Attenuation map at 9 MHz, estimated starting from synthetic permittivity and permeability data of the CI simulant-pure ice mixture and L5 ordinary chondrite-pure ice mixture. The attenuation is expressed in decibel unit per kilometer.

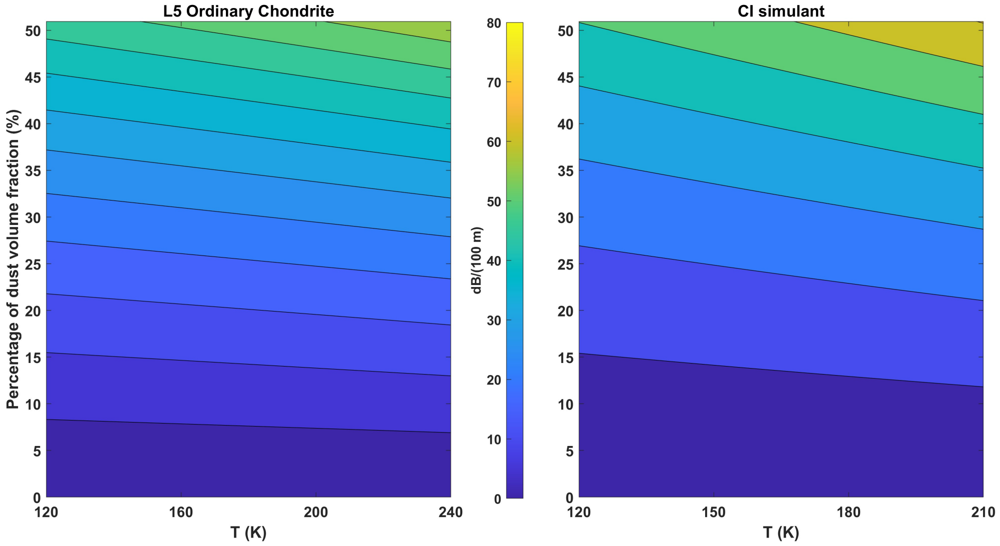

Figure 9.30: Attenuation map at 60 MHz, estimated starting from synthetic permittivity and permeability data of the two meteorite samples as a function of their air volume fraction. The attenuation is expressed in decibel unit per 100 meters.

Chapter 10

Electromagnetic Characterization of NaCl Doped Ice for the Europa Icy Crust

Europa is the most compelling target of the Juice and Europa Clipper missions in terms of the search for extra-terrestrial life: in fact, its vast subsurface ocean resting directly on the rocky mantle that diffuses heat through radiogenic heating could be the source of energy for possible simple cell life forms, and, last but not least, the subsurface ocean is the closest to the surface than the other two icy satellites, which makes it easier to detect by the radar sounders RIME and REASON. The two radars have been designed for the detection of the ocean beneath the ice crust and the possible upwelling of liquid material at shallow depths. Therefore, a comprehensive laboratory investigation is necessary to conduct dielectric characterization of ices similar to those hypothesized to exist within Europa's crust. This is essential for assessing radar signal attenuation, penetration depth, and the potentially detectable dielectric contrasts between ice and brine pockets and channels.

As detailed in subsection 1.1.1 and Tab. 1.2, impurities in the ice present over Europa can be generated by exogenous or endogenous phenomena; recent ground-based and space-based infrared observations pointed out that more pristine endogenous material may reflect a chloride-dominated composition [27]. Moreover, sodium chloride has been observed on the surface of the moon in chaos terrain regions, suggesting an interior source [30], [33].

For this reason, in this chapter the electrical properties of ice doped with NaCl have been studied as a function of the temperature and the salt concentration by means the VNA experimental setup. Additional measurements using liquid nitrogen and the experimental setup of the LCR meter were performed, so as to extend the temperature range at which to estimate the electrical proprieties of doped ice. Finally, a modeling of the real part of permittivity and conductivity of ice and brines at 9 MHz and 60 MHz has been carried out as a function of temperature and sodium chloride concentration.

10.1 Experimental Setup and Procedure

The NaCl solutions were prepared as described in subsection 8.2.2 and then poured directly in the measuring cell. At this point the conductivity of the NaCl liquid solution was measured by a conductivity meter GLP-31 (see Tab. 8.4). A first check on the goodness of the solution was performed by applying the Debye-Huckel-Onsager equation that allow to compute the theoretical conductivity for electrolite solutions up to 100 mM of salt concentration [225]:

$$\Lambda = \Lambda^{\circ} - (A + B\Lambda^{\circ})\, c^{1/2} \tag{10.1}$$

where c is the salt concentration, $A = 60.20$, $B = 0.229$ and for sodium chloride $\Lambda^{\circ} = 126.39$ at 25°C. The equation is valid for very dilute solutions. The theoretical values of conductivity obtained by solving eq. 10.1 were compared with the experimental values measured by the conductivity meter before each measurement for NaCl concentration up to 100 mM: in case the theoretical and experimental values did

not agree, the solution was prepared again.
The NaCl doped ice samples were then formed directly inside the cell using the freezing procedure discussed in 8.2.3: the ultrafreezer was employed for the measurements performed with the coaxial probe and the VNA setup, similarly to the measurements of dirty ice; while the climatic chamber was employed to freeze the solution inside the capacitive cell of the LCR setup, by means of a fast rate freezing cycle (2 K/min down to 200 K). Therefore, all ice samples measured in this chapter were formed with fast temperature cycles (see section 6.5).
It has been indicated that the moons' ice shells might display a chemically stratified structure, influenced by the thermal gradient during their formation. This stratification is marked by higher salt concentrations at the surface, corresponding to a steeper temperature gradient, and a gradual decline in impurity levels as one approaches the ice/ocean interface, where the temperature gradient becomes less intense [15]. Therefore, the type of ice studied in this dissertation is intended to be similar to that speculated to be at the surface and in the first kilometers of the crust of the icy satellites.
The list of all measurements carried out is given in Table 8.4.

10.1.1 Brine Volume Fraction Estimation

Above the eutectic temperature $T_e = 252\ K$, the NaCl doped ice is characterized by the appearance of brines pockets and channels within the ice matrix; these features increase until the total melting of the ice at about $273\ K$.
The brine volume fraction f_b has been estimated in this work generalizing the formula described in [185]; in particular, it was obtained by fixing the masses inside the measuring cell in different temperature intervals

$$T > 273.15\ K \rightarrow m_0 = m_l \tag{10.2}$$

$$T_e < T < 273.15\,K \rightarrow m_l = m_0 - m_i \tag{10.3}$$

i.e., above the freezing temperature the initial mass m_0 inside the measuring cell is equal to the mass of liquid solution m_l; otherwise, for temperatures between the freezing and eutectic points the mass of liquid solution is equal to the initial mass minus the mass of the ice m_i forming inside the cell. The brine volume V_b in the range of temperatures between the eutectic one and the freezing one is given by the sum of the volume of the salt V_s and that of the liquid V_l:

$$V_b = V_s + V_l = \frac{m_s}{\rho_s} + \frac{m_l}{\rho_l} = \frac{m_s + m_l}{\rho_b} \tag{10.4}$$

where ρ_s, ρ_l and ρ_b are respectively the density of salt, liquid and brines, m_s is the mass of the salt of the solution and m_l is the liquid mass defined in Eq. 10.3. The total volume V_{tot} of the samples is then given by:

$$V_{tot} = V_s + V_l + V_i = V_b + V_i = \frac{m_s + m_l}{\rho_b} + \frac{m_i}{\rho_i} = \frac{m_s + m_l}{\rho_b} + \frac{m_0 - m_l}{\rho_i} \tag{10.5}$$

The the equilibrium NaCl concentration C_{eq} and the initial NaCl concentration dissolved in the solution C_0 can defined respectively as:

$$C_{eq} = \frac{m_s}{m_s + m_l} \tag{10.6}$$

$$C_{in} = \frac{m_s + m_0}{m_l} \tag{10.7}$$

Manipulating the expression of the brine volume fraction, the following formula is obtained:

$$f_b(T_e < T < 273.15) = \frac{V_b}{V_{tot}} = \frac{(C_{eq}\rho_b)^{-1}}{(C_{eq}\rho_b)^{-1} - (C_{eq}\rho_i)^{-1} + (C_{in}\rho_i)^{-1}} \tag{10.8}$$

where C_{eq}, the equilibrium NaCl concentration as a function of temperature, can be inferred by the sodium chloride phase diagram (see Fig. 4.12). C_{eq} as function of temperature has been retrieved interpolating the phase diagram.
The formula in [185] is a limit of the equation 10.8, assuming that $\rho_i \simeq 1$ and $\rho_b = 1$, and thus obtaining

$f_b \simeq \frac{C_{in}}{C_{eq}}$. In this work, on the other hand, it was assumed that $\rho_i = 0.92$ and $\rho_b = 1.0008 * S_b$, where S_b is the brines salinity, as explained in [226].
Eq. 10.8 returns values slightly different from those predicted by the eq. 4.19 derived in [176] from experimental data of sea ice, due to the difference in electrical behavior between laboratory NaCl doped ice and natural sea ice.

The brine volume fraction depends on the temperature of the sample and its sodium chloride concentration. In Fig. 10.1 the brine volume fraction retrieved with Eq. 10.8 is shown as a function of temperature, and, as expected, the lower the initial concentration of sodium chloride the less will be the brines content within the frozen sample as a function of temperature (e.g., the 10 mM doped ice sample has a brine volume fraction consistently below 1% throughout the temperature range).

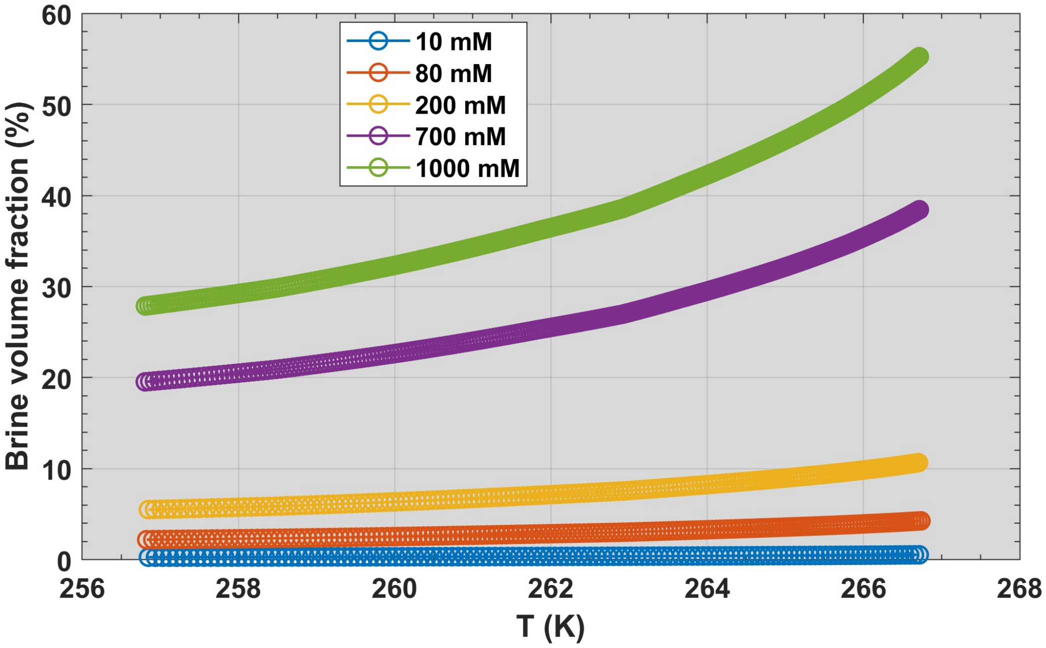

Figure 10.1: Brine volume fraction obtained through Eq. 10.8versus temperature for five doped ice samples, with sodium chloride concentration ranging from 10 mM to 1000 mM.

10.2 Measurements of NaCl Doped Ice Samples

During the measurement the ice sample experiences two phase transitions: one at 252 K, when pockets of liquid brine begin to appear within it, and at 273 K, when the sample totally melts.
Measurement of the real part of the permittivity was then used to verify the state of the sample; in Figure 10.2 three stages of measurement are shown: a) *ice region*, where the sample is completely frozen; b) *brines region*, where brines appear in the sample at different brine volume fractions $f_b(T)$; c) *liquid region*, where the sample is completely melt; d) *transition region* (TR) where the sample experiences the phase transition. The transition region data were not considered in the analysis of this work. In all measurements no brines were observed below 249 K, unlike the sea ice samples studied in [178], this difference is probably due to the way sea ice is formed in nature.

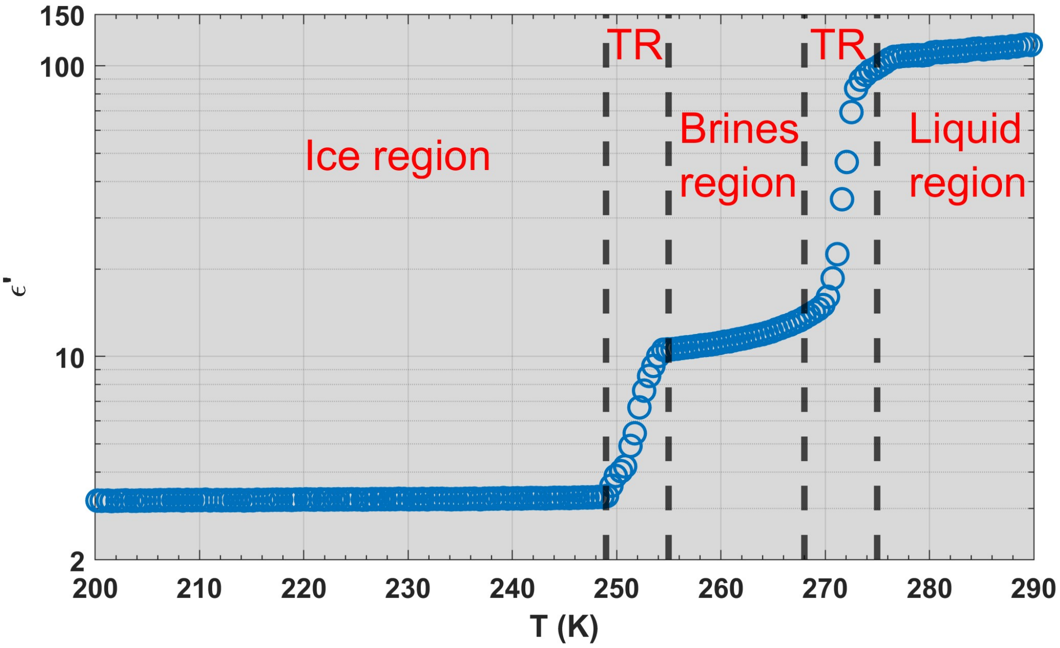

Figure 10.2: 200 mM NaCl doped ice transition phases identified in the measurement of the real part of the permittivity: 200 K-249 K, ice region; 249 K-255 K, first transition region; 255 K-268 K, brines region; 268 K-274 K, second transition region; 274 K-290 K, liquid region.

This work focused on the analysis of doped ice measurements made by VNA; measurements were then made with the LCR meter and liquid nitrogen to extend the temperature range at which to estimate the electrical properties of ice.

10.2.1 Ice Region

In this subsection the electrical properties of the samples in the ice region are reported as a function of the frequency and temperature.

ε vs ν

Figures 10.3-10.4 show the frequency spectra of electrical properties (ε', ε'' and σ) at a fixed temperature and different NaCl concentrations, obtained by means of the VNA and LCR meter setup, (20, 50, 200, 500 and 1000 mM for VNA, 20 and 200 mM for LCR meter, respectively). Gray areas in Fig. 10.3 at lower frequencies indicate unreliable values because of the VNA instrumental limit, since ices have very low dielectric losses not always measurable by the instrument. An air measurement was also reported as a reference measurement to identify the instrumental and NRW algorithm limit even at high frequencies. The real part of permittivity measured by the VNA in the frequency range 1 MHz-100 MHz is practically constant in the entire interval, and it is scattered below 6 MHz. The imaginary part of permittivity, on the other hand, constantly decreases up to 100 MHz; moreover it is important to note that the conductivity is fairly constant between 1 MHz and 10 MHz, and then increases at higher frequencies. The behavior of conductivity at higher frequencies is similar to those measured for sea ice in [178]. In any case, the real part of permittivity values rise as the sodium chloride concentration increases, whereas ice samples doped with 200, 500 and 1000 mM exhibit similar values of ε'' and σ. This is due to the presence of hydrate salts in the ice matrix and to the chloride substitution caused by the NaCl doping. Going to lower temperatures, it was observed that the 60 MHz data, of interest to the REASON radar, is not reliable at 220 K, using the VNA instrumental limits identified in subsection 5.7.3 (see Fig. 10.3).

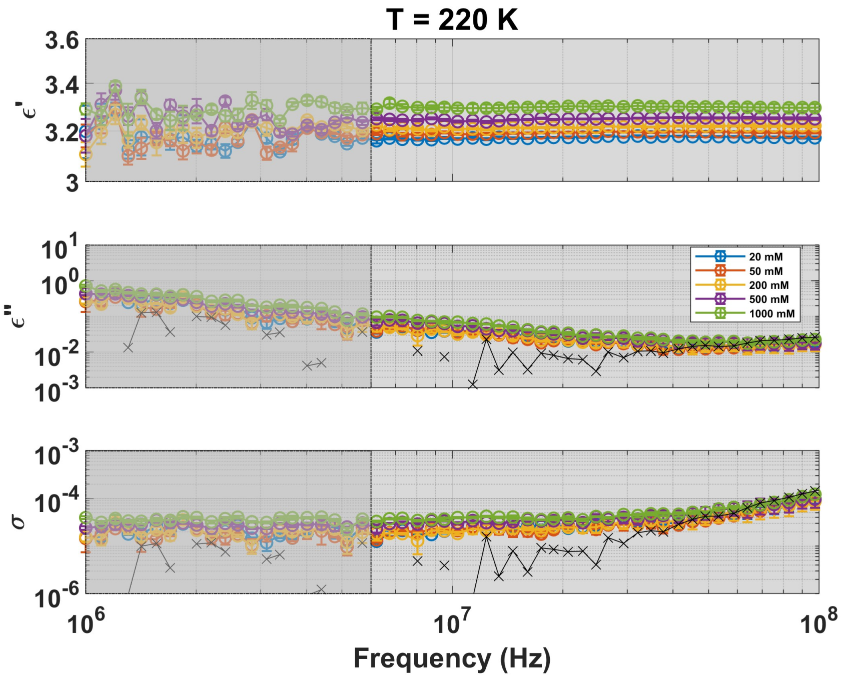

(a) *T = 220 K*

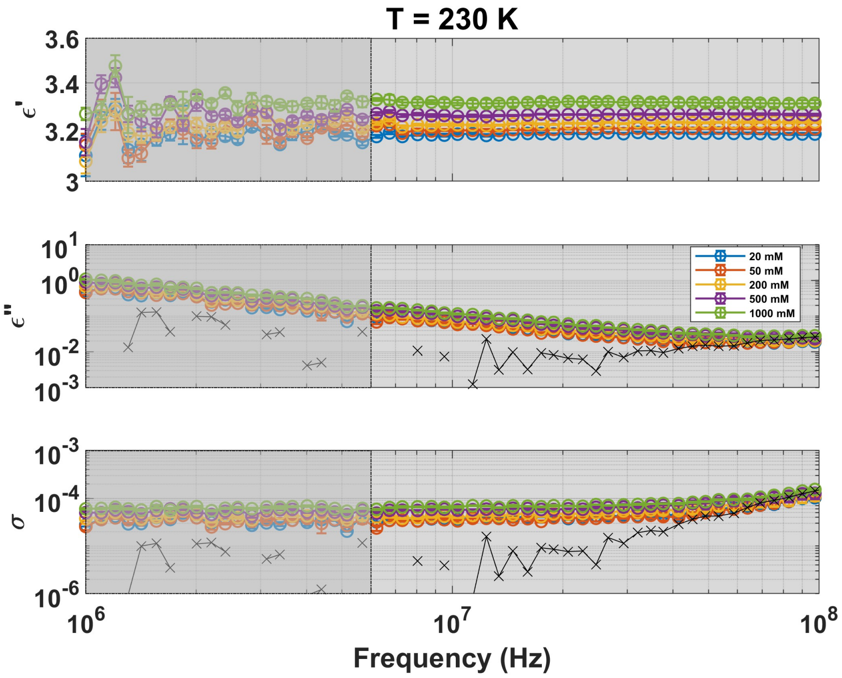

(b) *T = 230 K*

Figure 10.3: Frequency spectra of NaCl doped ice samples at two fixed temperatures in the ice region. The measurements were carried out by a VNA. The black line represents the air measurement, employed as a reference value for the instrumental limit. In contrast to the measurement at 230 K, at 60 MHz the measurement at 220 K is overlapped with the air values.

Frequency spectra measured by the LCR meter, on the other hand, exhibit clearly the ice relaxation, with the inflection point of the real part and the maximum of imaginary part that shift at higher frequencies as the sodium chloride concentration increases. Moreover, it is interesting to note that at lower frequencies, the highest values of complex permittivity are those of the lower concentration samples, probably due to the appearance of an additional relaxation at hundreds of Hz in these samples caused by the preparation of the sample with a high thermal gradient. The 200 mM measurement approaching 1 MHz exhibits higher values of conductivity than the 20 mM, as expected.

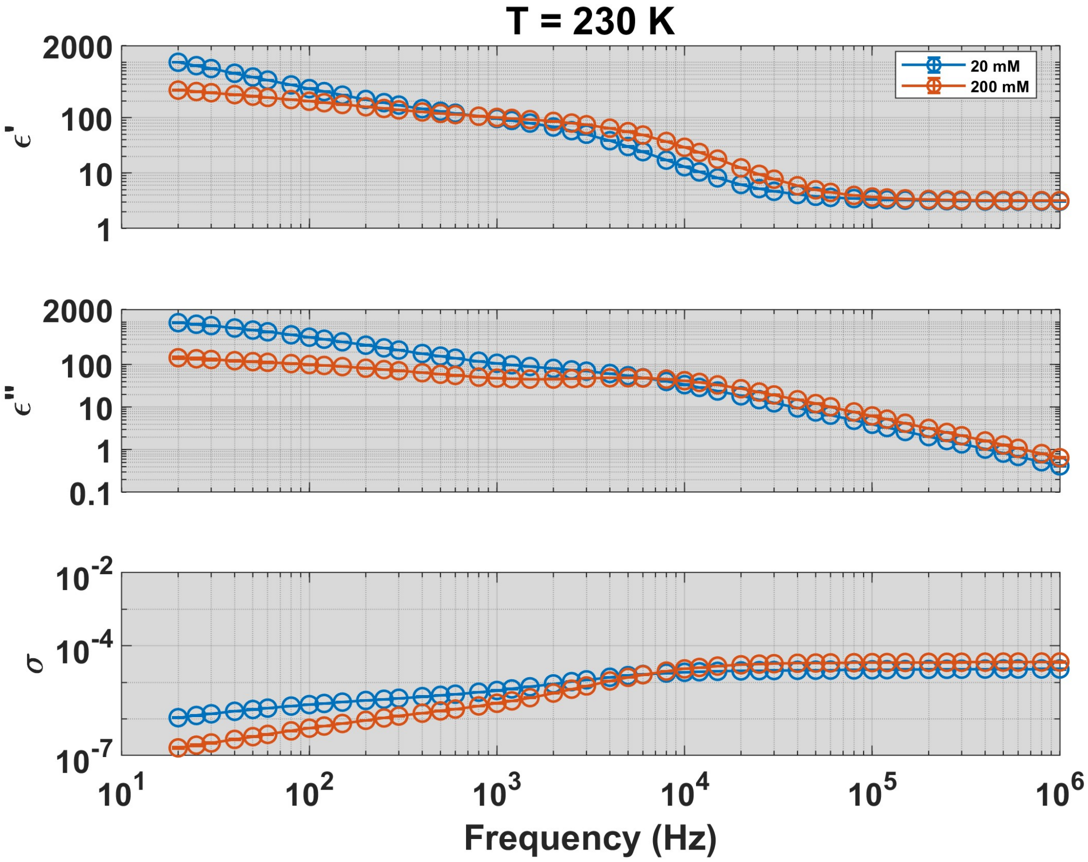

Figure 10.4: Frequency spectra of NaCl doped ice samples at a fixed temperature in the ice region. The measurements were carried out by a LCR meter.

The frequency spectra in the frequency range 20 Hz-100 MHz, obtained by combining the measurements made by the LCR meter and VNA, are illustrated in Fig. 10.5. The two measurements are in good agreement at 1 MHz: this implies that the formation of ice samples in the two cases, although occurring in different cells and by means of different instruments, is comparable. Furthermore, the conductivity is found to be constant from 100 kHz to 10 MHz.

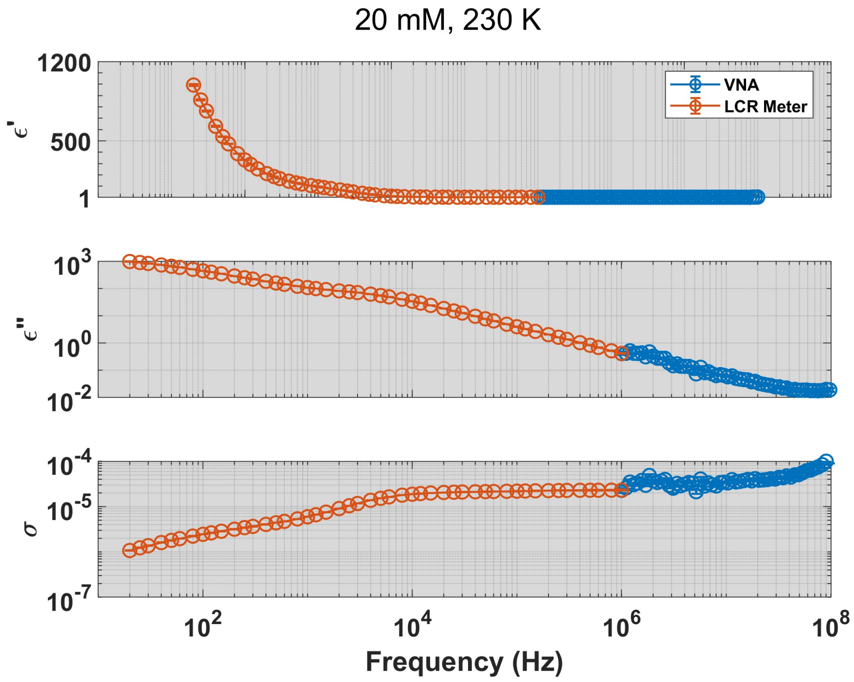

(a) *20 mM*

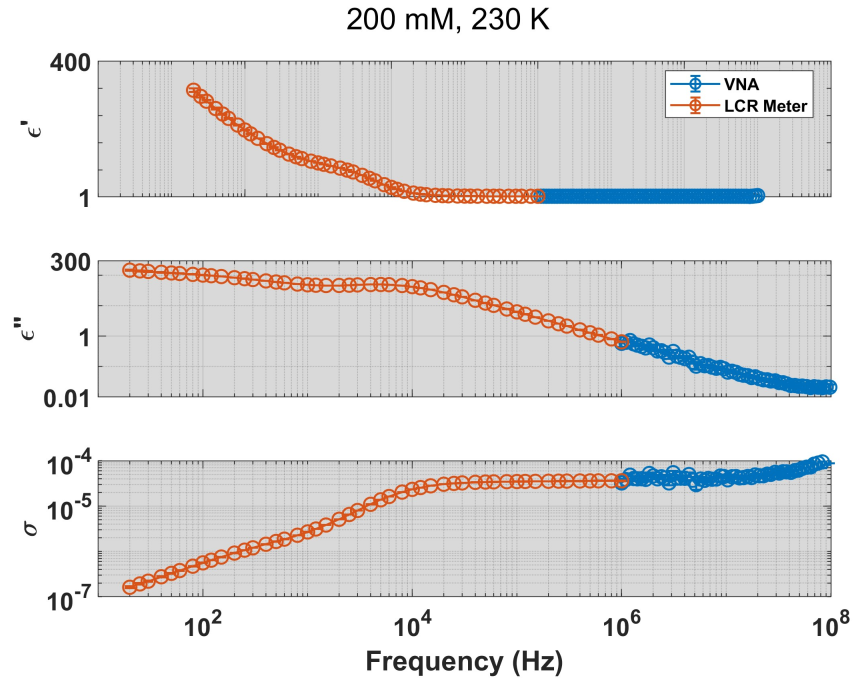

(b) *200 mM*

Figure 10.5: Electrical properties in the frequency range 20 Hz-100 MHz, obtained by combining measurements performed with the LCR meter and the VNA of samples doped at the same sodium chloride concentration.

ε vs T

The electrical properties at 9 MHz of five different NaCl doped ice samples as a function of temperature are reported in Fig. 10.6. The real part of permittivity has a linear dependence on temperature and its values increase as the concentration of sodium chloride in the sample; the imaginary part and the conductivity also have a dependence on temperature and sodium chloride concentration. It is important to note that below 210 K the imaginary part of permittivity and conductivity are not reliable because of 9 MHz VNA instrumental limit identified at the conductivity value of $\sigma_{9\,MHz}^{VNA} = 1.3\times10^{-5}\ S/m$ (see section 5.7). Figure 10.7 shows the dependence on temperature of the data at 60 MHz: the electrical properties at 60 MHz behave in temperature in a similar way to those at 9 MHz. As discussed in subsection 10.2.1, in this case below 225 K the imaginary part and conductivity are below the 60 MHz VNA instrumental limit identified at the conductivity value of $\sigma_{60\,MHz}^{VNA} = 4.2\times10^{-5}\ S/m$ (see section 5.7). For this reason in the following, the VNA data at 9 MHz and 60 MHz will be studied respectively in the temperature range 210 K - 249 K and 225 K - 249 K.

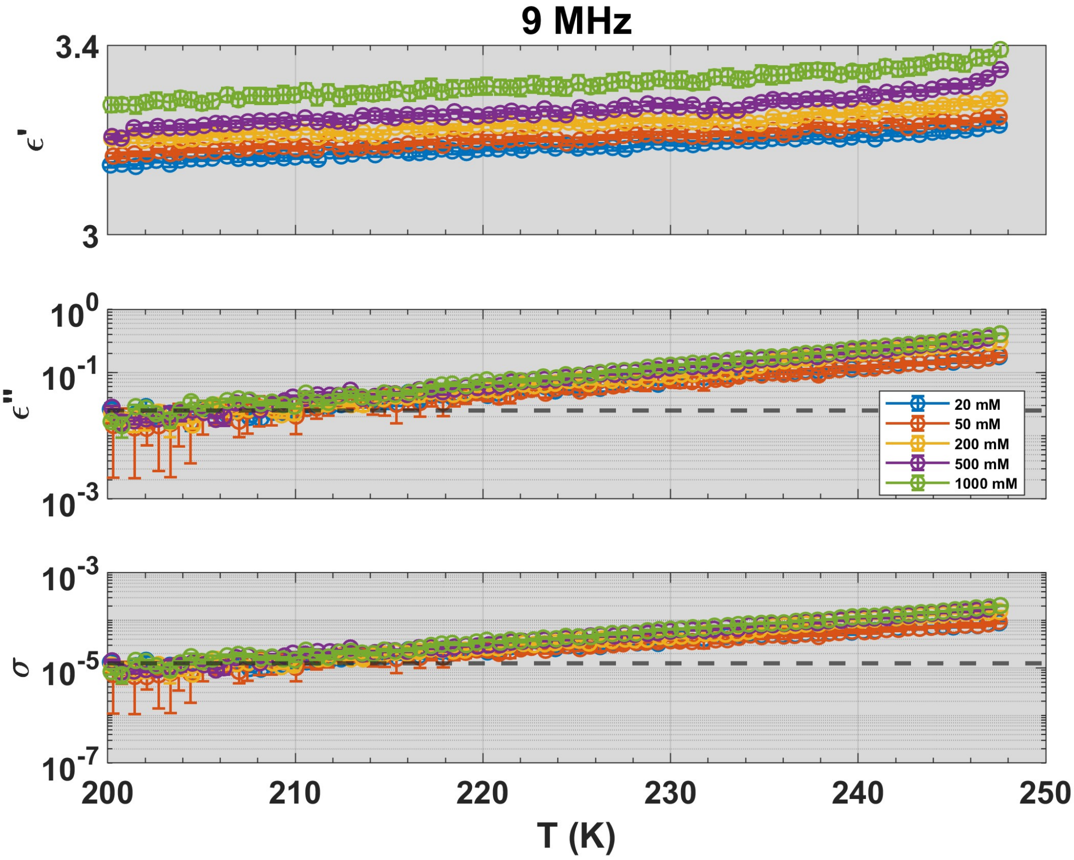

Figure 10.6: Electrical properties at 9 MHz of three different NaCl doped ice samples as a function of temperature in the ice region. The gray dashed line represents the VNA instrumental limit for the imaginary part of permittivity and conductivity.

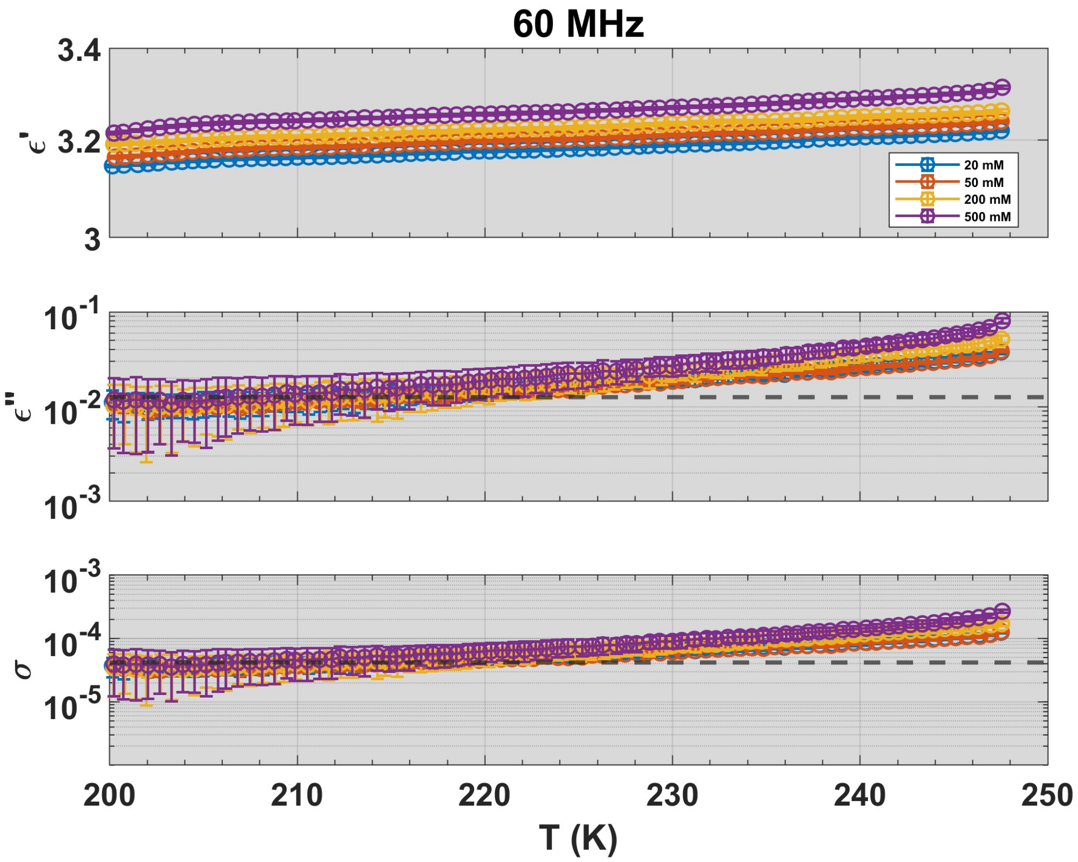

Figure 10.7: Electrical properties at 60 MHz of three different NaCl doped ice samples as a function of temperature in the ice region.

10.2.2 Brines Region

In this subsection the electrical properties of the samples in the brines region are reported as a function of the frequency and temperature. Only the dataset from VNA measurements was used to study the electrical properties of ice in the brines region. Measurements of ice samples doped at concentrations above 500 mM were not reported, because VNA was unable to estimate accurately the real part of permittivity in the entire range of frequencies, due to the appearance of additional polarization phenomena caused by the geometry of the brines pockets within the samples.

ε vs ν

Figure 10.8 shows the electrical properties as a function of frequency of several doped ice samples in the brines region. The values of complex permittivity and conductivity are appreciably higher than the ice region measurements, since the frequency spectra are dominated by conductive saline water behavior, especially at high NaCl concentrations. On the other hand, for low NaCl concentrations (e.g., 20 mM and 50 mM) the dielectric behavior has features of both ice and saline water: for example, the conductivity at high frequencies increases as in the ice region.
However, as expected, the higher the ε and σ values, since the brine volume fraction is also dependent on salt concentration.

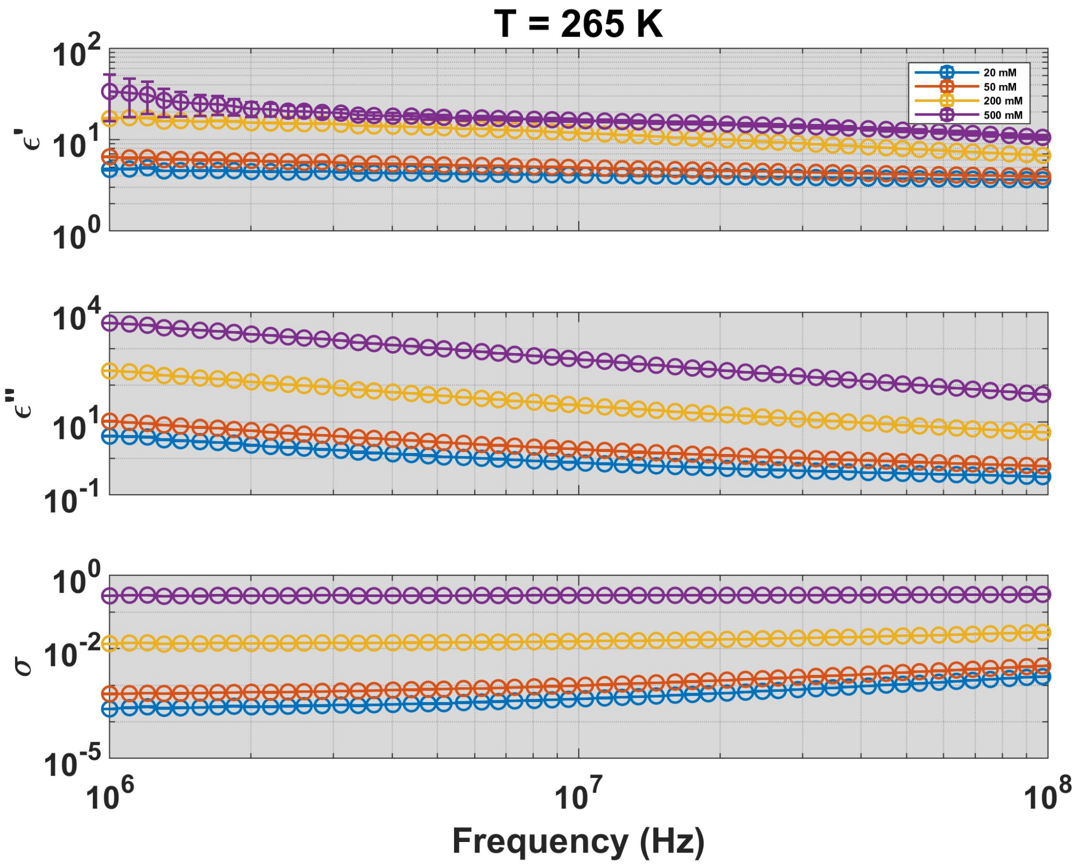

Figure 10.8: Frequency spectra of NaCl doped ice samples at a fixed temperature in the brines region. The measurements were carried out by a VNA.

ε vs T

The electrical properties versus temperature in the brines region are shown in Figures 10.9-10.10. Both complex permittivity and conductivity increase with temperature, as the brine volume fraction itself also increases within the samples. In particular the real part of permittivity values slowly grow as a function of temperature. This trend is particularly appreciable for samples doped with the highest concentrations of sodium chloride.

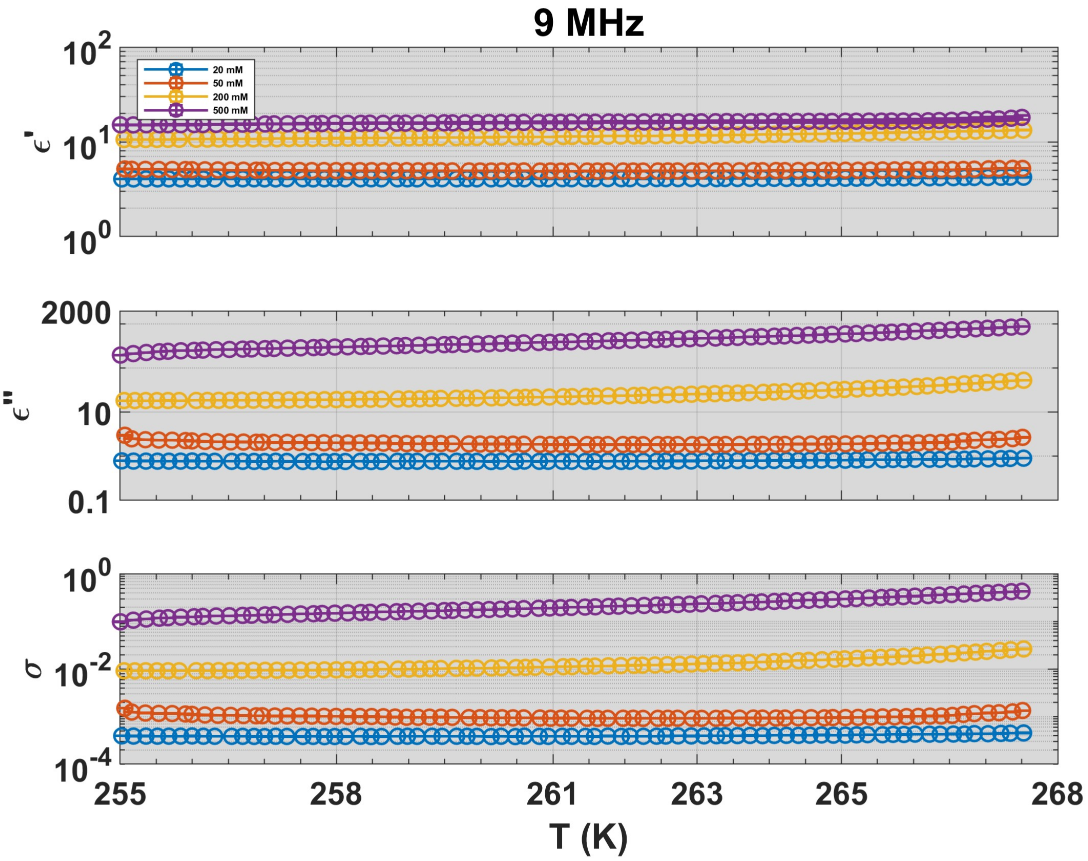

Figure 10.9: Electrical properties at 9 MHz of four different NaCl doped ice samples as a function of temperature in the brines region.

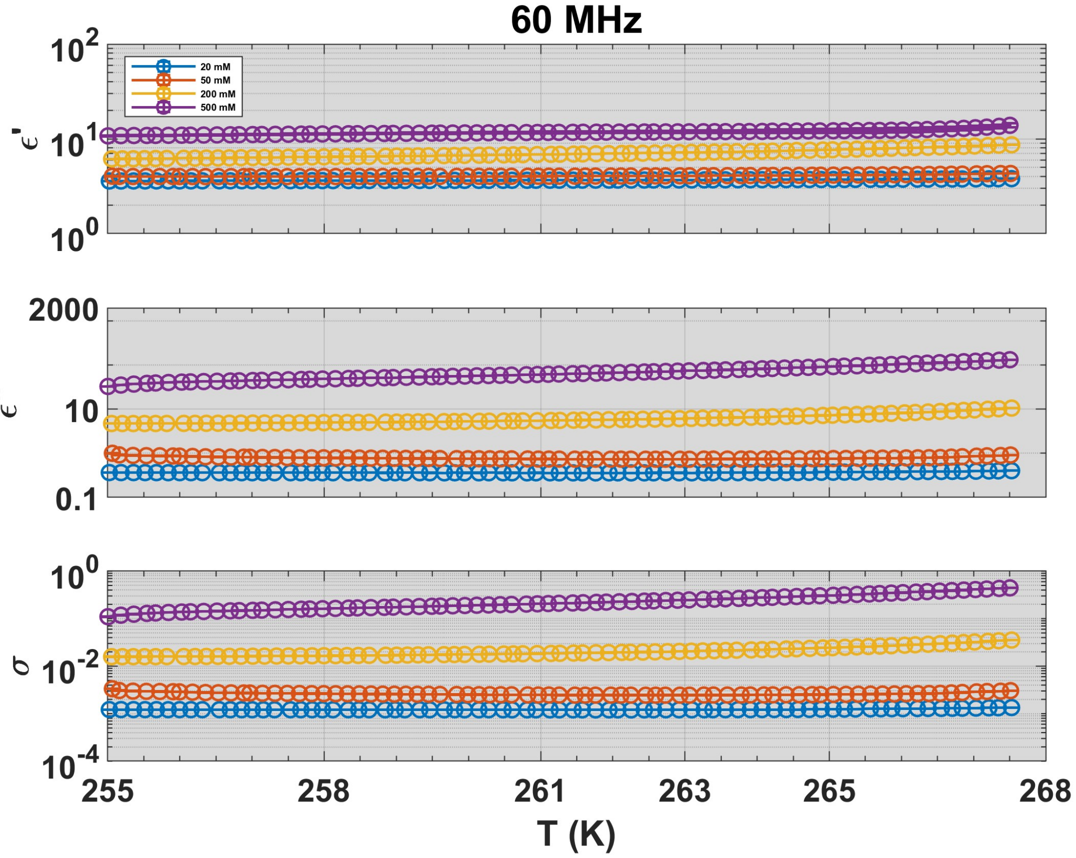

Figure 10.10: Electrical properties at 60 MHz of four different NaCl doped ice samples as a function of temperature in the brines region.

10.3 Extrapolation of Ice Electrical Properties to Lower Temperatures

The VNA experimental setup allowed measurements at 9 MHz only down to 210 K: for this reason, as in the case of dirty ice detailed in the previous chapter, measurements with LCR meter setup and liquid nitrogen were carried out in order to extrapolate the electrical properties at 9 MHz down in temperature. Figure 10.11 reports the electrical properties of two 200 mM doped ice samples measured with the LCR meter and the VNA. The conductivity measured by the LCR meter is reported at 200 kHz, since the conductivity measured by the LCR meter at 1 MHz is affected by excessive noise and, as shown in subsection 10.2.1, this parameter is constant in the frequency range 100 kHz-10 MHz. The LCR meter measurement was reported only down to 160 K, because below that temperature the instrument cannot measure accurately. Nevertheless, the two measurements are in good agreement.

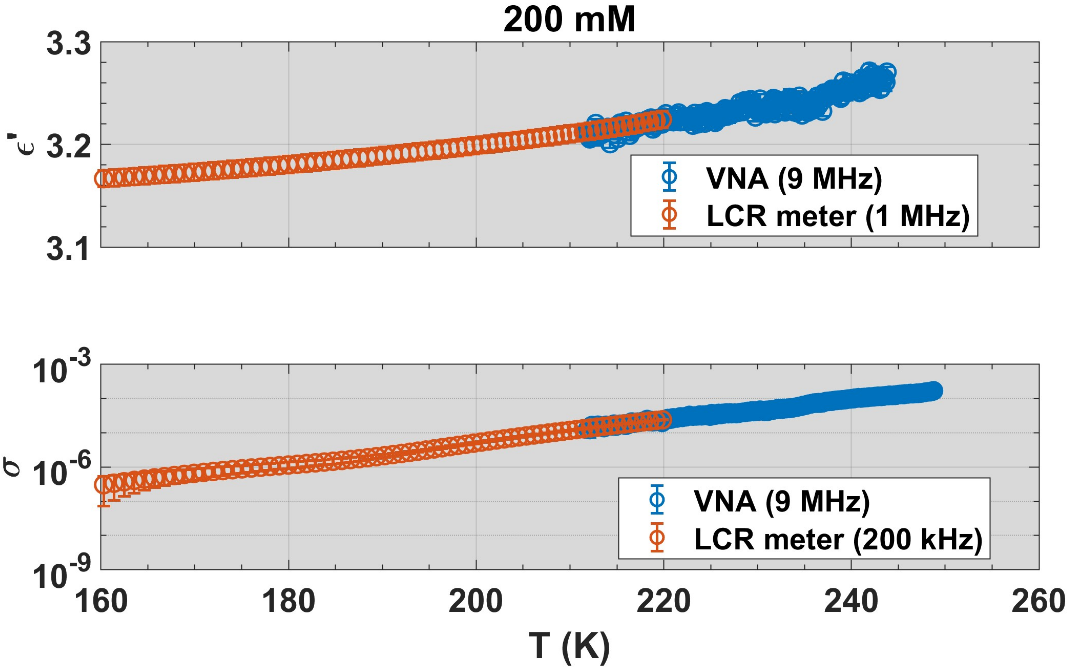

Figure 10.11: Extrapolation of electrical properties of 200 mM doped ice sample down to 160 K.

10.4 Discussion and Conclusion

All fits carried out in this section were performed following the grid mode procedure outlined in section 7.3.

10.4.1 Ice Region

The electrical properties in the ice region were modeled as a function of the sodium chloride concentration and temperature, using the set of measurements carried out with the VNA. The LCR measurements were employed to extrapolate the electrical properties down in temperature.

ε', σ vs NaCl concentration

The VNA measurements were used to model the trend of the electrical properties as a function of the NaCl concentration at a fixed temperature.

Fig. 10.12 shows the dependence of the real part of permittivity and conductivity on the sodium chloride concentration at 9 MHz and 60 MHz. It can be noticed that both parameters depend on both concentration and temperature. Specifically, at a given temperature, conductivity values remain constant above the concentration value of $\simeq 200\,mM$.

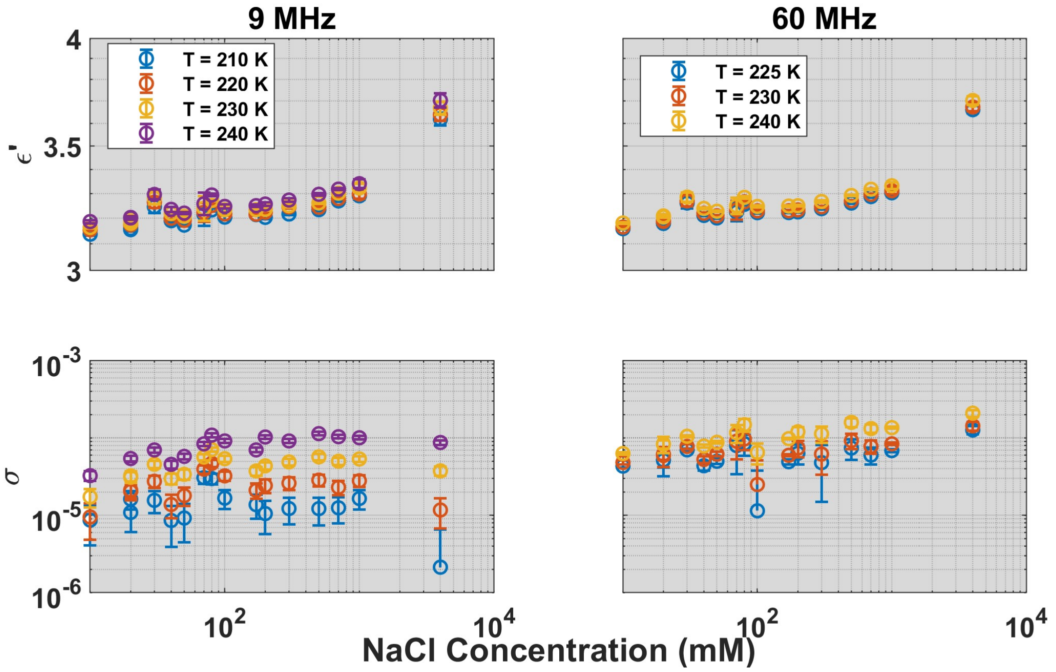

Figure 10.12: Real part of permittivity and conductivity measured by the VNA at 9 MHz and 60 MHz as a function of sodium chloride concentration, at different temperatures, taking into account the VNA instrumental limit at 9 and 60 MHz.

The real part of permittivity as a function of the sodium chloride concentration has been modeled with a power law

$$\varepsilon_0'(conc) = A\,conc^B \tag{10.9}$$

where A and B are parameters estimated through a non-linear fit and *conc* the sodium chloride concentration expressed in mM unit. For both 9 and 60 MHz, the fit parameters estimated at the temperature of 240 K are

$$A = 3.1 \pm 0.1 \tag{10.10}$$

$$B = 0.009 \pm 0.002 \tag{10.11}$$

For the fit of the real part of permittivity versus concentration 30 mM and 80 mM data were considered outliers. The result of the fit of the real part of permittivity at 240 K as a function of NaCl concentration is reported in Figure 10.13 for the two frequencies 9 and 60 MHz. Also the measurement at 4000 mM was not considered for the fit as it behaves as an outlier: for this reason, equation 10.9 can be considered valid in the range 0-1000 mM.

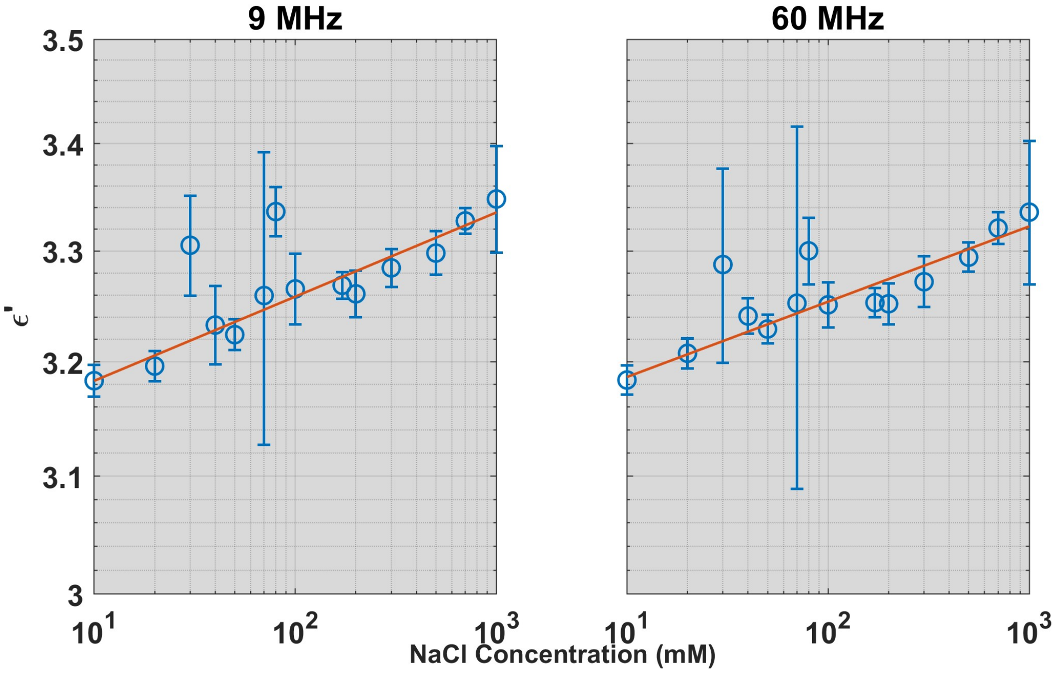

Figure 10.13: Fit of the real part of permittivity as a function of NaCl concentration at 240 K.

The real part of permittivity was fitted as a function of temperature with a Gough-like equation (see eq. 4.10)

$$\varepsilon'(conc,T) = \varepsilon'_0(conc) - C\,T + D\,T^2 \tag{10.12}$$

where $\varepsilon'_0(conc)$ is the value computed with equation 10.9 for a fixed NaCl concentration and C, D are the parameters retrieved through the fit. Equation 10.12 is valid only down to 160 K.
Since the real part has a constant behavior in the range 1 MHz -10 MHz, by combining the measurements performed by the VNA and the LCR meter at 1 MHz at lower temperatures it was possible to estimate the behavior of the real part of permittivity at 9 MHz over a wide range of temperatures: the results of the fit at 9 MHz applied to 200 mM NaCl doped ice measurements are shown in Figure 10.14.

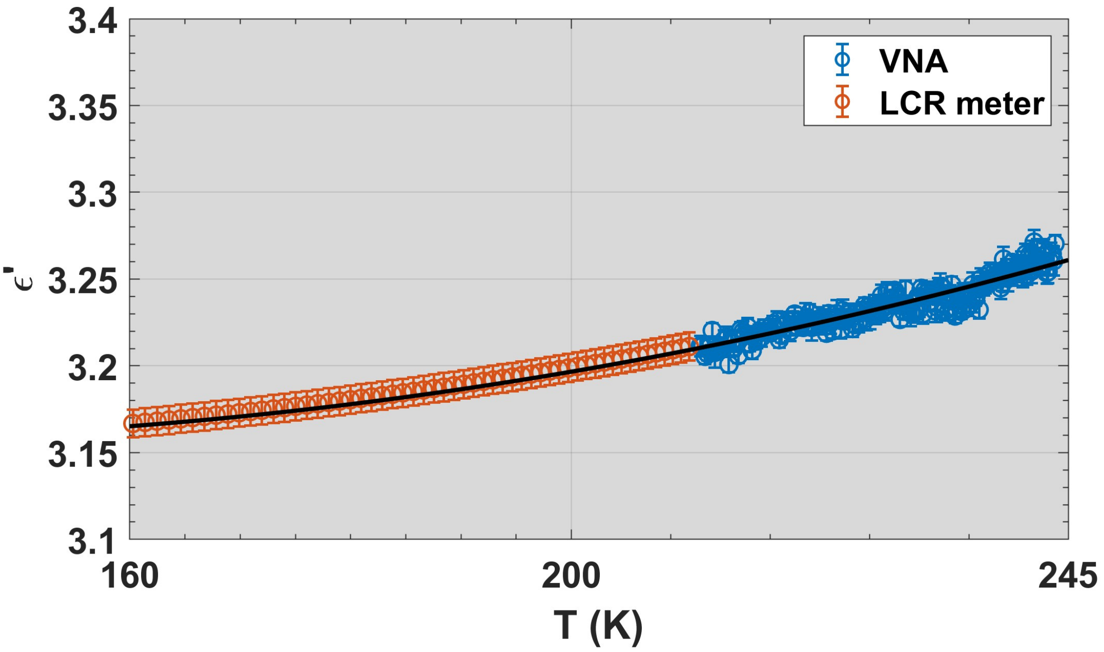

Figure 10.14: Fit of the real part of permittivity as a function of temperature at 9 MHz. The data reported in the figure are the ones of the 200 mM NaCl doped ice samples measured by the VNA and the LCR meter; the solid black line is the fit through eq. 10.12.

For the real part of permittivity at 60 MHz data of the LCR meter at 1 MHz could not be used, and therefore only VNA permittivity data from 225 K to 249 K were employed. The results of both fit procedures at 9 and 60 MHz are reported in Table 10.1.

	9 MHz (160 K- 249 K)	**60 MHz (225 K - 249 K)**
C	$(2.2 \pm 0.5) \times 10^{-3}$	$(1.9 \pm 0.2) \times 10^{-3}$
D	$(7.5 \pm 0.3) \times 10^{-6}$	$(7.0 \pm 0.5) \times 10^{-6}$

Table 10.1: Fit parameters at 9 MHz and 60 MHz for real part of permittivity versus temperature in the ice region.

The conductivity versus concentration, on the other hand, has been modeled with the equation

$$\sigma_0(conc < 200\, mM) = a\, conc^b \tag{10.13}$$

where a, b are the parameters retrieved by the non-linear fit and *conc* is the sodium chloride concentration expressed in mM unit. Above the concentration value of 200 mM the conductivity values saturate, remaining constant up to higher concentrations. The results of the fit of the conductivity at 240 K as a function of NaCl concentration are reported in Figure 10.15 and Table 10.2 for two frequencies, 9 and 60 MHz.

$\sigma_0(conc < 200\, mM)$	**a**	**b**
9 MHz	$(2.0 \pm 0.8) \times 10^{-5}$	0.31 ± 0.06
60 MHz	$(4 \pm 1) \times 10^{-5}$	0.24 ± 0.08

Table 10.2: Fit parameters at 9 MHz and 60 MHz for the conductivity versus concentration retrieved at 240 K.

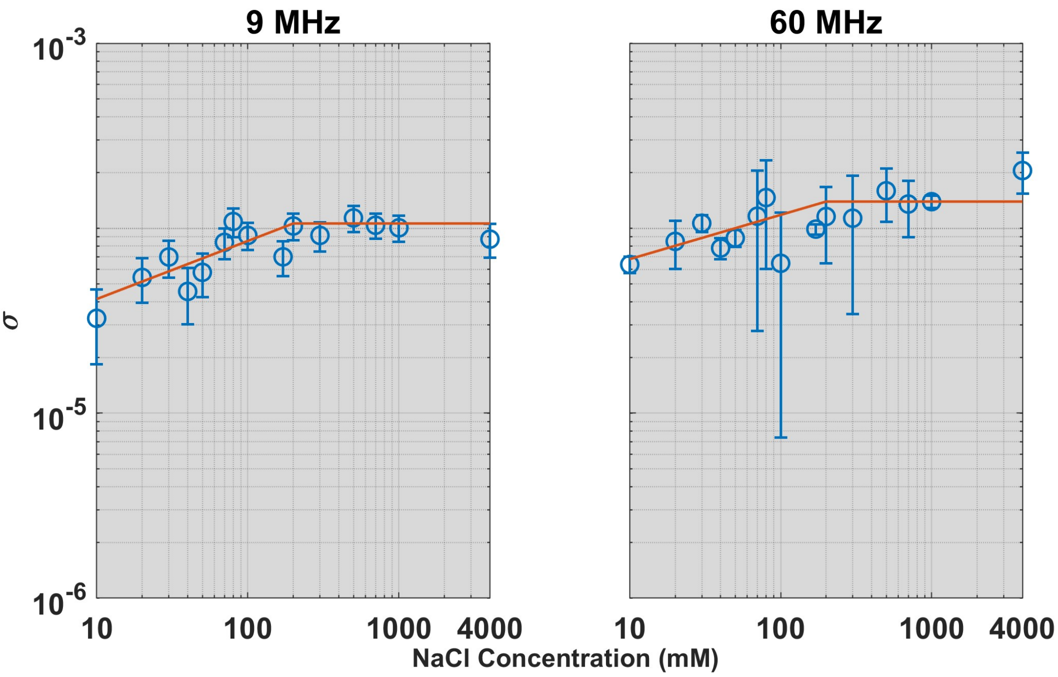

Figure 10.15: Fit of conductivity as a function of NaCl concentration at 240 K.

The trend of conductivity as a function of temperature was estimated by an Arrhenius-like equation (see eq. 2.89)

$$\sigma(conc, T) = \sigma_0(conc)\, e^{-\frac{E_a^\sigma}{k_b}\left(\frac{1}{T}-\frac{1}{T_0}\right)} \tag{10.14}$$

where $\sigma_0(conc)$ is the value computed with equation 10.13, E_a^σ is the conductivity activation energy, k_b is the Boltzmann constant and T_0 is the reference temperature at which $\sigma_0(conc)$ was computed (in this case $T_0 = 240\,K$).

The conductivity activation energy was estimated by fitting the conductivity values of the VNA measurements in the temperature range 230 K- 245 K; Fig. 10.16 shows the activation energy as a function of sodium chloride concentration at 9 and 60 MHz. Data at 60 MHz have a similar trend to those at 9 MHz and at high concentrations have similar values.

Although the data are rather scattered, the activation energy for both frequencies has clearly two populations of data: for example in the case of 9 MHz data, there is one group of data, below 200 mM, with $E_a^\sigma \simeq 0.25$ and another one, above the threshold of 200 mM, with $E_a^\sigma \simeq 0.30$. This behavior of NaCl doped ices was already observed in literature [185], where it has been calculated by means of an interpolation that the relaxation time of ice saturates for initial NaCl concentration of $\simeq 300\,mM$, having an activation energy that slightly increases up to $\simeq 0.29\,eV$.

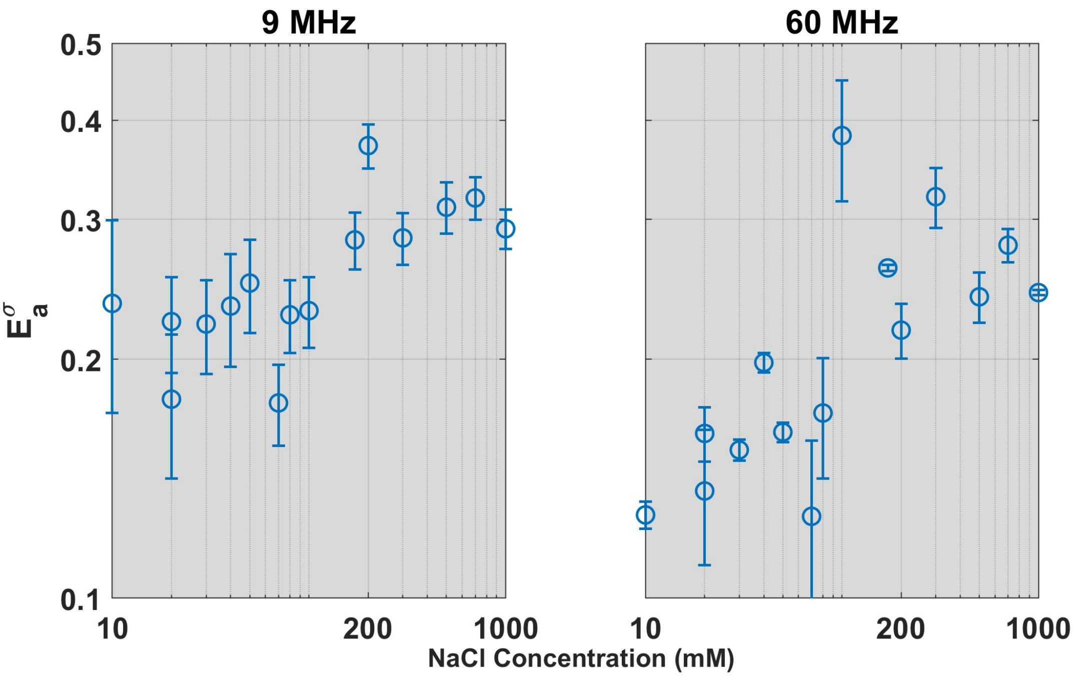

Figure 10.16: Conductivity activation energy as a function of NaCl concentration.

Also in the case of electrical conductivity, data from the LCR meter were used to extend the temperature range in which to fit the data selected at 9 MHz. Nevertheless, it was noted that the comprehensive trend of this parameter is not reproducible with equation 10.14, that is valid only in a limited range of temperatures. In fact, the conductivity versus temperature changes behavior, depending on the concentration of sodium chloride at which the ice was doped. In particular, two changes in conductivity slope were observed in the measurements, due to changes in activation energy. Several equations (such as $\sigma(conc, T) = \sigma_0(conc)\, e^{-\frac{E^{\sigma}_{a}}{k_b}\left(\frac{1}{T}-\frac{1}{T_0}\right)} + \sigma_1 e^{-\frac{E^{\sigma}_{1\,a}}{k_b}\left(\frac{1}{T}-\frac{1}{T_1}\right)} + \sigma_2 e^{-\frac{E^{\sigma}_{2\,a}}{k_b}\left(\frac{1}{T}-\frac{1}{T_2}\right)}$, where $E^{\sigma}_{1\,a}$, $E^{\sigma}_{2\,a}$ are two other activation energies) were tested to fit conductivity as a function of temperature, but they failed.
For this reason, three separate fits with eq. 10.14 were made in three separate temperature ranges: the results of these procedures are shown in the Fig 10.17. Tables 10.3-10.4 report the parameters retrieved by the fitting procedure at 9 MHz for the 20 mM and 200 mM doped ices, respectively. The parameters in the lowest temperature range are associated with relatively large uncertainties, since the measurements at those temperatures are quite affected by noise.

Temperature range	E^{σ}_{a}	σ_0	T_0
$170\,K < T < 186\,K$	0.21 ± 0.08	$(4.6 \pm 0.9) \times 10^{-7}$	175
$186\,K < T < 218\,K$	0.30 ± 0.01	$(1.6 \pm 0.1) \times 10^{-6}$	190
$218\,K < T < 249\,K$	0.223 ± 0.002	$\sigma_0(conc)$	240

Table 10.3: Fit parameters of the conductivity at 9 MHz versus temperature for the 20 mM doped ice.

Temperature range	E^{σ}_{a}	σ_0	T_0
$160\,K < T < 174\,K$	0.17 ± 0.05	$(4.6 \pm 0.8) \times 10^{-7}$	165
$174\,K < T < 186\,K$	0.15 ± 0.02	$(1.2 \pm 0.1) \times 10^{-6}$	180
$186\,K < T < 249\,K$	0.302 ± 0.001	$\sigma_0(conc)$	240

Table 10.4: Fit parameters of the conductivity at 9 MHz versus temperature for the 200 mM doped ice.

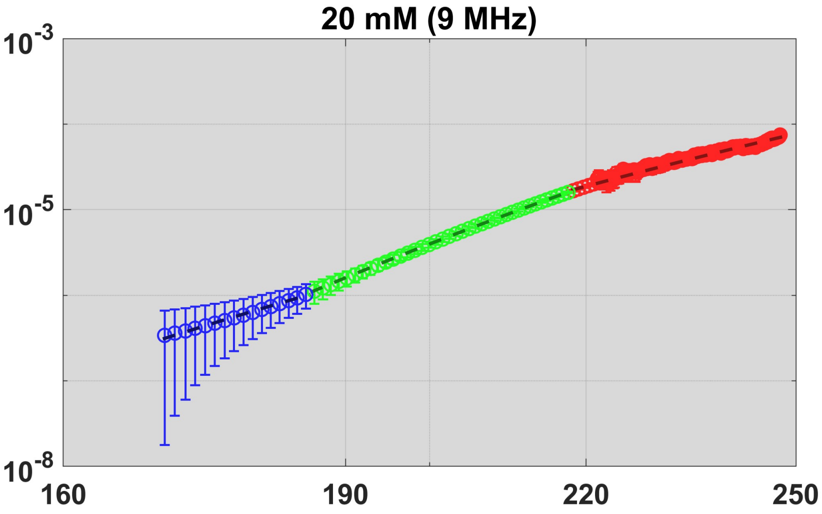

(a) *20 mM*

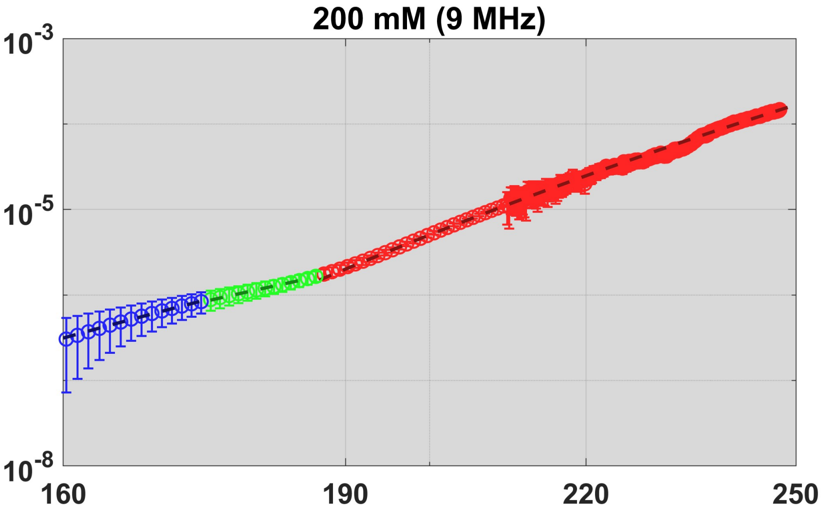

(b) *200 mM*

Figure 10.17: Fit of the conductivity of the 20 mM and 200 mM doped ices at 9 MHz versus temperature. The 20 mM doped ice conductivity was reported only down to 170 K since below this temperature the LCR meter is no longer able to measure accurately this parameter.

The 9 MHz conductivity as a function of temperature has two changes in slope at two different temperatures: one at higher temperatures (218 K and 186 K, respectively for the 20 mM and 200 mM samples) and the other one at lower temperature (186 K and 174 K, respectively for the 20 mM and 200 mM samples). The conductivity at 9 MHz can be treated as the high-frequency conductivity σ_∞. A crossover can explained by the increasing relative abundance of ionic defects, when L defects become the minority carrier carrier and H_3O^+ become the majority charge carrier, since NaCl solutions are suggested to contribute H_3O^+ and Cl^- to the ice [185]. Moreover, it was demonstrated that the high temperature crossover depends on the ice sample preparation: for example, pure ice samples prepared with stirring at water freezing, avoiding rapid ice crystallization, did not exhibit the high temperature crossover [172], [227].

The two temperatures differ between the 200 mM sample and the 20 mM sample, probably due to the influence of an additional relaxation in the 20 mM measurement at low frequencies (hundreds of Hz), already observed in Figure 10.4.

Further measurements at lower temperatures are needed to explain the conductivity trend in terms of defects and activation energies and the influence of the preparation of the doped ice sample on its dielectric properties.

Conductivity at 60 MHz was fitted with eq. 10.14 only in the temperature range 225 K - 249 K, due to VNA instrumental limit previously discussed and since LCR meter measurements cannot be used to extend electrical properties at frequencies higher than 10 MHz. In this case, no crossover temperatures are present; $\sigma_0(conc)$ is the one evaluated with eq. 10.13, and the activation energies for the 20 mM and 200 mM doped ices are respectively $E_a^\sigma(20\,mM) = 0.19 \pm 0.01$ and $E_a^\sigma(200\,mM) = 0.33 \pm 0.01$ (see Fig. 10.18).

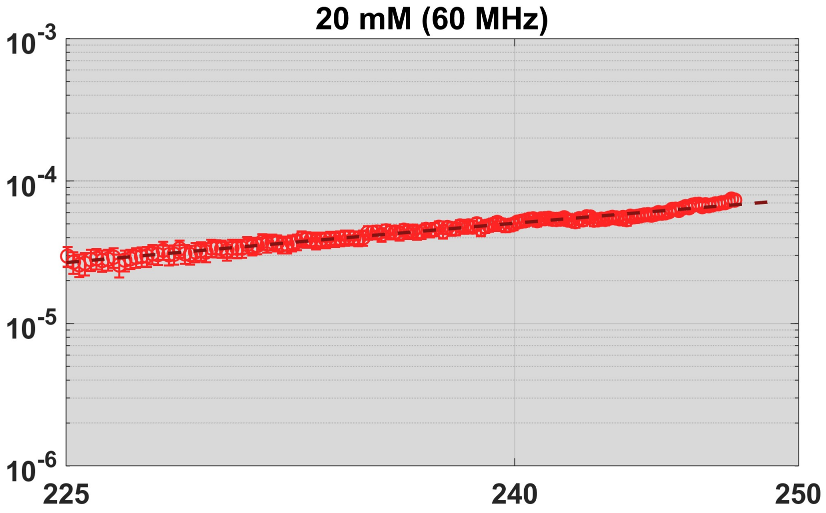

(a) *20 mM*

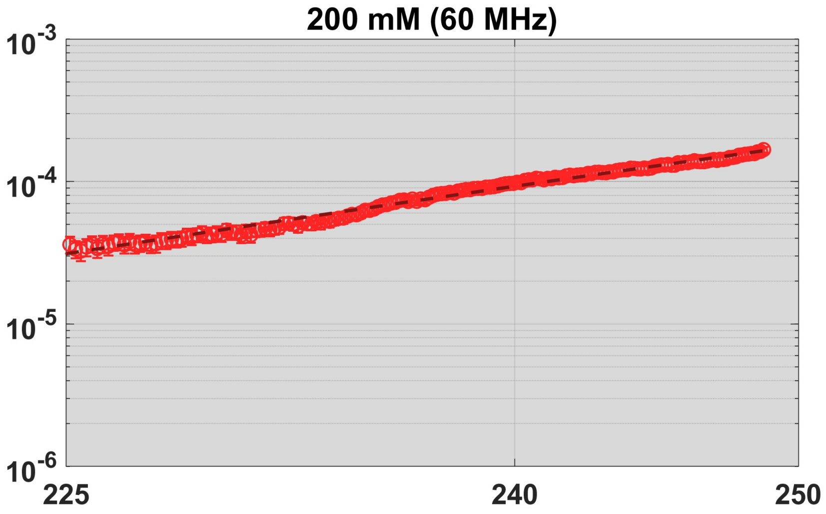

(b) *200 mM*

Figure 10.18: Fit of the conductivity of the 20 mM and 200 mM doped ices at 60 MHz versus temperature. The measurements are reported at only in temperature range 200 K - 249 K, since LCR meter measurements cannot be used to extract electrical properties at frequencies higher than 10 MHz.

In conclusion, it is important to emphasize that in any case below the conductivity value of $\sigma = 1 \times 10^{-6}\ S/m$ (i.e., generally below 180 K), the two-way attenuation at 9 MHz and 60 MHz generated by NaCl doped ices is very low, as:

$$A(\sigma \leq \times 10^{-6}\ S/m) < 2\,dB/km \tag{10.15}$$

Therefore, for the investigation of the shallow ice crust of Europa the attenuation generated by NaCl doped

ice should not play a significant role, only in case the temperatures are low, below 180 K. Nevertheless, the attenuation of the radar signal becomes relevant when investigating several kilometers of crust or when approaching higher temperatures.
As a reference, the attenuation (db/km) at 9 MHz as a function of temperature was estimated for the 200 mM sample (see Fig. 10.19).

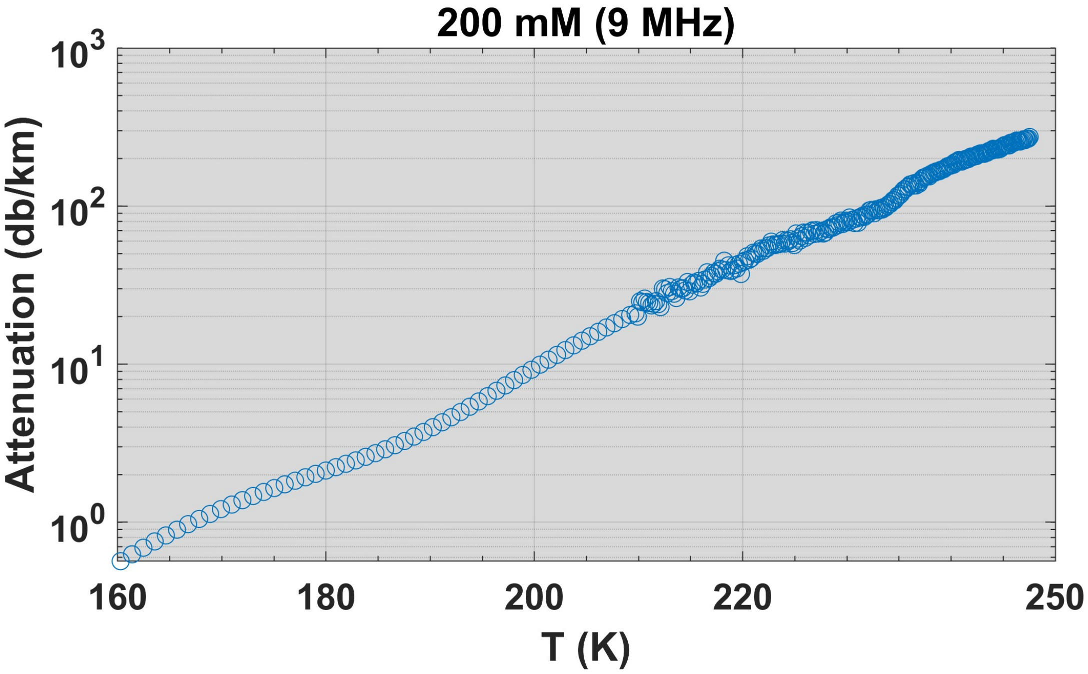

Figure 10.19: Attenuation (db/km) estimated for the 200 mM sample.

10.4.2 Brines Region

Only the measurements made with the VNA were used for the analysis of electrical properties in the brines region.
The conductivity of the doped ice samples in the brines region has been modeled with an Archie-like equation (see eq. 3.18)

$$\sigma_{br} = \sigma_{ice} + (\sigma_{wat} - \sigma_{ice}) f_b^m \tag{10.16}$$

where σ_{ice} is the conductivity of the doped ice sample in the ice region, σ_{wat} is the conductivity of the water in the liquid region, f_b is the brine volume fraction retrieved through eq. 10.8 and m is the geometric factor, that contains the information about the geometry of the brines pockets and channels (see section 3.4 for more details) .
The fit of the conductivity through the eq. 10.16 has been carried out by fixing the ice conductivity σ_{ice} and the water conductivity σ_{wat} for each sample, using the actual values obtained from the measurements. The results of the fitting procedure are in good agreement with the experimental data, both for samples doped with low and high sodium chloride concentrations. Figures 10.20-10.21 report the fit of the conductivity at 9 MHz and 60 MHz of four doped ice samples as a function of the brine volume fraction f_b.

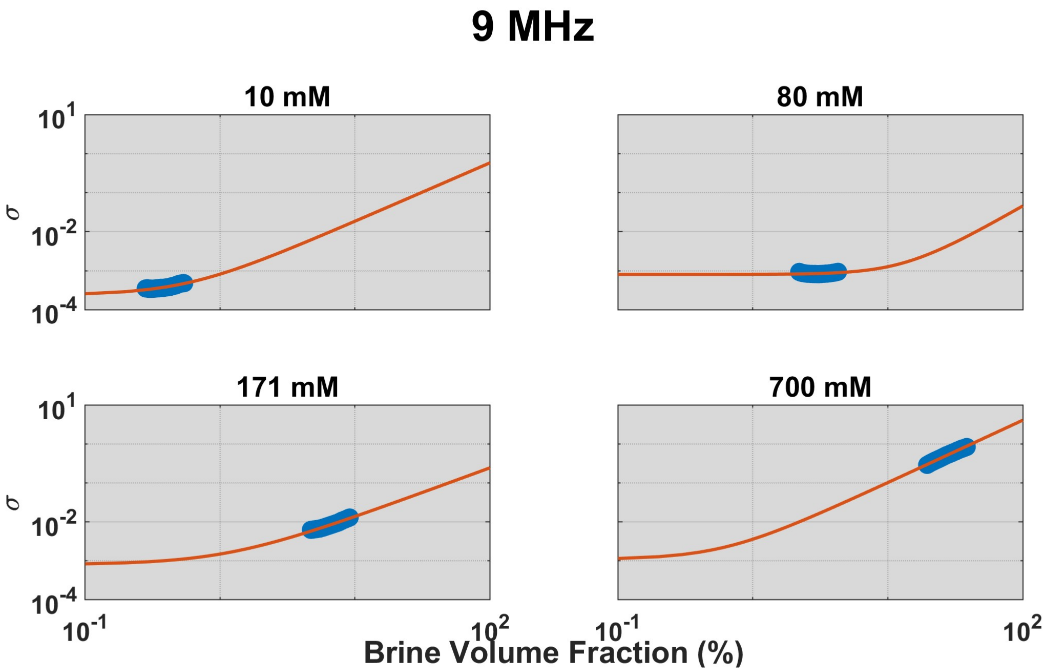

Figure 10.20: Fit of the conductivity of four doped ice samples as a function of the brine volume fraction at a fixed frequency (9 MHz).

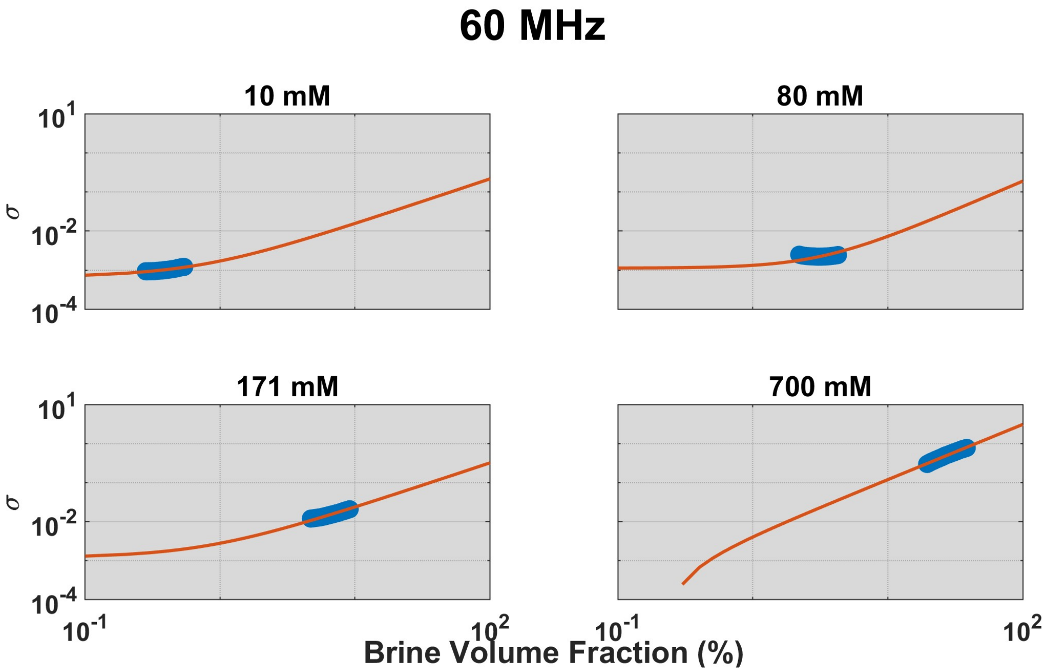

Figure 10.21: Fit of the conductivity of four doped ice samples as a function of the brine volume fraction at a fixed frequency (60 MHz).

The geometric factor m lies in the interval $m \in [1.1, 2.2]$ (see Fig. 10.22): especially at 60 MHz an increase in this parameter is recognizable as the salt concentration in the sample increases, although at low NaCl concentrations m exhibits a great variability, showing that the phenomenon of appearances of brines inside the ice matrix is stochastic and that cylindrical and plate-like inclusions can be randomly formed with their major axis perpendicular ($m > 1.5$) or parallel ($m < 1.4$) to the external electric field. Nevertheless, the m values are in general agreement with those found with a similar model for sea ice in

[181], where were found to be in the range $m \in [1.5, 1.8]$.

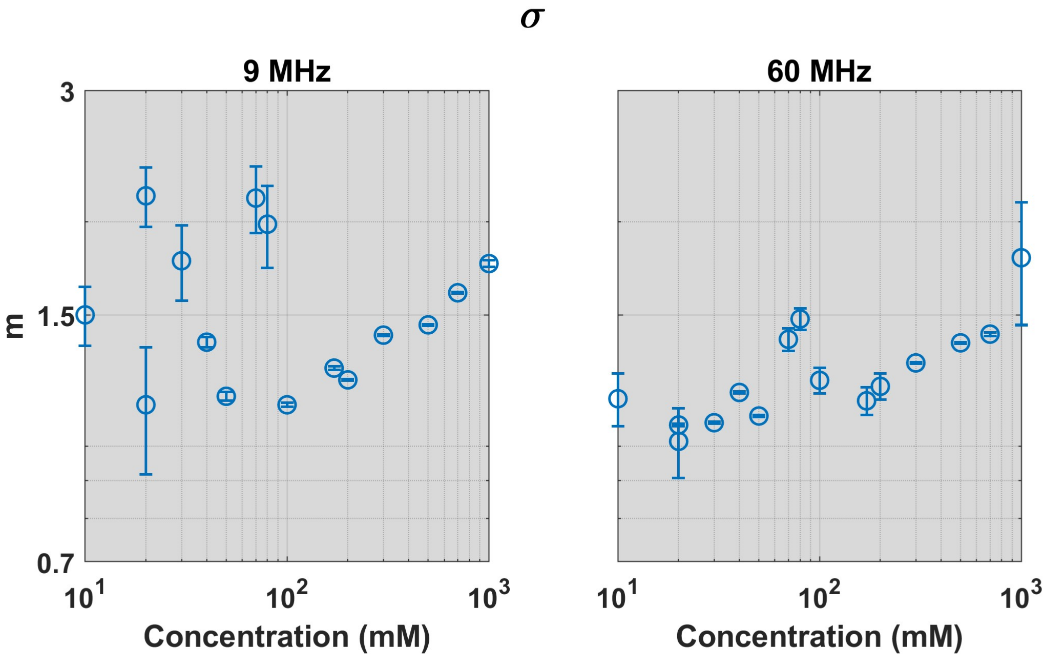

Figure 10.22: Geometric factor m obtained through the fit of conductivities versus NaCl concentration.

The conductivity of the entire data set at a fixed temperature in the brines region was plotted versus the corresponding brine volume fraction. The Archie-like model is able to reproduce the conductivity in the entire range of brines volume fraction: Fig. 10.23 reports both the fit and conductivity data for T = 262 K. In this case the m parameters are equal to $m = 2.65 \pm 0.05$ and $m = 2.54 \pm 0.05$ for 9 MHz and 60 MHz data respectively, but they do not have a geometrical meaning, since in this case the conductivity values of the entire dataset at a certain temperature are taken into account and no real brine geometry can be associated.

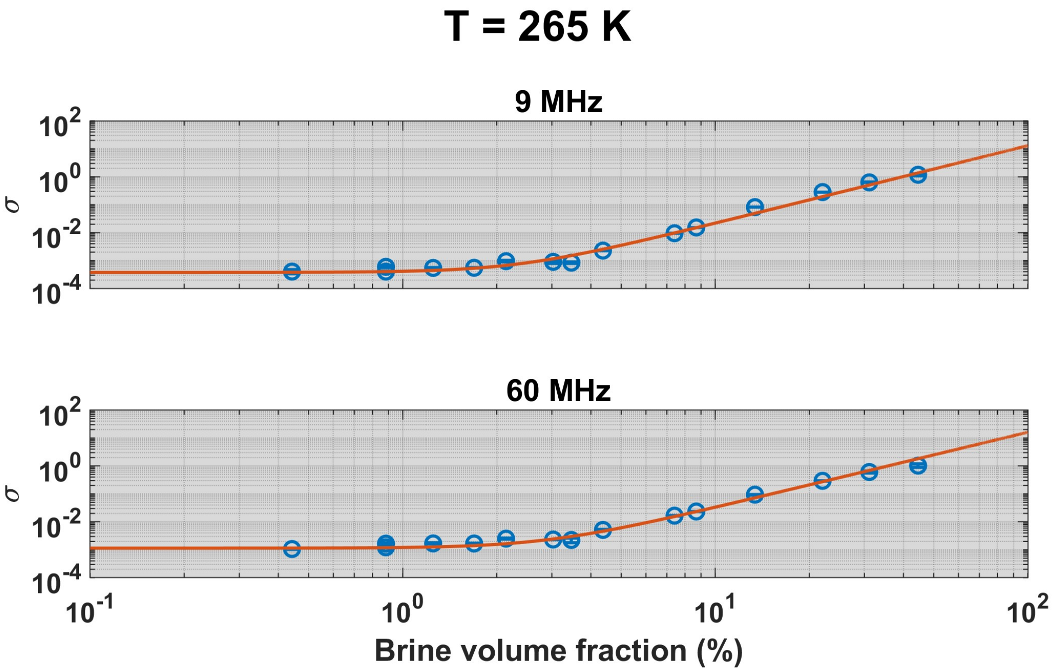

Figure 10.23: Real part of permittivity of the whole VNA dataset as a function of the brine volume fraction, at a fixed temperature and at 9 MHz.

Polynomial fits were performed on the real part of permittivity of the the doped ice samples in the brines region, without success, since they were not able to reproduce the real part of permittivity trend as a function of the brine volume fraction.
Therefore, in analogy with the case of conductivity, the real part of permittivity of the the doped ice samples in the brines region has been modeled using an Archie-like equation as well

$$\varepsilon'_{br} = \varepsilon'_{ice} + (\varepsilon'_{wat} - \varepsilon'_{ice}) f_b^m \tag{10.17}$$

where ε'_{ice} is the real part of permittivity of the doped ice sample in the ice region and ε'_{wat} is the real part of permittivity of water in the liquid region.
Nevertheless, at higher temperatures and higher brine volume fractions this parameter was difficult to estimate and consequently to model, probably because of the appearance of stochastic geometric configurations of pockets and channels of brines within the ice matrix capable of generating additional polarization that cannot be measured accurately by the VNA.
Figures 10.24-10.25 report the fit of the conductivity of four doped ice samples as a function of the brine volume fraction f_b; measurements of ices doped with concentrations 200 mM were not shown for the reasons outlined above.

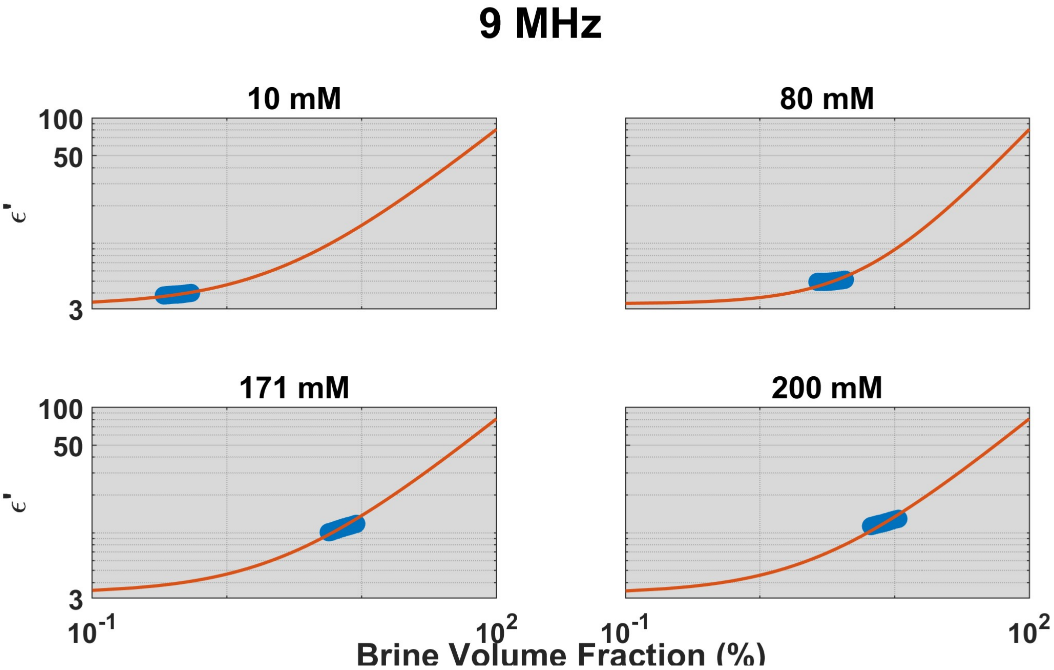

Figure 10.24: Fit of the real part of permittivity of four doped ice samples as a function of the brine volume fraction at a fixed frequency (9 MHz).

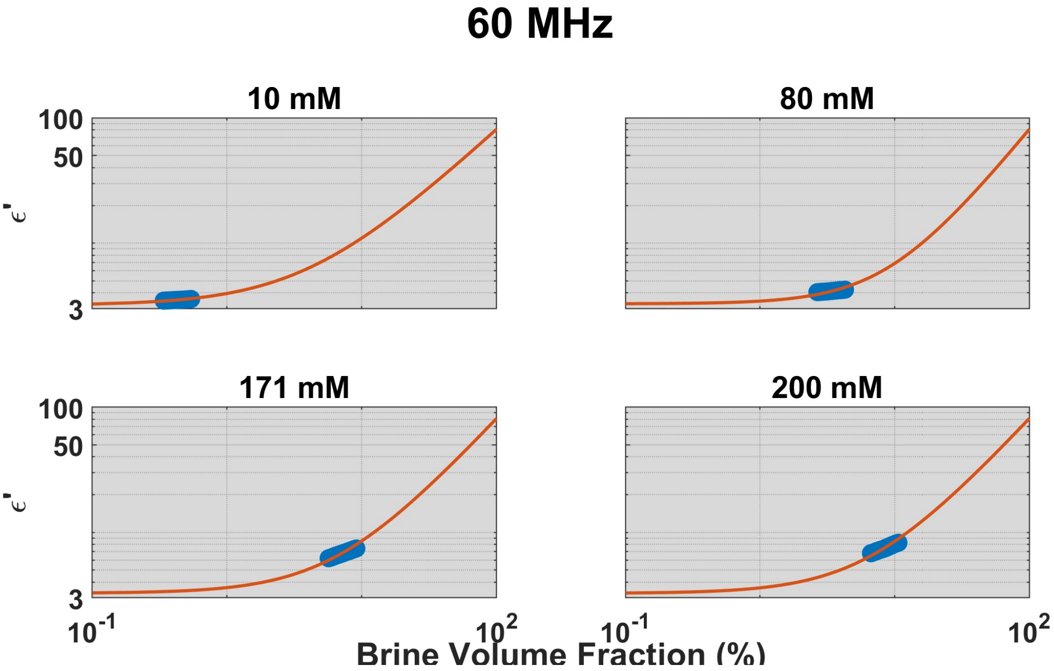

Figure 10.25: Fit of the real part of permittivity of four doped ice samples as a function of the brine volume fraction at a fixed frequency (60 MHz).

Fitting the real part of permittivity, the geometric factor m does not have a geometrical meaning, unlike the case of conductivity, since ε' is less dependent on the geometry of the brines inside the sample (see Fig. 10.26). However, the trend as a function of concentration is similar to the conductivity's analysis.

In Fig. 10.27 the real part of permittivity of the whole dataset at a fixed temperatures was plotted versus the corresponding brine volume fraction. Above $\simeq 13\%$ volumetric fraction of brines in the samples

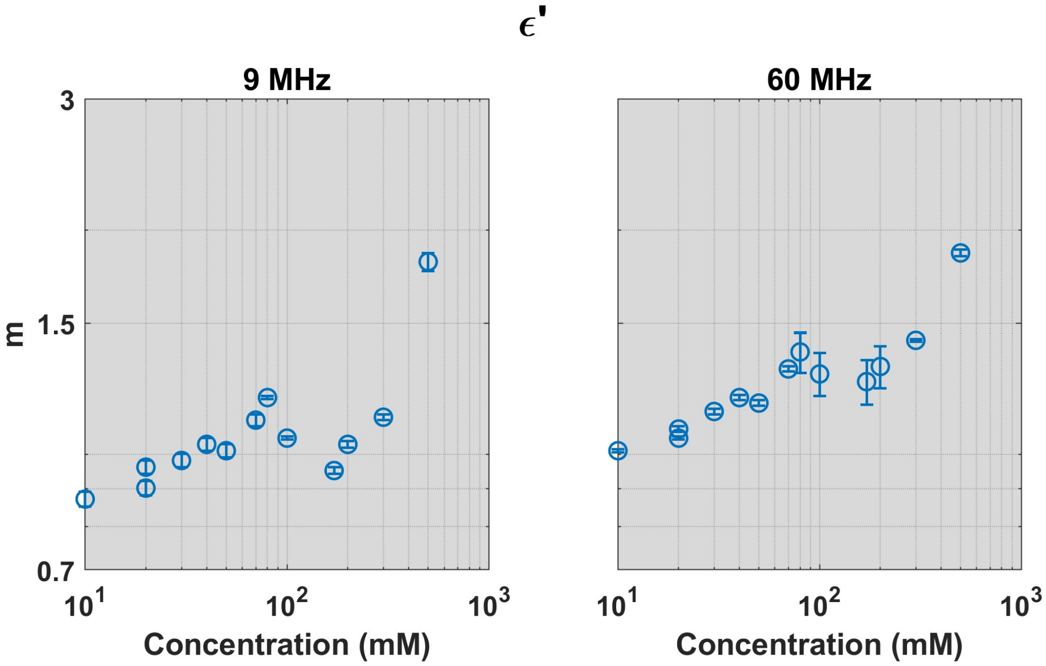

Figure 10.26: Geometric factor m obtained through the fit of the real part of permittivity versus NaCl concentration.

the real part of the permittivity is difficult to estimate by the VNA (gray areas in the plot): for this reason at higher temperatures the fit is not reliable, as already discussed.

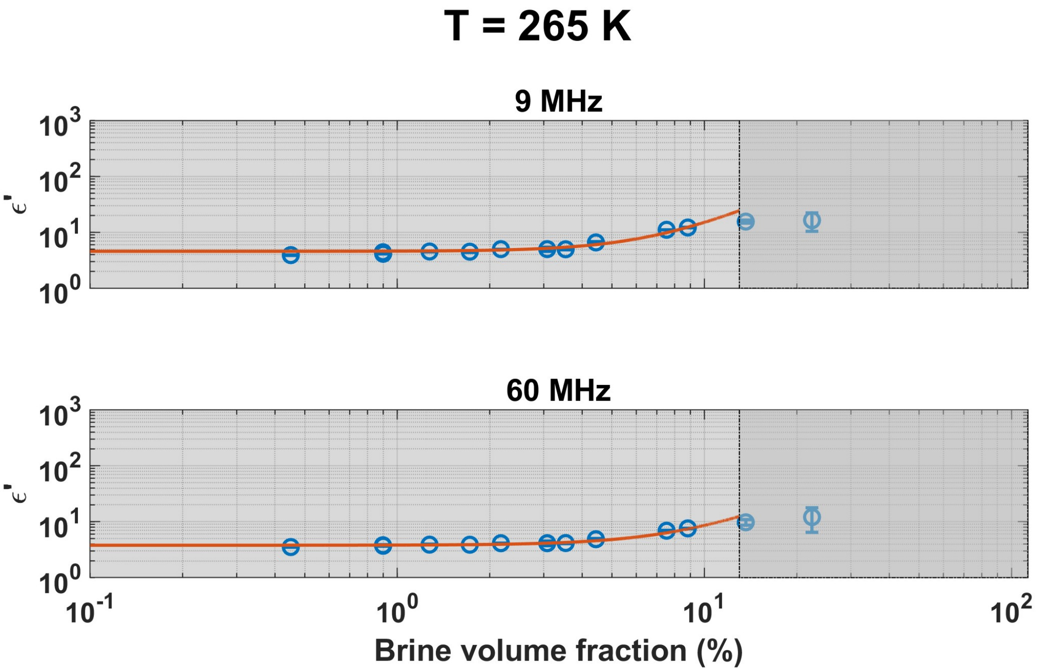

Figure 10.27: Real part of permittivity of the whole VNA dataset as a function of the brine volume fraction, at a fixed temperature and at 9 MHz.

To conclude, NaCl doped ice samples have very different electrical behavior depending on the region studied. The study and modeling of the complex permittivity and electrical conductivity in the ice region has proved particularly challenging, especially with regard to the characterization of electrical conductivity at temperatures below 200 K. Nevertheless, models were derived to characterize both conductivity and real part of permittivity as the initial concentration of sodium chloride in the samples and temperature changed. The conductivity values versus NaCl concentration are noteworthy, since they are fairly constant above a threshold limit of concentration, identified in this work at 200 mM. Further measurements are required to fully understand the influence of ice sample preparation on the conductivity and the crossovers observed, both at high and low temperature. Moreover, it is worth noting that at low temperatures (below 180 K), the attenuation of the radar signal is low, below $2\,dB/km$, even for ices with relatively high concentrations of sodium chloride. Therefore, it will be possible with radar sounders to penetrate deep into the ice and reach the ice-ocean interface, as long as temperatures remain low, below 180 K. As temperatures rise, the radar signal is quickly attenuated, but it will still be possible to detect upwelling of water or pockets of brines inside the icy crust.

Permittivity and conductivity of samples in the brines region are characterized by the gradual appearance of pockets and channels of salt water within the samples as the temperature changes. Because of instrumental limits, it was difficult to model the real part of the permittivity at brines volume fractions greater than 13%. The conductivity, on the other hand, was modeled with an Archie-like equation, obtaining good agreement with experimental data. The geometric factor m suggests that the brines are organized in channels with a moderately tortuous geometry.

Conclusion

The main goal of this thesis is the electromagnetic characterization of ice analogs of Jupiter's icy moon at the frequencies at which RIME and REASON will work. The intensive laboratory work involved a comprehensive study of the dielectric permittivity and magnetic permeability of ice samples as a function of the temperature, dust inclusions, salinity and water content, aiming to assess the performance of these radars in terms of attenuation and detection capability of interfaces in icy crusts. The results of this dissertation highlight the importance of laboratory work for the characterization of the influence of impurities and rocky inclusion on the ice electromagnetic behavior, given also the lack of such measurements in the literature.

In chapter 9 the electromagnetic properties of dirty ices were studied down to 120 K by means of two different instruments, a Vector Network analyzer and an LCR meter. Dirty ices were created using pure water ice and two meteoritic samples, an L5 ordinary chondrite granular sample and a carbonaceous chondrite simulant, following the indications of recent work regarding the composition of the ices of Ganymede and Callisto. The analysis of the measurements focus on the modeling of both the dielectric permittivity and magnetic permeability as a function of temperature and the meteorite inclusions by means of different mixing equations, creating a parametric electromagnetic model for these two dirty ice samples of interest for future spacecraft missions. The modeling is valid down to 120 K, a temperature expected on the surface of the moons. The magnetic properties of the dirty ice samples were also taken into account in estimating the attenuation of the radar signal, highlighting the importance of the magnetic phase in the evaluation of this parameter. As expected, the higher the temperature and the larger the dust inclusions, the higher will be the attenuation. Moreover, it was observed a dispersive behavior of the carbonaceous chondrite material saturated with ice at temperatures above 210 K, due to its composition similar to clay materials: since the mixing formulas do not work for clays, the dielectric properties of this sample saturated with ice were modeled only up to 210 K.
The experimental work will also be useful in the framework of space missions that will investigate asteroids by means of a radar sounder, such as the case of JuRa on board the Hera mission.

Chapter 10 addresses the dielectric properties of NaCl doped ices for the upcoming radar investigations of Europa's ice shell. The electrical properties of this type of ice were studied as a function of the sodium chloride concentration in the initial solution and temperature; measurements were divided into two regions, characterized by very different dielectric behavior: the ice region and the brines region. In the ice region the real part of permittivity and conductivity were modeled as a function of NaCl concentration and for temperatures down to 160 K both at 9 and 60 MHz. The conductivity versus temperature exhibits an interesting behavior, with two changes in slope at two different crossover temperatures, probably due to the preparation of the sample and to a change in the charge carriers induced by ice doping. Further measurements are necessary to address more consistently this conductivity behavior.
In any case, the two-way attenuation at 9 MHz and 60 MHz and below 180 K generated by NaCl doped ices is low, since it assumes values lower than 2 dB/km. The brines region is characterized by a more dispersive behavior and an Archie-like equation was able to reproduce the trend of both real permittivity and conductivity as a function of the brines volume fraction. The results were compatible with the presence of brines organized in channels with a moderately tortuous geometry. If large pockets of brines are present in Europa's shallow crust, they will be detectable by radar sounders, due to high permittivity contrast between brines and ice, as expected.

This work presents results and analyses that are intended to be the first step toward characterizing the electromagnetic properties of Jupiter's icy moons analogs: for this reason, further measurements of ice doped with other salts observed on the surfaces of Jupiter's moons will be needed in the future. In particular, once fully understood how the various salts observed on the surface of these moons affect the complex permittivity of ice, it will be crucial to study the electromagnetic properties of saline dirty ice, the presence of which has been observed on both Ganymede and Callisto.

Bibliography

[1] S. J. Peale and Man Hoi Lee. A primordial origin of the laplace relation among the galilean satellites. *Science*, 298:593–597, 2002.

[2] Wendy M. Calvin, Roger N. Clark, Robert H. Brown, and John R. Spencer. Spectra of the icy galilean satellites from 0.2 to 5μm: A compilation, new observations, and a recent summary. *Journal of Geophysical Research: Planets*, 100(E9):19041–19048, 1995.

[3] Adam P. Showman, Malhotra, and Renu. The galilean satellites. *Science*, 286(5437):77–84, 1999.

[4] Yosef Ashkenazy. The surface temperature of europa. *Heliyon*, 5(6), 2019.

[5] Geoffrey Collins and Francis Nimmo. Chaotic terrain on europa. *Europa*, pages 259–281, 2009.

[6] Riley Culberg, Dustin M. Schroeder, and Gregor Steinbrügge. Double ridge formation over shallow water sills on jupiter's moon europa. *Nature communications*, 13(1):2007, 2022.

[7] C. Paranicas, J. F. Cooper, H. B. Garrett, R. E. Johnson, and S. J. Sturner. Europa's radiation environment and its effects on the surface. *Europa*, pages 529–544, 2009.

[8] R. W. Carlson, W. M. Calvin, J. B. Dalton, G. B. Hansen, R. L. Hudson, R. E. Johnson, T. B. McCord, and M. H. Moore. Europa's surface composition. *Europa*, 283, 2009.

[9] Sarah A. Fagents, Ronald Greeley, Robert J. Sullivan, Robert T. Pappalardo, Louise M. Prockter, and Galileo S. S. I. Team. Cryomagmatic mechanisms for the formation of rhadamanthys linea, triple band margins, and other low-albedo features on europa. *Icarus*, 144(1):54–88, 2000.

[10] Lorenz Roth, Kurt D. Retherford, Nickolay Ivchenko, Nicola Schlatter, Darrell F. Strobel, Tracy M. Becker, and Cesare Grava. Detection of a hydrogen corona in hst $ly\alpha$ images of europa in transit of jupiter. *The Astronomical Journal*, 153(2):67, 2017.

[11] William B. Sparks, K. P. Hand, M. A. McGrath, E. Bergeron, M. Cracraft, and S. E. Deustua. Probing for evidence of plumes on europa with hst/stis. *The Astrophysical Journal*, 829(2):121, 2016.

[12] G. Schubert, F. Sohl, and H. Hussmann. Interior of europa. *Europa*, 35:3–367, 2009.

[13] David P. O'Brien, Paul Geissler, and Richard Greenberg. A melt-through model for chaos formation on europa. *Icarus*, 156(1):152–161, 2002.

[14] Robert T. Pappalardo, Michael J. S. Belton, H. H. Breneman, M. H. Carr, Clark R. Chapman, G. C. Collins, T. Denk, S. Fagents, Paul E. Geissler, and B. Giese. Does europa have a subsurface ocean? evaluation of the geological evidence. *Journal of Geophysical Research: Planets*, 104(E10):24015–24055, 1999.

[15] J. J. Buffo, Britney Elyce Schmidt, Christian Huber, and Catherine Colello Walker. Entrainment and dynamics of ocean-derived impurities within europa's ice shell. *Journal of Geophysical Research: Planets*, 125(10):e2020JE006394, 2020.

[16] Sunwoong Lee, Robert T. Pappalardo, and Nicholas C. Makris. Mechanics of tidally driven fractures in europa's ice shell. *Icarus*, 177(2):367–379, 2005.

[17] F. Nimmo, R. T. Pappalardo, and B. Giese. On the origins of band topography, europa. *Icarus*, 166(1):21–32, 2003.

[18] Robert M. Nelson, Mark D. Boryta, Bruce W. Hapke, Kenneth S. Manatt, Yuriy Shkuratov, Vladimir Psarev, Kurt Vandervoort, Desire Kroner, Adaze Nebedum, and Christina L. Vides. Laboratory simulations of planetary surfaces: Understanding regolith physical properties from remote photopolarimetric observations. *Icarus*, 302:483–498, 2018.

[19] Deborah Lynn Domingue, B. W. Hapke, G. W. Lockwood, and D. T. Thompson. Europa's phase curve: Implications for surface structure. *Icarus*, 90(1):30–42, 1991.

[20] Brandon C. Johnson, Rachel Y. Sheppard, Alyssa C. Pascuzzo, Elizabeth A. Fisher, and Sean E. Wiggins. Porosity and salt content determine if subduction can occur in europa's ice shell. *Journal of Geophysical Research: Planets*, 122(12):2765–2778, 2017.

[21] Simon A. Kattenhorn and Louise M. Prockter. Evidence for subduction in the ice shell of europa. *Nature Geoscience*, 7(10):762–767, 2014.

[22] Paul V. Johnson, Robert Hodyss, Tuan H. Vu, and Mathieu Choukroun. Insights into europa's ocean composition derived from its surface expression. *Icarus*, 321:857–865, 2019.

[23] M. E. Brown and K. P. Hand. Salts and radiation products on the surface of europa. *The Astronomical Journal*, 145(4):110, 2013.

[24] T. B. McCord, G. B. Hansen, F. P. Fanale, R. W. Carlson, D. L. Matson, T. V. Johnson, W. D. Smythe, J. K. Crowley, P. D. Martin, and A. Ocampo. Salts on europa's surface detected by galileo's near infrared mapping spectrometer. *Science*, 280(5367):1242–1245, 1998.

[25] J. B. Dalton, O. Prieto-Ballesteros, J. S. Kargel, C. S. Jamieson, J. Jolivet, and R. Quinn. Spectral comparison of heavily hydrated salts with disrupted terrains on europa. *Icarus*, 177(2):472–490, 2005.

[26] J. B. Dalton III, J. H. Shirley, and L. W. Kamp. Europa's icy bright plains and dark linea: Exogenic and endogenic contributions to composition and surface properties. *Journal of Geophysical Research: Planets*, 117(E3), 2012.

[27] Patrick D. Fischer, Michael E. Brown, and Kevin P. Hand. Spatially resolved spectroscopy of europa: The distinct spectrum of large-scale chaos. *The Astronomical Journal*, 150(5):164, 2015.

[28] N. Ligier, F. Poulet, J. Carter, R. Brunetto, and F. Gourgeot. Vlt/sinfoni observations of europa: New insights into the surface composition. *The Astronomical Journal*, 151(6):163, 2016.

[29] P. D. Fischer, M. E. Brown, S. K. Trumbo, and K. P. Hand. Spatially resolved spectroscopy of europa's large-scale compositional units at 3-4 μm with keck nirspec. *The Astronomical Journal*, 153(1):13, 2016.

[30] Samantha K. Trumbo, Michael E. Brown, and Kevin P. Hand. Sodium chloride on the surface of europa. *Science advances*, 5(6):eaaw7123, 2019.

[31] Samantha K. Trumbo, Michael E. Brown, and Kevin P. Hand. H2o2 within chaos terrain on europa's leading hemisphere. *The Astronomical Journal*, 158(3):127, 2019.

[32] Samantha K. Trumbo, Michael E. Brown, and Kevin P. Hand. Endogenic and exogenic contributions to visible-wavelength spectra of europa's trailing hemisphere. *The Astronomical Journal*, 160(6):282, 2020.

[33] Samantha K. Trumbo, Tracy M. Becker, Michael E. Brown, William T. P. Denman, Philippa Molyneux, Amanda Hendrix, Kurt D. Retherford, Lorenz Roth, and Juan Alday. A new uv spectral feature on europa: Confirmation of nacl in leading-hemisphere chaos terrain. *The Planetary Science Journal*, 3(2):27, 2022.

[34] Jodi R. Berdis, James R. Murphy, and Nancy J. Chanover. Europa's surface water-ice crystallinity and correlations between lineae and hydrate composition. *The Planetary Science Journal*, 3(2):36, 2022.

[35] Tracy M. Becker, Samantha K. Trumbo, Philippa M. Molyneux, Kurt D. Retherford, Amanda R. Hendrix, Lorenz Roth, Ujjwal Raut, Juan Alday, and Melissa A. McGrath. Mid-ultraviolet hubble observations of europa and the global surface distribution of so2. *The Planetary Science Journal*, 3(6):129, 2022.

[36] N. Ligier, C. Paranicas, J. Carter, F. Poulet, W. M. Calvin, T. A. Nordheim, Colin Snodgrass, and L. Ferellec. Surface composition and properties of ganymede: Updates from ground-based observations with the near-infrared imaging spectrometer sinfoni/vlt/eso. *Icarus*, 333:496–515, 2019.

[37] Paul M Schenk and William B McKinnon. Dark-ray and dark-floor craters on ganymede, and the provenance of large impactors in the jovian system. *Icarus (New York, N.Y. 1962)*, 89(2):318–346, 1991.

[38] Krishan K Khurana, Robert T Pappalardo, Nate Murphy, and Tilmann Denk. The origin of ganymede's polar caps. *Icarus (New York, N.Y. 1962)*, 191(1):193–202, 2007.

[39] Lucas Liuzzo, Andrew R. Poppe, Christopher Paranicas, Quentin Nénon, Shahab Fatemi, and Sven Simon. Variability in the energetic electron bombardment of ganymede. *Journal of Geophysical Research: Space Physics*, 125(9):e2020JA028347, 2020.

[40] Christina Plainaki, Stefano Massetti, Xianzhe Jia, Alessandro Mura, Anna Milillo, Davide Grassi, Giuseppe Sindoni, Emiliano D'Aversa, and Gianrico Filacchione. Kinetic simulations of the jovian energetic ion circulation around ganymede. *The Astrophysical Journal*, 900(1):74, 2020.

[41] S. Fatemi, A. R. Poppe, K. K. Khurana, M. Holmström, and G. T. Delory. On the formation of ganymede's surface brightness asymmetries: Kinetic simulations of ganymede's magnetosphere. *Geophysical Research Letters*, 43(10):4745–4754, 2016.

[42] A. R. Poppe, Shahab Fatemi, and K. K. Khurana. Thermal and energetic ion dynamics in ganymede's magnetosphere. *Journal of Geophysical Research: Space Physics*, 123(6):4614–4637, 2018.

[43] Robert W. Carlson, P. R. Weissman, William D. Smythe, J. C. Mahoney, N. I. M. S. Science, and Engineering Teams. Near-infrared mapping spectrometer experiment on galileo. *The Galileo Mission*, pages 457–502, 1992.

[44] Gary B. Hansen and Thomas B. McCord. Amorphous and crystalline ice on the galilean satellites: A balance between thermal and radiolytic processes. *Journal of Geophysical Research: Planets*, 109(E1), 2004.

[45] P. M. Molyneux, J. D. Nichols, T. M. Becker, U. Raut, and K. D. Retherford. Ganymede's far-ultraviolet reflectance: Constraining impurities in the surface ice. *Journal of Geophysical Research: Planets*, 125(9):e2020JE006476, 2020.

[46] Charles A. Hibbitts. Dark ray craters on ganymede: Impactor or endogenous origin. *Icarus*, 394:115400, 2023.

[47] Federico Tosi, Alessandro Mura, Alessandra Cofano, Francesca Zambon, Christopher R. Glein, Mauro Ciarniello, Jonathan I. Lunine, Giuseppe Piccioni, Christina Plainaki, Roberto Sordini, Alberto Adriani, Scott J. Bolton, Candice J. Hansen, Tom A. Nordheim, Alessandro Moirano, Livio Agostini, Francesca Altieri, Shawn M. Brooks, Andrea Cicchetti, Bianca Maria Dinelli, Davide Grassi, Alessandra Migliorini, Maria Luisa Moriconi, Raffaella Noschese, Pietro Scarica, Giuseppe Sindoni, Stefania Stefani, and Diego Turrini. Salts and organics on ganymede's surface observed by the jiram spectrometer onboard juno. *Nature Astronomy*, 8(1):82–93, 2024.

[48] Bockelée-Morvan, D., Lellouch, E., Poch, O., Quirico, E., Cazaux, S., de Pater, I., Fouchet, T., Fry, P. M., Rodriguez-Ovalle, P., Tosi, F., Wong, M. H., Boshuizen, I., de Kleer, K., Fletcher, L. N., Meunier, L., Mura, A., Roth, L., Saur, J., Schmitt, B., Trumbo, S. K., Brown, M. E., O'Donoghue, J., Orton, G. S., and Showalter, M. R. Composition and thermal properties of ganymede's surface from jwst/nirspec and miri observations. *A&A*, 681:A27, 2024.

[49] V. A. Kronrod and O. L. Kuskov. Chemical differentiation of the galilean satellites of jupiter: 4. isochemical models for the compositions of io, europa, and ganymede. *Geochemistry International*, 44:529–546, 2006.

[50] P. K. Byrne, P. V. Regensburger, C. Klimczak, D. R. Bohnenstiehl, S. A. Hauck, A. J. Dombard, and D. J. Hemingway. The geology of the rocky bodies inside enceladus, europa, titan, and ganymede. Number 2083, page 2905, 2018.

[51] Steve Vance, Mathieu Bouffard, Mathieu Choukroun, and Christophe Sotin. Ganymede's internal structure including thermodynamics of magnesium sulfate oceans in contact with ice. *Planetary and Space Science*, 96:62–70, 2014.

[52] Deborah L. Domingue, Arthur L. Lane, and Ross A. Beyer. Iue's detection of tenuous so2 frost on ganymede and its rapid time variability. *Geophysical research letters*, 25(16):3117–3120, 1998.

[53] Samantha K. Trumbo, Michael E. Brown, and Danica Adams. The geographic distribution of dense-phase o2 on ganymede. *The Planetary Science Journal*, 2(4):139, 2021.

[54] Oliver King and Leigh N. Fletcher. Global modeling of ganymede's surface composition: Near-ir mapping from vlt/sphere. *Journal of Geophysical Research: Planets*, 127(12):e2022JE007323, 2022.

[55] Kevin Zahnle, Paul Schenk, Harold Levison, and Luke Dones. Cratering rates in the outer solar system. *Icarus (New York, N.Y. 1962)*, 163(2):263–289, 2003.

[56] Robert T. Pappalardo, Geoffrey C. Collins, J. W. Head, Paul Helfenstein, Thomas B. McCord, Jeffrey M. Moore, Louise M. Prockter, Paul M. Schenk, and John R. Spencer. Geology of ganymede. *Jupiter: The planet, satellites and magnetosphere*, 2:363, 2004.

[57] F Sohl, T Spohn, D Breuer, and K Nagel. Implications from galileo observations on the interior structure and chemistry of the galilean satellites. *Icarus (New York, N.Y. 1962)*, 157(1):104–119, 2002.

[58] F. Nimmo and R. T. Pappalardo. Ocean worlds in the outer solar system. *Journal of Geophysical Research: Planets*, (121):1378–1399, 2016.

[59] M. G. Kivelson, K. K. Khurana, and M. Volwerk. The permanent and inductive magnetic moments of ganymede. *Icarus*, 157(2):507–522, 2002.

[60] Joachim Saur, Stefan Duling, Lorenz Roth, Xianzhe Jia, Darrell F. Strobel, Paul D. Feldman, Ulrich R. Christensen, Kurt D. Retherford, Melissa A. McGrath, and Fabrizio Musacchio. The search for a subsurface ocean in ganymede with hubble space telescope observations of its auroral ovals. *Journal of Geophysical Research: Space Physics*, 120(3):1715–1737, 2015.

[61] Tilman Spohn and Gerald Schubert. Oceans in the icy galilean satellites of jupiter? *Icarus (New York, N.Y. 1962)*, 161(2):456–467, 2003.

[62] Fran Bagenal, Timothy E. Dowling, William B. McKinnon, and William McKinnon. *Jupiter: the planet, satellites and magnetosphere*, volume 1. Cambridge University Press, 2006.

[63] Katrin Stephan, Charles A. Hibbitts, and Ralf Jaumann. H2o-ice particle size variations across ganymede's and callisto's surface. *Icarus*, 337:113440, 2020.

[64] C. A. Hibbitts, J. E. Klemaszewski, T. B. McCord, G. B. Hansen, and R. Greeley. Co2-rich impact craters on callisto. *Journal of Geophysical Research: Planets*, 107(E10):14–1, 2002.

[65] R. Hanel, J. C. Pearl, P. Lowman, S. Kumar, and L. Horn. Preliminary results from voyager 1 infrared observations of the jovian satellites. *EOS Transactions*, 60:308, 1979.

[66] T. B. a McCord, R. W. Carlson, W. D. Smythe, G. B. Hansen, R. N. Clark, C. A. Hibbitts, F. P. Fanale, J. C. Granahan, M. Segura, and D. L. Matson. Organics and other molecules in the surfaces of callisto and ganymede. *Science*, 278(5336):271–275, 1997.

[67] T. B. a McCord, G. B. Hansen, Roger N. Clark, P. D. Martin, C. A. Hibbitts, F. P. Fanale, J. C. Granahan, M. Segura, D. L. Matson, and T. V. Johnson. Non-water-ice constituents in the surface material of the icy galilean satellites from the galileo near-infrared mapping spectrometer investigation. *Journal of Geophysical Research: Planets*, 103(E4):8603–8626, 1998.

[68] C. A. Hibbitts, T. B. McCord, and G. B. Hansen. Distributions of co2 and so2 on the surface of callisto. *Journal of Geophysical Research: Planets*, 105(E9):22541–22557, 2000.

[69] Amanda R. Hendrix and Robert E. Johnson. Callisto: new insights from galileo disk-resolved uv measurements. *The Astrophysical Journal*, 687(1):706, 2008.

[70] Richard J. Cartwright, Tom A. Nordheim, Dale P. Cruikshank, Kevin P. Hand, Joseph E. Roser, William M. Grundy, Chloe B. Beddingfield, and Joshua P. Emery. Evidence for sulfur-bearing species on callisto's leading hemisphere: Sourced from jupiter's irregular satellites or io? *The Astrophysical Journal Letters*, 902(2):L38, 2020.

[71] K. K. Khurana, M. G. Kivelson, C. T. Russell, R. J. Walker, and D. J. Southwood. Absence of an internal magnetic field at callisto. *Nature*, 387(6630):262–264, 1997.

[72] J. D. Anderson, R. A. Jacobson, T. P. McElrath, W. B. Moore, G. Schubert, and P. C. Thomas. Shape, mean radius, gravity field, and interior structure of callisto. *Icarus*, 153(1):157–161, 2001.

[73] Christophe Zimmer, Krishan K. Khurana, and Margaret G. Kivelson. Subsurface oceans on europa and callisto: Constraints from galileo magnetometer observations. *Icarus*, 147(2):329–347, 2000.

[74] S. Plaut, S. Barabash, L. Bruzzone, M. K. Dougherty, C. Erd, L. Fletcher, R. Gladstone, O. Grasset, L. Gurvits, and Paul Hartogh. Jupiter icy moons explorer (juice): Science objectives, mission and instruments. 2014.

[75] Lorenzo Bruzzone, Jeffrey J. Plaut, Giovanni Alberti, Donald D. Blankenship, Francesca Bovolo, Bruce A. Campbell, Adamo Ferro, Yonggyu Gim, Wlodek Kofman, and Goro Komatsu. Rime: Radar for icy moon exploration. pages 3907–3910. IEEE, 2013.

[76] Lorenzo Bruzzone, Jeffrey J. Plaut, Giovanni Alberti, Donald D. Blankenship, Francesca Bovolo, Bruce A. Campbell, Davide Castelletti, Yonggyu Gim, Ana-Maria Ilisei, and Wlodek Kofman. Jupiter icy moon explorer (juice): Advances in the design of the radar for icy moons (rime). pages 1257–1260. IEEE, 2015.

[77] Robert T. Pappalardo, Bonnie J. Buratti, Haje Korth, David A. Senske, Diana L. Blaney, Donald D. Blankenship, James L. Burch, Philip R. Christensen, Sascha Kempf, and Margaret G. Kivelson. Science overview of the europa clipper mission. *Space Science Reviews*, 220(4):1–58, 2024.

[78] Donald D. Blankenship, Alina Moussessian, Elaine Chapin, Duncan A. Young, G. Wesley Patterson, Jeffrey J. Plaut, Adam P. Freedman, Dustin M. Schroeder, Cyril Grima, and Gregor Steinbrügge. Radar for europa assessment and sounding: Ocean to near-surface (reason). *Space science reviews*, 220(5):51, 2024.

[79] James Clerk Maxwell. *A treatise on electricity and magnetism*, volume 1. Oxford: Clarendon Press, 1873.

[80] Constantine A. Balanis. *Advanced engineering electromagnetics*. John Wiley & Sons, 2012.

[81] Kwan Chi Kao. *Dielectric phenomena in solids*. Elsevier, 2004.

[82] Arthur R. Von Hippel and S. O. Morgan. Dielectric materials and applications. *Journal of The Electrochemical Society*, 102(3):68Ca, 1955.

[83] Chloe Helene Martella. *Electromagnetic characterization of lunar soil simulants and Ground Penetrating Radar measurements for water ice detection within the shallow lunar subsurface*. PhD thesis, Università degli Studi Roma Tre, 2024.

[84] Elena Pettinelli, Barbara Cosciotti, Federico Di Paolo, Sebastian Emanuel Lauro, Elisabetta Mattei, Roberto Orosei, and Giuliano Vannaroni. Dielectric properties of jovian satellite ice analogs for subsurface radar exploration: A review. *Reviews of Geophysics*, 53(3):593–641, 2015.

[85] Ari H Sihvola. *Electromagnetic mixing formulas and applications*. Number 47. Iet, 1999.

[86] John David Jackson. *Classical electrodynamics*. John Wiley & Sons, 2021.

[87] A. K. Jonscher. A new understanding of the dielectric relaxation of solids. *Journal of materials science*, 16:2037–2060, 1981.

[88] Kenneth S. Cole and Robert H. Cole. Dispersion and absorption in dielectrics i. alternating current characteristics. *The Journal of chemical physics*, 9(4):341–351, 1941.

[89] S. Havriliak and S. Negami. A complex plane representation of dielectric and mechanical relaxation processes in some polymers. *Polymer*, 8:161–210, 1967.

[90] Gary R. Olhoeft. Electrical properties of rocks. *Physical properties of rocks and minerals*, 2:257–297, 1981.

[91] M. Saint-Amant and David W. Strangway. Dielectric properties of dry, geologic materials. *Geophysics*, 35(4):624–645, 1970.

[92] Theodore Richard Madden and Donald J. Marshall. *Induced Polarization: A Study of Its Causes and Magnitudes in Geologic Materials, Final Report*. MIT Department of Geology and Geophysics, 1959.

[93] John Barrett Hasted. *Aqueous dielectrics*, volume 122. Chapman and Hall London, 1973.

[94] J. A. Lane and J. A. Saxton. Dielectric dispersion in pure polar liquids at very high radio frequencies-iii. the effect of electrolytes in solution. *Proceedings of the Royal Society of London. Series A. Mathematical and Physical Sciences*, 214(1119):531–545, 1952.

[95] Lawrence Klein and C. Swift. An improved model for the dielectric constant of sea water at microwave frequencies. *IEEE transactions on antennas and propagation*, 25(1):104–111, 1977.

[96] David Long and Fawwaz Ulaby. *Microwave radar and radiometric remote sensing*. Artech, 2015.

[97] Christian Mätzler. *Thermal microwave radiation: applications for remote sensing*, volume 52. Iet, 2006.

[98] Malcolm J. Campbell and Juris Ulrichs. Electrical properties of rocks and their significance for lunar radar observations. *Journal of Geophysical Research*, 74(25):5867–5881, 1969.

[99] J. Baniamerian, S. E. Lauro, B. Cosciotti, A. Brin, C. Lefevre, E. Pettinelli, and E. Mattei. A novel experimental set-up for dielectric characterization of high-temperature planetary crusts. Submitted to Journal of Geophysical Research: Planets.

[100] Myron C. Dobson, Fawwaz T. Ulaby, Martti T. Hallikainen, and Mohamed A. El-rayes. Microwave dielectric behavior of wet soil-part ii: Dielectric mixing models. *IEEE Transactions on Geoscience and Remote Sensing*, GE-23(1):35–46, 1985.

[101] Barbara Cosciotti, Sebastian Emanuel Lauro, Francesco Gabbai, Elisabetta Mattei, Federico Di Paolo, Giovanni Pratesi, and Elena Pettinelli. Laboratory investigation into the dielectric properties of a l-chondrite (nwa 12857). *Icarus*, 362:114426, 2021.

[102] Wlodek Kofman, Alain Herique, Yves Barbin, Jean-Pierre Barriot, Valérie Ciarletti, Stephen Clifford, Peter Edenhofer, Charles Elachi, Christelle Eyraud, and Jean-Pierre Goutail. Properties of the 67p/churyumov-gerasimenko interior revealed by consert radar. *Science*, 349(6247):aab0639, 2015.

[103] Essam Heggy, Elizabeth M. Palmer, Wlodek Kofman, Stephen M. Clifford, Kevin Righter, and Alain Hérique. Radar properties of comets: Parametric dielectric modeling of comet 67p/churyumov-gerasimenko. *Icarus*, 221(2):925–939, 2012.

[104] Alessandro Brin, Sebastian Emanuel Lauro, Barbara Cosciotti, Elisabetta Mattei, and Elena Pettinelli. Electromagnetic characterization of a crushed l-chondrite for subsurface radar investigations of solar system bodies. *Icarus*, 374:114800, 2022.

[105] W. E. Fensler, E. F. Knott, A. Olte, and K. M. Siegel. The electromagnetic parameters of selected terrestrial and extraterrestrial rocks and glasses. volume 14, pages 545–565, 1962.

[106] A Herique, B Agnus, E Asphaug, A Barucci, P Beck, J Bellerose, J Biele, L Bonal, P Bousquet, L Bruzzone, C Buck, I Carnelli, A Cheng, V Ciarletti, M Delbo, J Du, X Du, C Eyraud, W Fa, J Gil Fernandez, O Gassot, R Granados-Alfaro, S.F Green, B Grieger, J.T Grundmann, J Grygorczuk, R Hahnel, E Heggy, T-M Ho, O Karatekin, Y Kasaba, T Kobayashi, W Kofman, C Krause, A Kumamoto, M Küppers, M Laabs, C Lange, J Lasue, A.C Levasseur-Regourd, A Mallet, P Michel, S Mottola, N Murdoch, M Mütze, J Oberst, R Orosei, D Plettemeier, S Rochat, R RodriguezSuquet, Y Rogez, P Schaffer, C Snodgrass, J-C Souyris, M Tokarz, S Ulamec, J-E Wahlund, and S Zine. Direct observations of asteroid interior and regolith structure: Science measurement requirements. *Advances in space research*, 62(8):2141–2162, 2018.

[107] Riley A. McGlasson, Ali M. Bramson, Gareth A. Morgan, and Michael M. Sori. Varied histories of outlier polar ice deposits on mars. *Journal of Geophysical Research: Planets*, 128(5):e2022JE007592, 2023.

[108] Gary R. Olhoeft. Electromagnetic field and material properties in ground penetrating radar. pages 144–147. IEEE, 2003.

[109] A. P. Annan. Ground penetrating radar applications, principles, procedures. *Mississauga, Canada: Sensors and Software*, 2004.

[110] Dylan C. Hickson. *Characterizing the Dielectric Properties of Geologic and Asteroid Regolith Analogue Material for Improved Planetary Radar Interpretation.* phdthesis, York University Toronto, Ontario, May 2019.

[111] J. C. Maxwell Garnett. Xii. colours in metal glasses and in metallic films. *Philosophical Transactions of the Royal Society of London. Series A, Containing Papers of a Mathematical or Physical Character*, 203(359-371):385–420, 1904.

[112] Von D. A. G. Bruggeman. Berechnung verschiedener physikalischer konstanten von heterogenen substanzen. i. dielektrizitätskonstanten und leitfähigkeiten der mischkörper aus isotropen substanzen. *Annalen der physik*, 416(7):636–664, 1935.

[113] D. C. Dube and R. Parshad. Study of böttcher's formula for dielectric correlation between powder and bulk. *Journal of Physics D: Applied Physics*, 3(5):677, 1970.

[114] M. D. Benadda, J. C. Carru, J. P. Amoureux, M. Castelain, and A. Chapoton. Experimental and theoretical study of the dielectric properties of 1-cyanoadamantane; spectrum of the compact crystal from measurements on powder. *Journal of Physics D: Applied Physics*, 15(8):1477, 1982.

[115] Rob J. Adams, Warren F. Perger, William I. Rose, and Alex Kostinski. Measurements of the complex dielectric constant of volcanic ash from 4 to 19 ghz. *Journal of Geophysical Research: Solid Earth*, 101(B4):8175–8185, 1996.

[116] H. Looyenga. Dielectric constants of heterogeneous mixtures. *Physica*, 31(3):401–406, 1965.

[117] Lev Davidovich Landau, John Stewart Bell, M. J. Kearsley, L. P. Pitaevskii, E. M. Lifshitz, and J. B. Sykes. *Electrodynamics of continuous media*, volume 8. elsevier, 2013.

[118] William M. Merrill, Rodolfo E. Diaz, Michael M. LoRe, Mark C. Squires, and Nicolaos G. Alexopoulos. Effective medium theories for artificial materials composed of multiple sizes of spherical inclusions in a host continuum. *IEEE Transactions on antennas and propagation*, 47(1):142–148, 1999.

[119] J. Robert Birchak, C. Gerald Gardner, Jackie E. Hipp, and Joe M. Victor. High dielectric constant microwave probes for sensing soil moisture. *Proceedings of the IEEE*, 62(1):93–98, 1974.

[120] Anatolij M. Shutko and E. M. Reutov. Mixture formulas applied in estimation of dielectric and radiative characteristics of soils and grounds at microwave frequencies. *IEEE Transactions on Geoscience and Remote Sensing*, (1):29–32, 1982.

[121] L. C. Shen, W. C. Savre, J. M. Price, and K. Athavale. Dielectric properties of reservoir rocks at ultra-high frequencies. *geophysics*, 50(4):692–704, 1985.

[122] Michael David Knoll. A petrophysical basis for ground penetrating radar and very early time electromagnetics: Electrical properties of sand-clay mixtures, 1996.

[123] Karl Lichtenecker. Die dielektrizitatskonstante naturlicher und kunstlicher mischkorper. *Physikalische Zeitschrift*, 27:115–158, 1926.

[124] A. V. Goncharenko, V. Z. Lozovski, and E. F. Venger. Lichtenecker's equation: applicability and limitations. *Optics Communications*, 174(1-4):19–32, 2000.

[125] Tarik Zakri, Jean-Paul Laurent, and Michel Vauclin. Theoretical evidence forlichtenecker's mixture formulae'based on the effective medium theory. *Journal of Physics D: Applied Physics*, 31(13):1589, 1998.

[126] Marcel Michel Yvon Saint-Amant. Frequency and temperature dependence of dielectric properties of some common rocks, 1968.

[127] G.R Olhoeft and D.W Strangway. Dielectric properties of the first 100 meters of the moon. *Earth and planetary science letters*, 24(3):394–404, 1975.

[128] Grant Heiken, David Vaniman, and Bevan M. French. *Lunar sourcebook: A user's guide to the Moon*. Number 1259. Cup Archive, 1991.

[129] Howard E. Bussey. Microwave dielectric measurements of lunar soil with a coaxial line resonator method. volume 10, pages 2175–2182, 1979.

[130] James B. Garvin, James W. Head, Gordon H. Pettengill, and Stanley H. Zisk. Venus global radar reflectivity and correlations with elevation. *Journal of Geophysical Research: Solid Earth*, 90(B8):6859–6871, 1985.

[131] W. David Carrier III, Gary R. Olhoeft, and Wendell Mendell. Physical properties of the lunar surface. *Lunar sourcebook, a user's guide to the moon*, pages 475–594, 1991.

[132] Bruce A. Campbell. *Radar remote sensing of planetary surfaces*. Cambridge University Press, 2002.

[133] M. Barmatz, D. Steinfeld, D. Winterhalter, D. Rickman, R. Gustafson, D. Butts, and M. Weinstein. Microwave permittivity and permeability measurements on lunar simulants. Number 1659, page 1050, 2012.

[134] Dylan Hickson, Alexandre Boivin, Michael G Daly, Rebecca Ghent, Michael C Nolan, Kimberly Tait, Alister Cunje, and Chun An Tsai. Near surface bulk density estimates of neas from radar observations and permittivity measurements of powdered geologic material. *Icarus (New York, N.Y. 1962)*, 306:16–24, 2018.

[135] Zvi Hashin and Shmuel Shtrikman. A variational approach to the theory of the effective magnetic permeability of multiphase materials. *Journal of applied Physics*, 33(10):3125–3131, 1962.

[136] Gustave E. Archie. The electrical resistivity log as an aid in determining some reservoir characteristics. *Transactions of the AIME*, 146(01):54–62, 1942.

[137] R. Freedman. Letter to the editor: Moving beyond archie's legacy in the 21st century. *Petrophysics*, 50(6):468, 2009.

[138] W. David Kennedy and David C. Herrick. Conductivity models for archie rocks. *Geophysics*, 77(3):WA109–WA128, 2012.

[139] P. N. Sen, C. Scala, and M. H. Cohen. A self-similar model for sedimentary rocks with application to the dielectric constant of fused glass beads. *Geophysics*, 46(5):781–795, 1981.

[140] Victor F. Petrenko and Robert W. Whitworth. *Physics of Ice*. Oxford University Press, 01 2002.

[141] Colin Snodgrass, Jessica Agarwal, Michael Combi, Alan Fitzsimmons, Aurelie Guilbert-Lepoutre, Henry H. Hsieh, Man-To Hui, Emmanuel Jehin, Michael S. P. Kelley, and Matthew M. Knight. The main belt comets and ice in the solar system. *The Astronomy and Astrophysics Review*, 25:1–59, 2017.

[142] David J. Lawrence, William C. Feldman, John O. Goldsten, Sylvestre Maurice, Patrick N. Peplowski, Brian J. Anderson, David Bazell, Ralph L. McNutt Jr, Larry R. Nittler, and Thomas H. Prettyman. Evidence for water ice near mercury's north pole from messenger neutron spectrometer measurements. *Science*, 339(6117):292–296, 2013.

[143] Anthony Colaprete, Peter Schultz, Jennifer Heldmann, Diane Wooden, Mark Shirley, Kimberly Ennico, Brendan Hermalyn, William Marshall, Antonio Ricco, and Richard C. Elphic. Detection of water in the lcross ejecta plume. *science*, 330(6003):463–468, 2010.

[144] Jean-Pierre Bibring, Yves Langevin, François Poulet, Aline Gendrin, Brigitte Gondet, Michel Berthé, Alain Soufflot, Pierre Drossart, Michel Combes, and Giancarlo Bellucci. Perennial water ice identified in the south polar cap of mars. *Nature*, 428(6983):627–630, 2004.

[145] John C. Armstrong, Timothy N. Titus, and Hugh H. Kieffer. Evidence for subsurface water ice in korolev crater, mars. *Icarus*, 174(2):360–372, 2005.

[146] H. B. Niemann, S. K. Atreya, G. R. Carignan, T. M. Donahue, J. A. Haberman, D. N. Harpold, R. E. Hartle, D. M. Hunten, W. T. Kasprzak, and P. R. Mahaffy. The composition of the jovian atmosphere as determined by the galileo probe mass spectrometer. *Journal of Geophysical Research: Planets*, 103(E10):22831–22845, 1998.

[147] Kevin H. Baines, Mona L. Delitsky, Thomas W. Momary, Robert H. Brown, Bonnie J. Buratti, Roger N. Clark, and Philip D. Nicholson. Storm clouds on saturn: Lightning-induced chemistry and associated materials consistent with cassini/vims spectra. *Planetary and Space Science*, 57(14-15):1650–1658, 2009.

[148] Philip D. Nicholson, Matthew M. Hedman, Roger N. Clark, Mark R. Showalter, Dale P. Cruikshank, Jeffrey N. Cuzzi, Gianrico Filacchione, Fabrizio Capaccioni, Priscilla Cerroni, and Gary B. Hansen. A close look at saturn's rings with cassini vims. *Icarus*, 193(1):182–212, 2008.

[149] Bin Yang, Jacqueline Keane, Karen Meech, Tobias Owen, and Richard Wainscoat. Multi-wavelength observations of comet c/2011 l4 (pan-starrs). *The Astrophysical Journal Letters*, 784(2):L23, 2014.

[150] Maria Cristina De Sanctis, Fabrizio Capaccioni, Mauro Ciarniello, Gianrico Filacchione, Michelangelo Formisano, S. Mottola, Andrea Raponi, Federico Tosi, D. Bockelée-Morvan, and S. Erard. The diurnal cycle of water ice on comet 67p/churyumov-gerasimenko. *Nature*, 525(7570):500–503, 2015.

[151] P. C. Thomas, J. Wm Parker, L. A. McFadden, Cc T. Russell, S. A. Stern, M. V. Sykes, and E. F. Young. Differentiation of the asteroid ceres as revealed by its shape. *Nature*, 437(7056):224–226, 2005.

[152] Chadwick A. Trujillo, Scott S. Sheppard, and Emily L. Schaller. A photometric system for detection of water and methane ices on kuiper belt objects. *The Astrophysical Journal*, 730(2):105, 2011.

[153] W. M. Grundy, R. P. Binzel, B. J. Buratti, J. C. Cook, D. P. Cruikshank, C. M. Dalle Ore, A. M. Earle, K. Ennico, C. J. A. Howett, and A. W. Lunsford. Surface compositions across pluto and charon. *Science*, 351(6279):aad9189, 2016.

[154] F. Franks. The properties of ice. pages 115–149. Springer, 1972.

[155] Niels Bjerrum. Structure and properties of ice. *Science*, 115(2989):385–390, 1952.

[156] Erland M. Schulson. The structure and mechanical behavior of ice. *Jom*, 51:21–27, 1999.

[157] John D. Bernal and Ralph H. Fowler. A theory of water and ionic solution, with particular reference to hydrogen and hydroxyl ions. *J. chem. Phys*, 1(8):515–548, 1933.

[158] G. P. Johari and Edward Whalley. The dielectric properties of ice ih in the range 272-133 k. *The Journal of Chemical Physics*, 75(3):1333–1340, 1981.

[159] Claude Jaccard. Étude théorique et expérimentale des propriétés électriques de la glace, 1959.

[160] Claude Jaccard. Thermodynamics of irreversible processes applied to ice. *Physik der kondensierten Materie*, 3:99–118, 1964.

[161] Robert P. Auty and Robert H. Cole. Dielectric properties of ice and solid d2o. *The Journal of Chemical Physics*, 20(8):1309–1314, 1952.

[162] Syuji Kawada. Dielectric anisotropy in ice ih. *Journal of the Physical Society of Japan*, 44(6):1881–1886, 1978.

[163] S. R. Gough and D. W. Davidson. Dielectric behavior of cubic and hexagonal ices at low temperatures. *The Journal of Chemical Physics*, 52(10):5442–5449, 1970.

[164] Gyan P. Johari and Sheila J. Jones. Dielectric properties of polycrystalline d2o ice ih (hexagonal). *Proceedings of the Royal Society of London. A. Mathematical and Physical Sciences*, 349(1659):467–495, 1976.

[165] Vasily G. Artemov. A unified mechanism for ice and water electrical conductivity from direct current to terahertz. *Physical Chemistry Chemical Physics*, 21(15):8067–8072, 2019.

[166] S. R. Gough. A low temperature dielectric cell and the permittivity of hexagonal ice to 2 k. *Canadian Journal of Chemistry*, 50(18):3046–3051, 1972.

[167] Peter Victor Hobbs. *Ice physics*. OUP Oxford, 2010.

[168] Ivan Popov, Ivan Lunev, Airat Khamzin, Anna Greenbaum (Gutina), Yuri Gusev, and Yuri Feldman. The low-temperature dynamic crossover in the dielectric relaxation of ice ih. *Phys. Chem. Chem. Phys.*, 19:28610–28620, 2017.

[169] Airat A. Khamzin, Ivan V. Lunev, Ivan I. Popov, Anna M. Greenbaum, and Yuri D. Feldman. Mechanisms of dielectric relaxation of hexagonal ice. *Radioelektron. Nanosistemy Inf. Tehnol*, 12:87–94, 2020.

[170] Iwao Takei and Norikazu Maeno. Dielectric properties of single crystals of hcl doped ice. *The Journal of chemical physics*, 81(12):6186–6190, 1984.

[171] F. Humbel, F. Jona, and P. Scherrer. Anisotropie der dielektrizitatskonstante des eises. *Helvetica Physica Acta*, 26(1):17–32, 1953.

[172] Kaito Sasaki, Rio Kita, Naoki Shinyashiki, and Shin Yagihara. Dielectric relaxation time of ice-ih with different preparation. *The Journal of Physical Chemistry B*, 120(16):3950–3953, 2016.

[173] G. P. Johari and S. J. Jones. The orientation polarization in hexagonal ice parallel and perpendicular to the c-axis. *Journal of Glaciology*, 21(85):259–276, 1978.

[174] M. R. Vant, R. O. Ramseier, and V. Makios. The complex-dielectric constant of sea ice at frequencies in the range 0.1-40 ghz. *Journal of Applied Physics*, 49(3):1264–1280, 1978.

[175] Andrew Assur. *Composition of sea ice and its tensile strength*, volume 44. US Army Snow, Ice and Permafrost Research Establishment, 1960.

[176] Guenther Frankenstein and Robert Garner. Equations for determining the brine volume of sea ice from -0.5 to -22.9 °c. *Journal of Glaciology*, 6(48):943–944, 1967.

[177] Kazuo Fujino. Electrical properties of sea ice. *Physics of Snow and Ice: proceedings*, 1(1):633–648, 1967.

[178] John Rundle Addison. Electrical properties of saline ice. *Journal of Applied Physics*, 40(8):3105–3114, 1969.

[179] J. R. Addison. Electrical relaxation in saline ice. *Journal of Applied physics*, 41(1):54–63, 1970.

[180] Rexford M. Morey, Austin Kovacs, and Gordon F. N. Cox. Electromagnetic properties of sea ice. *Cold Regions Science and Technology*, 9(1):53–75, 1984.

[181] A. Kovacs, R.M. Morey, and G.F.N. Cox. Modeling the electromagnetic property trends in sea ice, part i. *Cold Regions Science and Technology*, 14(3):207–235, 1987.

[182] Bryn Hubbard, Jean-Louis Tison, Frank Pattyn, Marie Dierckx, Thierry Boereboom, and Denis Samyn. Optical-televiewer-based identification and characterization of material facies associated with an antarctic ice-shelf rift. *Annals of Glaciology*, 53(60):137–146, 2012.

[183] Mike Craven, Ian Allison, Helen Amanda Fricker, and Roland Warner. Properties of a marine ice layer under the amery ice shelf, east antarctica. *Journal of Glaciology*, 55(192):717–728, 2009.

[184] John C. Moore, Andrew P. Reid, and Josef Kipfstuhl. Microstructure and electrical properties of marine ice and its relationship to meteoric ice and sea ice. *Journal of Geophysical Research: Oceans*, 99(C3):5171–5180, 1994.

[185] Robert E Grimm, David E Stillman, Steven F Dec, and Mark A Bullock. Low-frequency electrical properties of polycrystalline saline ice and salt hydrates. *The journal of physical chemistry. B*, 112(48):15382–15390, 2008.

[186] A. Stogryn. Equations for calculating the dielectric constant of saline water (correspondence). *IEEE transactions on microwave theory and Techniques*, 19(8):733–736, 1971.

[187] Jeffrey J. Plaut, Giovanni Picardi, Ali Safaeinili, Anton B. Ivanov, Sarah M. Milkovich, Andrea Cicchetti, Wlodek Kofman, Jérémie Mouginot, William M. Farrell, and Roger J. Phillips. Subsurface radar sounding of the south polar layered deposits of mars. *science*, 316(5821):92–95, 2007.

[188] David E. Stillman, Robert E. Grimm, and Steven F. Dec. Low-frequency electrical properties of ice silicate mixtures. *The Journal of Physical Chemistry B*, 114(18):6065–6073, 2010.

[189] E. Mattei, S. E. Lauro, G. Vannaroni, B. Cosciotti, F. Bella, and E. Pettinelli. Dielectric measurements and radar attenuation estimation of ice/basalt sand mixtures as martian polar caps analogues. *Icarus*, 229:428–433, 2014.

[190] A. Herique, J. Gilchrist, W. Kofman, and J. Klinger. Dielectric properties of comet analog refractory materials. *Planetary and Space Science*, 50(9):857–863, 2002.

[191] David M. Pozar. *Microwave engineering.* Wiley, 2007.

[192] Sebastian Lauro. Note sulla teoria delle linee di trasmissioni e le misure delle proprietà elettromagnetiche.

[193] Lin-Feng Chen, Chong Kim Ong, C. P. Neo, Vasundara V. Varadan, and Vijay K. Varadan. *Microwave electronics: measurement and materials characterization.* John Wiley & Sons, 2004.

[194] James Baker-Jarvis, Eric J. Vanzura, and William A. Kissick. Improved technique for determining complex permittivity with the transmission/reflection method. *IEEE Transactions on microwave theory and techniques*, 38(8):1096–1103, 1990.

[195] A. M. Nicolson and G. F. Ross. Measurement of the intrinsic properties of materials by time-domain techniques. *IEEE Transactions on instrumentation and measurement*, 19(4):377–382, 1970.

[196] William B. Weir. Automatic measurement of complex dielectric constant and permeability at microwave frequencies. *Proceedings of the IEEE*, 62(1):33–36, 1974.

[197] A. H. Boughriet, C. Legrand, and A. Chapoton. Noniterative stable transmission/reflection method for low-loss material complex permittivity determination. *IEEE Transactions on Microwave Theory Techniques*, 45(1):52–57, January 1997.

[198] Elisabetta Mattei, Sebastian Emanuel Lauro, Elena Pettinelli, and Giuliano Vannaroni. Coaxial-cage transmission line for electromagnetic parameters estimation. *IEEE transactions on instrumentation and measurement*, 62(11):2938–2942, 2013.

[199] J. Baker-Jarvis. Transmission/reflection and short-circuit line permittivity measurements. NASA STI/Recon Technical Report N, July 1990.

[200] Andrew P. Gregory and R. N. Clarke. Tables of the complex permittivity of dielectric reference liquids at frequencies up to 5 ghz. 2012.

[201] F. X. Hassion and R. H. Cole. Dielectric Properties of Liquid Ethanol and 2-Propanol. *The Journal of Chemical Physics*, 23(10):1756–1761, 10 1955.

[202] I. ISO. and B. I. P. M. OIML. *Guide to the Expression of Uncertainty in Measurement.* Aenor, 1993.

[203] John Taylor. An introduction to error analysis: The study of uncertainties in physical measurements, 1997.

[204] Yann Brouet, Luisa Neves, Pierre Sabouroux, Anny Chantal Levasseur-Regourd, Olivier Poch, Pierre Encrenaz, Antoine Pommerol, Nicolas Thomas, and Wlodek Kofman. Characterization of the permittivity of controlled porous water ice-dust mixtures to support the radar exploration of icy bodies. *Journal of Geophysical Research: Planets*, 121(12):2426–2443, 2016.

[205] A. L. Boivin, D. Hickson, C. Tsai, A. Cunje, R. R. Ghent, and M. G. Daly. Broadband measurements of the complex permittivity of carbonaceous asteroid regolith analog materials. *Journal of Geophysical Research: Planets*, 123(12):3088–3104, 2018.

[206] Barbara Cosciotti. *Dielectric measurements of Europa's and Mars' ice shell: implication for radar exploration.* PhD thesis, Università degli Studi Roma Tre, 2014.

[207] Klaus Mosegaard and Albert Tarantola. Probabilistic approach to inverse problems. *International Geophysics Series*, 81(A):237–268, 2002.

[208] Albert Tarantola. *Inverse problem theory and methods for model parameter estimation.* SIAM, 2005.

[209] Andreĭ Nikolaevich Kolmogorov and Albert T. Bharucha-Reid. *Foundations of the theory of probability: Second English Edition.* Courier Dover Publications, 2018.

[210] Nicholas Metropolis, Arianna W. Rosenbluth, Marshall N. Rosenbluth, Augusta H. Teller, and Edward Teller. Equation of state calculations by fast computing machines. *The journal of chemical physics*, 21(6):1087–1092, 1953.

[211] S. Calvari, M. Coltelli, M. Neri, M. Pompilio, and V. Scribano. The 1991-1993 etna eruption: Chronology and lava. *Acta Vulcanologica*, 4:1–14, 1994.

[212] Alessandro Brin, Giulia Salari, Sebastian Emanuel Lauro, Barbara Cosciotti, Elisabetta Mattei, and Elena Pettinelli. Electromagnetic and geochemical characterization of volcanic rock samples in the framework of radar exploration of terrestrial planets. pages EPSC2022–956, 2022.

[213] Monica Grady, Giovanni Pratesi, and Vanni Moggi Cecchi. Atlas of meteorites. *Atlas of Meteorites*, 2014.

[214] Philip A. Bland, Gordon Cressey, and Olwyn N. Menzies. Modal mineralogy of carbonaceous chondrites by x-ray diffraction and mössbauer spectroscopy. *Meteoritics & Planetary Science*, 39(1):3–16, 2004.

[215] Philip T. Metzger, Daniel T. Britt, Stephen Covey, Cody Schultz, Kevin M. Cannon, Kevin D. Grossman, James G. Mantovani, and Robert P. Mueller. Measuring the fidelity of asteroid regolith and cobble simulants. *Icarus*, 321:632–646, 2019.

[216] Daniel T. Britt, Kevin M. Cannon, Kerri Donaldson Hanna, Joanna Hogancamp, Olivier Poch, Pierre Beck, Dayl Martin, Jolantha Escrig, Lydie Bonal, and Philip T. Metzger. Simulated asteroid materials based on carbonaceous chondrite mineralogies. *Meteoritics & Planetary Science*, 54(9):2067–2082, 2019.

[217] Dustin M. Schroeder, Julian A. Dowdeswell, Martin J. Siegert, Robert G. Bingham, Winnie Chu, Emma J. MacKie, Matthew R. Siegfried, Katherine I. Vega, John R. Emmons, and Keith Winstein. Multidecadal observations of the antarctic ice sheet from restored analog radar records. *Proceedings of the National Academy of Sciences*, 116(38):18867–18873, 2019.

[218] Sebastian Emanuel Lauro, Elena Pettinelli, Graziella Caprarelli, Luca Guallini, Angelo Pio Rossi, Elisabetta Mattei, Barbara Cosciotti, Andrea Cicchetti, Francesco Soldovieri, Marco Cartacci, Federico Di Paolo, Raffaella Noschese, and Roberto Orosei. Multiple subglacial water bodies below the south pole of mars unveiled by new marsis data. *Nature Astronomy*, 5(1):63–70, 2021.

[219] Leonard J. Porcello, Roland L. Jordan, Jerrys. Zelenka, G. F. Adams, R. J. Phillips, W. E. Brown, S. H. Ward, and P. L. Jackson. The apollo lunar sounder radar system. *Proceedings of the IEEE*, 62(6):769–783, 1974.

[220] M. S. Robinson, P. C. Thomas, J. Veverka, S. L. Murchie, and B. B. Wilcox. The geology of 433 eros. *Meteoritics & Planetary Science*, 37(12):1651–1684, 2002.

[221] Henning Haack, Kaare L. Rasmussen, and Paul H. Warren. Effects of regolith/megaregolith insulation on the cooling histories of differentiated asteroids. *Journal of Geophysical Research: Solid Earth*, 95(B4):5111–5124, 1990.

[222] David Stillman and Gary Olhoeft. Frequency and temperature dependence in electromagnetic properties of martian analog minerals. *Journal of Geophysical Research: Planets*, 113(E9), 2008.

[223] Katherine de Kleer, Bryan Butler, Imke de Pater, Mark A. Gurwell, Arielle Moullet, Samantha Trumbo, and John Spencer. Ganymede's surface properties from millimeter and infrared thermal emission. *The Planetary Science Journal*, 2(1):5, jan 2021.

[224] John Robert Spencer. Surfaces of europa, ganymede, and callisto: an investigation using voyager iris thermal infrared spectra. Technical report, 1987.

[225] David R. Lide. *CRC handbook of chemistry and physics*, volume 85. CRC press, 2004.

[226] Gordon F. N. Cox and Wilford F. Weeks. Equations for determining the gas and brine volumes in sea-ice samples. *Journal of Glaciology*, 29(102):306–316, 1983.

[227] Airat A. Khamzin, Almaz I. Nasybullin, and Alexander S. Nikitin. Theoretical description of dielectric relaxation of ice with low concentration impurities. *Chemical Physics*, 541:111040, 2021.